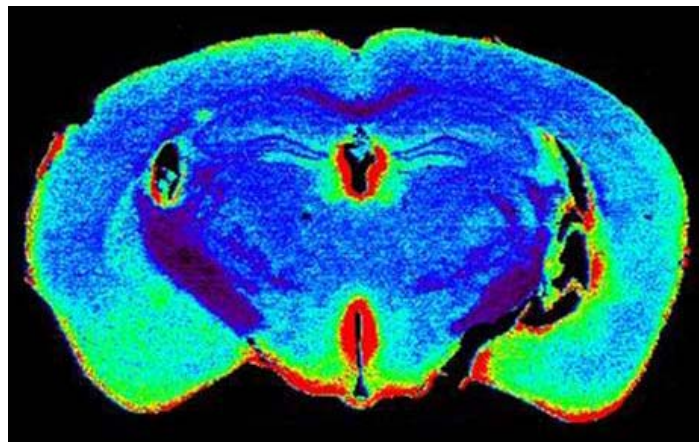


Instrumental considerations and applications of elemental bio-imaging

by Jessica Lear



A thesis submitted for the
Degree of Doctor of Philosophy (Science)
University of Technology, Sydney

2012

Certificate of authorship and originality

I certify that the work in this thesis has not previously been submitted for a degree nor has it been submitted as part of the requirements for a degree except as fully acknowledged within the text.

I also certify that the thesis has been written by me. Any help that I have received in my research work and the preparation of the thesis itself has been acknowledged. In addition, I certify that all the information sources and literature used are indicated in the thesis.

Jessica Lear

For Peter and Phyllis

Acknowledgements

Although it's just my name that appears on the cover page, there are a number of people who have been a part of this project's evolution either by direct involvement, funding or support, or simply buying me caffeinated beverages and sugary goodness.

Firstly, I'd like to acknowledge and thank Prof Philip Doble for his supervision, guidance and support throughout the project. His expert knowledge and enthusiasm for analytical chemistry was the reason I shifted towards this field in chemistry and decided to dedicate the last three years to this subject. His excitement regarding my work often exceeded my own and gave me the motivation to continue. His support has resulted in this project providing me with a great deal of experience which is not limited to chemistry.

My co-supervisor, Dr Dominic Hare, has also provided a great deal of support and his experience in all things ICP-MS was extremely useful. His assistance throughout the project has enabled me to complete the work in this timeframe as his expertise provided a solid foundation for the instrumental analyses. His feedback is always greatly appreciated and has helped transform my writing into a mature, academic and fit-for-purpose style.

I'd like to thank the members of the ICP-MS research group including Christine Austin, Amanda Van Gramberg and Alison Beavis for their support and help throughout the project. Thank you to Christine for using the ICP-MS before me so many times and tuning it wonderfully, and Amanda for listening to my thoughts about instrument functionality. Also thank you to Ilona Kramer and David Bishop for running the labs so efficiently. Dave's help was always greatly appreciated.

I'd like to mention and thank Fred Fryer from Agilent Technologies for providing unmatched experience and expertise in the ICP-MS field and allowing me to soak it all in.

Thank you to my collaborators, Paul Adlard and David Finkelstein at the MHRI, and Stephen Robinson from Monash University for the preparation of my brain samples and their expert interpretations of the results.

I'd also like to thank all of my friends for their support throughout this project. They have provided some wonderful memories and have allowed me to escape the clutches of monotonous data analyses with the consumption of cocktails and dumplings (not together).

Thank you to my family who have always been supportive of my undertakings. They're probably one of the least stressful families to be a part of. My parents have provided me with significant financial support over the years and I'd like to thank them for letting me invade their house again while I've had no idea what's happening with my career now I'm at the end of my PhD (and scholarship).

The final thank you goes to Rami Paul. I met him a week before I started my project and he has been there for me throughout. Rami's ability to take my mind off the project's more stressful aspects can't be matched and I appreciate every single little thing he has brought to my life.

Table of Contents

CERTIFICATE OF AUTHORSHIP AND ORIGINALITY	II
ACKNOWLEDGEMENTS	IV
LIST OF FIGURES	XI
LIST OF TABLES	XVIII
LIST OF PUBLICATIONS.....	XXII
LIST OF CONFERENCE PRESENTATIONS.....	XXIII
ABBREVIATIONS	XXIV
ABSTRACT	XXVI
CHAPTER 1: INTRODUCTION.....	2
1.1 ELEMENTAL BIO-IMAGING	2
1.2 LA-ICP-MS	2
1.2.1 Inductively coupled plasma - mass spectrometry.....	3
1.2.1.1 Inductively coupled plasma ion source.....	4
1.2.1.2 Mass spectrometry	6
1.2.1.2.1 Mass analysers.....	7
1.2.1.2.2 Mass detectors	10
1.2.2 Laser ablation.....	12
1.2.2.1 Lasers used in LA-ICP-MS	13
1.2.2.2 Ablation cell dynamics	16
1.2.3 Considerations for LA-ICP-MS.....	20
1.2.3.1 Elemental fractionation	20
1.2.3.2 Interferences.....	21
1.3 IMAGING USING LA-ICP-MS	25
1.3.1 Imaging methods.....	29
1.3.2 Quantification strategies.....	30

1.3.3	<i>Future direction of EBI</i>	35
1.4	PROJECT AIMS.....	36
CHAPTER 2:	EXPERIMENTAL	38
2.1	INSTRUMENTATION	38
2.1.1	<i>Inductively coupled plasma – mass spectrometer</i>	38
2.1.2	<i>Laser ablation</i>	39
2.1.3	<i>Solution ICP-MS operational parameters</i>	40
2.1.4	<i>LA-ICP-MS operational parameters</i>	41
2.2	DATA ACQUISITION AND PROCESSING.....	44
2.2.1	<i>Data acquisition</i>	44
2.2.2	<i>Data manipulation</i>	48
2.2.2.1	Normalisation and data organisation	48
2.2.2.2	Background subtraction.....	50
2.2.3	<i>Image construction</i>	51
2.3	EXPERIMENTAL METHODS.....	53
2.3.1	<i>Tissue standard preparation</i>	53
2.3.1.1	Microwave assisted acid digestion	56
2.3.1.2	Solution ICP-MS analysis.....	57
2.3.1.3	Tissue sectioning.....	58
2.3.1.4	LA-ICP-MS calibration	59
2.4	CALCULATIONS	61
2.4.1	<i>Linear regression analysis</i>	61
2.4.2	<i>Limits of analysis</i>	62
2.4.3	<i>Signal to noise ratios</i>	62
2.5	ANIMALS.....	63
2.5.1	<i>ZnT3 KO mouse brains</i>	63
2.5.2	<i>PBT-2 treated ZnT3 KO mice</i>	64

2.5.3	<i>AGE/Intermittent hypoxic mice</i>	65
CHAPTER 3:	IMPROVING MATRIX-MATCHED TISSUE STANDARD PREPARATION	68
3.1	CHAPTER OUTLINE.....	68
3.2	TISSUE HOMOGENEITY	70
3.3	CALIBRATION DATA	74
3.3.1	<i>SN-ICP-MS</i>	74
3.3.2	<i>LA-ICP-MS</i>	78
3.4	COMPARISON OF CALIBRATION DATA	81
3.5	CONCENTRATION RANGE AND NUMBER OF ANALYTES	82
3.6	CONCLUSIONS.....	84
CHAPTER 4:	INCREASING IMAGE ACQUISITION SPEED	86
4.1	CHAPTER OUTLINE.....	86
4.2	IMAGE CONSTRUCTION	88
4.3	LIMITATIONS TO SCAN CYCLE	90
4.4	LIMITS OF ANALYSIS.....	93
4.5	SIGNAL CARRY-OVER EXPERIMENTS.....	95
4.6	LASER FLUENCE	99
4.7	IMAGING WITH INCREASED LASER SCAN SPEED	99
4.7.1	<i>Background subtraction</i>	106
4.7.2	<i>Maintaining image dimensions</i>	108
4.8	CONCLUSIONS.....	109
CHAPTER 5:	APPLICATIONS OF INCREASED SPEED ELEMENTAL BIO-IMAGING	111
5.1	CHAPTER OUTLINE.....	111
5.2	BACKGROUND.....	112
5.2.1	<i>Neurodegeneration</i>	112
5.2.2	<i>Alzheimer's disease</i>	115
5.2.2.1	<i>AD pathogenesis</i>	115

5.3	APPLICATION 1: THE EFFECT OF PBT-2 ON METAL DISTRIBUTION IN THE BRAINS OF ZNT3 KO MICE.....	120
5.3.1	Outline.....	120
5.3.2	Treatment strategies for AD.....	121
5.3.3	ZnT3 knockout mice.....	125
5.3.4	Zinc deficits in ZnT3 KO animals.....	126
5.3.5	PBT-2 treated animals.....	129
5.3.5.1	Zinc.....	130
5.3.5.2	Other elements.....	133
5.4	APPLICATION 2: THE EFFECT OF AGES AND SLEEP APNOEA ON THE DISTRIBUTION OF METALS IN THE BRAIN	136
5.4.1	Outline.....	136
5.4.2	Advanced glycation end-products.....	138
5.4.3	Sleep apnoea and AD.....	143
5.4.4	Imaging.....	143
5.4.4.1	Effectiveness of the speed equation.....	145
5.4.4.2	Cobalt.....	146
5.4.4.3	Other elements.....	149
5.5	CONCLUSIONS.....	152
CHAPTER 6:	USING H₂ REACTIVE GAS TO IMPROVE SENSITIVITY FOR EBI.....	154
6.1	CHAPTER OUTLINE.....	154
6.2	RESTRICTIONS TO HIGH RESOLUTION EBI.....	156
6.3	THE REACTION CELL AND HYDROGEN AS A REACTIVE GAS.....	157
6.4	BACKGROUND LEVELS OF BIOLOGICALLY RELEVANT ANALYTES.....	162
6.5	CALIBRATION USING INCREASING VOLUMES OF HYDROGEN.....	165
6.5.1	Limits of analysis.....	166
6.5.2	Sensitivity.....	168
6.6	IMAGING USING INCREASING VOLUMES OF HYDROGEN.....	170
6.7	CONCLUSIONS.....	176

CHAPTER 7: HIGH RESOLUTION IMAGING EMPLOYING H₂ REACTIVE GAS.....	178
7.1 CHAPTER OUTLINE.....	178
7.2 PARKINSON'S DISEASE AND THE SUBSTANTIA NIGRA	179
7.3 IMAGING IRON AT HIGH RESOLUTION	181
7.3.1 <i>Images</i>	182
7.3.2 <i>Calibration</i>	186
7.4 CONCLUSION	190
CHAPTER 8: CONCLUSIONS AND RECOMMENDATIONS.....	192
APPENDIX.....	197
REFERENCES	200

List of figures

Figure 1-1: Analysis by ICP-MS.....	3
Figure 1-2: Schematic of ICP-MS interface [13; 14]	4
Figure 1-3: Formation of the inductively coupled plasma [14].....	5
Figure 1-4: Mechanism of conversion of a droplet to a positive ion in the ICP [14]	6
Figure 1-5: Diagram of a quadrupole mass analyser showing ion paths [22].....	9
Figure 1-6: Schematic of a discrete dynode electron multiplier [14]	11
Figure 1-7: Schematic of a typical Nd:YAG laser ablation unit [23]	12
Figure 1-8: Four energy level diagram for Nd ³⁺ ions in a Nd:YAG laser. Lasing occurs between the metastable levels [13; 25]	14
Figure 1-9: Schematic of a standard laser ablation cell [13].....	17
Figure 1-10: Schematic of the large format laser ablation cell.....	18
Figure 1-11: Particle size distribution after 40 second ablation of 40 µm craters in SRM 612 glass using argon and helium carrier gases [33]	19
Figure 1-12: A model for the differences in particle size distribution based on the thermal conductivities of the gases used in LA-ICP-MS [31]	20
Figure 1-13: Timeline of EBI	28
Figure 1-14: Workflow for imaging using LA-ICP-MS [1]	29
Figure 2-1: Agilent 7500ce ICP-MS.....	38
Figure 2-2: New Wave UP213 laser ablation unit fitted with a standard cell.....	39
Figure 2-3: Example of a microscope slide with sections of mouse brain prepared for LA-ICP-MS analysis.....	44

Figure 2-4: Representation of imaging experiments. Each line represents a scan file saved as a .csv file according to the numbers on the right.....	45
Figure 2-5: Laser traversing the surface of the sample in a continuous series of pulses, 20 Hz in these experiments	45
Figure 2-6: ICP-MS software showing the acquisition parameters and dwell times set for individual m/z	46
Figure 2-7: Example of a laser scan file for ⁶⁶ Zn represented as an x-y scatter plot prepared in MS Excel	47
Figure 2-8: A single scan file as opened from the saved .csv file.....	48
Figure 2-9: View of organised MS Excel data after utilising a macro in MS Excel	49
Figure 2-10: View of the organised MS Excel data after background subtraction. This particular section of data is mostly background so the majority of values are small or equal to zero.	50
Figure 2-11: a) Sequential scan files showing signal intensities for ⁶⁶ Zn; b) Image for ⁶⁶ Zn: the highlighted pixels indicate four sequential scan files	52
Figure 2-12: Flow-chart for tissue standard preparation.....	54
Figure 2-13: Acid digestion method.....	57
Figure 2-14: A typical signal profile for a tissue standard.....	59
Figure 3-1: Visual homogeneity of standards prepared using 1000 µg mL ⁻¹ single element standard solutions as observed through the microscope fitted to the laser ablation unit (500x magnification)	70
Figure 3-2: ¹³ C signal intensity during line ablation for tissue standards prepared using 1000 µg mL ⁻¹ standard single element solutions. Signal moves from gas blank to standard ablation and returns to gas blank.	71

Figure 3-3: Visual homogeneity of standards prepared using metal salt solutions as observed through the microscope fitted to the laser ablation unit (500x magnification).....	72
Figure 3-4: ^{13}C signal intensity during line ablation for tissue standards prepared using metal salt solutions. Signal moves from gas blank to standard ablation and returns to gas blank...	73
Figure 3-5: Comparison of the relative standard deviations of the ^{13}C signal during ablation of the prepared calibration standards	74
Figure 3-6: SN-ICP-MS calibration curves for each analyte in the aqueous standards.....	75
Figure 3-7: LA-ICP-MS calibration curves for each analyte in the tissue standards with error bars at 95% confidence.....	79
Figure 4-1: The effect of varying the laser scan speed on image dimensions	88
Figure 4-2: Counts per data point versus the dwell time of the quadrupole MS compared with the limiting signal at each dwell time for selected m/z. ($v_l = 3 \times \chi_s \mu\text{m}^{-1}$)	92
Figure 4-3: Limits of analysis with increasing v_l ($\chi_s = 30 \mu\text{m}^{-1}$).....	94
Figure 4-4: Washout times for a large format laser ablation cell	96
Figure 4-5: Comparison of normalised signal intensities for the total ion count (TIC) \pm standard deviations across laser spot diameters and increasing scan speed	97
Figure 4-6: Washout times for a standard laser ablation cell.....	98
Figure 4-7: Comparison of laser scan speed and resolution for ^{63}Cu using spot sizes of 15, 30, 65 and 100 μm where each segment broken by a dotted line indicates an increase in laser scan speed.....	102
Figure 4-8: Comparison of laser scan speed and resolution for ^{66}Zn using spot sizes of 15, 30, 65 and 100 μm where each segment broken by a dotted line indicates an increase in laser scan speed.....	103

Figure 4-9: Comparison of laser scan speed and resolution for ^{56}Fe using spot sizes of 15, 30, 65 and 100 μm where each segment broken by a dotted line indicates an increase in laser scan speed.....	104
Figure 4-10: Comparison of laser scan speed and resolution for ^{55}Mn using spot sizes of 15, 30, 65 and 100 μm where each segment broken by a dotted line indicates an increase in laser scan speed.....	105
Figure 4-11: Laser scan speed comparison for ^{56}Fe prior to background subtraction ($x_s = 15 \mu\text{m}$).....	106
Figure 4-12: Background drift of the isotopes imaged supporting the need for background subtraction in these experiments.....	107
Figure 4-13: Demonstration of the use of increased v_l while maintaining image dimensions equivalent to the original tissue section ($x_s = 30 \mu\text{m}$, $t_{sc} = 0.2372$ seconds and $v_l = 127 \mu\text{m s}^{-1}$).....	108
Figure 5-1: Reactive oxygen species generation by redox-active metals as the basis for neurodegenerative disorders that are related to oxidative damage [89].....	112
Figure 5-2: Model for the non-pathogenic metallobiology of β -amyloid ($\text{A}\beta$).....	116
Figure 5-3: Model for the metallobiology of β -amyloid ($\text{A}\beta$) in Alzheimer's Disease. Proposed sequence of events leading to AD [100].....	119
Figure 5-4: Chemical structure of Clioquinol (CQ).....	123
Figure 5-5: Proposed mechanism of action of clioquinol and similar metal-protein attenuation compounds (MPACs).....	124
Figure 5-6: Comparison of ^{66}Zn distribution in the brains of wild type mice and ZnT3 KO mice ($x_s = 40 \mu\text{m}$, $v_l = 40 \mu\text{m s}^{-1}$).....	128
Figure 5-7: Regions of interest from where data was extracted; RHS = right hand side, LHS = left hand side, CTX = cortex, Amyg = amygdala, 5 = hippocampus (HIPP), 1-4 = pyramidal layer of the hippocampus (HIPP).....	130

Figure 5-8: Images of ^{66}Zn for PBT-2 treated mouse brains compared to SSV mouse brains ($x_s = 30 \mu\text{m}$, $v_l = 120 \mu\text{m s}^{-1}$).....	131
Figure 5-9: Concentrations of $^{66}\text{Zn} \pm 95\%$ confidence interval for the selected regions of interest in PBT-2 and SSV mouse brains	132
Figure 5-10: Images of ^{63}Cu for PBT-2 treated mouse brains compared to SSV mouse brains ($x_s = 30 \mu\text{m}$, $v_l = 120 \mu\text{m s}^{-1}$).....	134
Figure 5-11: Images of ^{56}Fe for PBT-2 treated mouse brains compared to SSV mouse brains ($x_s = 30 \mu\text{m}$, $v_l = 120 \mu\text{m s}^{-1}$).....	135
Figure 5-12: Glucose and AGE formation pathways incorporating the polyol pathway and AGE formation by the α -oxoaldehydes glyoxal, methyl glyoxal and 3-DG. [114]	138
Figure 5-13: Formation of advanced glycation end-products (AGEs) starts by a reaction of the amino group of a protein and a reducing sugar (here: glucose) and completed by the reaction between 1,2-dicarbonyl compounds (here: glyoxal and methylglyoxal) and the Amadori product [115]	139
Figure 5-14: Structures of methylglyoxal-derived AGEs found in the Alzheimer's disease brain [115].....	142
Figure 5-15: Effectiveness of $v_l = x_s / t_{sc}$ in reproducing images with equivalent dimensions to the original tissue section	145
Figure 5-16: ^{59}Co distribution in the brains of LTIH and SIH mice fed low and high AGE diets, and control mice. Black and white images show where the brain sections should be had ^{59}Co been detected.....	147
Figure 5-17: Cobalt in Vitamin B ₁₂ (cobalamin).....	148
Figure 5-18: ^{63}Cu distribution in the brains of LTIH and SIH mice fed low and high AGE diets	149
Figure 5-19: ^{66}Zn distribution in the brains of LTIH and SIH mice fed low and high AGE diets	150

Figure 5-20: ^{57}Fe distribution in the brains of LTIH and SIH mice fed low and high AGE diets	151
Figure 6-1: Effect of varying x_s on the volume of tissue ablated per laser pulse ($h = 30 \mu\text{m}$)	157
Figure 6-2: Schematic of Agilent ICP-MS showing the Octopole Reaction System (ORS) cell [88]	158
Figure 6-3: Comparison of background signals; Log_{10} (counts per second) versus H_2 flow rate (mL min^{-1})	162
Figure 6-4: Comparison of the slope of calibration curves constructed for ^{56}Fe with increasing v_1 and increasing H_2 flow rates in the reaction cell. ($x_s = 30 \mu\text{m}$)	166
Figure 6-5: Limits of analysis ($\mu\text{g g}^{-1}$) for calibrated analytes with increasing H_2 flow rates in the reaction cell ($x_s = 30 \mu\text{m}$, $v_1 = 90 \mu\text{m s}^{-1}$)	167
Figure 6-6: Comparison of the LODs (dashed lines) and LOQs (solid lines) for ^{56}Fe and ^{44}Ca for H_2 flow rates of 0 (red) and 3 mL min^{-1} (blue) against the concentrations of the calibration standards	168
Figure 6-7: Signal (per $\mu\text{g g}^{-1}$) to noise ratios (SNR) for the calibrated analytes with increasing H_2 flow rates and increasing v_1 . ($x_s = 30 \mu\text{m}$, $v_1 = 30$ [○], 60 [■] and $90 \mu\text{m s}^{-1}$ [X])	169
Figure 6-8: Comparison of iron imaged with increasing H_2 flow rates	171
Figure 6-9: Comparison of ^{55}Mn imaged with increasing H_2 flow rates	172
Figure 6-10: Comparison of ^{63}Cu imaged with increasing H_2 flow rates	174
Figure 6-11: Comparison of ^{66}Zn imaged with increasing H_2 flow rates	175
Figure 7-1: Immunohistochemical stain of the right side of a section of mouse brain [1]. The area outlined corresponds to the area containing the SN. The area in the square represents an example of the area analysed in this experiment.	180
Figure 7-2: ^{56}Fe image of the lower left quarter of a mouse brain containing the substantia nigra	183

Figure 7-3: ^{63}Cu image of the lower left quarter of a mouse brain containing the substantia nigra 184

Figure 7-4: ^{66}Zn image of the lower left quarter of a mouse brain containing the substantia nigra 185

Figure 7-5: Signal to noise ratios for imaged isotopes using 3.0 and 0.0 mL min $^{-1}$ H $_2$ in the reaction cell..... 188

Figure 7-6: Comparison of the calibration data for ^{56}Fe with 3.0 and 0.0 mL min $^{-1}$ H $_2$ 189

List of tables

Table 1-1: Strengths and weaknesses of mass analysers [18]	7
Table 1-2: Characteristics of performance of mass analysers [19]	8
Table 1-3: Characteristic parameters of selected lasers used for LA-ICP-MS [13]	13
Table 1-4: Common polyatomic interferences from biological matrices. Adapted from [41] .	22
Table 1-5: Comparison of background signals measured by LA-ICP-MS and SN-ICP-MS; Adapted from [42]	24
Table 1-6: Main spatially resolved analytical techniques for chemical element imaging, quantification, and speciation in biological samples; adapted from [55]	26
Table 1-7: Advantages and drawbacks of quantification procedures for EBI [76]	32
Table 2-1: Typical operational parameters used during solution ICP-MS analysis using Agilent 7500ce ICP-MS	41
Table 2-2: Element concentrations in NIST Glass 612; * denotes certified value [84]	42
Table 2-3: Typical laser parameters used during tuning	42
Table 2-4: Typical operational parameters during LA-ICP-MS analysis in standard mode using Agilent 7500ce ICP-MS with cs lenses	43
Table 2-5: Typical operational parameters during LA-ICP-MS analysis in reaction mode using Agilent 7500ce ICP-MS with cs lenses. The same parameters were used for other volumes of H ₂ during the same analysis periods	43
Table 2-6: Representation of post-macro data organised into a single MS Excel file in Band Interleave by Line (BIL) format, prepared for interpretation by the ENVI Imaging Suite	49
Table 2-7: Soluble metal salts used to prepare high concentration salt solutions (Sigma-Aldrich)	54

Table 2-8: Approximate volume of concentrated salt solutions spiked into 5.0 g of chicken breast.....	55
Table 2-9: Approximate concentration of elements spiked into chicken breast.....	55
Table 2-10: Concentrations of elements in solution ICP-MS external calibration standards ($\mu\text{g kg}^{-1}$)	58
Table 2-11: Functions used for linear regression analysis in Excel and the corresponding calculations performed; where \bar{y} , \bar{x} and \bar{a} are sample averages; \hat{y} is the y-value calculated from the linear regression equation; n is the number of observations; y_0 is the average background signal	61
Table 2-12: Equations used for determining the limits of analysis; where y_0 is the average background signal, s_0 is the standard deviation of the background signal, b is the intercept, and m is the slope.....	62
Table 2-13: Equations used for calculating the signal to noise ratios; where y_0 is the average background signal, y_c is the average signal for a mid-range standard, and x_c is the known concentration of that mid-range standard.....	62
Table 3-1: Errors in the slope and intercept of the SN-ICP-MS calibration curves calculated using linear regression analysis, and the correlation coefficient, detection limit and background equivalent concentration calculated by the ICP-MS software	76
Table 3-2: Calculated analyte concentrations in each of the tissue standards prepared using metal salt solutions.....	77
Table 3-3: Errors in the slope and intercept, and the correlation coefficient, detection limit and background equivalent concentration of the LA-ICP-MS calibration curves calculated using linear regression analysis.	80
Table 3-4: Comparison of the error in slope, detection limits and correlation coefficient for the standards prepared with $1000 \mu\text{g mL}^{-1}$ solutions and those prepared with the metal salt solutions.....	81
Table 3-5: Volume of standard solutions added to tissue standards before homogenisation	82

Table 4-1: LA-ICP-MS operational parameters	90
Table 4-2: Selected minimum dwell times for each element in the prepared chicken standards	93
Table 4-3: Slopes of the calibration curves with increasing v_1 ($x_s = 30 \mu\text{m}$)	94
Table 5-1: Organisational framework for the involvement of metals in neurological diseases. The disorders listed are confined to instances where there is a prominent or primary neurological phenotype, and does not address secondary syndromes. Adapted from [89]	114
Table 5-2: Current symptomatic drug therapies for Alzheimer's disease [103-105].....	121
Table 5-3: LA-ICP-MS operational parameters prior to the development of imaging with increased v_1	127
Table 5-4: LA-ICP-MS operational parameters	129
Table 5-5: P-values from two-tailed t-tests assuming equal variances for the concentration of ^{66}Zn in selected regions of interest between PBT-2 and SSV mice	132
Table 5-6: P-values from two-tailed t-tests assuming equal variances for the concentration of ^{63}Cu in selected regions of interest between PBT-2 and SSV mice.....	133
Table 5-7: P-values from two-tailed t-tests assuming equal variances for the concentration of ^{56}Fe in selected regions of interest between PBT-2 and SSV mice	133
Table 5-8: Advanced glycation end-product (AGE) content of selected foods prepared by standard cooking methods [119; 120]	140
Table 5-9: LA-ICP-MS operational parameters	144
Table 5-10: Average concentrations of ^{59}Co in the mouse brain sections.....	146
Table 6-1: Possible reaction pathways that can resolve the analyte from interferences in a reaction cell [162]	158
Table 6-2: Important analytes for EBI analysis and their interferences	159

Table 6-3: LA-ICP-MS operational parameters	161
Table 7-1: LA-ICP-MS operational parameters	181
Table 7-2: Calibration statistics for isotopes with the use of reaction cell at 3.0 mL min ⁻¹ H ₂ , x _s = 6 μm; v _i = 16 μm s ⁻¹	186
Table 7-3: Calibration statistics for isotopes with the use of reaction cell at 0.0 mL min ⁻¹ H ₂ , x _s = 6 μm; v _i = 16 μm s ⁻¹	187

List of publications

- ❖ Lear, J., Hare, D., Adlard, P., Finkelstein, D., & Doble, P. (2012). Improving acquisition times of elemental bio-imaging for quadrupole-based LA-ICP-MS. *Journal of Analytical Atomic Spectrometry*, 27(1), 159-164.
- ❖ Lear, J., Hare, D., Fryer, F., Adlard, P., Finkelstein, D., & Doble, P. (2012). High-resolution elemental bio-imaging of Ca, Mn, Fe, Co, Cu and Zn employing LA-ICP-MS and hydrogen reaction gas. *Analytical Chemistry*, DOI: 10.1021/ac301156f
- ❖ Lear, J., Veasey, S. C., Zhu, Y., Doble, P., Hare, D., Wang, S., et al. (2012). Long-term Intermittent Hypoxia Results in Cobalt Accumulation in the Brain: Implications for Vitamin B12 in Obstructive Sleep Apnea. *Sleep*, Under Review.
- ❖ Austin, C., Fryer, F., Lear, J., Bishop, D., Hare, D., Rawling, T., Kirkup, L., McDonagh, A., & Doble, P. (2011). Factors affecting internal standard selection for quantitative elemental bio-imaging of soft tissues by LA-ICP-MS. *Journal of Analytical Atomic Spectrometry*, 26(7), 1494-1501.
- ❖ Hare, D., Lear, J., Bishop, D., Beavis, A., & Doble, P. (2012). Protocol for production of matrix-matched brain tissue standards for imaging by laser ablation-inductively coupled plasma-mass spectrometry. *Analytical Methods*, Under Review.
- ❖ Article in preparation by Paul Adlard and David Finkelstein of the Mental Health Research Institute (MHRI), Victoria; *PBT2: A Novel Neuroprotective Agent that Enhances Cognition in Ageing*

List of conference presentations

- ❖ Lear, J., Hare, D., & Doble, P. (2009). *Elemental bio-imaging of trace elements in neurological disorders: Improving the technique*. Paper presented at the 17th Annual RACI R&D Topics Conference.

- ❖ Lear, J., Hare, D., & Doble, P. (2011). *Elemental Bio-imaging: Can acquisition times be improved?* Paper presented at the 3rd International Symposium on Metallomics.

Abbreviations

µg	Micrograms
µm	Micrometres
AChE	Acetylcholinesterase
AD	Alzheimer's disease
AGE	Advanced glycation end-product
Ar	Argon
As	Arsenic
Aβ	Beta-amyloid
BBB	Blood brain barrier
BuChE	Butyrylcholinesterase
C	Carbon
Ca	Calcium
ChEI	Cholinesterase inhibitor
CNS	Central nervous system
Co	Cobalt
CPS	Counts per second
CQ	Clioquinol
CRM	Certified reference material
Cu	Copper
EBI	Elemental bio-imaging
Fe	Iron
g ⁻¹	per gram
H	Hydrogen
He	Helium
HNO ₃	Nitric acid
ICP	Inductively coupled plasma
K	Potassium
KO	Knockout
LA-ICP-MS	Laser ablation inductively coupled plasma mass spectrometry
LFC	Large format cell
<i>m/z</i>	Mass –to-charge ratio
MALDI	Matrix-assisted laser desorption/ionization
Mg	Magnesium

Mn	Manganese
MPAC	Metal-protein attenuation compound
MPO	Myeloperoxidase
MS	Mass spectrometry
Nd:YAG	Neodymium-doped yttrium aluminium garnet
NFT	Neurofibrillary tangles
Ni	Nickel
NIST	National Institute of Standards and Technology
NMDA	<i>N</i> -methyl-D-aspartate
O	Oxygen
P	Phosphorous
Pb	Lead
PBT-2	A second generation CQ derivative
PD	Parkinson's disease
Rh	Rhodium
RNS	Reactive nitrogen species
ROS	Reactive oxygen species
SRM	Standard reference material
s ⁻¹	per second
Se	Selenium
SN-ICP-MS	Solution nebulisation inductively coupled plasma mass spectrometry
TOF	Time-of-flight
Zn	Zinc
ZnT3	A synaptic zinc transporter
α ₂ M	α ₂ -Macroglobulin

Abstract

Elemental Bio-Imaging (EBI) is an established application of laser ablation inductively coupled plasma mass spectrometry (LA-ICP-MS) that determines spatial distributions of *in situ* trace element concentrations in thin sections of biological tissues. This project provides an examination of instrumental considerations relating to method development and refinement, and the utilisation of amended methods for the analysis of element concentration distributions in specific biological samples.

The first instrumental consideration examined improving the methods used for matrix-matched tissue standard preparation. The main disadvantage to the previously proposed tissue standard preparation was a decrease in the homogeneity of sectioned tissue as the concentrations of spiked elements increased. The decrease in homogeneity was due to the use of relatively low concentration ($1000 \mu\text{g mL}^{-1}$) certified single element standard solutions. Substituting the low concentration solutions for higher concentration solutions, prepared using soluble metal salts, allowed for smaller quantities of solution to be spiked into the tissue. This increased homogeneity and the ability to spike a greater number of analytes into each tissue standard.

The appropriateness of increasing laser scan speed for the reduction of total experimental analysis time was also examined. EBI experiments normally employ scan speeds where the distance traversed in one second is equal to or less than the diameter of the laser beam. Consequently, data for a higher-resolution (pixel size = $15 \mu\text{m} \times 15 \mu\text{m}$) image of a 5 mm x 5 mm tissue section can take upwards of 30 hours to acquire. Appropriate laser scan speeds may be calculated by consideration of the relationship between laser scan speed, laser spot diameter and the total scan cycle of the quadrupole mass analyser. A simple method to

calculate the laser scan speeds capable of reducing the acquisition time by up to a factor of five whilst maintaining dimensional integrity of the image is presented in this thesis.

Two applications were developed utilising increased laser scan speeds. Both applications were related to the study of the neurodegenerative disorder, Alzheimer's disease, and examined particular variables and their effects on the distribution of metals in the brain. The first application examined the effectiveness of a new drug, PBT-2, on the redistribution of elements in mouse brains with the zinc transporter-3 gene removed. Results indicated PBT-2 had little effect on the distribution of ^{66}Zn , ^{63}Cu and ^{56}Fe in the midbrain. The second application examined the effect of intermittent hypoxia and a diet of advanced glycation end-products on element distribution in the brain. The most intriguing results were seen in the images for ^{59}Co . A 100-fold elevation in the concentrations of ^{59}Co was observed between mice exposed to intermittent hypoxia, those in a control environment and wild-type mice not exposed to the experiment's settings.

An examination into the use of H_2 as a reaction gas was conducted. The improvement of the analytical performance of imaging experiments was considered for a range of masses with spectral interferences, including the $^{40}\text{Ar}^{16}\text{O}^+$ spectral interference on $^{56}\text{Fe}^+$. At low ($< 1.0 \text{ mL min}^{-1}$) H_2 flow rates, greater spectral interference due to H^+ adducts were observed for ^{57}Fe than with the reaction mode off. At higher flow rates, up to 3.0 mL H_2 per minute, the spectral interferences were reduced leading to an improvement in the limits of analysis for masses with O- and N-based polyatomic interferences.

EBI is typically performed using spatial resolutions of $30 \mu\text{m} \times 30 \mu\text{m}$ and above. Higher resolution imaging is desirable for many biological applications. As a culmination of the project, the combination of the use of improved matrix-matched tissue standards with the use of the reaction cell and increased image acquisition speeds was employed. The

combination of improved parameters resulted in a high quality image of the area of the brain including the substantia nigra being prepared at a resolution of $6\ \mu\text{m} \times 6\ \mu\text{m}$ for ^{56}Fe .

Chapter 1: Introduction

Chapter 1: Introduction

1.1 Elemental bio-imaging

Elemental bio-imaging (EBI) is an application of laser ablation inductively coupled plasma mass spectrometry (LA-ICP-MS) that is used to determine *in situ* trace element concentrations in thin sections of biological tissues [1-3]. Over recent years it has become a powerful tool for profiling spatial trace element distribution in tissue sections [4]. The technique has continued to evolve since early studies [5; 6], with focus now directed towards continued analytical development [7-9] and application to biological [10; 11] and clinical research [2; 3; 12]. Increased interest in LA-ICP-MS imaging from the biological community has continued to drive development towards high spatial resolution images approaching the dimensions of a single cell.

This chapter provides a discussion on the instrumentation and imaging techniques used for EBI.

1.2 LA-ICP-MS

LA-ICP-MS is used for direct analysis of the elemental and isotopic compositions of solid samples [13; 14]. The benefits of LA-ICP-MS are [14];

- analysis of a wide range of solid materials including biological materials
- elimination of labour intensive sample preparation
- minimisation of sample contamination as the sample is analysed directly
- reduction of polyatomic spectral interferences compared to SN-ICP-MS

- examination of microfeatures; and
- the possibility of elemental mapping of the sample surface.

1.2.1 Inductively coupled plasma - mass spectrometry

ICP-MS was developed as a commercial analytical technique in the early 1980s. It has been applied to almost every analytical field for the determination of the concentrations of trace, minor and major elements [14; 15]. The general process of ICP-MS analysis involves the introduction of the sample to be analysed into a nebulisation and particle size separation device, the atomisation and ionisation of small particles introduced to the ICP, and the detection and quantification of the ions generated. An outline of the processes involved in ICP-MS analysis is presented in Figure 1-1.

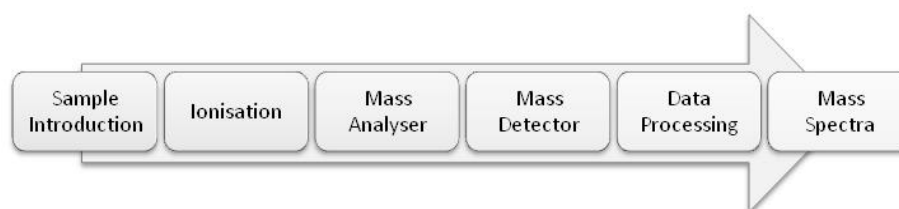


Figure 1-1: Analysis by ICP-MS

A schematic of the components of an ICP-MS is presented in Figure 1-2. The ICP generated in the torch using a radio frequency discharge is followed by a plasma sampling interface that allows ions to pass from atmospheric pressure into a vacuum (10^{-6} Torr), where the mass filter operates. Ion lenses focus the ion beam before it passes through the mass filter where ions are separated based on their mass to charge (m/z) ratio. Upon leaving the mass filter, ions are passed to the detector where quantification takes place and the resulting signal for each m/z is processed by computer software, resulting in mass spectra.

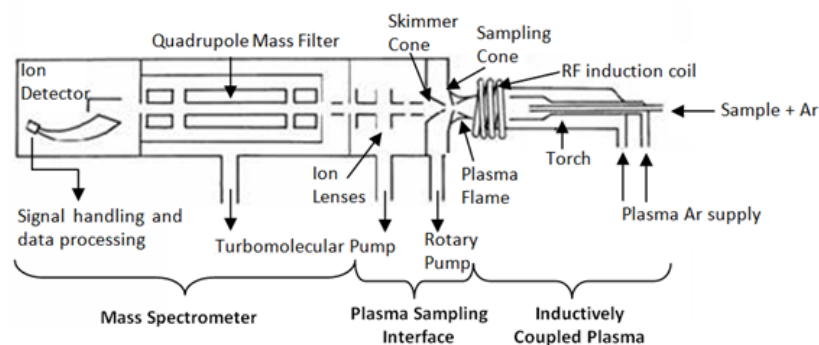


Figure 1-2: Schematic of ICP-MS interface [13; 14]

1.2.1.1 Inductively coupled plasma ion source

Inductively coupled plasma is one available inorganic ion source for mass spectrometry. The plasma source is made up of a hot flame produced by inductive coupling into which particulates are introduced [16]. A cooled induction coil surrounds the top of three concentric quartz tubes and this coil is powered by a radio frequency (RF) generator. Initially, the gas at atmospheric pressure is made conductive using a Tesla discharge that ionise the flowing argon gas. The Tesla discharge produces electrons that interact with the high frequency oscillating inductive field generated by the RF current. The high frequency accelerates the electrons and causes them to collide with the argon. The argon atoms are ionised by the collision with electrons. The argon ionisation and ion-electron recombination processes are balanced and the plasma is formed. Particle collisions heat the plasma to around 10 000 K and this plasma is isolated from the sides of the quartz torch by a fast flowing stream of argon gas ($\approx 10 \text{ L min}^{-1}$) (Figure 1-3). [14; 16]

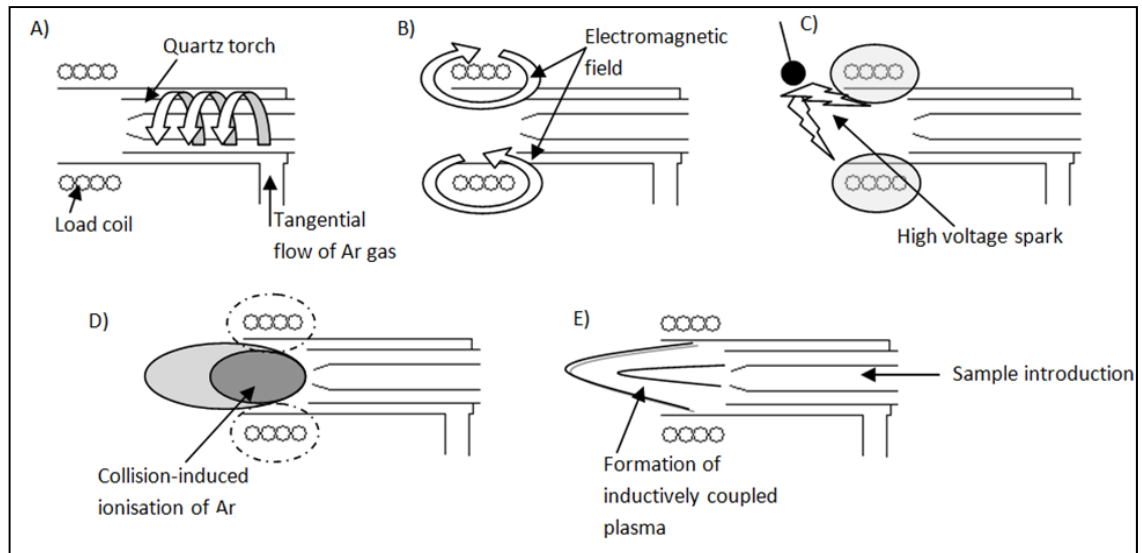


Figure 1-3: Formation of the inductively coupled plasma [14]

(A) A tangential flow of argon passes between the outer and middle tube of the quartz torch; (B) RF power is applied to the coil producing an intense electromagnetic field; (C) Tesla spark produces free electrons; (D) Free electrons are accelerated by the RF field and collisions and ionisation of Ar gas occurs; (E) ICP is formed at the open end of the torch and sample introduction can begin.

The high temperature atmospheric pressure environment of the plasma is an efficient excitation source that results in most elements being efficiently ionised to single-charge positive ions (Figure 1-4). When the sample aerosol is introduced, it is carried in an argon gas stream ($\approx 1 \text{ Lmin}^{-1}$) into the plasma where it undergoes a number of physical changes and is rapidly desolvated, vaporised and the majority of the aerosol is ionised. When the aerosol enters the plasma it is made up of a fine mist of mineral components and hydrated metal salts. During desolvation, water molecules are evaporated and the metal salts become small solid particles. The process of desolvation is not required for samples delivered to the plasma following laser ablation. Particles move through the plasma where they are transformed firstly into a gaseous form and then into a ground state atom. The atom is converted to an ion by collisions with energetic electrons (and to lesser extent argon ions). [14; 16]

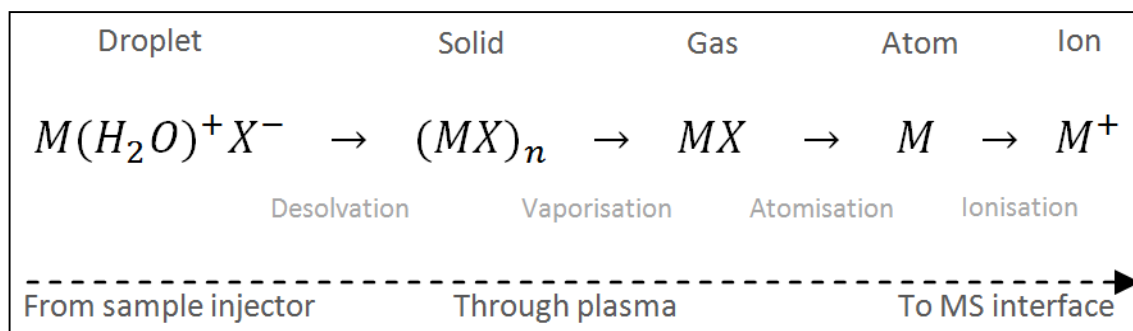


Figure 1-4: Mechanism of conversion of a droplet to a positive ion in the ICP [14]

After ionisation, the ions are directed to an interface region which consists of a sample cone with an orifice of 0.8 – 1.2 mm and a skimmer cone with an orifice of around 0.4 – 0.8 mm. The ions then pass through an ion focusing system that is intended to transport analyte ions from the interface to the mass spectrometer while rejecting as many of the matrix components and nonanalyte-based species as possible. The role of the interface region is to transport ions consistently and with electrical integrity from atmospheric pressure (760 Torr) to the mass spectrometer analyser at approximately 10^{-6} Torr. [14]

1.2.1.2 Mass spectrometry

Mass Spectrometry (MS) is a technique that was first developed about a century ago [17]. It is a sensitive analytical technique that enables the quantification of known analytes and the identification of unknown analytes at picomole and femtomole levels.

A mass spectrometer is an instrument which separates gas-phase ions using an electric field in a vacuum according to a dimensionless, independent variable known as the mass to charge (m/z) ratio. After sample introduction and ionisation, the ions move to the mass spectrometer where they pass through a mass analyser to a mass detector which is used to quantify the abundance of ions. Data are presented with the aid of a computerised system. [17-19]

Advances in MS facilitate the analysis of polymers, metals, oxides, thermally labile biomolecules and other solid state materials. Numerous fields involving the application of MS have been developed including biotechnology, microelectronics, materials science, geochemistry, forensic research and surface analysis [20; 21].

1.2.1.2.1 Mass analysers

Mass analysers are designed to separate ions according to their m/z . There are different methods employed to achieve the separation of ions, all of which use an electric field, sometimes in conjunction with magnetic fields, to enable discrimination of ions with different m/z [18]. There are five main types of analysers outlined in Table 1-1. The table also includes two popular instruments incorporating two mass analysers, the triple quadrupole and the quadrupole-time-of-flight (Q-ToF).

Table 1-1: Strengths and weaknesses of mass analysers [18]

	Price	Size	Resolution	Mass Range	MS/MS
Sector	+	+	++	++	+
Quadrupole	+++	+++	+	+	-
Triple quad	++	+++	+	++	++
Ion trap	++	+++	+	++	+++
TOF	++	++	++	+++	+
Q-TOF	+	++	++	+++	++
FTICR*	-	+	+++	++	+++

Low price, small size, high resolution, large mass range and good MS/MS abilities are all seen as desirable and rate “+++”. Comparatively poorer aspects rate “++”, “+” or “-”

*Fourier Transform Ion Cyclotron Resonance

The main characteristics for measuring the performance of the mass analyser are summarised in Table 1-2. These are the properties of mass analysers that must be considered when determining the fitness-for-purpose for an analysis [19].

Table 1-2: Characteristics of performance of mass analysers [19]

Characteristic	Description
Mass Range Limit	limit of m/z over which the analyser can measure ions
Analysis Speed	or scan speed is the rate at which the analyser measures over a particular mass range
Transmission Efficiency	the ratio between the number of ions reaching the detector and the number of ions entering the mass analyser
Mass Accuracy	the accuracy of the m/z provided to the mass analyser
Resolving Power	A measure of the ability of a mass analyser to separate and distinguish ions of different m/z values
Dynamic range	The range of reliable response over which the observed signal is directly proportional to the amount of analyte supplied to the ion source

Quadrupole mass analysers are the most commonly used mass analysers for work with LA-ICP-MS so will be the mass analyser that is discussed here. Quadrupole-based systems account for approximately 95% of all ICP-MS systems used today [14]. Quadrupole mass analysers consist of four parallel rods arranged as in Figure 1-5. The rods are typically made of stainless steel or molybdenum and sometimes coated with a ceramic coating for corrosion resistance. Quadrupole rods used in ICP-MS are typically 15 – 20 cm in length, about 1 cm in diameter and operate at a frequency of 2-3 MHz. Applied between the alternate pairs of opposite and electrically connected rods are a direct current (DC) voltage and an alternating current (AC) or radio frequency current. By applying specific AC/DC ratios to each pair of rods, ions of selected mass are allowed to pass through to the detector while other ions are unstable, ejected from the quadrupole and pumped to waste. Ion selection is achieved by

oscillating the polarity of the field. As a positive ion enters the quadrupole, it is drawn towards the negatively charged rod. The field changes polarity before the selected ion reaches it and the ion is forced in the opposite direction. Under the influence of this combination of fields, the ions undergo complex trajectories. Within certain limits, these trajectories are stable and ions of a certain m/z are transmitted by the device using specific AC/DC ratios. The unstable ions are therefore lost by collision with the rods or escape between the rods. Also to be noted is the ions must be accelerated before entering the quadrupole assembly because the applied electric field provides no forward momentum. [14; 18; 19]

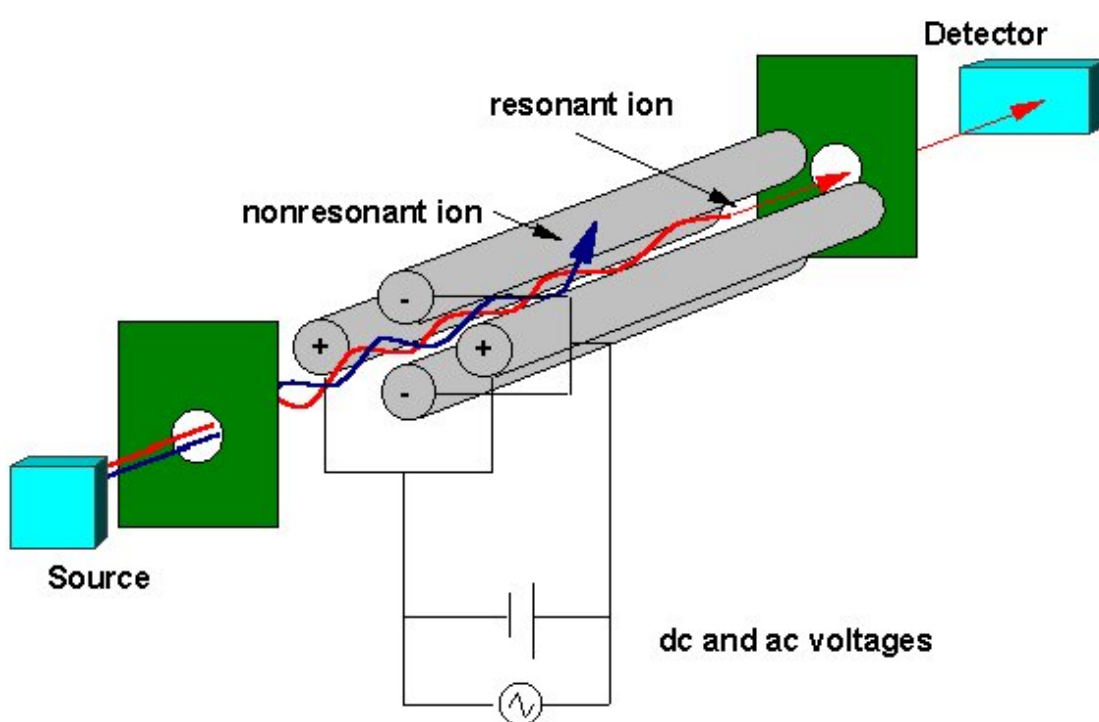


Figure 1-5: Diagram of a quadrupole mass analyser showing ion paths [22]

For use with ICP-MS, a quadrupole mass analyser is sufficiently adequate. It is compact, simple to use and relatively inexpensive. It is well suited to coupling with atmospheric pressure sources as it does not operate at high voltages. It has good reproducibility, and a

scan speed of a minimum $1000\ m/z\ s^{-1}$ and mass range in excess of $2000\ m/z$ which is well within the limits of measuring the ionised atoms produced by the ICP.

The resolution of the quadrupole is relatively limited compared to other mass analysers. The ability to separate different masses with a quadrupole is determined by a combination of factors including shape, diameter and length of the rods, frequency of quadrupole power supply, operating vacuum, applied AC/DC voltages, and the motion and kinetic energy of the ions entering and exiting the quadrupole. These factors all have a direct impact on the stability of the ions as they travel between the rods and therefore impact the quadrupole's ability to separate ions of different m/z . In theory, the resolution of the quadrupole can be varied between 0.3 and 3.0 amu but is usually kept around 0.7 – 1.0 amu [14]. Low resolution (3.0 amu) has the benefit of high sensitivity however the peak width is much wider and may overlap adjacent m/z values resulting in loss of discrimination of certain masses, generally those with a lower abundance. High resolution (0.3 amu) has a very narrow peak width however there is a loss of sensitivity and therefore reduction in detection limits. A compromise depending on the sample and detection limits must be made and the resolution can be tuned to accommodate these aspects.

1.2.1.2.2 Mass detectors

The majority of ICP-MS systems are used for ultra-trace analysis and use detectors that are based on the discrete dynode electron multiplier [14]. These detectors are very sophisticated and focus on converting the ion currents emerging from the quadrupole into electrical signals which can be analysed using a computer.

Discrete dynode electron multipliers utilise dynodes to carry out electron multiplication to amplify the analytical signal. In order to minimise background noise from stray radiation and

neutral species coming from the ion source, the detector is positioned off-axis. When an ion emerges from the quadrupole, it follows a curved path and strikes the first dynode where it liberates secondary electrons. The electro-optic design of the dynodes accelerates the secondary electrons to the next dynode where more electrons are generated. The process is repeated until the pulse of electrons generated is captured by the multiplier collector or anode [14]. Electron multiplication is represented in Figure 1-6.

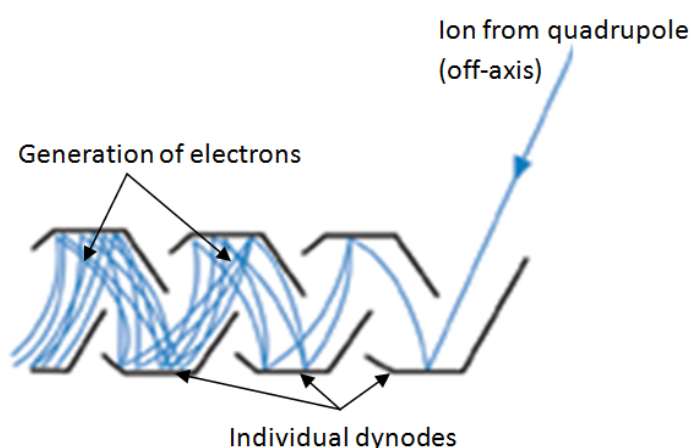


Figure 1-6: Schematic of a discrete dynode electron multiplier [14]

When ICP-MS was first marketed, its dynamic range was five orders of magnitude. In order to be able to measure high and low count rates effectively, newer ICP-MS models use one detector which is able to measure in both pulse and analogue modes. Digital, pulse-counting mode provides the highest sensitivity, while operating in analogue mode is used to reduce the sensitivity of the detector, thus extending the range over which ion signals can be measured. Analogue mode is achieved by reducing the voltage applied to the detector. [14]

1.2.2 Laser ablation

Laser ablation (LA) is a method of sample introduction for analysis of solid samples using ICP-MS. The method involves the sample being placed in a chamber or cell which is filled with an inert gas, generally argon or helium. A high-powered laser traverses the surface of a sample and the topmost layers are removed to form a laser induced aerosol. This aerosol is then transported by a stream of the inert gas into the ICP-MS for analysis [13; 14]. A schematic of a typical laser ablation unit is presented in Figure 1-7.

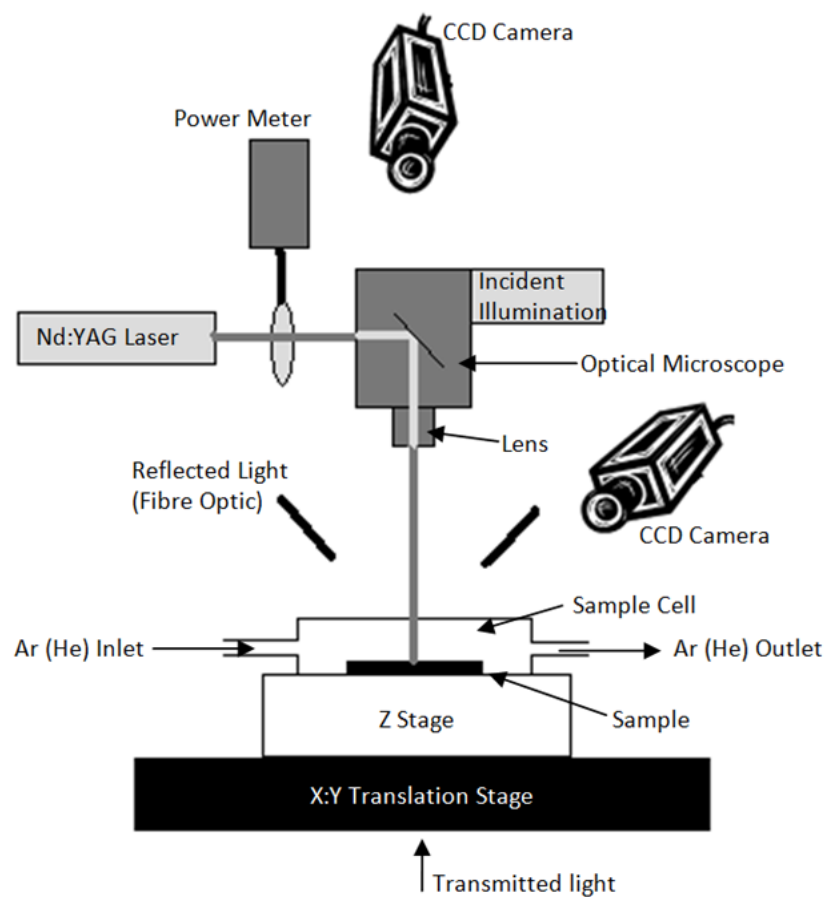


Figure 1-7: Schematic of a typical Nd:YAG laser ablation unit [23]

1.2.2.1 Lasers used in LA-ICP-MS

Laser is an acronym for *light amplification by stimulated emission of radiation*. The light emitted by a laser is monochromatic, coherent and directional making it suitable for direct interaction with solid samples. Several different types of lasers are available on the market and can be classified into four groups, namely solid-state, gas, dye and semiconductor. The specifications for some selected lasers which are used for LA-ICP-MS are presented in Table 1-3.

Table 1-3: Characteristic parameters of selected lasers used for LA-ICP-MS [13]

Laser Type	Wavelength (nm)	Pulse Duration	Energy (mJ)	Comments
Excimer				
ArF	193	13 ns	200	High maintenance, higher pulse energy, better crater profile
KrF	248	20 ns	200-500	
XeCl	308	25 ns	200	
Solid State				
Ruby (Cr-Al ₂ O ₃)	694	ns - μs	1000	Low maintenance, compact size, relatively easy handling
Nd:YAG	213	5-10 ns	2	
Nd:YAG	266	5-10 ns	4	
Nd:YAG	1064	10-15 ns	200-500	
Ti:Sapphire	775	150 fs	0.5	

NB: Solid state lasers only exhibit pulse durations in the ranges stated when Q-switching is applied.

Solid-state lasers are more popular because they are less expensive and have acceptable output characteristics. In these types of lasers the lasing material is distributed in a solid matrix. The solid matrix is usually a transparent crystal or glass which is doped with small amounts of trivalent metal ions, for example neodymium (III) (Nd³⁺). Neodymium-doped yttrium aluminium garnet (Nd-YAIO) lasers, or Nd-YAG lasers, are common solid-state lasers. The process of laser production for Nd³⁺ is presented in Figure 1-8. Nd ions are excited to a higher energy level by optical pumping which is followed by decay to a metastable level. The generation of population inversion between the upper and lower metastable levels is the basic step for the laser process. Initial and final states for lasing action can be split into

several crystal field levels and therefore several wavelengths are possible, the most powerful being 1064 nm. Harmonic generation, or frequency doubling, helps to convert this wavelength to within the ultraviolet region, commonly 213 nm. Wavelengths in the ultraviolet region are able to analyse a wider range of materials. Applying Q-switching reduces the pulse duration of Nd:YAG laser output by creating pulses with high peak power. Q-switched pulses have much higher energy than continuous wave pulses. The laser oscillation builds up more rapidly than continuous mode ablation. Consequently, very short, high power pulses are produced, reducing thermal effects of the laser. [13; 24]

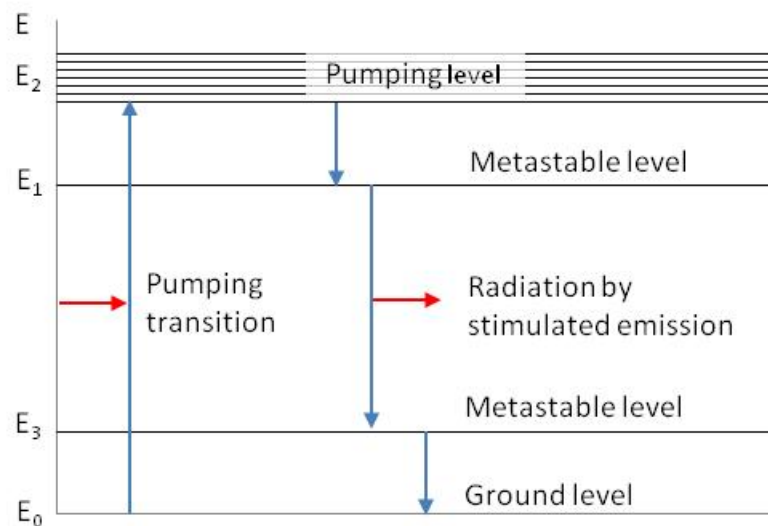


Figure 1-8: Four energy level diagram for Nd^{3+} ions in a Nd:YAG laser. Lasing occurs between the metastable levels [13; 25]

Excimer lasers are part of the gas laser category and are increasing in popularity. These lasers consist of a mixture of reactive or reactive and inert gases that, when electrically stimulated by a discharge, produce a pseudo molecule (dimer) that is excited. When lasing, this dimer produces light in the ultraviolet range. [13]

There are several properties which make the laser suitable for the ablation process required for sample introduction in the ICP-MS. These include the following [13; 14]:

1. **Laser Wavelength** - The wavelength of the laser system has a significant effect on the ablation process, ablation rate, fractionation process and the materials that are able to be ablated. In general, a lower laser wavelength in the UV region is preferred because there are fewer restrictions on the materials that can be analysed. Lasers with wavelengths in the infra-red region tend to melt or fracture so IR and visible wavelength lasers need to undergo harmonic generation to double, quadruple or quintuple the frequency.
2. **Pulse Energy** – At a given pulse energy the ablation rate will vary with the composition of the material. Pulse energy is able to be controlled by apertures, filters, variable optical attenuators, or by the flashlamp voltage.
3. **Pulse Frequency** – The rate of repetition of the laser can vary with the lasing medium. Pulse frequency can have a significant effect on the ablation process because at higher frequency, the laser can be shielded from the material to be ablated by the previous shot's laser-induced plasma which lingers above the sample.
4. **Pulse Duration** – The longer the laser pulse, the greater the influence of thermal effects on the ablation process. As materials with lower melting points are melted during the interaction with the laser, the physicochemical properties of the sample are changed and mixing of the sample occurs. This leads to lower local spatial and depth resolution. Shorter laser durations will reduce this effect and research is currently being conducted into the use of “cold” lasers with pulse durations of femtoseconds [26-29].
5. **Laser Beam Profile** – The beam profile can also affect the spatial and depth resolution. The energy profile of the beam affects the resulting ablation crater

geometry. Most lasers apply a Gaussian profile whereby the energy of the beam is greatest at the centre and the energy slowly drops off towards the edges. The highest resolution can be achieved using a flat-top beam profile where the energy is uniform across the beam. This can be achieved using the appropriate optics.

6. **Spot Size** – This property is linked to the lateral resolution obtainable during analysis. The aspect ratio of the crater which is formed (quotient of crater depth to crater diameter) also has an influence on the transport of ablated material. The higher the ratio, the lower the amount of material which is transferred from the bottom of the crater to the ICP-MS.

1.2.2.2 *Ablation cell dynamics*

The laser ablation sample cell is an important feature which aids in the transfer of ablated sample to the ICP-MS for analysis. The cell's volume and geometry, the type of carrier gas and its flow properties, and the tubing properties of the transport line between the cell and the ICP-MS are all important characteristics which contribute to the transport process and transient signal structure [13].

The ablation cell consists of a gas inlet and gas outlet, a cell window which is transparent to the laser wavelength used (usually fused silica), and optical arrangements for sample illumination which use either transmitted or reflected light. The sample stage is controlled remotely by computer and allows the positioning of the sample in the x, y and z directions. Displacement of around a few micrometres is able to be achieved without difficulty [13; 30]. The cell itself is flushed with an inert gas (Ar, He or, the more recently researched, Ne [31]) which carries the laser induced aerosol to the ICP-MS. A schematic of a standard laser ablation cell is presented in Figure 1-9.

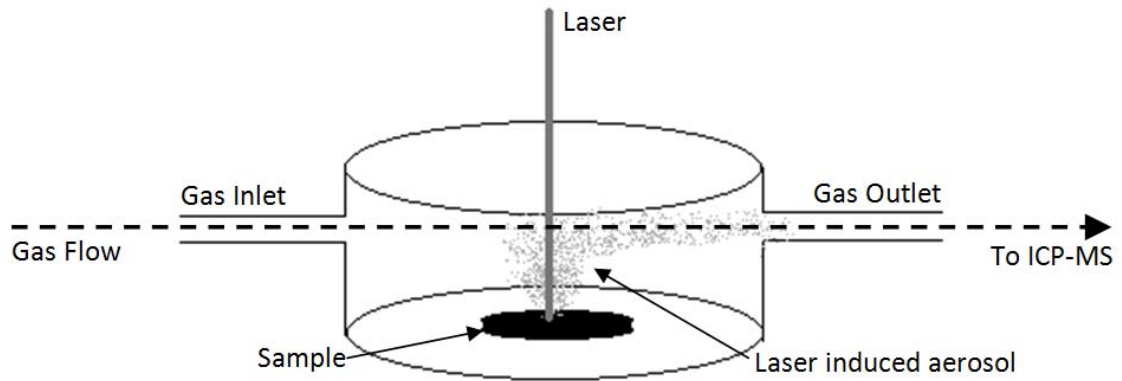


Figure 1-9: Schematic of a standard laser ablation cell [13]

The total transport efficiency of laser ablation is reported to be between about 5 - 25% of the total amount of material which is ablated [31]. There is therefore a restriction on the detection capabilities of the ICP-MS. If the transport efficiency is improved, then the limit of detection is decreased and a greater resolution can be achieved since the size of the laser spot can be reduced. Laser ablation sample cells can range between 0.25 and over 100 cm³. An inlet nozzle introduces the gas into the cell. This nozzle can have varying internal diameters and this will affect the geometry of the gas injection zone. In the centre of this zone is a high efficiency transport area. Outside this area are different aerosol transport efficiencies which lead to non-uniform signal intensities for different sample positions within the cell. There is a reduction in resolution in larger cells because of signal dispersion. As the cell volume increases the density of the aerosol decreases, there is greater gas circulation and longer transport times. Smaller cells also have an issue with greater deposition of the aerosol on the cell walls which leads to partial loss of the aerosol. Even though there is sample loss, the reduction in cell volume gives sharper single-shot signals. [13; 31]

The large format cell (LFC) (Electro Scientific Industries) (Figure 1-10) was designed to accept large samples up to 150 mm x 150 mm, without sacrificing analytical performance due to a

large cell volume. The LFC has a superior performance in signal intensity with improved washout time. This is due to a "roving" cup within the cell constraining the spread of the aerosol, a limitation seen in larger cells [32].

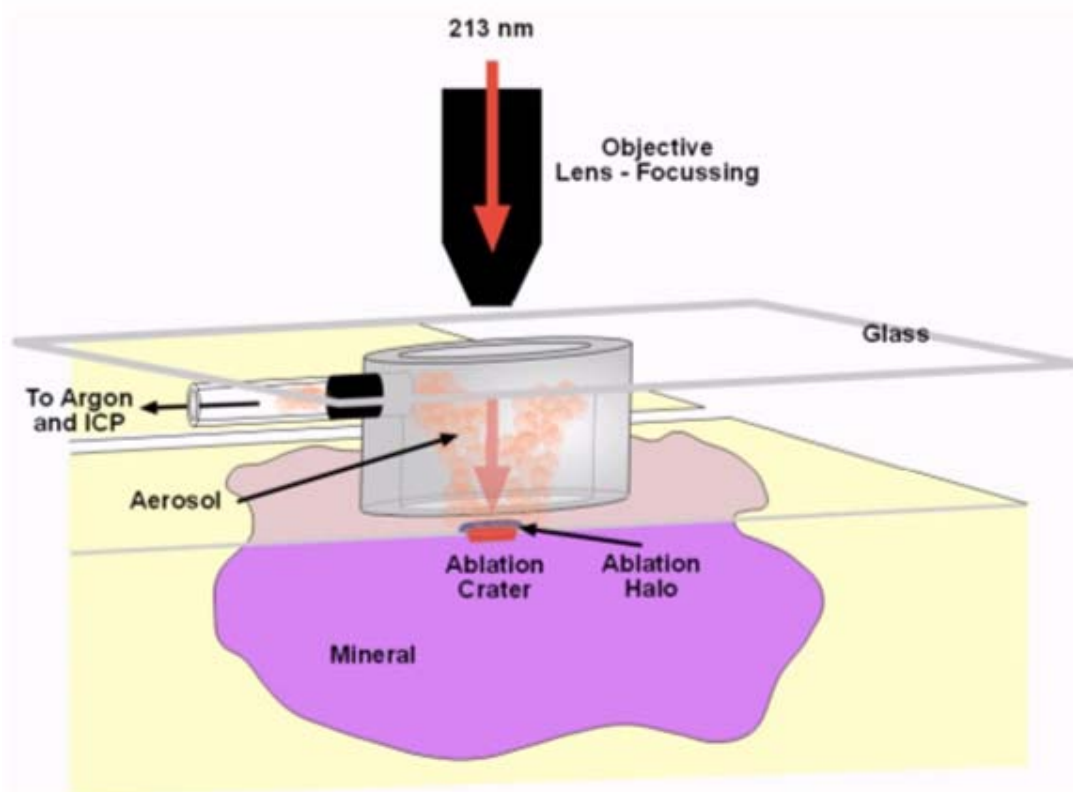


Figure 1-10: Schematic of the large format laser ablation cell

The transfer tubing diameter and length also affect the resulting signal obtained during analysis. Gas velocity increases linearly with a decreasing internal diameter of the tubing and experimental data has previously shown that an internal diameter of 4 mm has an experimentally optimum signal-to-noise ratio. Signal dispersion increases with increasing tube length so to minimise dispersion and transient signals, the shortest tubing possible between the laser ablation unit and the ICP-MS needs to be utilised. [13]

The carrier gas used for the transport of ablated materials has been reported to influence the signal intensities and background levels obtained [13; 31]. Argon is the most commonly used

carrier gas in laser ablation as it can be passed directly into the plasma without changing the plasma conditions. Altering the plasma conditions will result in differences in the ionisation efficiencies and may lead to non-stoichiometric signal responses [13]. In recent years however several reports on using helium as a carrier gas and mixing argon in the stream after the ablation cell suggest enhanced signal-to-noise ratios [13; 25; 31; 33]. A two to three times increase in the signal intensities across the entire mass range is possible increasing the detection limit capabilities by about one order of magnitude [33]. It was observed that particle deposition around the ablated spot reduced when helium was utilised as a carrier gas (Figure 1-11) [25; 33]. Both helium and argon have very different thermal conductivity properties and form different laser-induced microplasmas on the sample surface. Helium has a higher thermal conductivity which may result in the faster removal of thermal energy away from the laser induced plasma yielding to shorter condensational processes which lead to the production of smaller particles (Figure 1-12) [31]. Lower particle size distribution leads to improved sample transport efficiency and increased atomisation of particles in the ICP [34; 35]. However, helium has a slower washout time to argon. Therefore, argon is often the preferred carrier gas [36].

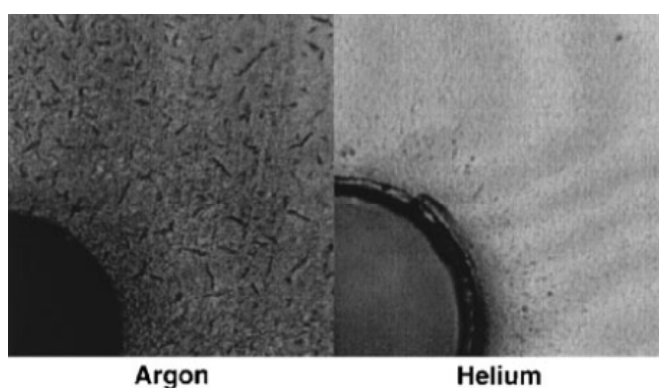


Figure 1-11: Particle size distribution after 40 second ablation of 40 µm craters in SRM 612 glass using argon and helium carrier gases [33]

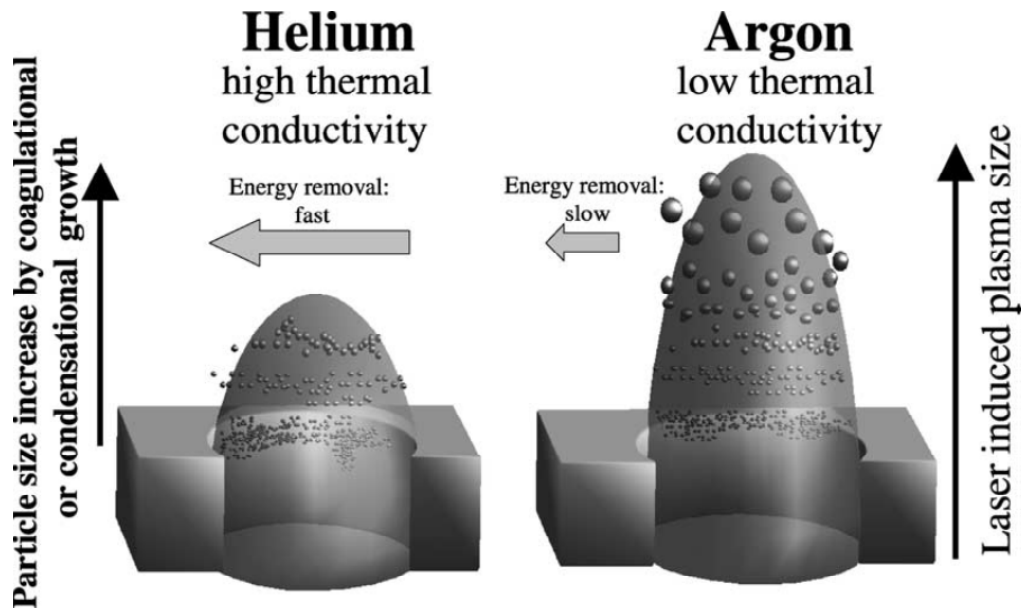


Figure 1-12: A model for the differences in particle size distribution based on the thermal conductivities of the gases used in LA-ICP-MS [31]

1.2.3 Considerations for LA-ICP-MS

1.2.3.1 Elemental fractionation

Elemental fractionation is one limitation of LA-ICP-MS. Sometimes the signal intensities observed do not reflect the stoichiometric sample composition. This limits accurate chemical analysis, as the ablated mass composition is not the same as the actual sample composition [13; 30]. Elemental fractionation can occur during the laser ablation process, the aerosol transport process and the vaporisation, atomisation and ionisation processes in the ICP. Laser energy and wavelength, the pulse duration and the beam profile influence the amount of elemental fractionation. Particle size distribution of the ablated sample plays a major role in elemental fractionation occurring in the ICP. Particle size distribution is a function of the laser wavelength and absorption of the material, and is also dependent on the carrier gas used. The efficiency of the ICP to form ions is dependent on the particle size of the ablated

particles and therefore directly affects the degree of elemental fractionation. [13; 30; 31; 37-39]

1.2.3.2 Interferences

Interferences in ICP-MS are any species which obscure the signal of the analyte of interest. Interferences can be spectral or matrix-based. Spectral interferences have the same nominal mass as the target analyte and are caused by molecular (polyatomic) or atomic (isobaric and doubly-charged) species. Matrix-based interferences mainly lead to signal suppression or even signal enhancement and are not due to spectral overlap. [13; 14; 40]

- **Polyatomic interferences** – These are produced by a combination of two or more atomic ions. They are usually associated with either the plasma or nebuliser gas used, matrix components in the solvent or sample, other elements in the sample, or oxygen and nitrogen from the surrounding atmosphere. Common polyatomic interferences are outlined in Table 1-4. Polyatomic interferences caused by argon ions are the most common. The most abundant ion of argon is ^{40}Ar and when combined with oxygen forms the most significant interference, $^{40}\text{Ar}^{16}\text{O}^+$, which has the same mass as iron's most abundant isotope. Other polyatomic interferences are caused by interactions of elements with H^+ , $^{16}\text{O}^+$, or $^{16}\text{OH}^+$ (either from water or air) to form molecular hydrides, oxides and hydroxides.

Table 1-4: Common polyatomic interferences from biological matrices. Adapted from [41]

Analyte	Interfering Species
$^{27}\text{Al}^+$	$^{12}\text{C}^{15}\text{N}^+$, $^{13}\text{C}^{14}\text{N}^+$, $^{14}\text{N}_2^+$ (spread from m/z 28)
$^{75}\text{As}^+$	$^{40}\text{Ar}^{35}\text{Cl}^+$, $^{59}\text{Co}^{16}\text{O}^+$, $^{36}\text{Ar}^{39}\text{K}^+$, $^{43}\text{Ca}^{16}\text{O}_2^+$, $^{23}\text{Na}^{12}\text{C}^{40}\text{Ar}^+$
$^{43}\text{Ca}^+$	$^{27}\text{Al}^{16}\text{O}^+$
$^{44}\text{Ca}^+$	$^{12}\text{C}^{16}\text{O}_2^+$, $^{14}\text{N}_2^{16}\text{O}^+$, $^{28}\text{Si}^{16}\text{O}^+$
$^{111}\text{Cd}^+$	$^{95}\text{Mo}^{16}\text{O}^+$
$^{112}\text{Cd}^+$	$^{40}\text{Ca}_2^{16}\text{O}_2^+$, $^{40}\text{Ar}_2^{16}\text{O}_2^+$
$^{59}\text{Co}^+$	$^{43}\text{Ca}^{16}\text{O}^+$, $^{24}\text{Mg}^{35}\text{Cl}^+$
$^{63}\text{Cu}^+$	$^{40}\text{Ar}^{23}\text{Na}^+$, $^{40}\text{Ca}^{23}\text{Na}^+$, $^{31}\text{P}^{16}\text{O}_2^+$
$^{65}\text{Cu}^+$	$^{40}\text{Ar}^{25}\text{Mg}^+$
$^{56}\text{Fe}^+$	$^{40}\text{Ar}^{16}\text{O}^+$, $^{40}\text{Ca}^{16}\text{O}^+$
$^{57}\text{Fe}^+$	$^{40}\text{Ar}^{16}\text{OH}^+$, $^{40}\text{Ca}^{16}\text{OH}^+$
$^{24}\text{Mg}^+$	$^{12}\text{C}_2^+$
$^{25}\text{Mg}^+$	$^{12}\text{C}_2\text{H}^+$
$^{26}\text{Mg}^+$	$^{12}\text{C}^{14}\text{N}^+$, $^{12}\text{C}_2\text{H}_2^+$, $^{12}\text{C}^{13}\text{CH}^+$
$^{55}\text{Mn}^+$	$^{40}\text{Ar}^{14}\text{NH}^+$, $^{39}\text{K}^{16}\text{O}^+$
$^{31}\text{P}^+$	$^{14}\text{N}^{16}\text{OH}^+$
$^{78}\text{Se}^+$	$^{40}\text{Ar}^{38}\text{Ar}^+$
$^{80}\text{Se}^+$	$^{40}\text{Ar}_2^+$
$^{64}\text{Zn}^+$	$^{32}\text{S}^{16}\text{O}_2^+$
$^{66}\text{Zn}^+$	$^{34}\text{S}^{16}\text{O}_2^+$, $^{40}\text{Ar}^{14}\text{N}_2^+$

- Isobaric overlaps** – These are produced mainly by different isotopes of other elements in the sample interfering with the analyte of interest. For instance, ^{58}Ni is the most abundant (67.9%) isotope of nickel, and it shares its mass with ^{58}Fe (0.31% abundance). Accurate determination of ^{58}Ni in a matrix like steel would obviously be impaired by the high concentration of Fe. Isobaric interferences can generally be overcome by selecting another isotope, however this is sometimes unfeasible so mathematical corrections using the ICP-MS software can be made.
- Doubly-charged species** - One less common spectral interference is that of doubly charged species. If the ionisation potential for a certain element is low enough, then ions with a 2+ charge will form. This will affect the m/z ratio with a doubly charged species effectively appearing to have half the mass.

Several compensatory methods have been implemented to eliminate the problem of ICP-MS interferences. These generally include mathematical correction equations, cool/cold plasma technology and collision/reaction cells.

- **Mathematical correction equations** – These equations have been successfully used to compensate for isobaric interferences and some less severe polyatomic overlaps. This method involves the measurement of the interfering isotope or interfering species at another mass that, ideally, is free of interferences. A correction can then be applied knowing the ratio of the interfering species' isotopes. This method is not ideal when the interference signal intensity is large and the analyte signal intensity is small.
- **Cool/Cold plasma** – Lowering the plasma temperature minimises certain argon-based polyatomic species. Cooling the plasma changes the ionisation conditions and less polyatomic species are formed. This technique is limited to a small group of elements in aqueous-type solutions that are prone to argon-based interferences. There is little benefit for the majority of other elements because of a significantly lower ionisation temperature compared to normal conditions.
- **Collision/reaction cells** – This technique utilises ion-molecule collisions and reactions to cleanse the ion beam of polyatomic interferences before entering the mass analyser. A collision or reaction gas (eg. He or H₂) is bled into the cell which consists of a multipole operated in RF-only mode. The RF-only mode does not separate the ions like the quadrupole but effectively focuses the ions which then collide with the collision/reaction gas. Different collision and reaction mechanisms result in the removal of polyatomic species. This technology shows enormous potential in elimination of spectral interferences.

The interferences in LA-ICP-MS have been reported to be minimal compared to solution nebulisation (SN)-ICP-MS [14]. This is mainly due to direct analysis of a dry sample so interferences related to a solution matrix are reduced. There is no influence from H₂O, other than that present in the sample being ablated, which is significantly less than in a solution. Potential interfering species can be sourced from impurities in the Ar gas, entrainment of atmospheric O₂ and N₂, and desorption of gases within the system [42]. A comparison of background signals obtained in a LA and SN-ICP-MS system is presented in Table 1-5. A significant reduction in O- and H-based interferences can be seen in the ratio of peak intensities. Argide based interferences still show a significant influence and should be duly noted.

Table 1-5: Comparison of background signals measured by LA-ICP-MS and SN-ICP-MS; Adapted from [42]

***Blank 1% HNO₃ solution**

m/z	Interfering Species	Analyte (% natural abundance)	Ratio of Peak Intensities (LA-ICP-MS : SN-ICP-MS*)
28	¹⁴ N ₂ ⁺	²⁸ Si ⁺ (92.18)	0.04
29	¹⁴ N ₂ H ⁺	²⁹ Si (4.71)	0.20
30	¹⁴ N ¹⁶ O ⁺	³⁰ Si (3.12)	0.19
31	¹⁵ N ¹⁶ O ⁺ , ¹⁴ N ¹⁶ OH ⁺	³¹ P (100)	0.002
32	¹⁶ O ₂ ⁺	³² S (95.02)	0.01
33	¹⁶ O ₂ H ⁺	³³ S (0.75)	0.0003
34	¹⁶ O ¹⁸ O ⁺	³⁴ S (4.22)	0.02
54	⁴⁰ Ar ¹⁴ N ⁺	⁵⁴ Fe (5.90), ⁵⁴ Cr (2.38)	0.07
56	⁴⁰ Ar ¹⁶ O ⁺	⁵⁶ Fe (91.52)	0.01
57	⁴⁰ Ar ¹⁶ OH ⁺	⁵⁷ Fe (2.25)	0.01
76	³⁶ Ar ⁴⁰ Ar ⁺	⁷⁶ Ge (7.76), ⁷⁶ Se (9.12)	0.42
80	⁴⁰ Ar ₂ ⁺	⁸⁰ Se (59.96), Kr (2.27)	1.03

1.3 Imaging using LA-ICP-MS

Imaging that utilises mass spectrometry has gained substantial interest in recent years because of its ability to acquire molecule- and element-specific images with spatial resolutions in the micrometre range [43]. Imaging in this way can provide extensive information about molecular and elemental distribution. Quantification can be made for a single pixel, or the average concentration of an area, such as the substantia nigra in the brain, a feat that without quantitative imaging, requires dissection and removal of a section of interest before utilising digestion methods and analysis [44; 45]. Dissection is a difficult process, especially when using small rodents for biological experiments. Staining methods were also utilised in the past to visualise the distribution of elements in a sample, however this technique is insufficient for quantitative analysis [46-48].

The first research to conceive the use of mass spectrometry to provide spatially resolved information was conducted in 1962 by Castaing and Slodzian [49]. Their research formed the basis of secondary ion mass spectrometry (SIMS) and reasoned that it could be possible to build an ion-optical collection system to preserve the spatially resolved information obtained from analysis. Since then, extensive research into the field of imaging has been conducted with analytical methods utilising such techniques as synchrotron radiation microprobe analysis, matrix assisted laser desorption ionization (MALDI) and LA-ICP-MS [50-60]. A comparison of techniques used for imaging biological samples is outlined in Table 1-6. MALDI imaging is not able to provide measurable elemental or quantifiable data so is therefore not suitable for elemental analysis in neurological tissue. Synchrotron radiation microprobe analysis and SIMS are limited by either expense and limited beamline time, or significant matrix effects, respectively. LA-ICP-MS is the method of choice because it is robust, cost-effective and is highly sensitive which is beneficial for trace element analysis. [1; 61-63].

Table 1-6: Main spatially resolved analytical techniques for chemical element imaging, quantification, and speciation in biological samples; adapted from [55]

These characteristics can vary for each technique from one instrument to another one. They have been estimated for standard instruments and considering the analysis of inorganic elements such as transition metals, within a biological matrix such as an isolated cell or a tissue section.

Technique	Detection Limit ($\mu\text{g/g}$)	Spatial Resolution (μm)	Selectivity	Quantification	Analytical depth (μm)
Electron microprobe EDS	100-1000	0.5	Multielement ($Z \geq 6$)	Quantitative	0.1-1
EELS	1000	0.001	Multielement ($Z \geq 6$) chemical species	Quantitative	<0.05
Ion beam microprobe	1-10	0.2-2	Multielement (all Z)	Quantitative with local organic mass content determined	10-100
Synchrotron radiation microprobe	0.1-1	0.1-1	Multielement ($Z \geq 6$)	Quantitative	>100
μ -XAS	100	0.1-1	Chemical species		>100
LA-ICP MS	0.01	15-100	Multielement and isotopic	Quantitative	200
SIMS in dynamic mode	0.1	0.05	Multielement and isotopic	Quantitative with local organic mass content determined	0.1

EDS: Energy-dispersive spectrometry; EELS: Electron energy loss spectroscopy; μ -XAS: micro-X-ray absorption spectroscopy

In 1994, research into the feasibility of LA-ICP-MS as a tool for multi-element analysis of biological tissues was conducted by Durrant and Ward [64]. It was found that LA-ICP-MS offered rapid semi-quantitative analysis with little or no sample preparation. In the same year, Wang *et al.* [65] performed a study which attempted to image biological samples using LA-ICP-MS and were able to achieve spatial resolutions as low as 30 μm , a value comparable to today's image resolutions. Extensive research over recent years into the application of LA-ICP-MS for imaging biological samples has shown enormous potential in aiding the determination of trace element compositions in thin sections of tissue [1; 61-70]. Methods for progressing quantification have also been determined. The progression of imaging since the first images produced by Wang *et al.* [65] is outlined in Figure 1-13. Recent developments in EBI have lead to the development of 3-dimensional (3-D) image production [7] and imaging at high resolution [71].

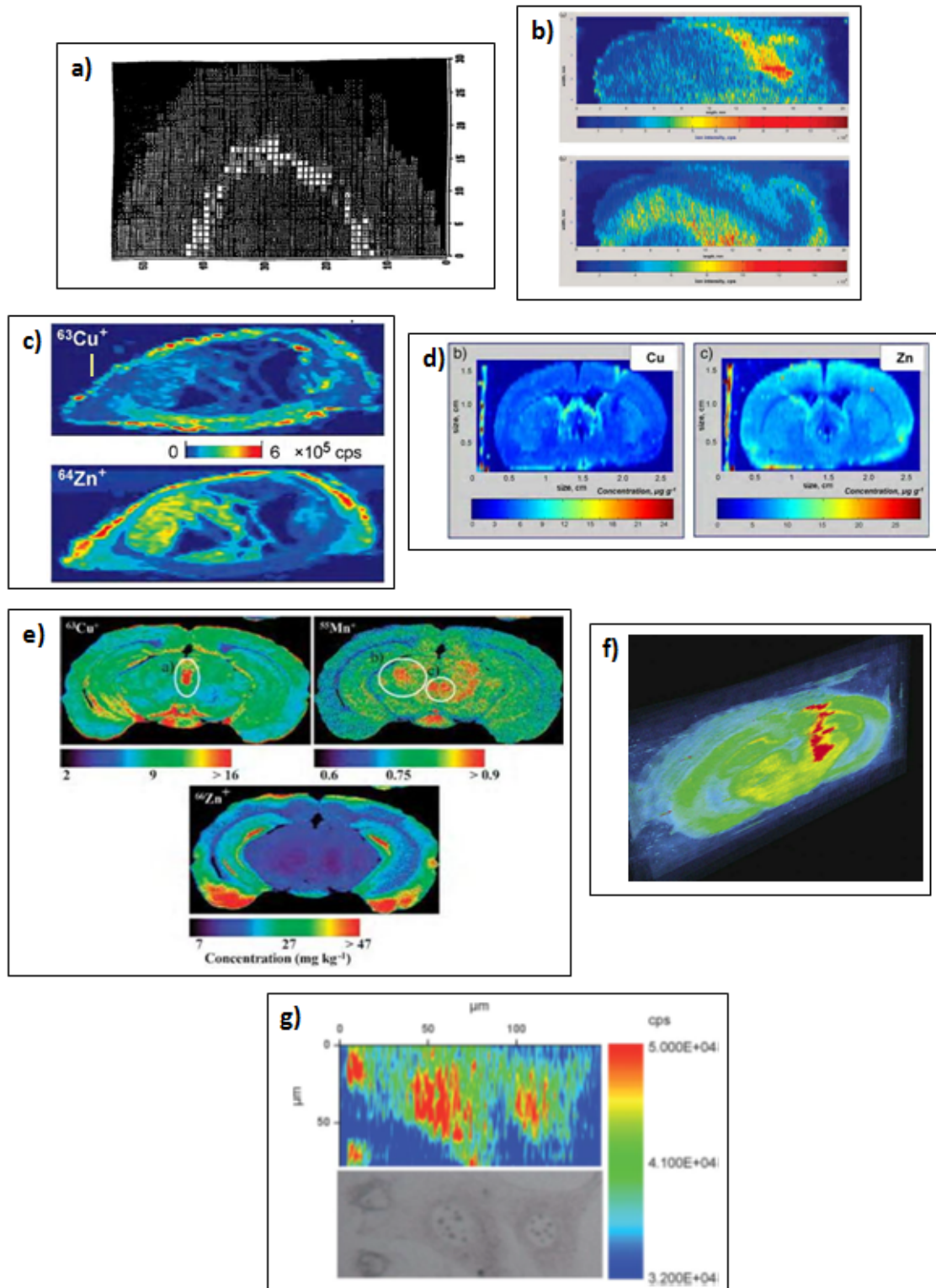


Figure 1-13: Timeline of EBI

a) Wang et al. 1994, resolution = 30 μm [65]; b) Becker et al. 2005, resolution = 50 μm [62]; c) Becker et al. 2007, resolution = 50 μm [72]; d) Zoiry et al. 2008, resolution = 50 μm [73]; e) Hare et al. 2008, resolution = 30 μm [36]; f) 3-D imaging, Hare et al. 2010, resolution = 100 μm [7]; g) Geisen et al. 2011, resolution = 4 μm [71]

1.3.1 Imaging methods

The general process of EBI is outlined in Figure 1-14. A tissue sample, such as a mouse brain, is sourced in a fixed, frozen or paraffin-infiltrated form. The tissue is sectioned with a cryostat to an appropriate width (in the μm range) and mounted on a suitable support. The sample is then analysed using LA-ICP-MS where multiple isotopes can be detected in the same analysis. After analysis, data treatment combined with external calibration can produce elemental concentrations per data point and elemental ratio information including signal normalisation using an internal standard. [1; 9; 47; 63; 67; 69; 70]

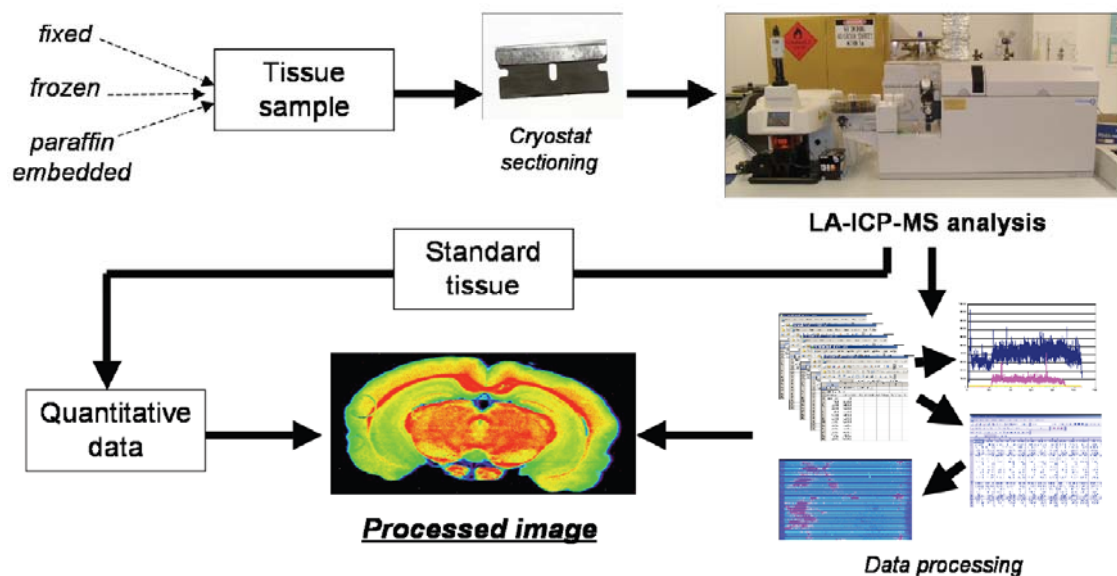


Figure 1-14: Workflow for imaging using LA-ICP-MS [1]

Variables of the imaging process are dependent on instrument parameters, such as the ablation cell, carrier gases and mass analysers, as well as user preferences, the required resolution of the resulting image, and access to different data processing software. EBI is moving beyond the method development stage; however it is still evolving and much of the

software used for data treatment must be specifically prepared by the user to perform the required processing.

One downfall of imaging with LA-ICP-MS is its destructive nature as the laser removes tissue from the sample. It must therefore be used as the final analysis in a workflow and follow such analytical techniques as vibrational spectroscopy and MALDI-MS.

The instrumentation discussed earlier is well suited to imaging using this process. A quadrupole mass filter can measure 1000 m/z s^{-1} . The measurement is not simultaneous, however the speed is fast compared to the time response of laser ablation sample introduction. One disadvantage of quadrupoles occurs when there are large particles entering the ICP. This leads to spatial changes (enhancements or depressions in the signal level and chemistry) in the ICP and since transition through the ICP is only a few milliseconds, the quadrupole can only scan fast enough for one mass measurement from these particles. Errors due to these large particles may be overcome using a TOF instrument. Double focusing electrostatic–magnetic sector instruments are another option and have very low background levels and high resolution. These instruments can acquire data at high speed within limited regions, but they have many of the same deficiencies as quadrupole systems and cannot switch fast enough over large mass regions required for full trace element analysis. [30; 74; 75]

1.3.2 Quantification strategies

For quantitative trace element determination an accurate and precise relationship between the signal response and elemental concentration must be made. For successful quantification of trace elements in solid samples three main criteria must be met;

1. the exact amount of sample transported to the ICP is known;
2. the composition of the laser-induced aerosol represents the stoichiometry of the original sample; and
3. the particles transported to the ICP are fully atomised and ionised within the plasma.

[13]

These criteria however are rarely completely fulfilled so relative calibration techniques have to be developed for the best possible results. Calibration techniques have been established for LA-ICP-MS and include calibration using matrix-matched external standards, non-matrix-matched calibration, and on-line solution-based calibration strategies. A recent comprehensive review by Hare *et al.* [76] examined the quantification strategies for EBI. Table 1-7 presents the noted advantages and drawbacks of each quantification method currently used for EBI.

Table 1-7: Advantages and drawbacks of quantification procedures for EBI [76]

Quantification approach	Advantages	Disadvantages
Internal standardisation	Rapid intrinsic correction for drift and fractionation; suitable for direct comparison of signal response	Not quantitative; limited choices available
Normalisation by acoustic wave generation	Improved precision	Not quantitative; difficult to apply to spatial measurements
Normalisation by measurement of light scattering	Improved precision; applicable to imaging	Not quantitative
Certified reference materials (CRMs)	Matrix-matched (where possible); rapid; independently certified concentrations	Limited number commercially available; singlepoint calibration; limited control of concentration ranges; typically dehydrated
Laboratory prepared standards	Matrix-matched; controlled concentration ranges; equivalent H ₂ O content	Application specific; lengthy preparation
Online addition	Rapid; reduced fractionation; increased number of analytes	Limited imaging applications described
Isotope dilution	Robust single point calibration; precise	Homogenous mixing with sample not possible; challenging delivery method
Printing	Rapid; easily adaptable to new applications; capable of matrix-matching	Limited imaging applications described

The most common calibration strategy for analysis of trace elements in biological tissues to date is the matrix-matched external calibration. It has the benefit of the sample being the same composition as the calibration standards and therefore, both will interact with the ICP in much the same manner, have similar flow dynamics and the ablation rate of the sample and standard will be similar. [13; 30]

Matrix-matched internal standards closely match the samples both chemically and physically. An internal standard must also be used to correct for differences in laser ablation yields, signal drifts and matrix effects. The internal standard should be a major element found in both the sample and standard which has a consistent concentration and the response of this isotope is used to normalise the analyte signal response. The best choice for matrix-matched external standards is the use of a certified reference material (CRM). For biological samples however, there are few commercially available CRMs. Therefore, matrix-matched standards must be prepared using a mixture of an appropriate matrix material with the analyte/s. This is often difficult as obtaining an exact match of the sample is not an easy task. Internal standardisation is limited by the requirements of one element present or added with known concentration. Elements used as the internal standard must be distributed homogeneously and behave in a similar manner to analytes during the laser ablation process. [9; 13; 30; 39]

A commonly used technique for calibration in elemental bio-imaging is the preparation of matrix-matched standards by spiking blank tissue, homogenising the standard and sectioning the standard to produce multi-point calibration curves using ^{13}C as an internal standard [1; 62; 63; 67; 69; 73]. Other standard preparation techniques have also included powdered TORT-2 (lobster hepatopancreas), DOLT-2 (dogfish liver) and DORM-2 (dogfish muscle) being pressed as pellets. These were used to build multipoint curves with correlation coefficients from 0.982 to 0.997 [6].

The techniques used for standard preparation for the purpose of EBI are not yet perfected. Using ^{13}C may be problematic due to the inhomogeneous nature especially of the sample where tissue density may decrease in certain areas [9]. Also, adding increasing amounts of liquid to tissue standards of higher concentrations decreases the carbon tissue density and inhomogeneous standards result.

Recent novel approaches to quantification methods show significant potential for EBI. Isotope dilution MS (IDMS) is not a new analytical technique but application to ICP-MS has grown significantly in recent years. IDMS involves the use of a sample spiked with a standard where one or more isotopes are enriched at a known ratio. This method relies on the accurate knowledge of the isotopic abundance of the analyte in the sample, the concentration and weight of the added enriched isotope, the mass of the sample and accurate measurement of isotopic ratios by ICP-MS. Austin *et al.* [77] recently described the use of poly(methylmethacrylate) (PMMA) films for external calibration which have the potential to utilise the IDMS theories. Essentially, PMMA in an organic solvent is spiked with an organometallic standard and the solution is spin-coated onto a quartz slide. Statistical analyses of the spin-coated standards revealed the method was comparable to matrix-matched quantification. Another novel technique proposed by Bellis and Santamaria-Fernandez [78] is employing an inkjet printer to apply a thin coat of standard solution onto a substrate and altering concentration distribution by varying the colour density output or transparency of the printed solution. [76]

1.3.3 Future direction of EBI

EBI has recently been moving away from method development and toward advanced application analysis. Applications for imaging with LA-ICP-MS are continuing to appear. Although much has been done in the area of EBI method development, these new applications are continually driving further development and improvement of EBI.

EBI still has significant development opportunities. As mentioned before, calibration is yet to be perfected. New approaches to standard preparation and the types of standards should be investigated. The development of CRMs for EBI is imminent. Software development for fast and simple data manipulation is also needed. With appropriate software available it would also be possible to produce images with ease. Currently quantification is performed on a 2-dimensional section of a 3-dimensional object so further development of 3D imaging will open further possibilities of biological and clinical research. Spatial resolutions of images are currently limited. Biological applications require high spatial resolutions in order to visualise element concentrations in a single cell. Single cell imaging is currently being examined and future development of EBI will see increased imaging sensitivities and high spatial resolutions comparable to other elemental imaging techniques.

Recently, the use of femtosecond lasers with short UV wavelengths has been a key area of research for LA-ICP-MS. The deposition of laser energy is so fast that the thermal diffusion length is dramatically reduced (about 100 nm compared to 1 μm for nanosecond pulses) [13; 79]. This means that there is greater breaking of physical bonds and the laser is much more efficient at ablating material than nanosecond lasers. Femtosecond lasers have been reported to have reduced fractionation, improved precision of LA-ICP-MS in experiments ablating NIST standard glass samples, and a 95% transport efficiency. [80-83]

1.4 Project aims

This thesis describes the improvement of established LA-ICP-MS techniques used for the purposes of EBI and the application of improved analytical methods to research in neuroscience. The specific aims of the project were;

1. The refinement of the methods of preparing matrix-matched tissue standards in order to increase homogeneity and the number of analytes per standard, and improve analytical validity
2. The development of new data acquisition protocols which reduce the experimental acquisition times by increasing the laser scan speed of EBI experiments
3. The application of increased laser scan speeds for imaging the distribution of elements in zinc-knockout mouse brains treated with a new clioquinol derivative, PBT-2
4. The application of increased laser scan speeds for imaging the distribution of elements in mouse models for sleep apnoea and diets of varying levels of advanced glycation end-products
5. The evaluation of the effectiveness of using H₂ as a reactive gas for the elimination of elevated polyatomic background signals for LA-ICP-MS imaging whilst maintaining the detection limits of analytes not subject to spectral interferences; and
6. The application of refined EBI techniques to preparing high resolution images that approach the dimensions of a single cell.

Chapter 2: Experimental

Chapter 2: Experimental

All experiments were carried out at the Elemental Bio-Imaging facility in the Department of Chemistry and Forensic Science at the University of Technology, Sydney, Broadway, New South Wales, Australia.

2.1 Instrumentation

2.1.1 Inductively coupled plasma – mass spectrometer

All ICP-MS experiments were performed using an Agilent Technologies Inc. 7500ce Series Inductively Coupled Plasma - Mass Spectrometer (Agilent Technologies, Inc. Australia, Forrest Hill, Victoria, Australia) (Figure 2-1). To increase sensitivity, the ICP-MS *ce* lens assembly was replaced with a *cs* model. Platinum sampling and skimmer cones were used. The ICP-MS was controlled by Agilent Technologies ICP-MS ChemStation software (B.03.07) on a Hewlett Packard desktop PC via a 10base-T Ethernet connection. All experiments used ultra high purity liquid argon (Ace Cryogenics, Castle Hill, New South Wales, Australia).

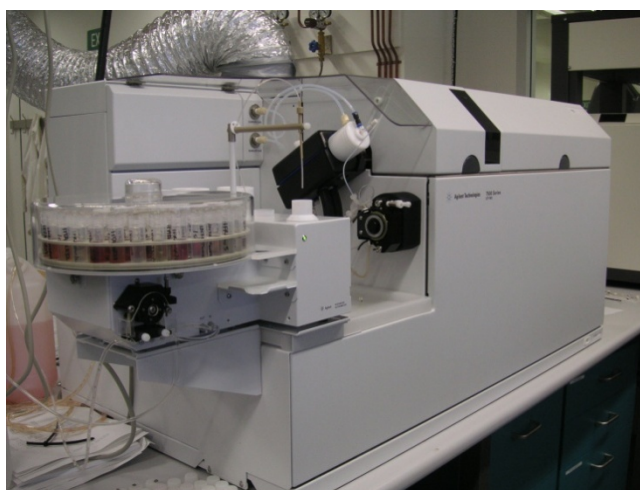


Figure 2-1: Agilent 7500ce ICP-MS

2.1.2 Laser ablation

During laser ablation experiments the conventional sample introduction system of the ICP-MS was bypassed. Tygon tubing with an internal diameter of 3.2 mm was connected between the 'gas out' valve of the laser ablation unit and the ICP torch by a simple quartz ball-and-socket joint. Argon carrier gas was sourced from the ICP-MS carrier gas outlet and carried via a Tygon tube to the 'gas in' valve on the laser unit. Gas valves within the laser unit were controlled using the laser software. The laser ablation system was controlled by New Wave Laser Ablation System software (B.1.8.13.0) on a Hewlett Packard desktop PC independent of the ICP-MS controller.

The laser ablation unit used in all imaging experiments was a New Wave UP213 (Kenelec, Mitcham, Victoria, Australia), equipped with an Nd:YAG laser emitting in the fifth harmonic at 213 nm (Figure 2-2). A large format laser ablation cell (LFC) (New Wave) on an x-y stage with adjustment in the z plane was used in most experiments. A standard laser ablation cell (New Wave) was used during some reaction cell experiments to prepare the images in Chapter 7. All other experiments in this chapter were conducted using a LFC. Argon was used as the carrier gas.



Figure 2-2: New Wave UP213 laser ablation unit fitted with a standard cell

2.1.3 Solution ICP-MS operational parameters

Solution ICP-MS was used for the analysis of digested tissue standards. Solutions for analysis were placed in an Agilent Technologies I-AS autosampler. Solutions were delivered to the ICP-MS via 1.02 mm internal diameter Tygon tubing and a three channel peristaltic pump. The solution was delivered at a rate of 1.0 mL min^{-1} . An internal standard composed of $100 \mu\text{g g}^{-1}$ Rh in 1% HNO_3 was delivered online via 0.19 mm internal diameter Tygon tubing and added to the analyte solution via a T-connector post-pump. The solutions were delivered to the plasma via an Ezylok Micromist nebuliser and Scott-type double pass spray chamber (Glass Expansion, West Melbourne, Victoria, Australia). The ICP-MS was run in reaction mode using the fitted octopole reaction system (ORS). The ORS was delivered 4.5 mL min^{-1} ultra high purity He (BOC Australia, North Ryde, NSW, Australia) to attenuate polyatomic interferences from the analysis.

The instrument was tuned daily for sensitivity using an approximately $1 \mu\text{g L}^{-1}$ solution of Li, Co, Y, Ce and Tl in 1% HNO_3/HCl (Choice Analytical, Thornleigh, NSW, Australia). An auto-tune was performed to determine the best operational parameters. Minor alterations were made to the tuning parameters to ensure the best sensitivity and low background levels were obtained.

Table 2-1: Typical operational parameters used during solution ICP-MS analysis using Agilent 7500ce ICP-MS

Plasma Conditions		Ion Lenses	
RF Power	1550 W	Extract 1	4.6 V
RF Matching	1.70 V	Extract 2	-135.0 V
Sample Depth	6.0 mm	Omega Bias – cs	-30 V
Torch Position	0.6 mm (H) 0.2 mm (V)	Omega Lens – cs	7.4 V
Carrier Gas	1.20 L/min	Cell entrance	-30 V
Makeup Gas	0.0 L/min	QP Focus	-12 V
Optional Gas	0 %	Cell exit	-40 V
Nebuliser Pump	0.1 rps	Octopole Parameters	
Quadrupole Parameters		Octopole RF	180 V
AMU Grain	122	Octopole Bias	-20 V
AMU Offset	127	Detector Parameters	
Axis Grain	0.9992	Discriminator	8 mV
Axis Offset	0.01	Analog HV	1660 V
QP Bias	-16 V	Pulse HV	1210 V
		Reaction Cell	
		He Gas	4.5 mL/min

2.1.4 LA-ICP-MS operational parameters

Before the ICP torch was ignited, the LFC was ‘evacuated’ before being purged with argon gas for at least ten minutes, several times, and allowed to move to ‘online’ mode where the gas continued to the ICP interface. The ICP was then ignited and the gas was allowed to continue running through the cell. The available space in the LFC meant it did not need to be re-opened to replace samples after the initial evacuation and purge.

The standard cell was purged for at least 60 seconds, three times before the ICP torch was ignited. The standard cell was moved from ‘online’ to ‘bypass’ mode when changing the sample in the cell. The cell was purged again before returning to ‘online’ mode.

The instrument was tuned before each use with National Institute of Standards and Technology’s (NIST) 612 Trace Elements in Glass standard. NIST 612 glass contains

approximately $50 \mu\text{g g}^{-1}$ of a range of elements (Table 2-2). Laser parameters used during tuning are outlined in Table 2-3. Typical ICP-MS tuning parameters are outlined for standard mode and reaction mode in Table 2-4 and Table 2-5 respectively.

Table 2-2: Element concentrations in NIST Glass 612; * denotes certified value [84]

Element	Concentration ($\mu\text{g g}^{-1}$)	Element	Concentration ($\mu\text{g g}^{-1}$)	Element	Concentration ($\mu\text{g g}^{-1}$)
Ag*	21.92	Ge	34.64	S	16.00
As	37.33	Hf	34.77	Sb	38.44
Au	5.09	Ho	37.87	Sc	41.05
B	34.73	In	42.93	Sm	36.72
Ba	37.74	K	66.26	Sn	37.96
Be	37.73	La	35.77	Sr*	76.15
Bi	29.84	Li	41.54	Ta	39.77
Cd	28.32	Lu	37.71	Tb	35.92
Ce	38.35	Mg	77.44	Th*	37.23
Co	35.26	Mn	38.43	Ti	48.11
Cr	39.88	Mo	38.3	Tl	15.07
Cs	41.64	Nb	38.06	Tm	37.55
Cu	36.71	Nd	35.24	U*	37.15
Dy	35.97	Ni*	38.44	V	39.22
Er	37.43	P	55.16	W	39.55
Eu	34.44	Pb*	38.96	Y	38.25
Fe*	56.33	Pr	37.16	Yb	39.95
Ga	36.24	Rb*	31.63	Zn	37.92
Gd	36.95	Re	8.12	Zr	35.99

Table 2-3: Typical laser parameters used during tuning

Laser Parameters	
Laser Spot Size	100 μm
Laser Scan Speed	5 μms^{-1}
Laser Power	100%
Laser Pulse Rate	20 Hz
Mode	Continuous
Substrate being ablated	NIST 612

Table 2-4: Typical operational parameters during LA-ICP-MS analysis in standard mode using Agilent 7500ce ICP-MS with cs lenses

Plasma Conditions		Ion Lenses	
RF Power	1300 W	Extract 1	4.6 V
RF Matching	1.70 V	Extract 2	-100.0 V
Sample Depth	4.0 mm	Omega Bias – cs	-30 V
Torch Position	0.6 mm (H)	Omega Lens – cs	7.6 V
	0.2 mm (V)	Cell entrance	-30 V
Carrier Gas	1.20 L/min	QP Focus	0 V
Makeup Gas	0.0 L/min	Cell exit	-40 V
Optional Gas	0 %	Octopole Parameters	
Nebuliser Pump	--- rps	Octopole RF	180 V
Quadrupole Parameters		Octopole Bias	-6 V
AMU Grain	122	Detector Parameters	
AMU Offset	127	Discriminator	8 mV
Axis Grain	0.9992	Analog HV	1660 V
Axis Offset	0.01	Pulse HV	1210 V
QP Bias	-3 V	Reaction Cell	
		OFF	

Table 2-5: Typical operational parameters during LA-ICP-MS analysis in reaction mode using Agilent 7500ce ICP-MS with cs lenses. The same parameters were used for other volumes of H₂ during the same analysis periods

Plasma Conditions		Ion Lenses	
RF Power	1300 W	Extract 1	4.6 V
RF Matching	1.70 V	Extract 2	-100.0 V
Sample Depth	4.0 mm	Omega Bias – cs	-30 V
Torch Position	0.6 mm (H)	Omega Lens – cs	7.6 V
	0.2 mm (V)	Cell entrance	-30 V
Carrier Gas	1.20 L/min	QP Focus	-10 V
Makeup Gas	0.0 L/min	Cell exit	-40 V
Optional Gas	0 %	Octopole Parameters	
Nebuliser Pump	--- rps	Octopole RF	180 V
Quadrupole Parameters		Octopole Bias	-20 V
AMU Grain	122	Detector Parameters	
AMU Offset	127	Discriminator	8 mV
Axis Grain	0.9992	Analog HV	1660 V
Axis Offset	0.01	Pulse HV	1210 V
QP Bias	-18 V	Reaction Cell	
		H ₂	3 mL min ⁻¹

2.2 Data acquisition and processing

Data were acquired by the ablation of thin (10 - 50 μm thickness) sections of tissue. Tissue samples were received affixed to microscope slides. An example of brain sections which have been prepared and placed on a microscope slide for analysis using LA-ICP-MS is given in Figure 2-3.

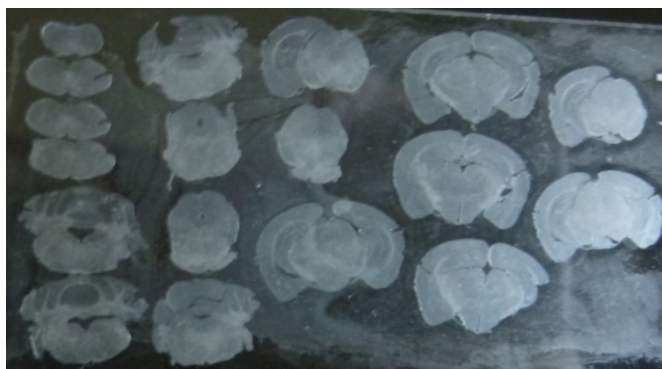


Figure 2-3: Example of a microscope slide with sections of mouse brain prepared for LA-ICP-MS analysis

2.2.1 Data acquisition

After tuning the instrument, the laser software was used to prepare an ablation program. A sequence of ablation lines was prepared in order for the laser to ablate the entire tissue sample to be analysed and imaged. This is represented in Figure 2-4 which also outlines how each line being saved as a separate data file.

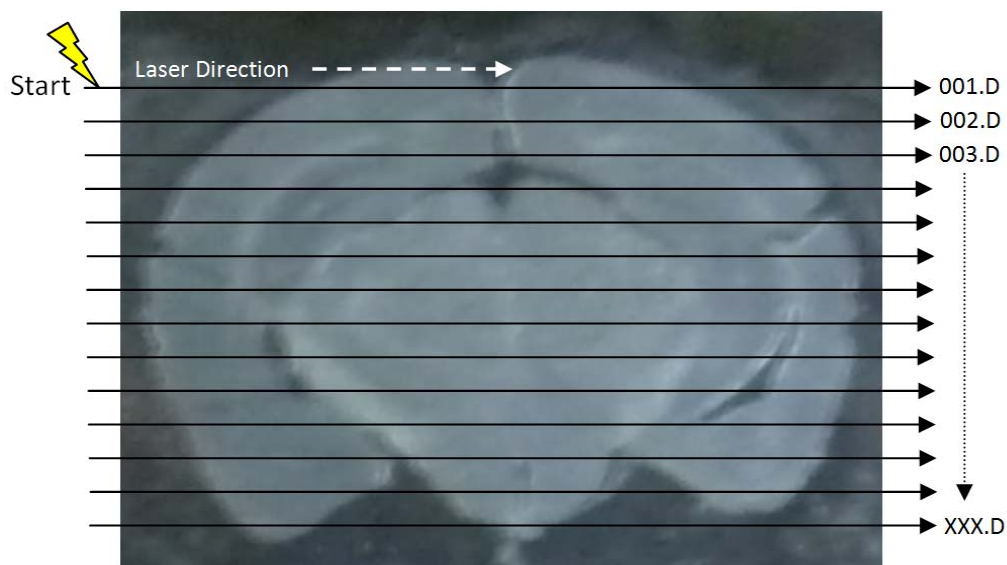


Figure 2-4: Representation of imaging experiments. Each line represents a scan file saved as a .csv file according to the numbers on the right

An aperture wheel, through which the incident beam is passed, was used to alter the size of the laser beam spot, typically producing circular spots in the μm -diameter range. The appropriate laser spot diameter (x_s) was selected for analysis at the required resolution. The sample stage was moved at a defined speed (v_l), passing the tissue surface through a series of continuous laser pulses. Therefore, the resulting ablated line was essentially rectangular in shape (Figure 2-5). Ablated material was swept to the ICP by a carrier gas where positive ions are produced and transferred to a mass analyser.

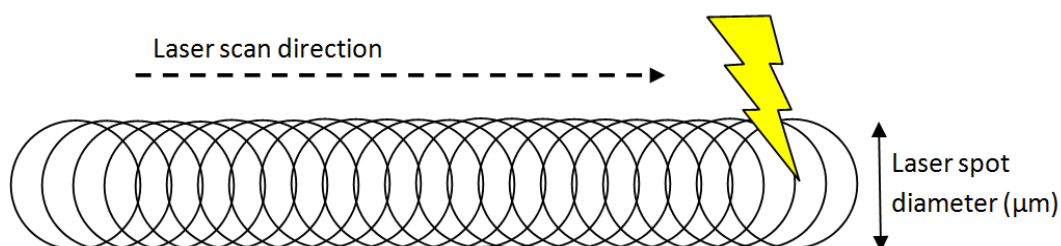


Figure 2-5: Laser traversing the surface of the sample in a continuous series of pulses, 20 Hz in these experiments

The quadrupole mass analyser used in these experiments acquired data for an allocated mass to charge ratio (m/z) for a specified time period, or dwell time, before moving to the next m/z . This continued until data has been acquired for all designated m/z . The scan cycle repeated and this continued for the length of each acquisition period, or in this case, the time required for the laser ablation system to complete the single ablation line.

Dwell time can be adjusted in the ICP-MS software. Typical imaging experiments will measure several masses in the same acquisition. Different m/z values can be assigned specific dwell times independent of other measured masses. The scan cycle (t_{sc}), or sampling period, is equal to the sum of dwell times for each m/z plus the time taken for the quadrupole to move between masses. For imaging experiments each scan cycle equates to one data point, with each data point corresponding to one pixel in the final image. Typical image construction methods are independent of dwell times for m/z , as each pixel was expressed as counts per second, no matter what proportion of the scan cycle the dwell time was. Thus the pixel size will remain constant for all m/z . The ICP-MS software where dwell time for each m/z can be set, and the resulting calculated scan cycle is presented in Figure 2-6.

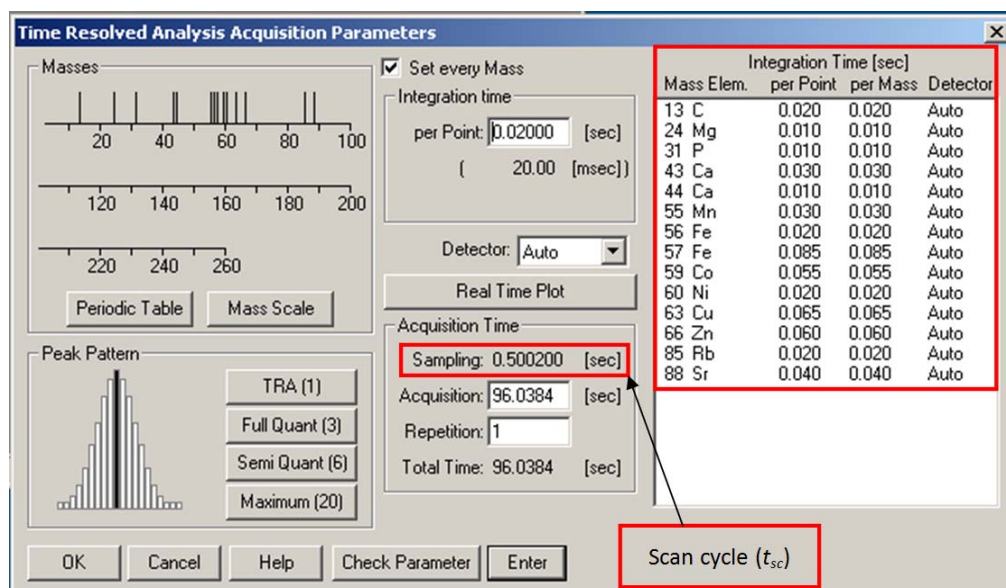


Figure 2-6: ICP-MS software showing the acquisition parameters and dwell times set for individual m/z

A mass spectrum for each measured mass was recorded in a time-resolved manner, and these spectra were reduced to two-dimensional maps that represent relative signal intensity as a function of the image dimensions. The change in signal intensity for ^{66}Zn throughout a single ablation line is represented in Figure 2-7. At the end of a line, data were stored in Comma Separated Value (.csv) file format which was viewed in MS Excel (Figure 2-8).

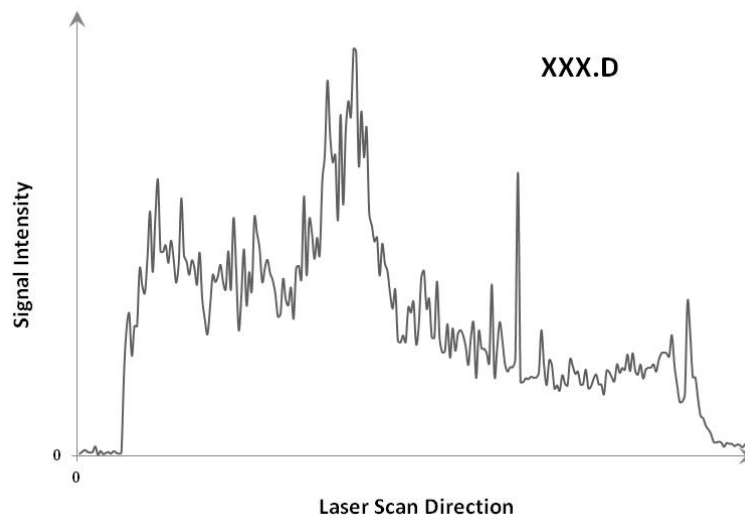


Figure 2-7: Example of a laser scan file for ^{66}Zn represented as an x-y scatter plot prepared in MS Excel

The screenshot shows a Microsoft Excel spreadsheet with the following structure:

- Row 1:** File path: C:\PCPCHEM\1\DATA\VESSICA\REACTION\111213\1m\30.b\001.D
- Row 2:** Intensity CPS
- Row 3:** Time [Sec] C13
- Row 4:** Headers for elements: Mg24, Mg25, P31, K39, Ca43, Ca44, Cr52, Cr53, Mn55, Fe56, Fe57, Co59, Ni60, Cu63, Zn66, As75, S80, S82
- Rows 4-39:** Data rows containing intensity values for each element at specific time intervals.

Figure 2-8: A single scan file as opened from the saved .csv file

2.2.2 Data manipulation

2.2.2.1 Normalisation and data organisation

Raw data were normalised to data collected for ^{13}C in order to eliminate any effect from signal drift over long acquisitions. The signal for ^{13}C , which is relatively constant over a tissue section, was chosen as the reference element to act as an internal standard. Data needed to be presented in a single file in Band Interleave by Line (BIL) format that could be read by ITT Visual Information Solutions ENVI hyperspectral data analysis suite (Boulder, Colorado, USA). Data were normalised and arranged using a macro in Microsoft Excel 2003 written in Visual Basic for Applications 6.0 programming language (Appendix Table 1). Data were arranged by scan file in the rows with a single blank row between each scan file. The output is represented in Table 2-6 and the data in MS Excel are presented in Figure 2-9.

Table 2-6: Representation of post-macro data organised into a single MS Excel file in Band Interleave by Line (BIL) format, prepared for interpretation by the ENVI Imaging Suite

	A	B	C	D	E	F	G	H	...
Scan File 001	C	C	C	C	C	C	C	C	...
	P	P	P	P	P	P	P	P	...
	Mn	Mn	Mn	Mn	Mn	Mn	Mn	Mn	...
	Fe	Fe	Fe	Fe	Fe	Fe	Fe	Fe	...
	Cu	Cu	Cu	Cu	Cu	Cu	Cu	Cu	...
	Zn	Zn	Zn	Zn	Zn	Zn	Zn	Zn	...
Scan File 002	C	C	C	C	C	C	C	C	...
	P	P	P	P	P	P	P	P	...
	Mn	Mn	Mn	Mn	Mn	Mn	Mn	Mn	...
	Fe	Fe	Fe	Fe	Fe	Fe	Fe	Fe	...
	Cu	Cu	Cu	Cu	Cu	Cu	Cu	Cu	...
	Zn	Zn	Zn	Zn	Zn	Zn	Zn	Zn	...
Etc...

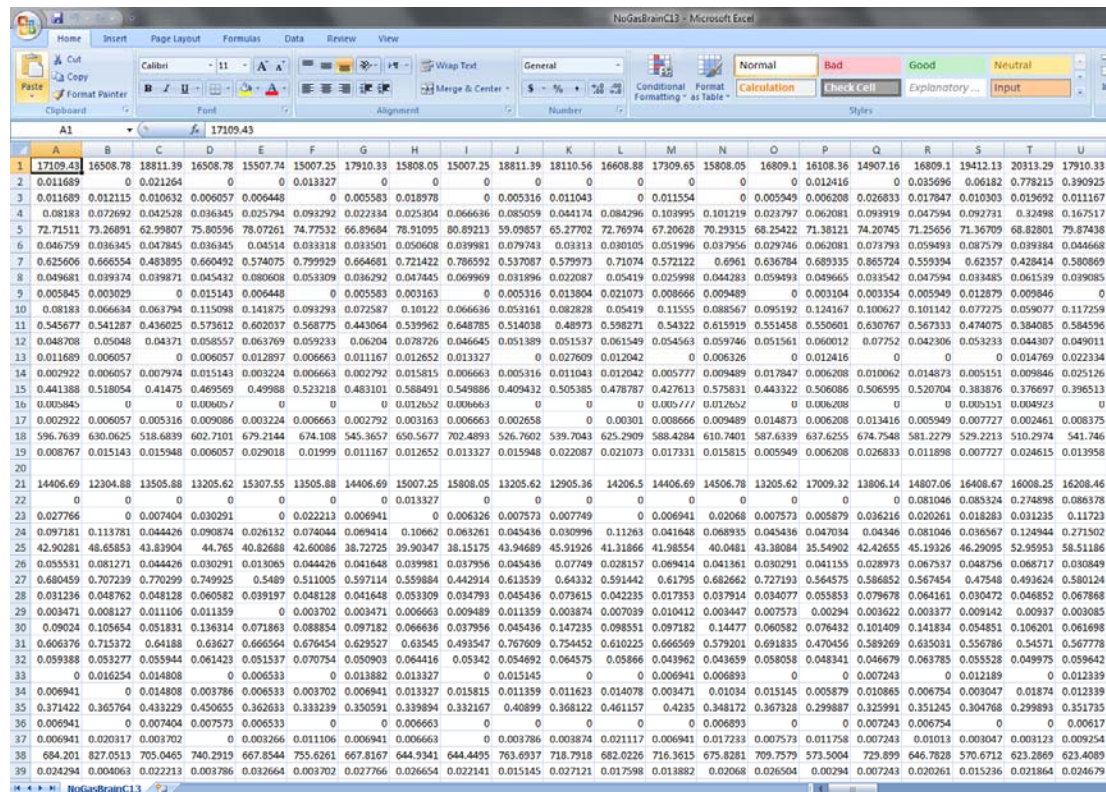


Figure 2-9: View of organised MS Excel data after utilising a macro in MS Excel

2.2.2.2 Background subtraction

In order to reduce the interference from background signal present for a number of m/z in certain images, the average of the background signal was subtracted from each data point collected for the image. This process was undertaken post-macro in MS Excel using the following “IF” function;

=IF((Sheet1!A2-(AVERAGE(Sheet1!\$A2:\$H2)))<0,0,(Sheet1!A2-(AVERAGE(Sheet1!\$A2:\$H2))))).

This function indicates that if the cell’s value minus the average of the gas blank is less than zero, then the answer will be zero. If this is not true, the answer will be the cell’s value minus the average of the gas blank. Using the “IF” function, the background signal was subtracted from the image without the result providing an unworkable negative value. Figure 2-10 shows the Excel file from Figure 2-9 after background subtraction.

	A	B	C	D	E	F	G	H	I	J	K	L	M	N	O	P	Q	R	S	T	U
1	0	0	1701.96	0	0	0	800.9	0	0	1701.96	1001.13	0	200.22	0	0	0	0	2302.7	3203.86	800.9	0
2	0.005099	0	0.014674	0	0	0.006736	0	0	0	0	0	0	0	0	0.005825	0	0.029105	0.055229	0.771624	0.384334	0
3	0.002301	0.002726	0.001243	0	0	0	0	0.009589	0	0	0.001655	0	0.002166	0	0	0	0.017445	0.008459	0.000914	0.010304	0.001778
4	0.029992	0.020854	0	0	0.041454	0	0	0.014799	0.033221	0	0.032458	0.052157	0.049382	0	0.010244	0.042081	0	0.040893	0.273143	0.11568	0
5	0.142979	0.696777	0	3.233827	5.500483	2.203187	0	6.338819	8.319996	0	0.197607	0	0	0	0	1.625316	0	0	0	7.302248	0
6	0.004272	0	0.005358	0	0.002653	0	0	0.008122	0	0.037256	0	0	0.009509	0	0.019595	0.031306	0.017007	0.045093	0	0.002181	0
7	0.023482	0.064429	0	0.058367	0	0.197805	0.062557	0.119298	0.184468	0	0	0.108615	0	0.093976	0.03466	0.087211	0.263599	0	0.021446	0	0
8	0	0	0	0.029615	0.002316	0	0	0.018976	0	0	0.003197	0	0	0.0085	0	0	0	0	0	0.010545	0
9	0	0	0	0.00905	0.000355	0	0	0	0	0.007711	0.01498	0.002579	0.003996	0	0	0	0	0	0.006785	0.003753	0
10	0	0	0	0.021251	0.048029	0	0	0.007374	0	0	0	0.021784	0	0.001346	0.030321	0.006781	0.007296	0	0	0.023413	0
11	0.00595	0.001559	0	0.033885	0.062309	0.029048	0	0.001225	0.109058	0	0	0.058543	0.003492	0.076192	0.011731	0.010874	0.091039	0.027605	0	0.044869	0
12	0	0	0.005512	0.010725	0.006188	0.008995	0.025681	0	0	0	0.008504	0.001519	0.006701	0	0.000968	0.024475	0	0.000189	0	0	0
13	0.004349	0	0	0.005557	0	0.003827	0.005312	0.005987	0	0.020269	0.004702	0	0	0	0.005076	0	0	0	0.007428	0.014984	0
14	0	0	0.00091	0.008079	0	0	0.00875	0	0	0.003979	0.004977	0	0.002425	0.010783	0	0.002998	0.007809	0	0.002782	0.018061	0
15	0	0.049326	0	0.000841	0.031152	0.054489	0.014373	0.119762	0.081157	0	0.036656	0.010058	0	0.107103	0	0.037358	0.037867	0.051975	0	0	0
16	0.003464	0	0.003677	0	0	0	0.010271	0.004283	0	0	0.003397	0.010271	0	0.003828	0	0	0.002771	0.002542	0	0	0
17	0	0.000736	0	0.003765	0	0.001342	0	0	0	0	0.003344	0.004168	0.009552	0.000887	0.008095	0.000628	0.002406	0	0.003054	0	0
18	0	24.5752	0	0.003765	0	73.72742	68.62105	0	45.08078	97.00238	0	0	19.80395	0	5.25317	0	32.13859	69.26784	0	0	0
19	0	0.000157	0.000961	0	0.014032	0.005004	0	0	0.000961	0.0071	0.006086	0.002345	0.000828	0	0	0.011847	0	0	0.009628	0	0
20	0	0	0	0	0	0	0	0	0	0	0	0	0	0	0	0	0	0	0	0	0
21	0	0	0	0	900.86	0	0	850.36	1401.36	0	0	0	0	100.09	0	2602.63	0	400.37	2001.98	1801.56	1801.77
22	0	0	0	0	0	0	0	0.13327	0	0	0	0	0	0	0	0	0	0.081046	0.085324	0.274898	0.086378
23	0.014673	0	0.017199	0	0.00912	0	0	0	0	0	0	0	0	0.007388	0	0	0.023124	0.007188	0.055191	0.018142	0.104138
24	0.022703	0.039302	0.016395	0	0	0.012142	0	0	0	0.038151	0	0	0	0	0	0	0	0.006567	0.050465	0.197023	0
25	0	4.460076	0.366546	0	0	0	0	0	0	1.720808	0	0	0	0	0	0	0	0.994808	2.092493	8.781075	14.31341
26	0.010614	0.036354	0	0	0	0	0	0.000519	0.032573	0	0.024497	0	0	0	0.038221	0.003839	0.022621	0.003839	0.0238	0	0
27	0	0.015874	0.078934	0.038561	0	0	0	0	0	0	0	0	0	0.033829	0	0	0	0	0	0	0
28	0	0.003181	0.002547	0.015001	0	0.002547	0	0.007728	0	0.028034	0	0	0	0	0.010273	0.034097	0.01858	0	0.001271	0.022287	0
29	0	0.001314	0.004294	0.004546	0	0	0.002678	0.004546	0	0.000227	0.003399	0	0.00076	0	0	0	0.002329	0.002358	0	0	0
30	0	0.014474	0	0.045134	0	0	0.006002	0	0	0.056055	0.007371	0.006002	0.05359	0	0	0.010229	0.050654	0	0.015021	0	0
31	0	0.06208	0	0.013271	0.023162	0	0	0.114316	0.10118	0	0.013277	0	0.038542	0	0	0	0	0	0	0	0
32	0.003074	0	0.005109	0.014444	0	0.008102	0	0	0.008261	0.002347	0	0.001744	0	0	0.001744	0	0	0.007471	0	0.003328	0
33	0	0.008735	0.007289	0	0	0.006363	0.005808	0	0.007636	0	0	0	0	0	0	0	0	0.00467	0	0.00482	0
34	0.000528	0	0.000395	0.000119	0	0.000528	0.000913	0.009401	0.004945	0.005209	0.007664	0	0.003026	0.000731	0	0.004451	0.00034	0	0.012327	0.005926	0
35	0	0.036488	0.033914	0	0	0	0	0.01225	0	0.064417	0.02676	0	0	0	0	0	0	0	0	0	0
36	0.001251	0	0.001714	0.001882	0.000843	0	0.000973	0	0	0	0	0	0.001203	0	0	0.001553	0.001663	0	0.000479	0	0
37	9.59E-05	0.013472	0	0	0.004261	9.59E-05	0	0	0	0.014272	9.59E-05	0.010388	0.000727	0.004913	0.000398	0.003285	0	0	0.002409	0	0
38	0	102.1622	0	15.40287	0	30.73708	0	0	0	38.80472	0	0	0	0	0	5.009968	0	0	0	0	0
39	0.00689	0	0.004808	0	0.01526	0	0.010361	0.00925	0.004736	0	0.009716	0.000193	0	0.003276	0.0091	0	0.002856	0	0.00446	0.007275	0

Figure 2-10: View of the organised MS Excel data after background subtraction. This particular section of data is mostly background so the majority of values are small or equal to zero.

2.2.3 Image construction

After running the macro and the construction of a single .csv file, the data was imported into ENVI using ASCII translation. Each ablation line is equidistant and contains an equal number of pixels, effectively creating a map of the intensity distribution of each m/z on the tissue surface. A representation of how the scan files are aligned is presented in Figure 2-11 a). The resulting signal intensities for each scan file were converted to a colour in the red-green-blue (RGB) colour scale. Cold colours represent areas of low signal intensities and warm colours represent areas with high signal intensities. Figure 2-11 b) is a processed image for ^{66}Zn with the highlighted section corresponding to the four sequential scan files.

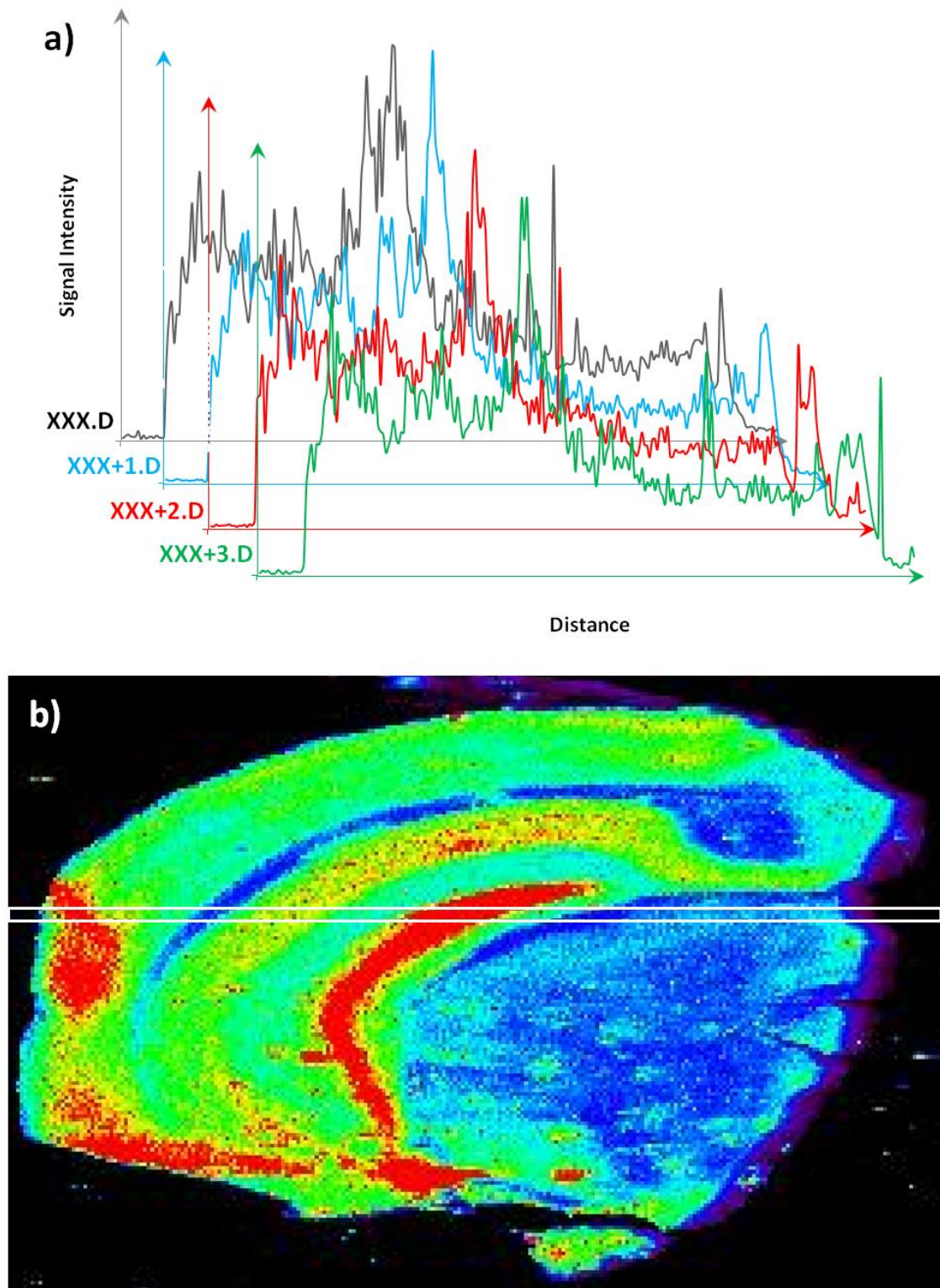


Figure 2-11: a) Sequential scan files showing signal intensities for ^{66}Zn ; b) Image for ^{66}Zn : the highlighted pixels indicate four sequential scan files

2.3 Experimental methods

All methods utilising sectioned mouse brains conformed to the Australian National Health and Medical Research Council published code of practice for animal research and were approved by the University of Melbourne Animal Ethics Committee.

2.3.1 Tissue standard preparation

Experiments were run using 30 µm thick tissue standard sections prepared using chicken breast. The chicken breast was removed of any fat or connective tissue and spiked with Mg, P, Ca, Mn, Fe, Co, Ni, Cu, Zn, Rb and Sr solutions. The general tissue standard preparation process is outline in Figure 2-12. Salt solutions relative to the metal contained in them were prepared using the appropriate soluble metal salts outlined in Table 2-7 (Sigma-Aldrich, Castle Hill, NSW, Australia). These salts were separately dissolved in 1% HNO₃ and made up to concentrations of approximately 100 000 µg mL⁻¹ and 10 000 µg mL⁻¹. Aliquots of the chicken breast were weighed to 5.0 g in acid washed flat-bottomed polypropylene vials (Kelly Scientific) then spiked with varying concentrations of each of the elements (Table 2-8 and Table 2-9) and homogenised using an OmniTech TH tissue homogeniser fitted with polycarbonate probes. Six approximately 250 mg aliquots of each homogenised tissue standard were acid digested using a method adapted from EPA Method 3050B - Acid digestion of sediments, sludges and soils [85] (see *infra*, Section 2.3.1.1) and made up to a final mass of 50 g using 1% HNO₃. Solution ICP-MS analysis was then performed to determine the concentration of each element in the tissue standards. The spiked tissue was then frozen and sectioned into 30 µm sections and placed onto glass microscope slides for analysis (see *infra*, Section 2.3.1.3). Development of this method is outlined in Chapter 3. The final tissue concentrations are outlined in Chapter 3, Table 3-2.

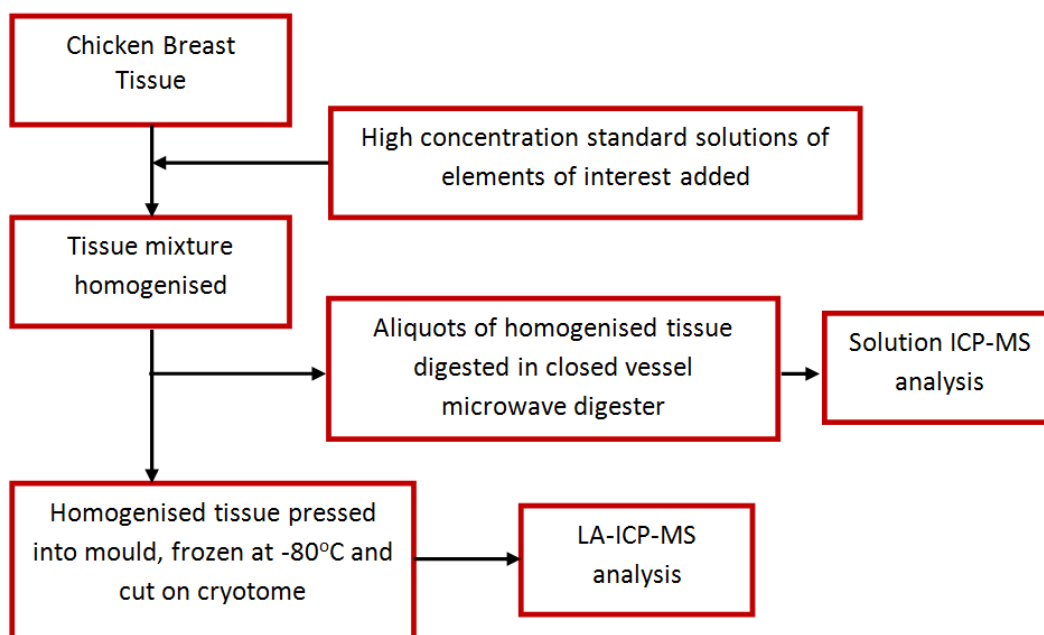



Figure 2-12: Flow-chart for tissue standard preparation

Table 2-7: Soluble metal salts used to prepare high concentration salt solutions (Sigma-Aldrich)

Metal Salt	Certified purity (%)
Strontium Nitrate	99.9995
Calcium Nitrate Hydrate	99.997
Magnesium Nitrate Hexahydrate	99.999
Iron (II) Sulfate Hydrate	99.999
Copper Nitrate Hydrate	99.999
Zinc Nitrate Hydrate	99.999
Cobalt (II) Nitrate Hexahydrate	99.999
Nickel (II) Nitrate Hexahydrate	99.999
Rubidium Sulfate	99.990
Manganese (II) Chloride Hydrate	99.999

Table 2-8: Approximate volume of concentrated salt solutions spiked into 5.0 g of chicken breast

Approximate volume of salt solutions spiked in each standard (μL)										
Std	$\text{Ca}(\text{NO}_3)_2$	$\text{Co}(\text{NO}_3)_2$	$\text{Cu}(\text{NO}_3)_2$	FeSO_4	$\text{Mg}(\text{NO}_3)_2$	MnCl_2	$\text{Ni}(\text{NO}_3)_2$	Rb_2SO_4	$\text{Sr}(\text{NO}_3)_2$	$\text{Zn}(\text{NO}_3)_2$
Blank	0	0	0	0	0	0	0	0	0	0
A	20	5	5	15	10	1	5	2	2	20
B	10	25	15	6	20	2	25	10	4	4
C	15	5	3	12	4	1	5	20	10	8
D	25	10	5	20	8	2	10	4	14	15
E	40	15	10	30	12	3	15	6	20	25
F	45	20	12	35	16	4	20	8	30	30
G	60	25	15	45	20	5	25	10	4	40

 10 000 $\mu\text{g mL}^{-1}$ solution

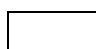
 100 000 $\mu\text{g mL}^{-1}$ solution

Table 2-9: Approximate concentration of elements spiked into chicken breast

Approximate amount of element spiked in each standard ($\mu\text{g g}^{-1}$)										
Std	Ca	Co	Cu	Fe	Mg	Mn	Ni	Rb	Sr	Zn
Blank	0.0	0.0	0.0	0.0	0.0	0.0	0.0	0.0	0.0	0.0
A	9.8	3.2	3.4	11.0	3.3	1.1	3.2	2.6	1.7	13.8
B	48.9	16.1	10.2	44.1	6.6	2.3	16.1	12.8	3.3	27.6
C	73.3	32.2	20.3	88.2	13.1	11.3	3.2	25.6	8.3	55.2
D	122	64.4	33.9	147	26.2	22.5	64.3	51.2	11.6	104
E	195	96.6	67.8	221	39.3	33.8	96.4	76.8	16.6	173
F	220	129	81.3	257	52.4	45.1	129	102	24.8	207
G	293	161	102	331	65.5	56.3	161	128	33.1	276

This method of tissue standard preparation was compared against a previously outlined method described by Hare [1], and adapted from Becker *et al* [5]. The experimental method for the preparation of these standards followed the same procedure, however the high concentration salt solutions prepared with soluble metal salts were substituted in lieu of Fe, Cu, Zn and Mn sourced from certified 1000 $\mu\text{g mL}^{-1}$ single element standard solutions in 2% (v/v) HNO_3 (Choice Analytical).

2.3.1.1 *Microwave assisted acid digestion*

In order to determine the accurate concentrations of elements in the tissue by solution ICP-MS analysis, 250 mg aliquots of spiked chicken breast tissue were digested using a method adapted from EPA Method 3050B - Acid digestion of sediments, sludges and soils [85]. Six approximately 250 mg aliquots of each spiked tissue standard were accurately weighed in acid washed Teflon vessels from a Milestone MLS 1200 Microwave Digester (Kelly Scientific). To each vessel, 5.0 mL of 69% (w/v) Seastar Baseline grade HNO₃ (Choice Analytical) was delivered and the vessels covered with a lid. After 5 minutes, the lid was removed and 1.0 mL of 31% (w/v) Ultrapur H₂O₂ solution (Merck, Kilsyth, Victoria, Australia) was added to each vessel. The lids were replaced and the Teflon vessels were sealed in the microwave carousel. The carousel was placed in the microwave digestion unit and run using the program outlined in Figure 2-13.

After the program completed, the carousel was removed and allowed to cool in a running water bath for at least 15 minutes. The vessels were opened in the fume cupboard and the digested material was added to weighed 50 mL acid washed polypropylene tubes. The Teflon vessels were washed out with small volumes of 1% HNO₃ which was added to the solution in the tubes. The digested solution was made up to approximately 50 g using the 1% HNO₃ solution and the actual mass accurately recorded.

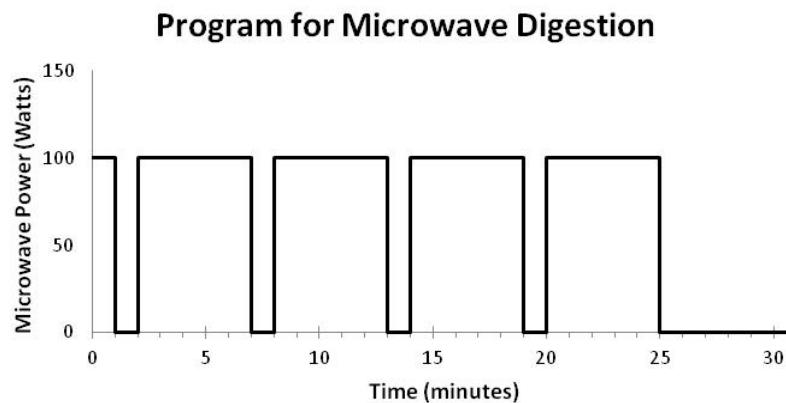


Figure 2-13: Acid digestion method

2.3.1.2 Solution ICP-MS analysis

Solution ICP-MS analysis was performed to determine the accurate concentrations of elements in the digested tissue solutions using an Agilent 7500ce ICP-MS. Calibration standard solutions were prepared by accurately weighing varying amounts of certified 10 mg L⁻¹ and 100 mg L⁻¹ solutions of Mg, P, Ca, Mn, Fe, Co, Ni, Cu, Zn, Rb and Sr in 2% HNO₃ (Choice Analytical). All calibration standards were prepared in 5.0 mL acid washed flat-bottomed polypropylene vials (Kelly Scientific). The standard solutions were made up to approximately 5.0 g with 1% HNO₃ and the accurate mass of the final solution was recorded. The accurate masses of elements added to each calibration standard and the final mass was used to calculate the accurate concentration of elements in each standard (Table 2-10). The digested tissue samples were transferred to separate 5.0 mL acid washed flat-bottomed polypropylene vials and placed in the instrument's I-AS autosampler carousel along with the calibration standards and "blank" 1% HNO₃ solutions.

Table 2-10: Concentrations of elements in solution ICP-MS external calibration standards ($\mu\text{g kg}^{-1}$)

Standard	Ca	Co	Cu	Fe	Mg	Mn	Ni	Rb	Sr	Zn
Blank	0	0	0	0	0	0	0	0	0	0
1	48.7	10.3	13.2	48.3	98.3	7.2	8.9	9.8	11.1	46.8
2	93.3	39.2	48.8	99.2	463.8	12.1	44.4	52.5	46.1	95.6
3	252	101	102	252	758	24.3	102	102	102	252
4	510	204	203	510	1530	50.5	204	204	153	511
5	984	292	293	984	1950	97.7	292	291	194	830
6	1570	469	468	1520	2530	203	472	468	252	1020
7	2000	610	612	1970	3000	301	613	611	302	1505

2.3.1.3 Tissue sectioning

Tissue sectioning was conducted by Dr Dominic Hare as outlined in [1].

Homogenised tissue standards were packed into plastic 15 x 15 x 5 mm disposable histology molds (ProSciTech, Thuringowa, Queensland, Australia) and frozen in isopentane and liquid nitrogen (Merck). After complete freezing, the tissue was removed from the mold and the base of the block was mounted in TissueTek O.C.T. compound (ProSciTech) on a steel chuck. O.C.T. is a mixture of soluble polyvinyl alcohol and polyethylene glycol that freezes at $-10\text{ }^{\circ}\text{C}$ and provides support for soft tissue during cutting. O.C.T. rapidly evaporates on sectioning. Along with supporting the tissue block, O.C.T. ensured no part of the tissue came into direct contact with the stainless steel chuck.

Sections were cut to $30\text{ }\mu\text{m}$ and $10\text{ }\mu\text{m}$ thicknesses using a microm HM550 cryotome (Waldorf, Germany) fitted with C.L. Sturkey Diamond low-profile microtome blades (ProSciTech) and mounted on microscope slides. [1]

2.3.1.4 LA-ICP-MS calibration

Sectioned tissue standards were used to perform matrix-matched calibrations for LA-ICP-MS experiments. The tissue standards were placed in the laser ablation cell and the cell was evacuated and purged. With the aid of the laser ablation software and the adjoined CCD camera, 7 lines were drawn for each standard. Lines were separated at a distance at least 50% greater than the spot diameter. The length of each line was calculated based on the scan speed and a desired ablation period of at least 30 seconds. Data for a 10 second period during laser warm-up was collected prior to tissue ablation. At the end of each ablation line, a wash out period of at least 15 seconds, depending on the cell format, was performed. A typical data acquisition for a line of a calibration standard is presented in Figure 2-14.

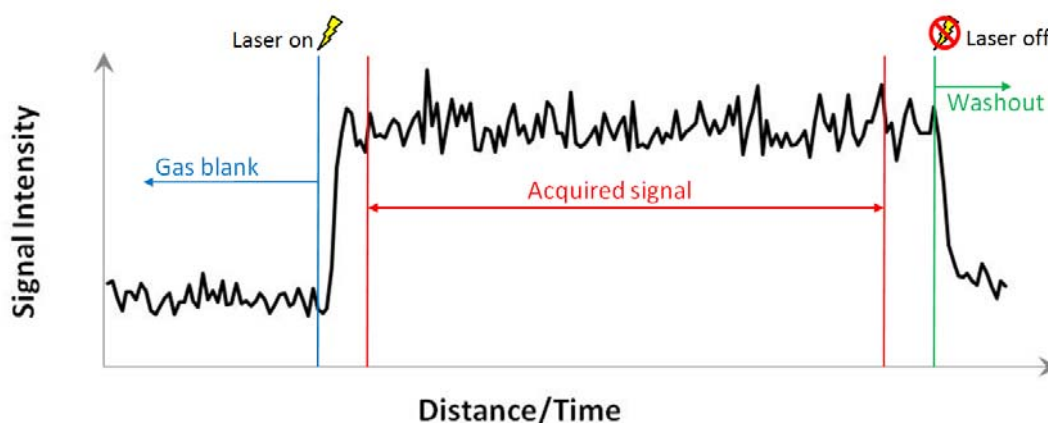


Figure 2-14: A typical signal profile for a tissue standard

After data acquisition, the .csv files were opened in Microsoft Office Excel 2003/2007. The signal acquired for the 7 ablation lines for each standard were averaged. If ^{13}C normalisation was being performed, the signal for each mass was divided by the signal representing ^{13}C . The signal intensities acquired during the ablation period for each isotope were averaged and a standard deviation calculated. Any statistical outliers (spikes or troughs) in the data were removed from the calculated averages and standard deviations. Using the concentrations

verified by solution ICP-MS analysis for each element and the average signal intensities acquired for each isotope, linear regression analysis using the least squares method was performed and calibration curves for each isotope were constructed. The functions used in Excel calculations are outlined in Section 2.4, Table 2-11.

2.4 Calculations

2.4.1 Linear regression analysis

Table 2-11: Functions used for linear regression analysis in Excel and the corresponding calculations performed; where \bar{y} , \bar{x} and \bar{a} are sample averages; \hat{y} is the y-value calculated from the linear regression equation; n is the number of observations; \bar{y}_0 is the average background signal

Function	Excel Syntax	Equation
Average	=AVERAGE(number1, number2,...)	$\bar{a} = \frac{1}{n} \sum_{i=1}^n a_i$
Standard Deviation	=STDEV(number1, number2,...)	$s = \sqrt{\frac{\sum(x - \bar{x})^2}{(n - 1)}}$
Slope (m)	=SLOPE(known_y's,known_x's)	$m = \frac{\sum(x - \bar{x})(y - \bar{y})}{\sum(x - \bar{x})^2}$
Intercept (b)	= INTERCEPT(known_y's,known_x's)	$b = \bar{y} - m\bar{x}$
Linearity (r^2)	=RSQ(known_y's,known_x's)	$r^2 = \frac{\sum(x - \bar{x})(y - \bar{y})}{\sqrt{\sum(x - \bar{x})^2 \sum(y - \bar{y})^2}}$
Error in slope (s_m)	Calculated using =LINEST(known_y's,known_x's,TRUE,TRUE)	$s_m = \sqrt{\frac{\frac{1}{n-2} \sum(y - \hat{y})^2}{\sum(x - \bar{x})^2}}$
Error in intercept (s_b)	Calculated using =LINEST(known_y's,known_x's,TRUE,TRUE)	$s_b = \sqrt{\frac{\sum(y - \hat{y})^2 \sum x^2}{n(n-2) \sum(x - \bar{x})^2}}$
95% confidence interval	= CONFIDENCE(0.05,standard_dev,size)	$CI_{95\%} = \bar{x} \pm 1.96 \left(\frac{s}{\sqrt{n}} \right)$
Background equivalent concentration (BEC)		$BEC = \frac{\bar{y}_0 - b}{m}$

2.4.2 Limits of analysis

Table 2-12: Equations used for determining the limits of analysis; where \bar{y}_0 is the average background signal, s_0 is the standard deviation of the background signal, b is the intercept, and m is the slope.

Function	Equation
Limit of detection	$LOD = \frac{(\bar{y}_0 + 3s_0) - b}{m}$
Limit of quantification	$LOQ = \frac{(\bar{y}_0 + 10s_0) - b}{m}$
Limiting signal	$LS = \bar{y}_0 + 10s_0$

2.4.3 Signal to noise ratios

Table 2-13: Equations used for calculating the signal to noise ratios; where \bar{y}_0 is the average background signal, \bar{y}_c is the average signal for a mid-range standard, and x_c is the known concentration of that mid-range standard.

Function	Equation
Signal to noise ratio	$SNR = \frac{\bar{y}_c}{\bar{y}_0}$
Signal (per $\mu\text{g g}^{-1}$) to noise ratio	$SNR = \frac{\bar{y}_c/x_c}{\bar{y}_0}$

2.5 Animals

EBI was performed using the brains of animals prepared offsite. Mice for all experiments are C57BL/6 genetic strains, the most widely used mouse for models of human disease, which have been modified to suit their specific purpose. Calibration for each experiment was performed prior to the ablation of each sectioned tissue sample using the calibration curves constructed from representative ablation lines of the prepared matrix-matched tissue standards (see Section 2.3.1.4). Data acquisition methods are outlined in Section 2.2.

2.5.1 ZnT3 KO mouse brains

Zinc transporter-3 knockout (ZnT3 KO) mouse brains were sourced from adult wild type mice prepared by the Mental Health Research Institute (MHRI), Victoria, Australia. All animal experimentation was approved by the Howard Florey Animal Ethics Committee and conformed to the Code of Practice established by the National Health and Medical Research Council of Australia for the Care and Use of Animals for Scientific Purposes, Seventh Edition (2004).

Female ZnT3 KO and wildtype littermates were raised to 3, 6 and 24 months of age. In the four weeks prior to culling, animals underwent behavioural testing. Animals were then culled and tissues collected. One hemisphere of the brain was fixed with 4% paraformaldehyde for 4 hours and retained for histological endpoints. The other hemisphere was micro-dissected and frozen for LA-ICP-MS analysis. Brain hemispheres were cryosectioned at 30 μm and mounted on microscope slides. Sections that showed similar characteristics were used during the analyses.

ZnT3 KO mouse brains were used for the following experiments;

- Chapter 4, Section 4.7: Imaging with increased laser scan speed;
- Chapter 5, Section 5.3.4: Zinc deficits in ZnT3 KO animals; and
- Chapter 6, Section 6.6: Imaging using increasing volumes of hydrogen.

2.5.2 PBT-2 treated ZnT3 KO mice

ZnT3 KO mice treated with PBT-2 were prepared by the Mental Health Research Institute (MHRI), Victoria, Australia. All animal experimentation was approved by the Howard Florey Animal Ethics Committee and conformed to the Code of Practice established by the National Health and Medical Research Council of Australia for the Care and Use of Animals for Scientific Purposes, Seventh Edition (2004).

ZnT3 KO mice and wildtype littermates were aged to 6 months, at which point they were culled. For six weeks prior to culling, animals were treated with a daily gavage of a placebo (SSV) or PBT-2 ($30 \mu\text{g g}^{-1}$, made up in SSV). Behaviour testing was carried out prior to culling. The brain was dissected and frozen before being cryosectioned at $30 \mu\text{m}$ for LA-ICP-MS analysis.

These mouse brains were used for the following experiment;

- Chapter 5, Section 5.3.5: PBT-2 treated animals.

2.5.3 AGE/Intermittent hypoxic mice

Young adult male C57BL/6J mice (The Jackson Laboratory, Bar Harbor, ME) were studied. Mice were 8 weeks of age at the start of long-term intermittent hypoxia (LTIH) experiments. The methods and study protocols were approved in full by the Institutional Animal Care and Use Committee of the University of Pennsylvania and conformed to the revised National Institutes of Health Office of Laboratory Animal Welfare Policy. Food and water were provided *ad libitum*. Mice were confirmed pathogen free at the time of studies.

Eleven mice were exposed for eight weeks to an experimental model of obstructive sleep apnea, as developed for rats by Gozal *et al.* [86] and modified for mice by Veasey *et al.* [87]. Throughout both LTIH (n = 5) and sham LTIH (n = 6), home cages of mice (4 to a cage) were placed within Plexiglas chambers (64 cm x 50 cm X 50 cm; Biospherix, Redfield, NY). The flow rates of > 99% nitrogen and > 99% oxygen into the chambers were varied with an automated oxygen profile system (Oxycycler model A84XOV; Biospherix, Redfield, NY) to produce episodic (90-second cycle length) reductions from an ambient oxygen level. In the LTIH condition, ambient oxygen concentration fluctuated between 21% and 9%, with the 9% nadir being maintained for 5 seconds. This protocol causes oxyhemoglobin saturation to fluctuate between 94 and 98%, and 76 and 84% (Veasey *et al.* [87]), which is comparable to the magnitude of desaturation observed during apneic episodes in humans. LTIH conditions were produced for 10 hours of the lights-on period. The control condition (sham LTIH) consisted of mice that were housed under identical conditions except that the ambient oxygen level fluctuated between 21% and 19% over the same cycle length as in the LTIH protocol. This protocol causes oxyhemoglobin saturation to fluctuate very slightly (96 – 98% to 96 - 97%; Veasey *et al.* [87]). Humidity, ambient CO₂, and environmental temperature were held constant within and across exposures.

At the conclusion of 8 weeks of exposure to either LTIH or sham LTIH, mice were killed by an injection of sodium pentobarbitone (80 mg kg⁻¹ I.P.) and then perfused transcardially with 0.1M phosphate buffered saline, followed by 4% paraformaldehyde in 0.1M phosphate buffer. Brains were post-fixed, cryoprotected in sucrose solutions, and then sectioned in the coronal plane at 40µm thickness on a cryotome. Sections were stored at 4°C in 0.1M phosphate buffer containing sodium azide. Sections passing through the rostral hippocampus were mounted onto glass microscope slides and then air dried.

These mouse brains were used for the following experiment;

- Chapter 5, Section 5.4.4: Imaging.

***Chapter 3: Improving matrix-
matched tissue standard
preparation***

Chapter 3: Improving matrix-matched tissue standard preparation

3.1 Chapter outline

Even with recent advances in tissue analysis using LA-ICP-MS, one of the major challenges continues to be the preparation of analytically viable matrix-matched tissue standards.

This chapter details improvement to a matrix-matched tissue standard preparation technique proposed by Hare [1], originally adapted from Becker *et al* [5]. For an improvement in the tissue standards to be observed there must be;

- a. an increase in tissue and analyte homogeneity
- b. an increase in linearity
- c. an increase in the number of analytes present; and
- d. an increase in the range of analyte concentration to better suit tissue analysis

The main disadvantage to the previously proposed tissue standard preparation was a decrease in the homogeneity of sectioned tissue as the concentrations of spiked elements increased. Using $1000 \mu\text{g mL}^{-1}$ certified single element standard solutions in 2% HNO_3 resulted in relatively high ratios of liquid being spiked into the tissue. Upon freezing and sectioning the tissue standards, large areas void of tissue, and therefore analyte, were obtained.

Substituting the $1000 \mu\text{g mL}^{-1}$ standard solutions for higher concentration solutions would prevent the issues of the previous standard preparation technique. These high concentration

standard solutions were prepared using soluble metal salts free from trace metals (Sigma-Aldrich, Castle Hill, NSW, Australia).

Single element standard solutions containing approximately 10 000 $\mu\text{g mL}^{-1}$ and 100 000 $\mu\text{g mL}^{-1}$ of each analyte were prepared and used to spike chicken breast tissue. Higher concentration salt solutions allowed for the use of smaller quantities of solution to be spiked into the tissue. The concentration of analytes in tissue with no spiked metal salts (Blank Standard) was also measured to obtain a baseline concentration of analytes in chicken breast tissue.

The experimental methods for this chapter are outlined in Chapter 2, Sections 2.3.1.

Accompanying Publication:

Hare, D., Lear, J., Bishop, D., Beavis, A., & Doble, P. (2012). Protocol for production of matrix-matched brain tissue standards for imaging by laser ablation-inductively coupled plasma-mass spectrometry. *Analytical Methods*, Under Review.

3.2 Tissue homogeneity

The benefit of using high concentration solutions prepared with soluble metal salts is immediately evident upon visual inspection of the sectioned tissue standards. With the aid of the microscope attached to the laser ablation unit, the homogeneity of each tissue standard was observed.

The tissue standards prepared using $1000 \mu\text{g mL}^{-1}$ single element standard solutions are presented in Figure 3-1. As the analyte concentration increases, there is an increase in areas void of tissue and therefore a decrease in tissue homogeneity.

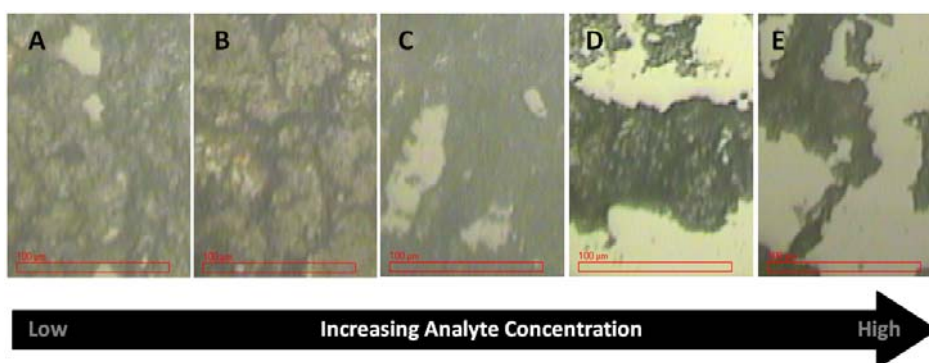


Figure 3-1: Visual homogeneity of standards prepared using $1000 \mu\text{g mL}^{-1}$ single element standard solutions as observed through the microscope fitted to the laser ablation unit (500x magnification)

Inhomogeneity in the tissue is also observed in the ^{13}C signal intensity during ablation of the tissue standard. As the laser traverses the surface of the tissue, it moves across areas of tissue where high ^{13}C signal intensity is observed, and areas with no tissue where a low ^{13}C signal intensity is observed (Figure 3-2). As the concentration of analyte, and therefore volume of liquid in the standard increased, there was an increase in the number of areas of low signal intensity.

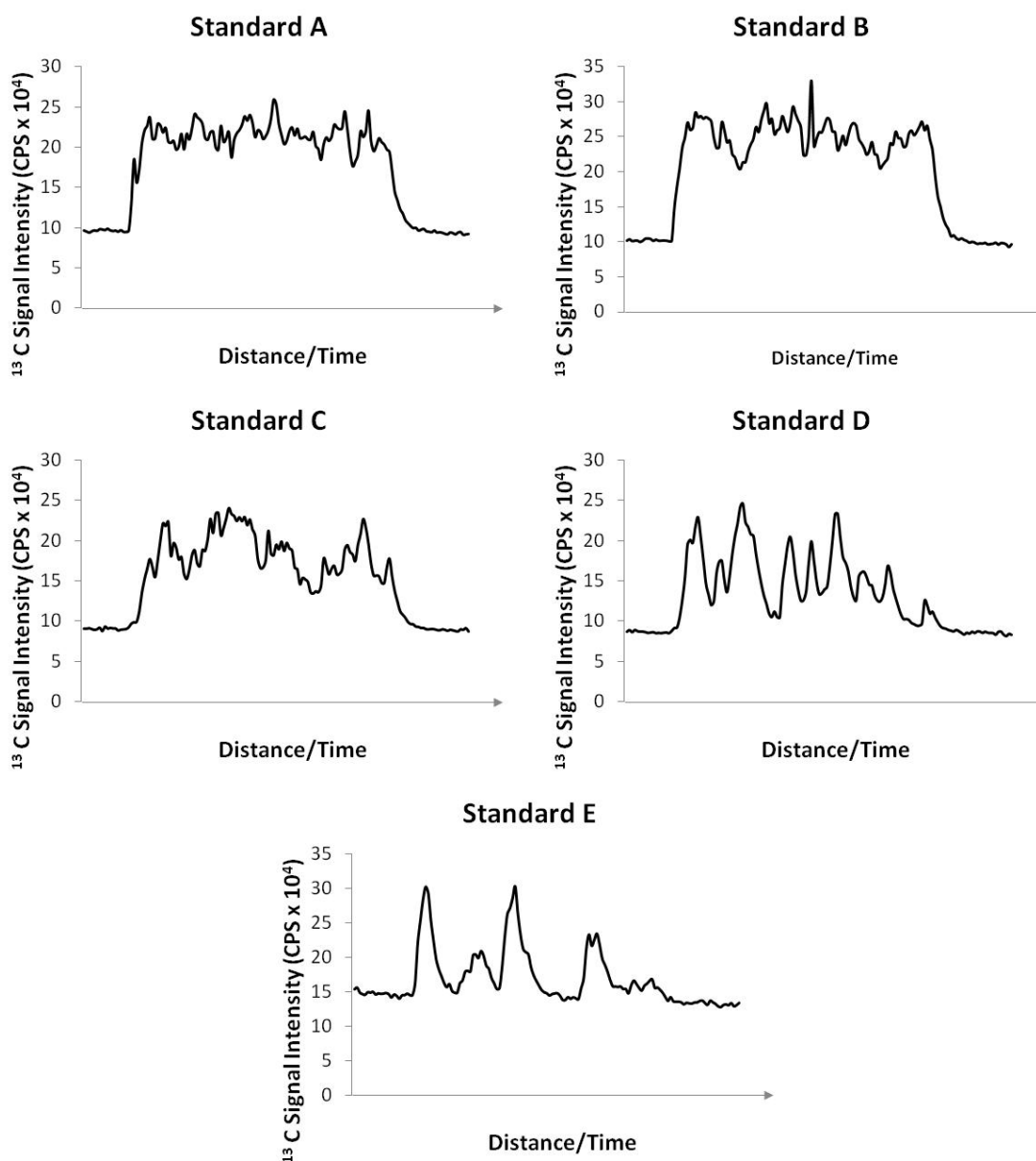


Figure 3-2: ^{13}C signal intensity during line ablation for tissue standards prepared using $1000 \mu\text{g mL}^{-1}$ standard single element solutions. Signal moves from gas blank to standard ablation and returns to gas blank.

For higher analyte concentration tissue standards, the amount of tissue being ablated was minimal and this decreased the accuracy of the results, especially when averaging the signal of several ablation lines. Concentrations lower than the true concentrations of the analytes were observed. In these cases and not ideally, data was manually selected and rejected in order to estimate a true representation of the analyte concentrations.

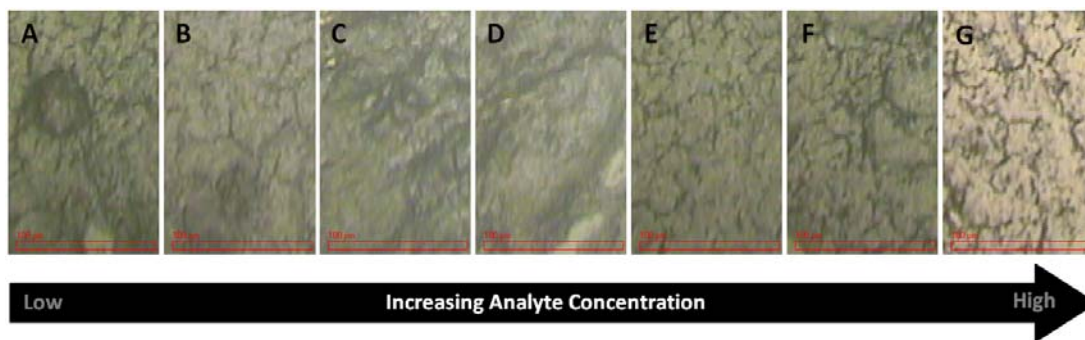


Figure 3-3: Visual homogeneity of standards prepared using metal salt solutions as observed through the microscope fitted to the laser ablation unit (500x magnification)

The homogeneity of the tissue standards prepared using the high concentration metal salt solutions is represented in Figure 3-3. Upon visual inspection, there is a marked improvement in homogeneity for the high analyte concentration tissue standards and uniformity in tissue distribution for all of the tissue standards.

The ^{13}C signal intensity for these tissue standards is represented in Figure 3-4. Variation in the signal intensity was still observed. This was expected as relative standard deviations of the signals during ablation are comparably higher than SN-ICP-MS analysis. There was an improvement in the uniformity of the signal intensity during the ablation of the tissue, as well as an improvement in the uniformity of the average signal intensity between tissue standards when compared to the standards prepared with $1000 \mu\text{g mL}^{-1}$ single element standard solutions. An improvement in uniformity indicated that a similar quantity of tissue was ablated across all tissue standards. Therefore, a more accurate representation of the true analyte concentration was obtained.

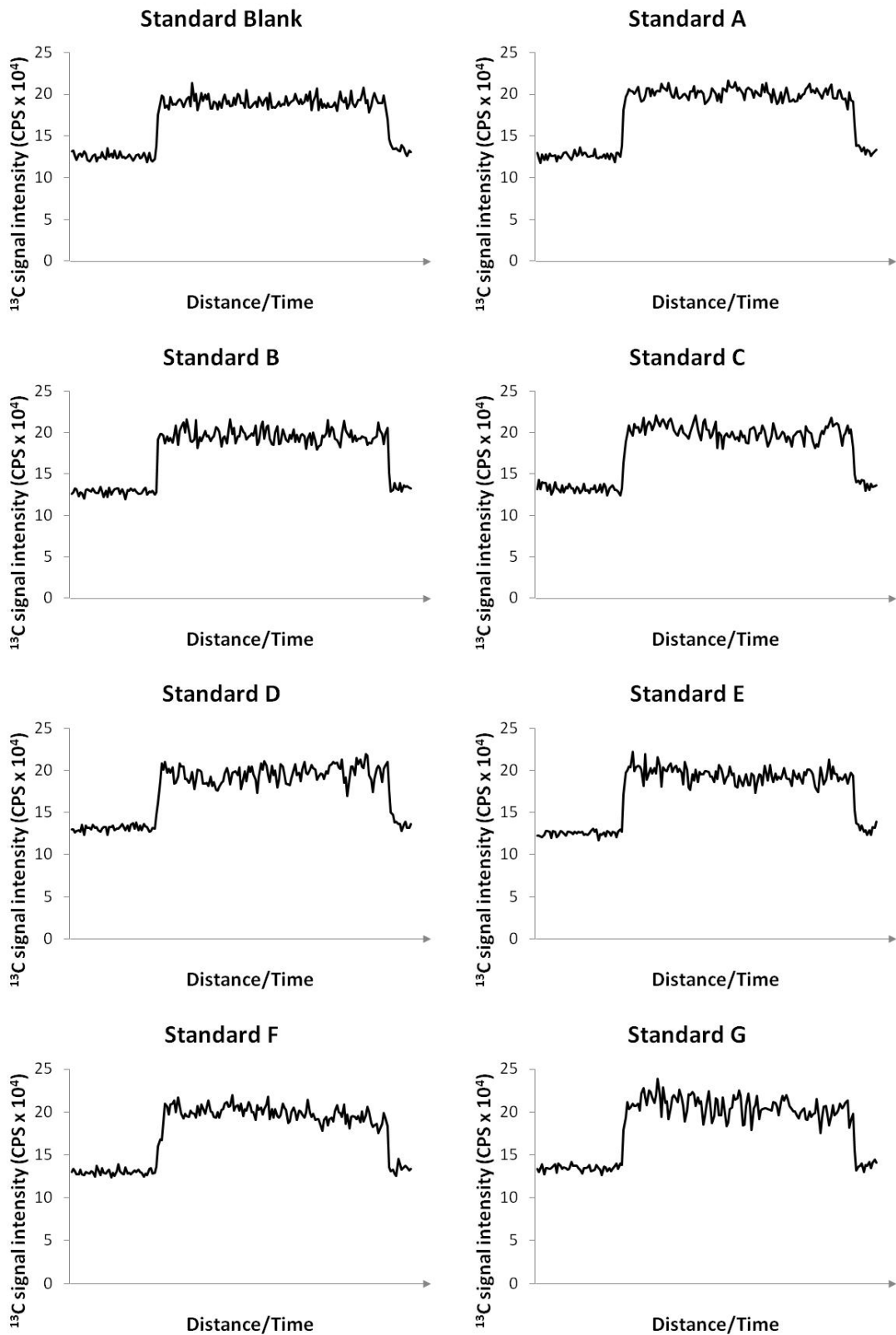


Figure 3-4: ^{13}C signal intensity during line ablation for tissue standards prepared using metal salt solutions. Signal moves from gas blank to standard ablation and returns to gas blank.

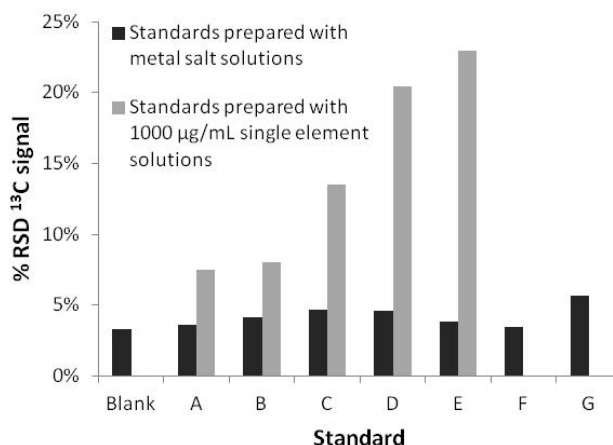


Figure 3-5: Comparison of the relative standard deviations of the ¹³C signal during ablation of the prepared calibration standards

Figure 3-5 compares both standard preparation techniques numerically. A significant difference in the uniformity of the tissue between standard preparation techniques was observed. This confirmed the benefit that high concentration metal salt solutions used to prepare matrix-matched tissue standards has on tissue sample homogeneity.

3.3 Calibration data

3.3.1 SN-ICP-MS

The concentration of each analyte in the prepared tissue standards was determined following acid digestion of the tissue standards, forming a solution that was analysed using SN-ICP-MS. Calibration data for the digested tissue standards is presented in Figure 3-6. Data on the errors in the slope and intercept, as well as the correlation coefficients, detection limits and background equivalent concentrations (BECs) are presented in Table 3-1.

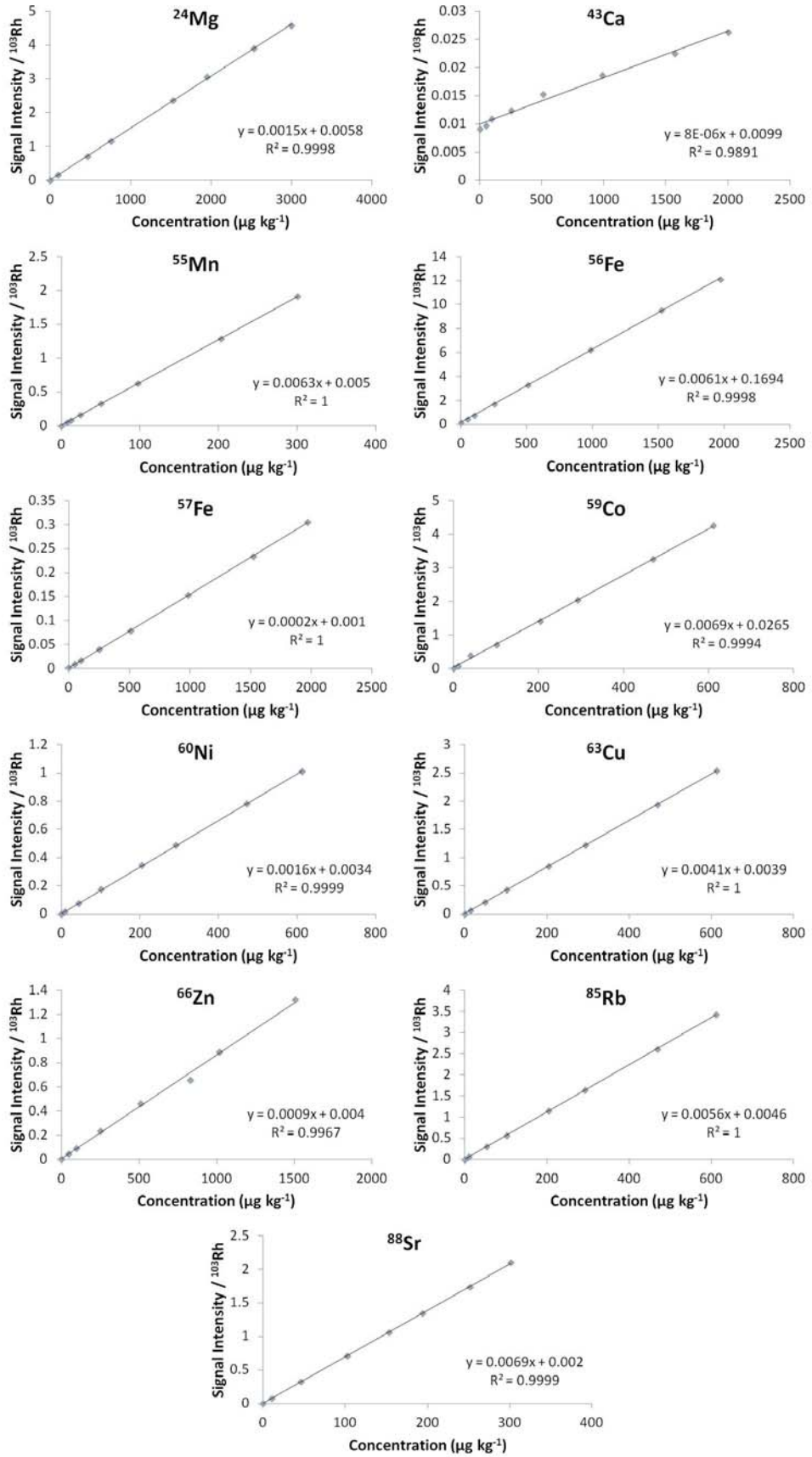


Figure 3-6: SN-ICP-MS calibration curves for each analyte in the aqueous standards

Table 3-1: Errors in the slope and intercept of the SN-ICP-MS calibration curves calculated using linear regression analysis, and the correlation coefficient, detection limit and background equivalent concentration calculated by the ICP-MS software

m/z	Slope (± 95% confidence interval)	Intercept (± 95% confidence interval)	Correlation Coefficient (r ²)	Detection limit (µg kg ⁻¹)	BEC (µg kg ⁻¹)
24	1.54 x10 ⁻³ ± 2.29 x10 ⁻⁵	5.84 x10 ⁻³ ± 3.82 x10 ⁻²	0.9998	2.10	3.72
43	8.25 x10 ⁻⁶ ± 8.64 x10 ⁻⁷	9.95 x10 ⁻³ ± 8.53 x10 ⁻⁴	0.9891	131	1210
55	6.34 x10 ⁻³ ± 4.08 x10 ⁻⁵	4.97 x10 ⁻³ ± 5.49 x10 ⁻³	1.0000	4.77 x10 ⁻³	0.78
56	6.10 x10 ⁻³ ± 8.19 x10 ⁻⁵	1.69 x10 ⁻¹ ± 7.94 x10 ⁻²	0.9998	2.25	27.8
57	1.54 x10 ⁻⁴ ± 9.59 x10 ⁻⁷	1.03 x10 ⁻³ ± 9.30 x10 ⁻⁴	1.0000	7.48	6.72
59	6.91 x10 ⁻³ ± 1.75 x10 ⁻⁴	2.65 x10 ⁻² ± 5.30 x10 ⁻²	0.9994	8.99 x10 ⁻³	3.82
60	1.65 x10 ⁻³ ± 1.50 x10 ⁻⁵	3.39 x10 ⁻³ ± 4.55 x10 ⁻³	0.9999	4.36 x10 ⁻²	2.05
63	4.14 x10 ⁻³ ± 1.10 x10 ⁻⁵	3.91 x10 ⁻³ ± 3.32 x10 ⁻³	1.0000	4.94 x10 ⁻²	0.92
66	8.62 x10 ⁻⁴ ± 4.94 x10 ⁻⁵	4.01 x10 ⁻³ ± 3.63 x10 ⁻²	0.9967	0.225	9.52
85	5.59 x10 ⁻³ ± 2.70 x10 ⁻⁵	4.64 x10 ⁻³ ± 8.18 x10 ⁻³	1.0000	9.19 x10 ⁻³	0.81
88	6.93 x10 ⁻³ ± 6.44 x10 ⁻⁵	2.00 x10 ⁻³ ± 1.09 x10 ⁻²	0.9999	6.63 x10 ⁻³	0.29

NB: BEC is the influence of the background signal intensity on the measured signal.

$$\text{Analyte concentration in tissue (}\mu\text{g g}^{-1}\text{)} = \text{Element concentration calculated from SN-ICP-MS analysis (}\mu\text{g g}^{-1}\text{)} \times \frac{\text{Final mass of digested solution (g)}}{\text{Mass of tissue digested (g)}}$$

Equation 3-1: Calculating final analyte concentration in tissue standards

These calibration curves were used to calculate each analyte concentration in the tissue using Equation 3-1. The calculated concentrations for each of the analytes in the prepared tissue standards are presented in Table 3-2. The error to 95% confidence is quoted and was calculated using the standard deviations of six repeat experiments.

Table 3-2: Calculated analyte concentrations in each of the tissue standards prepared using metal salt solutions

m/z	Analyte concentration \pm 95% confidence interval ($\mu\text{g g}^{-1}$)							
	Blank	A	B	C	D	E	F	G
24	339	349	354	364	389	409	417	418
	± 13.33	± 12.63	± 8.77	± 9.57	± 7.95	± 7.68	± 8.01	± 5.02
43	41.7	51.7	80.6	106	184	163	180	205
	± 5.46	± 3.23	± 13.17	± 5.76	± 37.67	± 10.17	± 5.39	± 6.81
55	0.15	1.02	4.52	5.32	10.5	17.2	23.8	26.9
	± 0.03	± 0.02	± 0.14	± 0.13	± 0.30	± 0.32	± 0.28	± 0.55
56	4.79	9.94	27.9	50.6	88.4	129	162	188
	± 0.60	± 0.39	± 1.74	± 1.43	± 1.96	± 3.49	± 2.90	± 4.90
57	4.61	9.14	26.8	49.0	87.1	128	161	186
	± 0.70	± 0.33	± 1.79	± 1.30	± 2.40	± 3.66	± 2.41	± 4.77
59	0.00	1.71	10.3	19.5	44.1	73.7	94.9	100
	± 0.03	± 0.09	± 0.29	± 0.52	± 1.72	± 1.24	± 1.23	± 4.46
60	0.00	2.34	10.2	18.0	40.9	65.4	84.7	91.6
	± 0.10	± 0.75	± 0.54	± 0.72	± 1.33	± 0.93	± 0.84	± 3.13
63	0.19	2.20	7.40	14.2	25.8	59.1	67.7	80.3
	± 0.10	± 0.11	± 0.19	± 0.35	± 0.84	± 1.89	± 0.70	± 1.48
66	4.55	11.1	17.9	33.1	61.5	93.2	116	130
	± 0.91	± 0.28	± 0.36	± 0.85	± 0.99	± 2.04	± 1.15	± 3.96
85	6.75	9.46	19.7	32.6	58.4	93.9	124	140
	± 0.12	± 0.15	± 0.37	± 0.79	± 2.13	± 1.27	± 1.97	± 3.38
88	0.00	1.69	3.41	9.14	13.0	19.3	30.4	33.3
	± 0.01	± 0.05	± 0.09	± 0.24	± 0.62	± 0.34	± 0.40	± 0.46

3.3.2 LA-ICP-MS

Calibration curves for the tissue standards were constructed using the analyte concentrations calculated from SN-ICP-MS analysis of the digested tissue. Calibration curves are outline in Figure 3-7.

Magnesium and calcium were relatively difficult to analyse in chicken breast tissue. Calcium was challenging as the background noise from the gas blank for m/z 43 and 44 was high and interfered with the acquired signal for both masses across the concentration range of the standards. The construction of linear calibration curves for a viable analysis was not possible without manipulation of the collected data. This involves selecting data where tissue has been ablated and rejecting anything below levels in the gas blank. This resulted in obtaining broad error bars which could not be considered to deliver viably quantifiable data.

The same occurrences were seen for m/z 24 and 25 however the gas blank signal for these masses was low compared to the signal that was acquired during ablation. Calculation of the concentration range of masses in the digested tissue resulted in a sequential increase of concentrations which was not observed in the LA-ICP-MS calibrations. This could be due to the high concentration of Mg in the non-spiked chicken breast and an inhomogeneity of Mg between tissue standards, as well as contamination from external sources. Again, the result was broad error bars which could not be considered to deliver viably quantifiable data.

These results can also be seen in the data presented in Table 3-3. The results for ^{24}Mg and ^{43}Ca presented in the table are the results after correction by removing data from areas where no tissue was present and estimating a representation of the tissue concentrations. Results for ^{25}Mg and ^{44}Ca were not rectifiable so have not been presented.

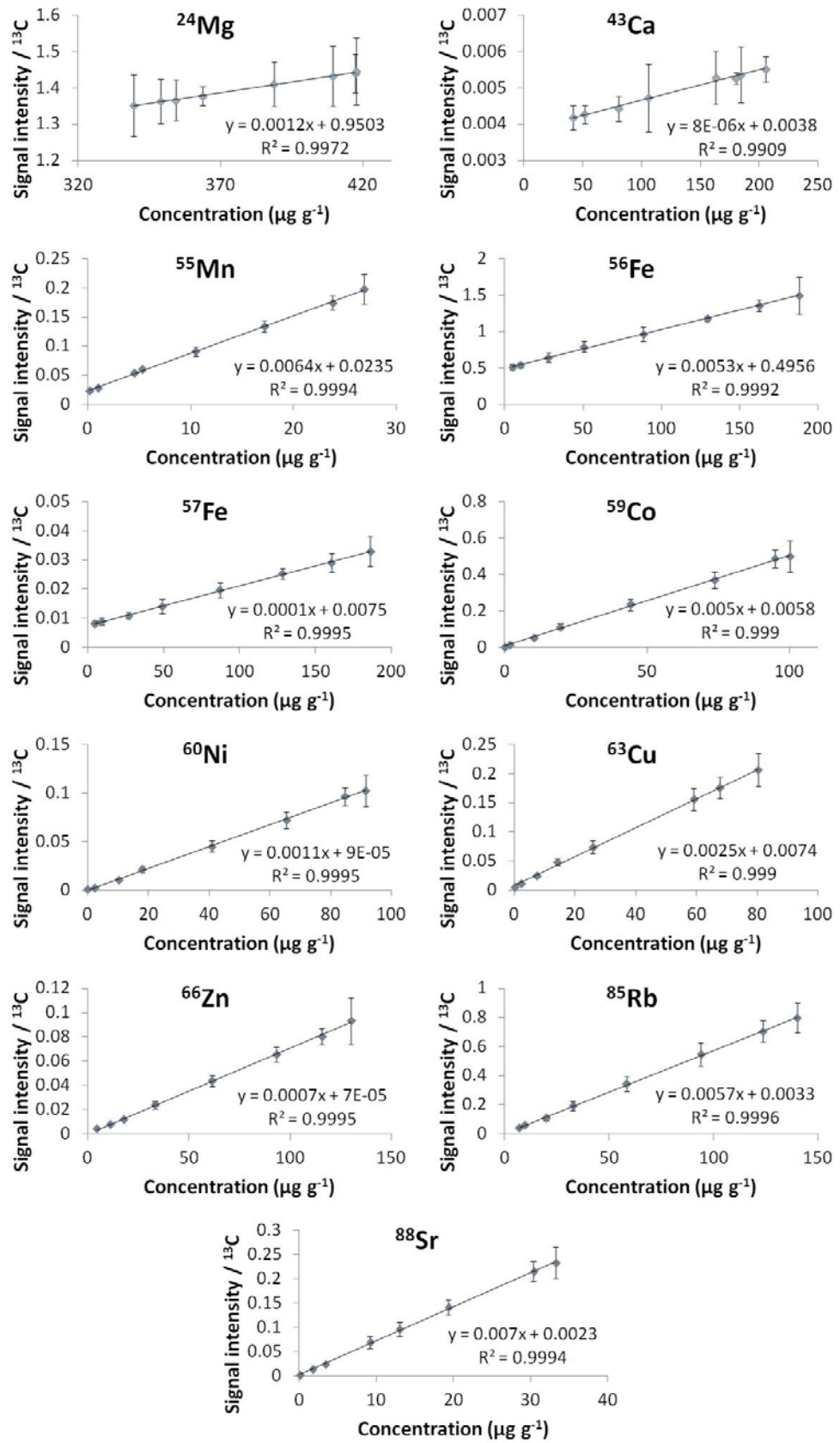


Figure 3-7: LA-ICP-MS calibration curves for each analyte in the tissue standards with error bars at 95% confidence

**Table 3-3: Errors in the slope and intercept, and the correlation coefficient, detection limit and background equivalent concentration of the LA-ICP-MS calibration curves calculated using linear regression analysis.
(LOD = $3s_y/m$)**

m/z	Slope (\pm 95% confidence interval)		Intercept (\pm 95% confidence interval)		Correlation coefficient (r^2)	Detection limit ($\mu\text{g g}^{-1}$)	BEC ($\mu\text{g g}^{-1}$)
24*	1.18×10^{-3}	$\pm 6.29 \times 10^{-5}$	9.50×10^{-1}	$\pm 2.40 \times 10^{-2}$	0.9972	5.58	-805
43*	8.33×10^{-6}	$\pm 7.96 \times 10^{-7}$	3.83×10^{-3}	$\pm 1.12 \times 10^{-4}$	0.9909	20.0	22.4
55	6.45×10^{-3}	$\pm 1.58 \times 10^{-4}$	2.35×10^{-2}	$\pm 2.33 \times 10^{-3}$	0.9994	0.82	-0.02
56	5.33×10^{-3}	$\pm 1.49 \times 10^{-4}$	4.96×10^{-1}	$\pm 1.57 \times 10^{-2}$	0.9992	6.40	9.79
57	1.36×10^{-4}	$\pm 3.19 \times 10^{-6}$	7.52×10^{-3}	$\pm 3.34 \times 10^{-4}$	0.9995	5.34	4.62
59	5.01×10^{-3}	$\pm 1.55 \times 10^{-4}$	5.77×10^{-3}	$\pm 9.01 \times 10^{-3}$	0.9990	4.18	-0.90
60	1.12×10^{-3}	$\pm 2.50 \times 10^{-5}$	8.56×10^{-5}	$\pm 1.13 \times 10^{-3}$	0.9995	2.69	0.73
63	2.50×10^{-3}	$\pm 8.05 \times 10^{-5}$	7.43×10^{-3}	$\pm 3.54 \times 10^{-3}$	0.9990	3.35	-0.86
66	7.06×10^{-4}	$\pm 1.65 \times 10^{-5}$	6.71×10^{-5}	$\pm 1.23 \times 10^{-3}$	0.9995	3.75	1.39
85	5.70×10^{-3}	$\pm 1.12 \times 10^{-4}$	3.32×10^{-3}	$\pm 8.77 \times 10^{-3}$	0.9996	3.36	-0.27
88	7.03×10^{-3}	$\pm 1.78 \times 10^{-4}$	2.31×10^{-3}	$\pm 3.25 \times 10^{-3}$	0.9994	1.05	-0.19

*Results after correction by removing data from areas where no tissue was present and estimating a representation of the tissue concentrations. See Section 3.2.

NB: BEC is the influence of the background signal intensity on the measured signal.

Analytes m/z 55 to 88 showed good linearity and reasonable detection limits for tissue analysis. Several of the analytes showed a negative BEC which occurs when the intercept is greater than the measured average background signal.

3.4 Comparison of calibration data

A comparison of the calibration data for both standard preparation methods is presented in Table 3-4. Four analytes, namely m/z of 56, 57, 63 and 66, their percentage error in the slope with 95% confidence, detection limits and correlation coefficients were compared. The data for the calibrations prepared using the $1000 \mu\text{g mL}^{-1}$ single element standard solution standards has been corrected by removing spikes and troughs in order to obtain comparable linearity. The result for the calibrations prepared using the high concentration metal salt solutions is the data as collected by the ICP-MS, that is, without correction.

Table 3-4: Comparison of the error in slope, detection limits and correlation coefficient for the standards prepared with $1000 \mu\text{g mL}^{-1}$ solutions and those prepared with the metal salt solutions

m/z	Percentage error in slope with $\rho = 0.05$		Detection limits ($\mu\text{g g}^{-1}$)		Correlation Coefficient (r^2)	
	$1000 \mu\text{g mL}^{-1}$ solution standards	Metal salt solution standards	$1000 \mu\text{g mL}^{-1}$ solution standards	Metal salt solution standards	$1000 \mu\text{g mL}^{-1}$ solution standards	Metal salt solution standards
56	$\pm 14.4\%^*$	$\pm 2.73\%$	6.97*	6.40	0.9959*	0.9992
57	$\pm 9.67\%^*$	$\pm 2.48\%$	4.67*	5.34	0.9982*	0.9995
63	$\pm 3.95\%^*$	$\pm 3.22\%$	3.15*	3.35	0.9995*	0.9990
66	$\pm 4.07\%^*$	$\pm 2.51\%$	1.87*	3.75	0.9997*	0.9995

***After correction by removing data from areas where no tissue was present and estimating a representation of the tissue concentrations. See Section 3.2.**

Good correlation between both standard preparation techniques was observed. The percentage error in the slope was generally higher for the standards prepared with $1000 \mu\text{g mL}^{-1}$ standard solutions because there are fewer tissue standards in the standard set. This means that the confidence interval calculation uses a higher student's t value, namely 3.182, since $n=5$. The Student's t value for the metal salt solution standards is 2.447 as $n=8$. A

higher error in the slope means that all other parameters that rely on the slope in their calculations, such as the detection limits, also have a greater error in the result.

3.5 Concentration range and number of analytes

Preparing high concentration standard solutions using high purity metal salts resulted in a smaller volume of liquid being added to each tissue standard. The high concentration standard solutions prepared in this study had approximately 10 000 and 100 000 $\mu\text{g mL}^{-1}$ of analyte in each prepared solution compared to 1000 $\mu\text{g mL}^{-1}$ in the single element standard solutions used previously. A comparison of the total volumes of standard solution added to each tissue standard is outlined in Table 3-5.

Table 3-5: Volume of standard solutions added to tissue standards before homogenisation

Standard	Total volume of standard solutions added (μL)	
	1000 $\mu\text{g mL}^{-1}$ standard solution	High concentration metal salt solution
Blank	0	0
A	110	99
B	250	149
C	950	88
D	1600	123
E	2500	193
F	-	241
G	-	274

Another important point to note is the number of elements added to the tissue standards. For the high concentration metal salt solution tissue standards, ten elements were spiked into each standard with a total volume not exceeding 274 μL . The tissue standards prepared using the 1000 $\mu\text{g mL}^{-1}$ standard solutions had three elements spiked into each tissue standard with volumes not less than 110 μL . Standard G had 2500 μL of solution added to 5 g of tissue, which made the solution account for about one third of the total weight of the standard.

The ability to add more elements to the tissue standards using smaller volumes of liquid is beneficial not only to the homogeneity discussed in Section 3.2, but it also allowed the possibility for much higher concentration tissue standards to be prepared and therefore, a much wider analyte range is achieved in order to better suit a variety of tissue analyses.

3.6 Conclusions

Both standard preparation methods had comparable calibration data. Homogeneity issues however caused areas void of tissue and unusable data in the tissue standards prepared using $1000 \mu\text{g mL}^{-1}$ single element standard solutions. Comparable calibration results were only achieved after careful examination of the data and omitting data collected for the areas void of tissue. Without this data omission, analytically viable calibrations were difficult to achieve.

There was a definite increase in the homogeneity of the tissue after sectioning in the tissue standards prepared using the high concentration metal salt solution standards. Not only did this homogeneity reduce the need to search for areas of tissue to ablate during analysis, but it also removed the need to correct the resulting data. Not having to correct the data also meant that the resulting calibration was not an estimation of the true representation of the concentrations of analyte in the tissue.

The use of high concentration metal salt solutions was also beneficial as a greater number of elements were spiked into each tissue standard at low volumes of solution. This meant only one set of tissue standards was required. Higher concentrations of analytes could be added to the tissue standards, meaning calibration could occur over a wider range of concentrations, suiting a variety of tissue analyses.

***Chapter 4: Increasing image
acquisition speed***

Chapter 4: Increasing image acquisition speed

4.1 Chapter outline

Typical data acquisition times for a 5 mm x 5 mm specimen vary from over two hours for a low resolution image (pixel size = 100 μm x 100 μm) to more than 30 hours for a more detailed, higher resolution image (pixel size = 15 μm x 15 μm) [1-3; 10; 61; 63; 67-70; 73]. For many biological applications, high resolution images are desirable to show fine detail, such as the substantia nigra in brains of Parkinsonism mouse models [10]. Higher-resolution EBI images using LA-ICP-MS require significant reductions in analysis time in order to remain at the forefront of accessible μm -scale trace element imaging technology.

This chapter presents an investigation into the relationship between laser scan speed (v_l), quadrupole dwell time (t_{sc}) and laser spot diameter (x_s) for the purposes of decreasing typical total acquisition times for image construction.

For imaging with increased acquisition speeds to be a viable method of image construction, the differences in images prepared with increased v_l must not be significant. This means that concentrations when imaging with increasing v_l must not differ significantly from concentrations obtained when using a v_l where the distance traversed in one second is equal to or less than the diameter of the laser beam. The washout times of the acquired signal must also not significantly interfere with the signal of subsequent data points when imaging with increased v_l .

The lower limits of the individual dwell times were calculated in order to aid in determining the maximum v_l possible for any given experiment. An equation was proposed to demonstrate the relationship between v_l , t_{sc} and x_s .

Accompanying Publication:

Lear, J., Hare, D., Adlard, P., Finkelstein, D., & Doble, P. (2012). Improving acquisition times of elemental bio-imaging for quadrupole-based LA-ICP-MS. *Journal of Analytical Atomic Spectrometry*, 27(1), 159-164. [8]

4.2 Image construction

Typical bio-imaging experiments normally employ scan speeds where the distance traversed in one second is equal to or less than the diameter of the laser beam. For example, a $X \mu\text{m}$ laser spot diameter moving at a scan speed of $X \mu\text{ms}^{-1}$ would move $X \mu\text{m}$ in one second. If the t_{sc} is equal to one second, a square pixel representative of $X \mu\text{m}$ is recorded every scan cycle. If t_{sc} is the only variable altered and is either greater or less than one second, a true representation of the relative dimensions is lost. As all pixels are squares, the resulting image is either compressed or expanded. In the case of the former, a loss of resolution occurs.

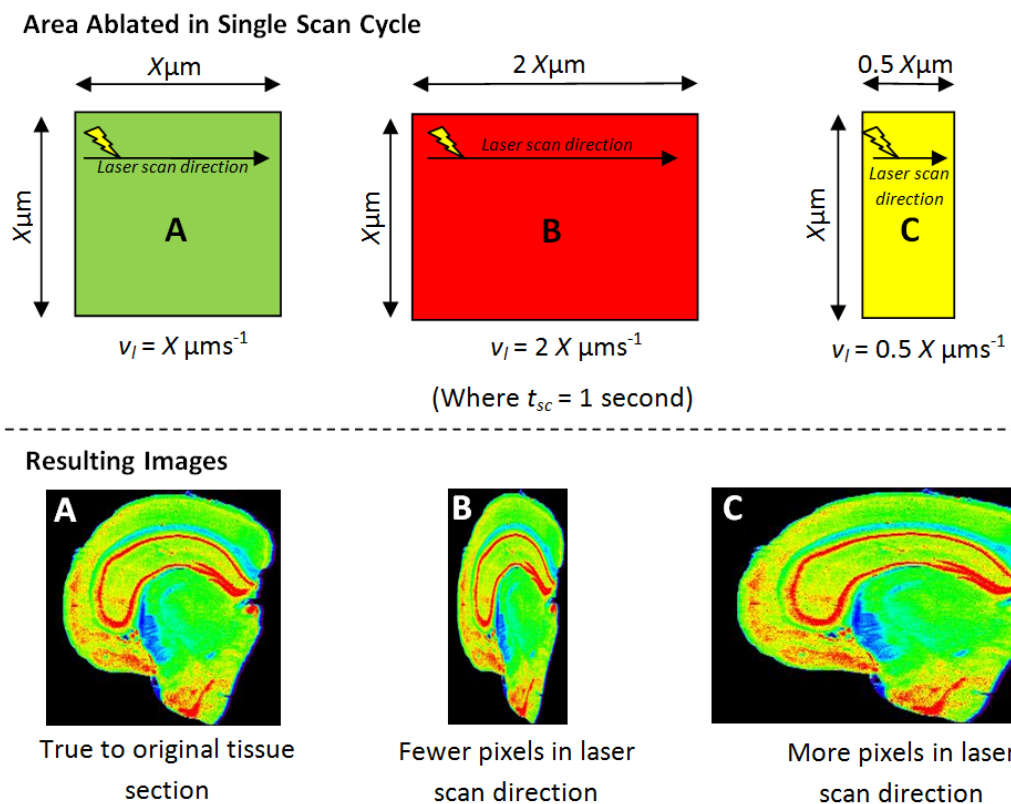


Figure 4-1: The effect of varying the laser scan speed on image dimensions

This is best described by consideration of Figure 4-1. The distance taken for one sampling cycle to complete based on an $X \mu\text{m}$ spot diameter and t_{sc} equal to one second and varying

only scan speed of $X \mu\text{ms}^{-1}$ is schematically represented. Each box represents one data point that is converted to a single pixel when the image is processed. Box A provides a true representation of the dimensions of the original tissue section. Box B consists of two times the distance for a sample cycle to complete and fewer data points will be collected on a line scan equidistant to that of Box A. Therefore the image will be compressed in the direction of the line scan and results in a loss of resolution. Box C is the opposite of this. More data points are collected and the resulting image has more pixels and therefore higher resolution in the X direction.

The benefit of using t_{sc} less than one second is that scan speed may be increased whilst maintaining the relative dimensions of the original tissue section through image post-processing. If t_{sc} is known, the scan speed can be calculated in order to maintain a resolution equivalent to $X \mu\text{m}^2$. The original relative dimensions of the sample are maintained if the scan speed is equal to the spot diameter divided by t_{sc} as described by Equation 4-1, where v_l is the laser scan speed and x_s is the laser spot diameter.

Equation 4-1

$$v_l = x_s / t_{sc}$$

The operational parameters used in these experiments are outlined in Table 4-1.

Table 4-1: LA-ICP-MS operational parameters

Laser parameters	
x_s	15; 30; 65; 100 μm
v_l	1, 2, 3, 4 and 5 x $x_s \mu\text{m s}^{-1}$
Line spacing (centre to centre)	≥ 15 ; 30; 65; 100 μm
Laser energy output	≈ 0.3 to 0.5 J cm^{-2}
Frequency	20 Hz
ICP-MS parameters	
Monitored in brain section analysis, m/z	13, 31, 55, 56, 57, 63, 66
Monitored in all other experiments, m/z	13, 24, 31, 43, 44, 55, 56, 57, 59, 60, 63, 66, 85, 88
t_{sc}	1.33; 0.665; 0.443; 0.333; 0.266; 0.2372 s
Dwell times for masses analysed	
m/z 13	0.100; 0.050; 0.035; 0.025; 0.020 s
m/z 31	0.050; 0.025; 0.015; 0.013; 0.010 s
m/z 55	0.100; 0.050; 0.035; 0.025; 0.020 s
m/z 56	0.100; 0.050; 0.035; 0.025; 0.020 s
m/z 57	0.400; 0.200; 0.140; 0.100; 0.080 s
m/z 63	0.300; 0.150; 0.100; 0.075; 0.060 s
m/z 66	0.280; 0.140; 0.090; 0.070; 0.055 s

4.3 Limitations to scan cycle

In order to estimate theoretical maximum laser scan speeds when using Equation 4-1, the lowest dwell times for biologically significant isotopes were determined, based on determining the limiting signal. The shortest dwell times of the mass spectrometer that maintained sufficient signal intensity, i.e. raw counts greater than the limiting signal were determined by analysing the lowest concentration tissue standard for 14 isotopes. Limiting signal experiments were performed using 11 dwell times for each measured mass (0.001, 0.005, 0.01, 0.015, 0.02, 0.025, 0.03, 0.035, 0.04, 0.045 and 0.05 seconds). A 30 μm spot diameter was used for each experiment run at a scan speed (v_l) of 3, 4 and 5 times the spot

diameter (x_s) per second. With each increasing v_l , the laser fluence was increased to ensure sufficient tissue ablation across all scan speeds. Each of the experiments was repeated five times for statistical purposes. The raw counts per data point and limiting signal (averaged at v_l of 3, 4 and 5 times x_s per second) were plotted against increasing dwell time (selected examples are shown in Figure 4-2). A two-tailed t -test ($p = 0.01$) confirmed that the minimum dwell time required to exceed the limiting signal was applicable to each tested laser scan speed for each m/z .

The minimum dwell time cut-off for each m/z was determined as the minimum dwell time at which the raw counts per point were at least 1000 counts per second and above the limiting signal. These dwell times and maximum v_l for each experiment for each measured m/z are presented in Table 4-2. For example, an analysis of m/z 13, 31, 55, 56, 57, 63 and 66, produced a t_{sc} of 0.146 seconds, not including the time the quadrupole took to move between masses. Using Equation 4-1 and a x_s of 30 μm , the maximum v_l is 205 μms^{-1} . The maximum v_l for these seven m/z is more than 6.8 times a v_l of 30 μms^{-1} . This would reduce an 8.5 hour runtime for a 5 mm x 5 mm sample to a less than 2 hours. Higher maximum v_l may be employed when fewer masses are measured as the minimum dwell times per m/z may be increased whilst maintaining tissue dimensions. These values are instrument-specific and must be determined for each quadrupole ICP-MS system.

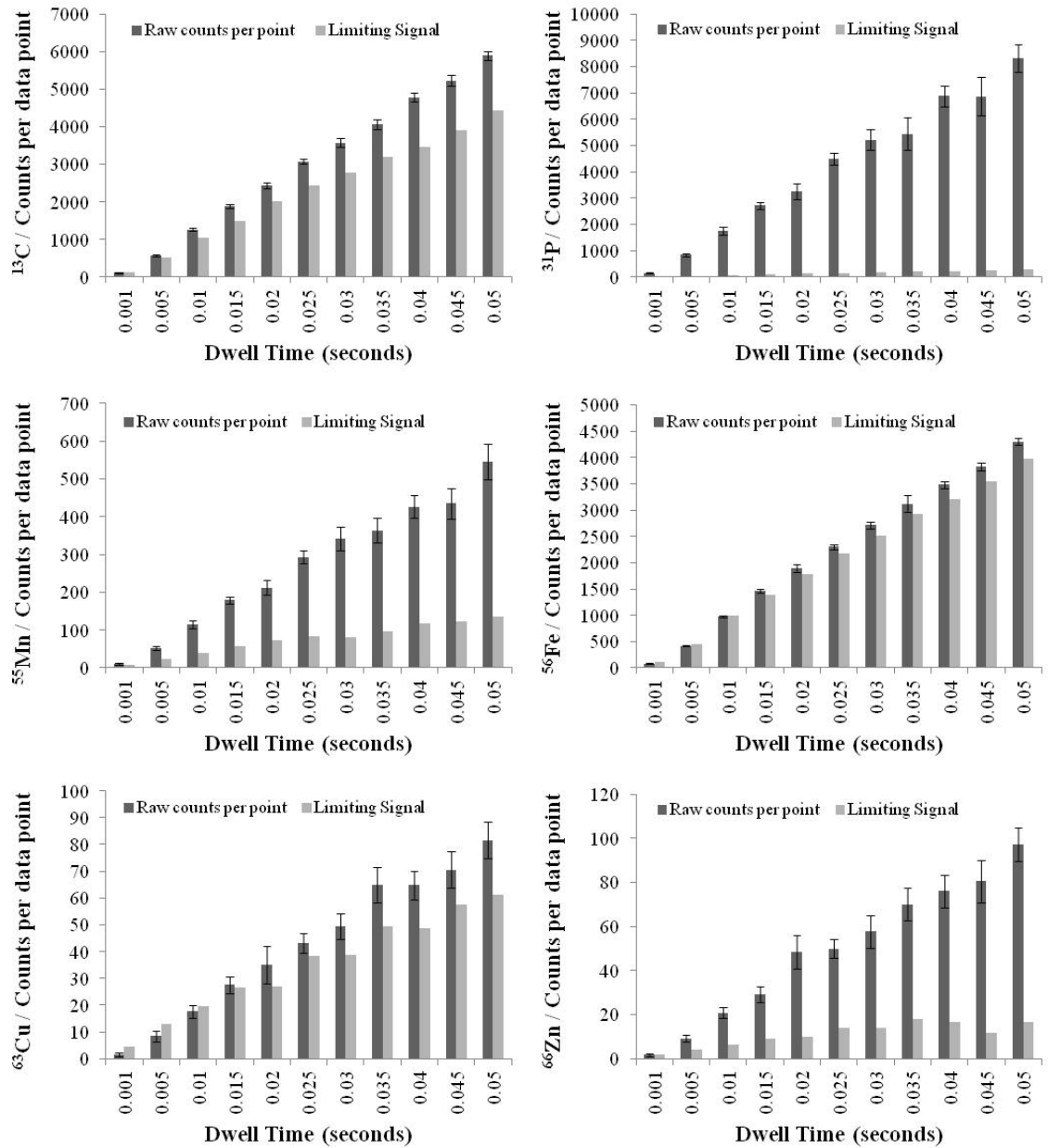


Figure 4-2: Counts per data point versus the dwell time of the quadrupole MS compared with the limiting signal at each dwell time for selected m/z . ($v_1 = 3 \times 10^5 \text{ } \mu\text{m s}^{-1}$)

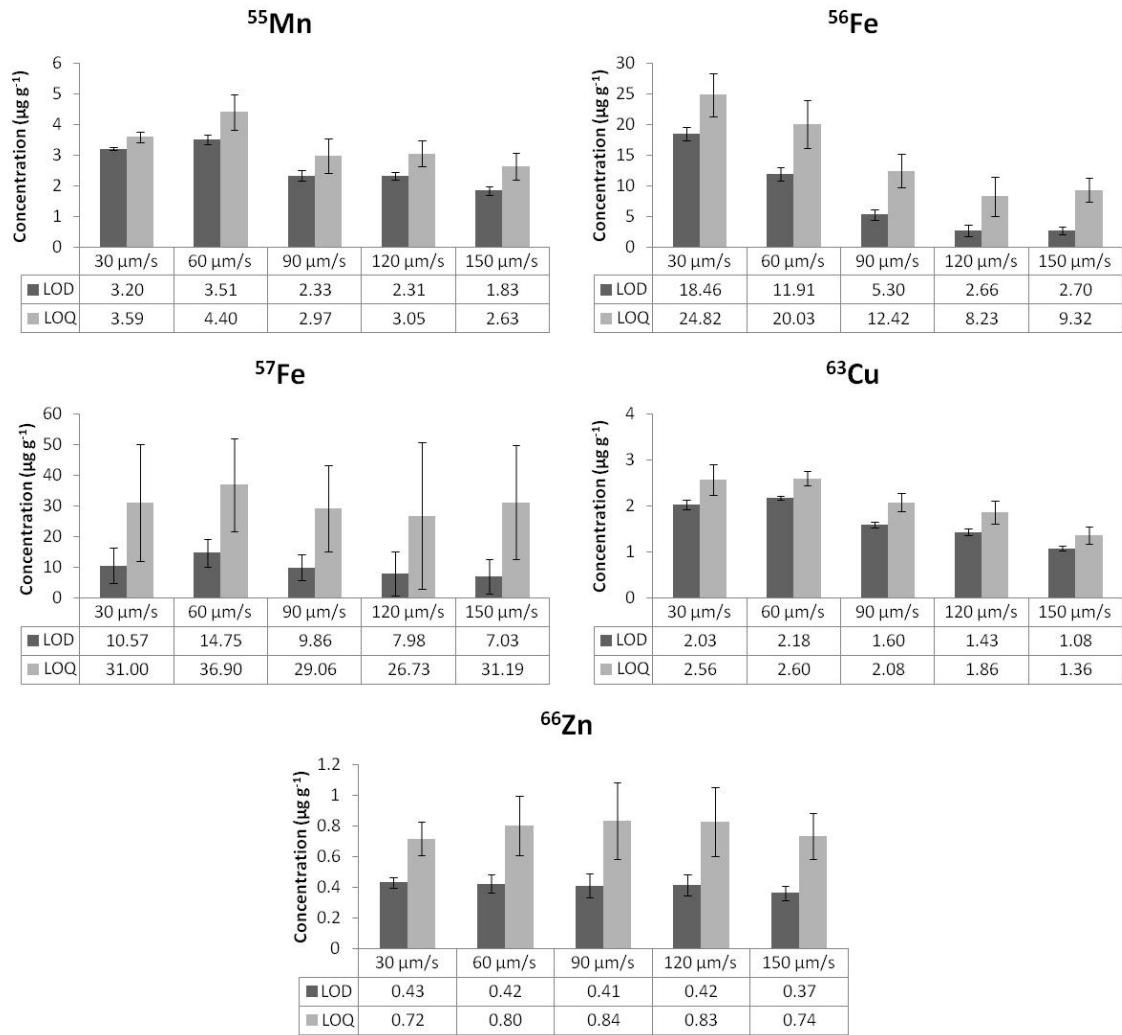
Table 4-2: Selected minimum dwell times for each element in the prepared chicken standards

* Did not pass the limiting signal and are therefore not quantifiable, but are above limit of detection

<i>m/z</i>	Selected minimum MS Dwell Times (seconds)
13	0.010
24	0.005
31	0.001
44	0.005
55	0.005
56	0.015
57	0.090*
59	0.010
60	0.300*
63	0.020
66	0.005
85	0.001
88	0.005

4.4 Limits of analysis

The limiting signal was calculated equivalent to a limit of quantification (LOQ) using a gas blank for each analysis. The limits of analysis are comparable across the range of v_i tested. An improvement in the limits of analysis is seen for ^{55}Mn , ^{56}Fe and ^{63}Cu as the v_i increases. The limits of analysis are outlined in Figure 4-3. As v_i increased the sensitivity increased. This was expected as the amount of material ablated per unit time increased as v_i increased, thus increasing the material being analysed by the ICP-MS. An increased sensitivity and a reduction in the limits of analysis is related to an increased slope of the calibration curve. Table 4-3 shows that as v_i increased, the slope of the curve generally increased. Therefore, the faster the v_i , the lower the limits of analysis for the v_i tested.

Figure 4-3: Limits of analysis with increasing v_1 ($x_s = 30 \mu\text{m}^{-1}$)Table 4-3: Slopes of the calibration curves with increasing v_1 ($x_s = 30 \mu\text{m}$)

v_1	m/z				
	55	56	57	63	66
$1 \times x_s \text{ s}^{-1}$	4.08×10^{-3}	2.97×10^{-3}	7.84×10^{-5}	1.65×10^{-3}	5.59×10^{-4}
$2 \times x_s \text{ s}^{-1}$	3.89×10^{-3}	3.34×10^{-3}	7.48×10^{-5}	1.83×10^{-3}	6.49×10^{-4}
$3 \times x_s \text{ s}^{-1}$	6.22×10^{-3}	4.52×10^{-3}	1.03×10^{-4}	2.55×10^{-3}	8.09×10^{-4}
$4 \times x_s \text{ s}^{-1}$	6.61×10^{-3}	4.18×10^{-3}	1.03×10^{-4}	2.71×10^{-3}	8.50×10^{-4}
$5 \times x_s \text{ s}^{-1}$	9.06×10^{-3}	5.87×10^{-3}	1.31×10^{-4}	3.34×10^{-3}	9.83×10^{-4}

4.5 Signal carry-over experiments

Analysis of the signal carry-over from preceding data points was performed to determine the effect of increasing v_l on washout times and signal intensity. Increasing washout time increases the interference of the signal from a previous data point on following data points, resulting in image “blurring”. Using the highest concentration tissue standard, a line was ablated half on tissue and half on the glass mount for x_s of 15, 30, 65 and 100 μm and v_l equal to 1, 2, 3, 4, and 5 times x_s per second. Laser fluence was altered for each increase in v_l to ensure sufficient ablation of the tissue as the laser spent less time at each point on the tissue with increasing velocity.

For a v_l of 1, 2 and 3 times x_s per second (15, 30 and 65 μm), between two and three data points after completion of the ablation of tissue is required to reach background signal levels (Figure 4-4). Four to six data points were required to reach background for v_l of 4 and 5 times. At x_s of 100 μm up to 8 data points were required to reach background. In general the washout times increased with increasing scan speed. This was expected as the amount of material ablated per unit time increased as v_l increased. The relationship between the normalised signal intensity of the total ion count (TIC), and increasing scan speeds and spot diameters is represented in Figure 4-5. This was due to an increasing sample load on the plasma. The longer washout times in the LFC were not of sufficient magnitude to significantly affect the quality of images acquired at higher speed.

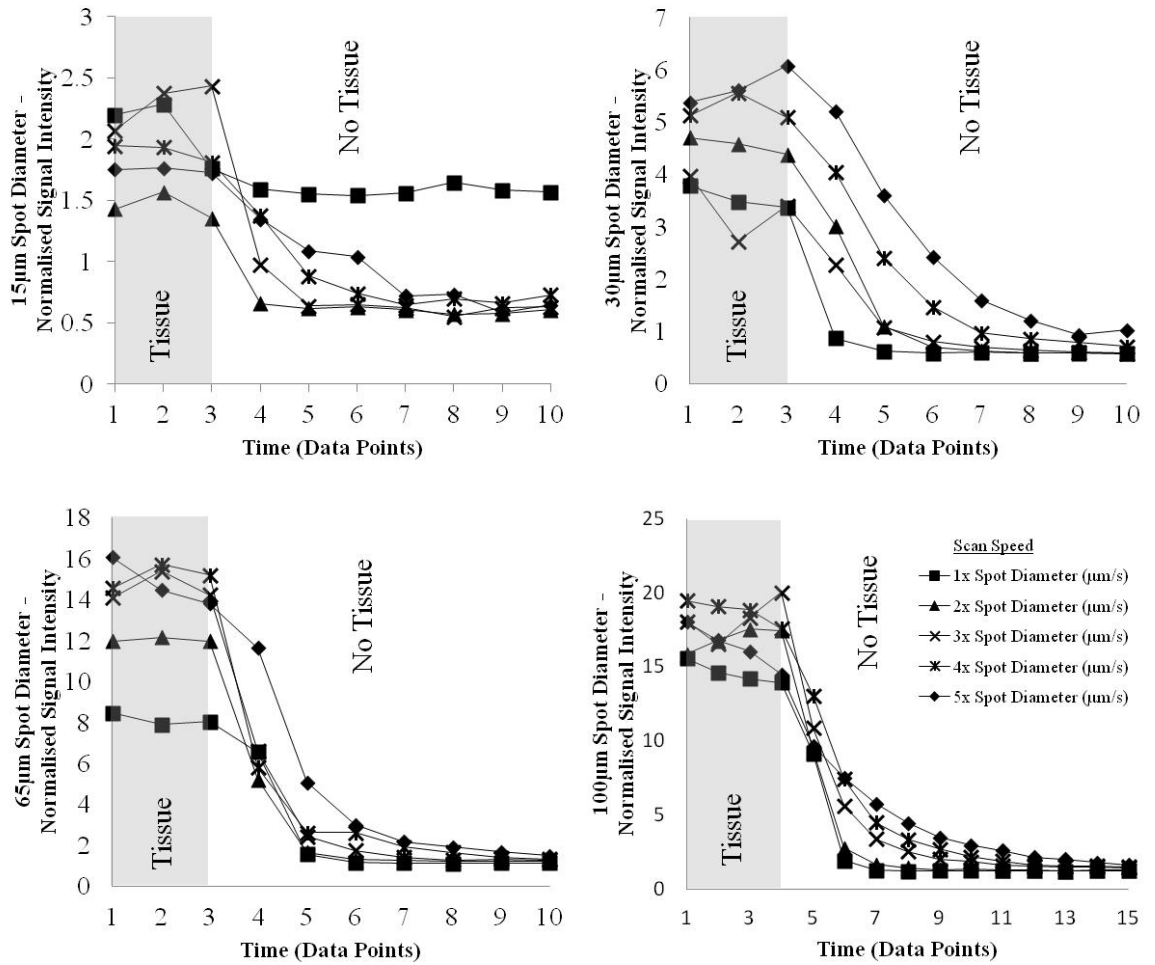


Figure 4-4: Washout times for a large format laser ablation cell

Time taken (in data points) for total ion count (TIC) to reach background levels after tissue ablation using increasing scan speeds

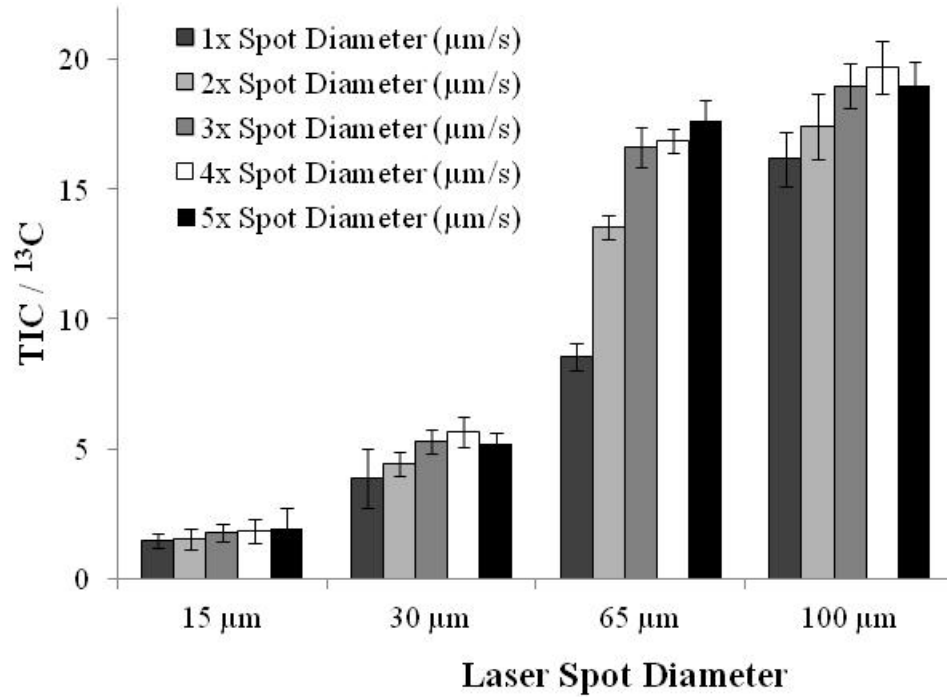


Figure 4-5: Comparison of normalised signal intensities for the total ion count (TIC) \pm standard deviations across laser spot diameters and increasing scan speed

An increase in the number of data points required for the signal to reach background levels after completion of the ablation of tissue is observed for the standard ablation cell when compared to the LFC. There are between 9 and 21 data points required to reach background levels for a v_l of 1 times x_s per second, and between 12 and 23 data points for a v_l of 5 times x_s per second (Figure 4-6). This not only shows the superiority of the LFC's washout capabilities, but also highlights that washout times in the LFC have less impact on image production than standard ablation cells.

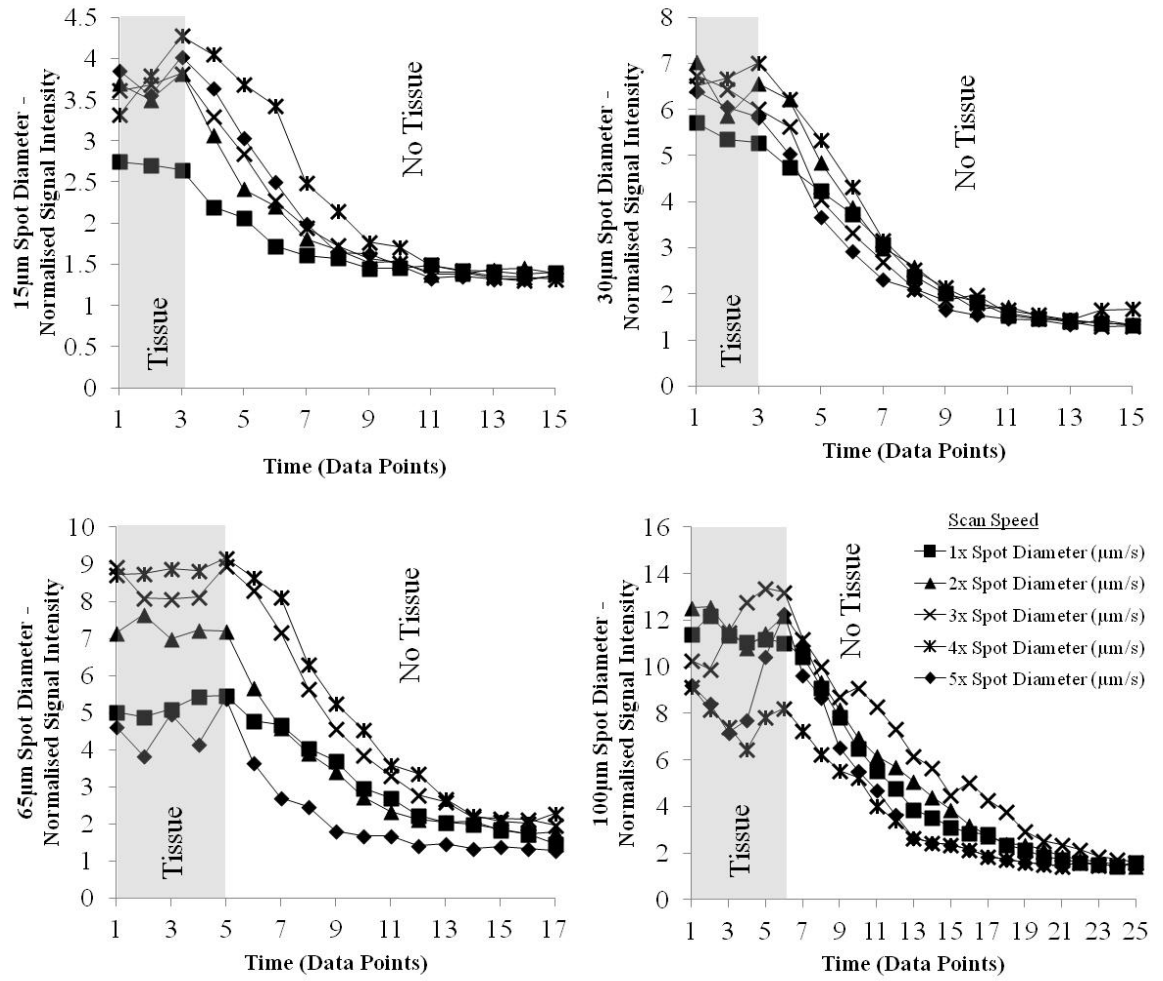


Figure 4-6: Washout times for a standard laser ablation cell

Time taken (in data points) for total ion count (TIC) to reach background levels after tissue ablation using increasing scan speeds

4.6 Laser fluence

In all experiments, the laser's fluence was adjusted to ablate sufficient material without penetrating to the glass substrate. This was to ensure that variations in tissue density and thickness could be normalised by dividing the signal by m/z 13, i.e. ^{13}C . Increasing scan speeds required increasing the laser's energy as the laser spent less time at each point, reducing the total energy transferred to the tissue. Higher scan speeds also improved the normalised signal. As laser fluence did not vary linearly with decreased spot size or increased scan speed, and laser fluence varied between days, a visual inspection for selection of an appropriate value for laser fluence was undertaken.

4.7 Imaging with increased laser scan speed

Representative mouse brain sections at similar stereotaxic coordinates were imaged to test the applicability of Equation 4-1. Four brain sections were ablated using x_s at 15, 30, 65 and 100 μm . Each brain section was divided into five evenly defined segments with each segment imaged at different speeds, namely v_l of 1, 2, 3, 4 and 5 times x_s per second for the x_s at 15, 65 and 100 μm brains. The t_{sc} were 1.33, 0.665, 0.443, 0.333 and 0.266 seconds, respectively. The parameters used for the analysis of the 30 μm section were v_l of 1, 3, 4, 5 and 6 times x_s . The t_{sc} used were 1.16, 0.39, 0.39, 0.33 and 0.28 seconds respectively. Quantification was performed using matrix-matched tissue standards. A new calibration curve was constructed for every change in v_l and x_s allowing comparison of images on the same scale. A fourth brain section prepared from a wild-type was imaged using t_{sc} and v_l which maintained the samples relative dimensions.

In all cases the images were acquired with t_{sc} values approximately 30% greater than equivalent dimensions. These values were calculated relative to v_l in order to allow whole

number multiples of v_l . The software allows only two significant figures and up to three decimal places for each dwell time. Consequently the t_{sc} of all experiments was approximately 30% more than that required for image equivalent dimensions, resulting in image compression of 30%.

Nevertheless, Figure 4-7 to Figure 4-10 are representative images of ^{63}Cu , ^{66}Zn , ^{56}Fe and ^{55}Mn respectively. The scan speed was increased from 1 to 5 times x_s per second at resolutions of 15×15 , 65×65 and $100 \times 100 \mu\text{m}$. As the scan speed increased the t_{sc} were proportionally decreased. In the images, when $x_s = 30 \mu\text{m}$, loss of resolution across the horizontal plane between speed regions was observed. This phenomenon was outlined in Figure 4-1. Because the t_{sc} were not calculated proportionally to v_l , loss of resolution as v_l increases has been demonstrated in these images.

Visual inspection of Figure 4-7 to Figure 4-10 indicated that there were no significant variations in calculated concentrations between scan speeds or image resolutions. Recalling that a loss of detail is observed with increasing spot size, the continuity between different v_l and the resolutions is sound and supports the justification for using increasing v_l . The relative dimensions of each segment (i.e 30% compression relative to sample) were also maintained at each of the scan speeds, indicating that Equation 4-1 was applicable. Increasing v_l means that the overall analysis time can be significantly reduced and the results indicate that this can be done without a reduction in image quality. A reduction in overall analysis time is greatly beneficial as a higher throughput is possible and there are reduced costs for consumables with respect to each sample.

Certain m/z are difficult to analyse as spectral polyatomic interferences are potentially formed due to impurities in plasma gas, particularly $m/z = 55$ and 56 . The interferences seen in these m/z (Figure 4-9) are well documented [13; 14; 88] and are considered to be caused

by polyatomic nitrides and oxides, namely $^{40}\text{Ar}^{14}\text{N}^1\text{H}^+$ for $m/z = 55$ and $^{40}\text{Ar}^{16}\text{O}^+$ for $m/z = 56$. Collision or reaction cells are commonly used in SN-ICP-MS to reduce interferences. The use of reaction cells in imaging using LA-ICP-MS is investigated in Chapter 6. One effective way of reducing the effect of polyatomic interferences is to perform a background subtraction to remove interferences arising from impurities in the plasma gas which exhibit an elevated background signal (*infra*, Section 4.7.1).

The upper limit of the concentration observed in the images for $m/z = 55$ was > 0.6 mg/kg, which is below the limit of detection for $m/z = 55$ reported in Table 3-3. However the images for $m/z = 55$ will still be discussed with the detection limit in mind. The low concentration of $m/z = 55$ in tissue can be attributed to the relatively poorer quality of the images as the instrument approaches the limit of detection (Figure 4-10). The instrument was unable to consistently distinguish between the background levels of $m/z = 55$ and the concentration of $m/z = 55$ in the tissue. With respect to the differences in analyte detection and image quality between spot sizes, it is likely that a small elevation in the background concentration of $m/z = 55$ between brain section analyses can result in the low concentration of $m/z = 55$ in tissue being obscured.

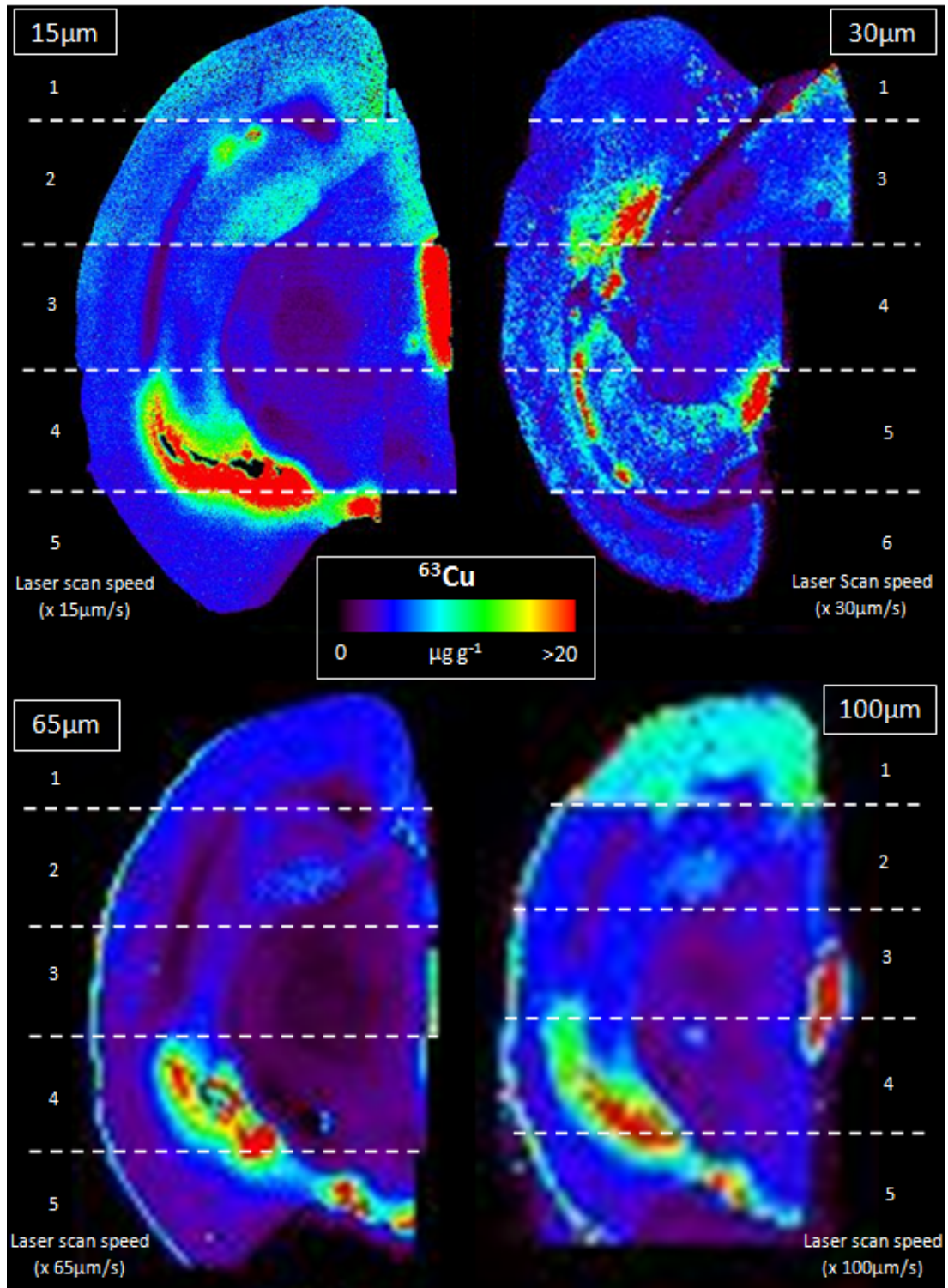


Figure 4-7: Comparison of laser scan speed and resolution for ^{63}Cu using spot sizes of 15, 30, 65 and $100\ \mu\text{m}$ where each segment broken by a dotted line indicates an increase in laser scan speed.

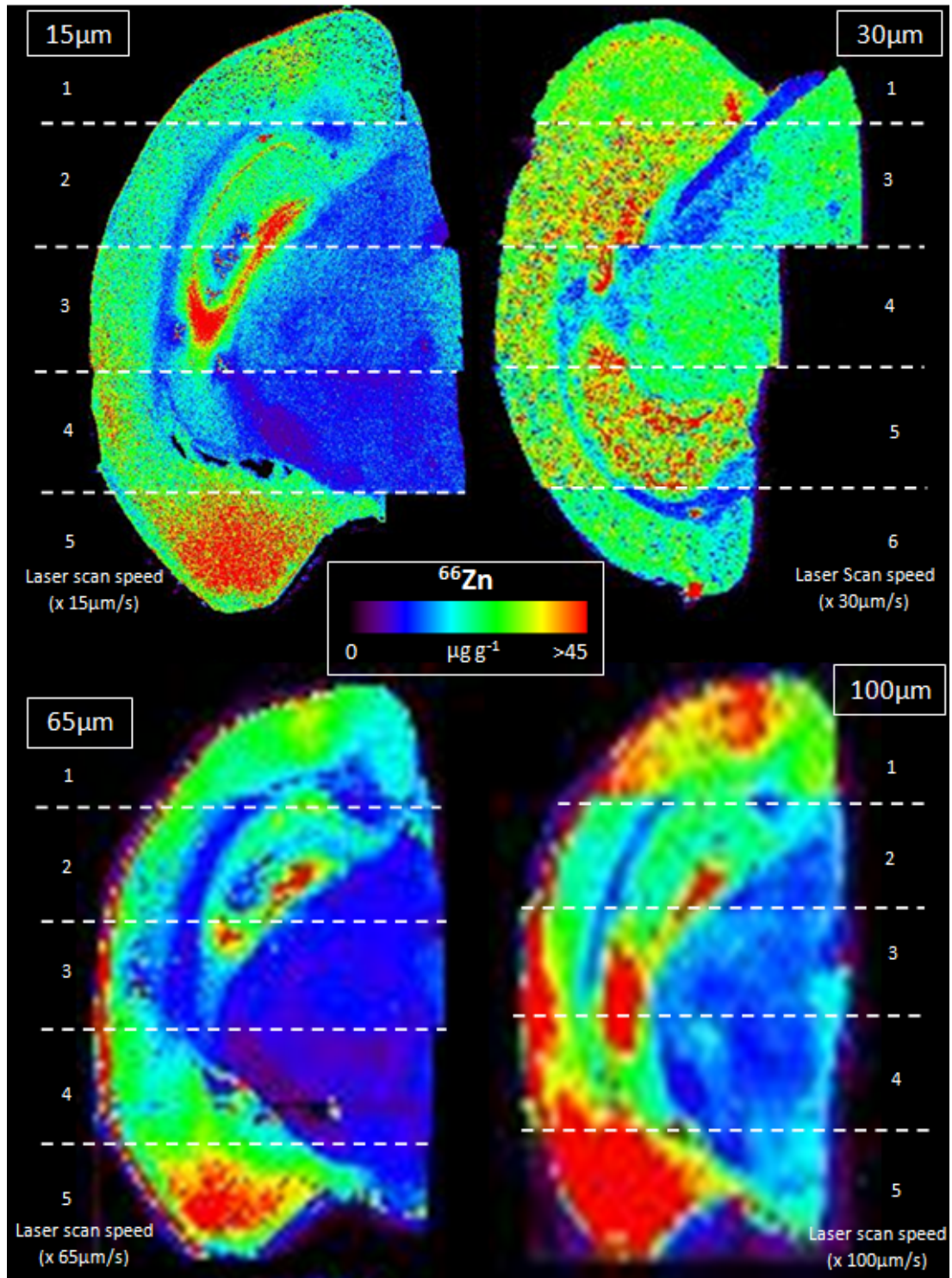


Figure 4-8: Comparison of laser scan speed and resolution for ^{66}Zn using spot sizes of 15, 30, 65 and 100 μm where each segment broken by a dotted line indicates an increase in laser scan speed.

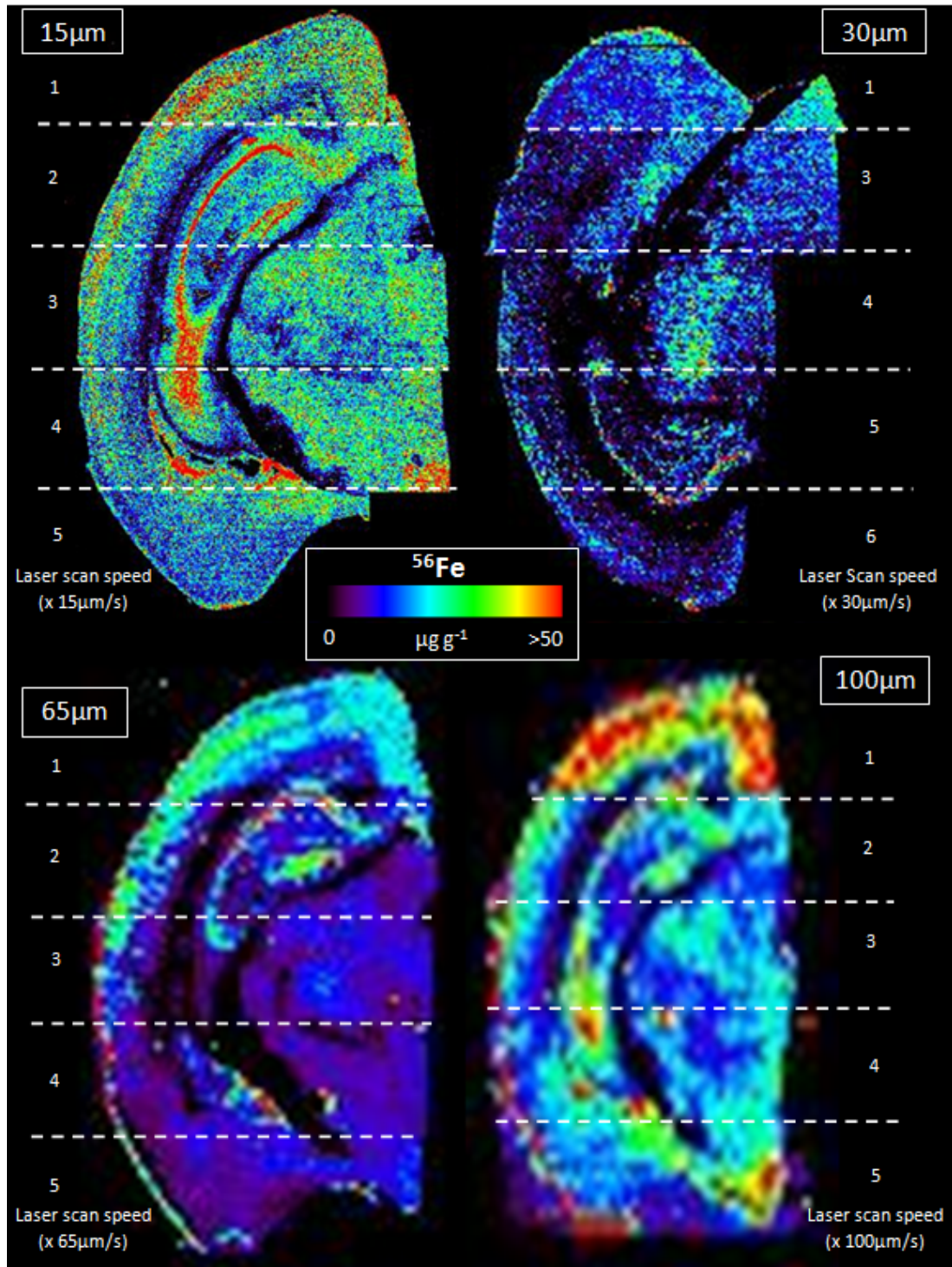


Figure 4-9: Comparison of laser scan speed and resolution for ^{56}Fe using spot sizes of 15, 30, 65 and 100 μm where each segment broken by a dotted line indicates an increase in laser scan speed.

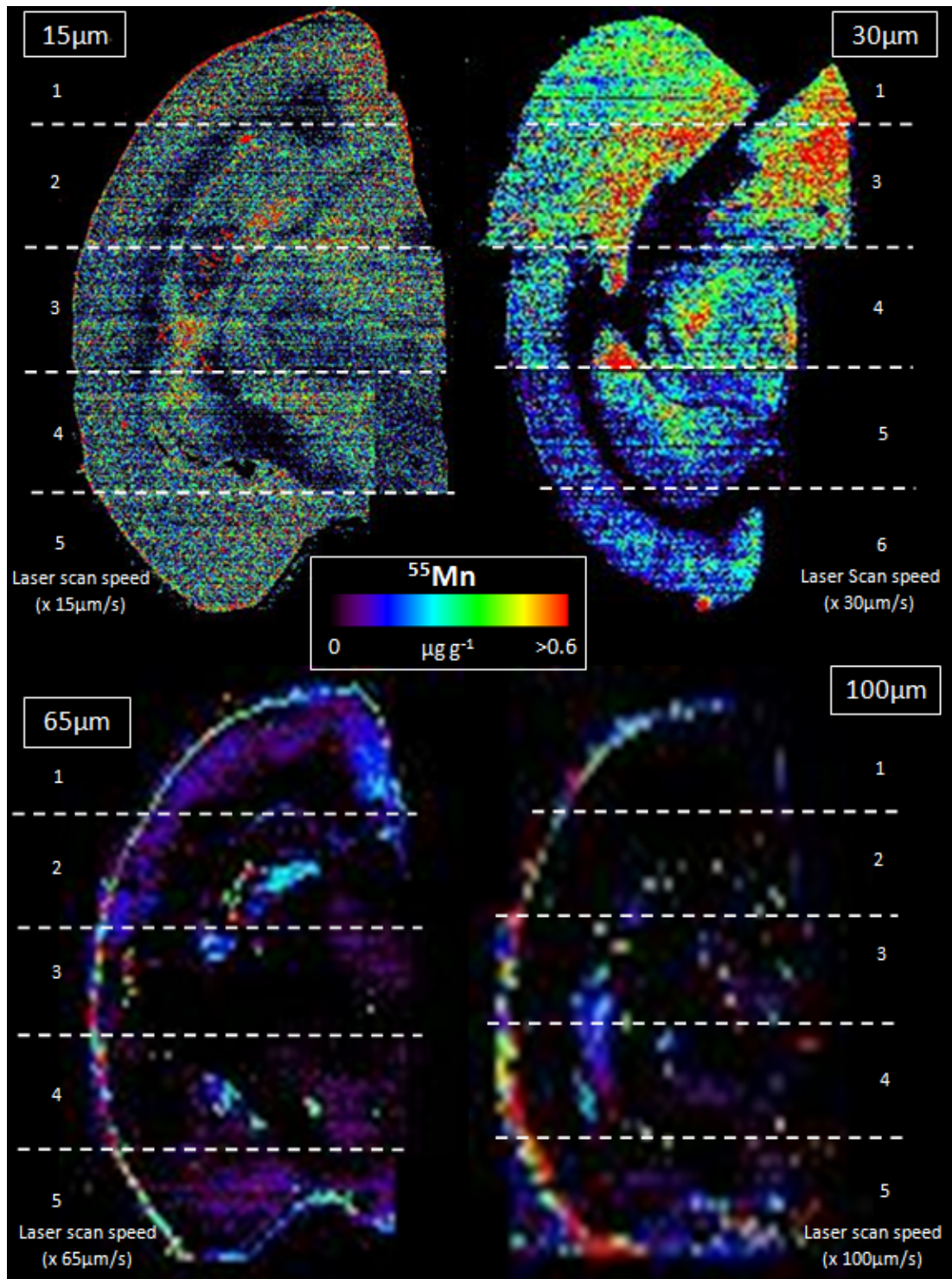


Figure 4-10: Comparison of laser scan speed and resolution for ^{55}Mn using spot sizes of 15, 30, 65 and 100 μm where each segment broken by a dotted line indicates an increase in laser scan speed.

4.7.1 Background subtraction

The importance of background removal is highlighted in Figure 4-11 that shows a comparison of increasing v_l prior to background subtraction. This is a reconstruction of the same image in Figure 4-9 where the background has been subtracted. The beneficial effect of background removal when there is significant background drift over time is obvious. The background drifts for the isotopes imaged are outlined in Figure 4-12 and support the need for background subtraction in these experiments.

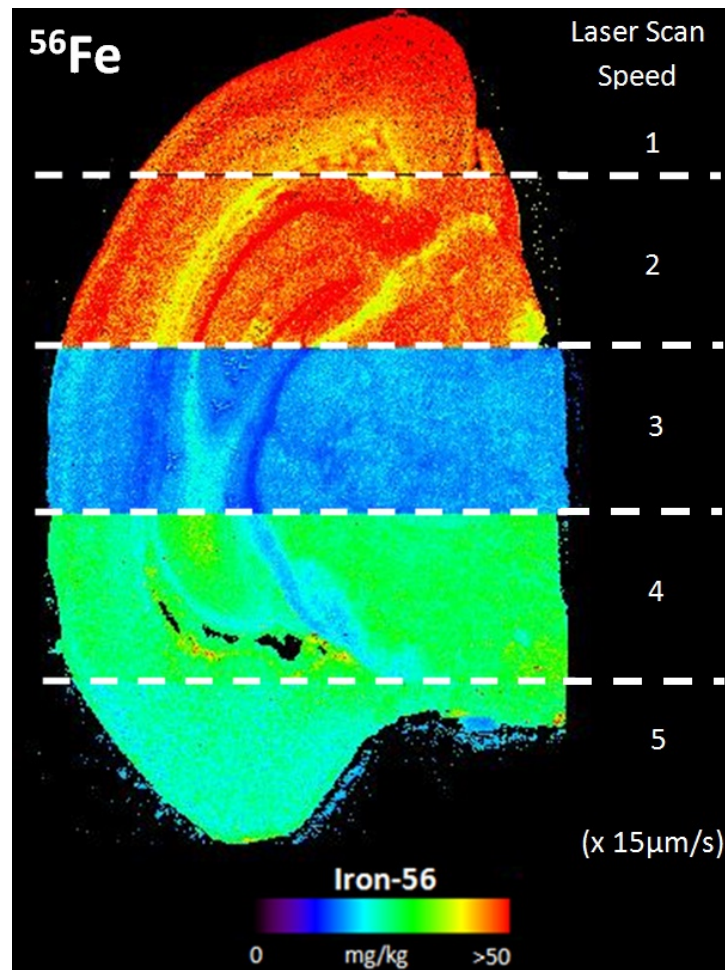


Figure 4-11: Laser scan speed comparison for ^{56}Fe prior to background subtraction ($x_s = 15 \mu\text{m}$)

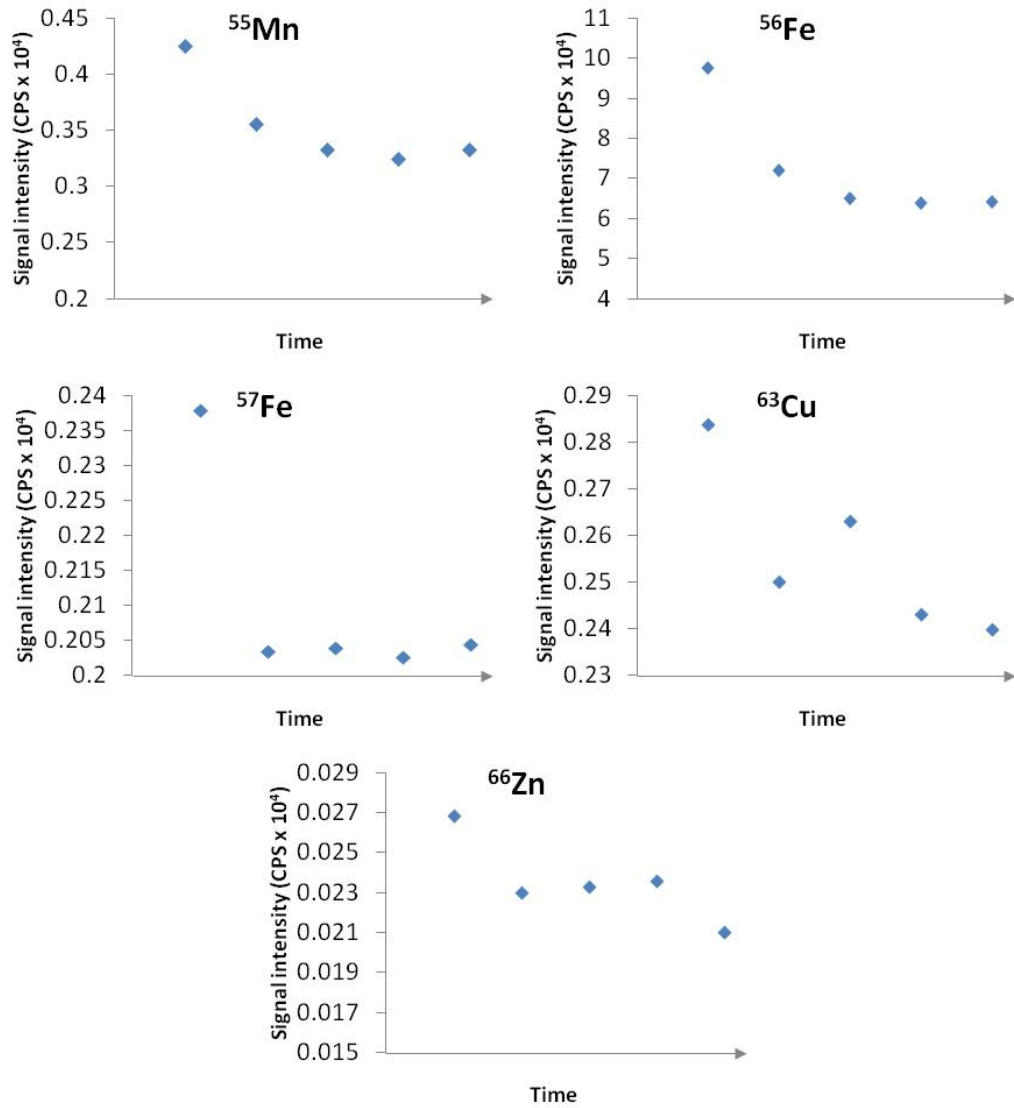


Figure 4-12: Background drift of the isotopes imaged supporting the need for background subtraction in these experiments

4.7.2 Maintaining image dimensions

Figure 4-13 shows a representative image of ^{63}Cu of a coronal slice of a mouse brain with t_{sc} selected to maintain the sample dimensions. This section was ablated with x_s of $30\ \mu\text{m}$, t_{sc} of 0.2372 seconds and v_l of $127\ \mu\text{m}\ \text{s}^{-1}$. This resulted in a total acquisition time of 6.5 hours, representing a 4.2 times reduction of acquisition time when compared to typical data acquisition parameters, whilst maintaining the sample's relative dimensions.

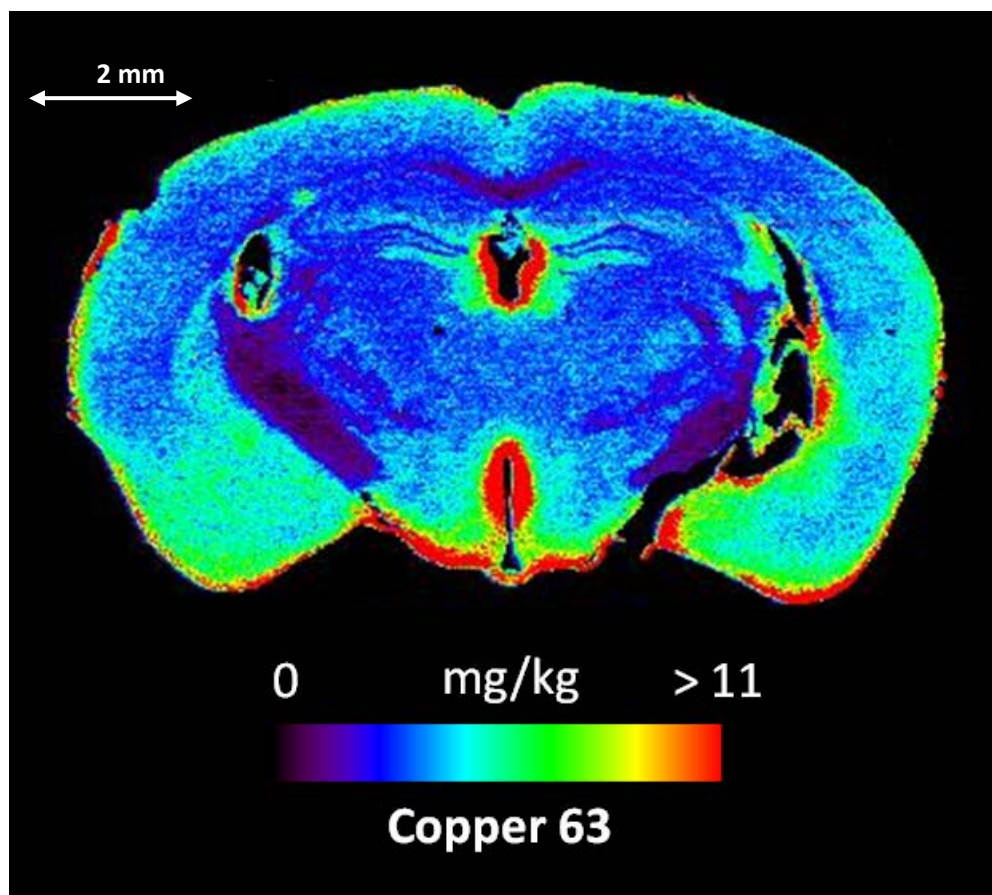


Figure 4-13: Demonstration of the use of increased v_l while maintaining image dimensions equivalent to the original tissue section ($x_s = 30\ \mu\text{m}$, $t_{sc} = 0.2372$ seconds and $v_l = 127\ \mu\text{m}\ \text{s}^{-1}$)

4.8 Conclusions

Decreasing the scan cycle of the quadrupole and increasing the laser scan speed were viable means for reducing the acquisition times of EBI. By increasing v_l and decreasing t_{sc} it was possible to construct images of tissue sections in a shorter period of time for faster turnaround of samples. An equation was deduced to calculate the v_l required to maintain sample dimensions when using a specific x_s and t_{sc} of each measured m/z .

The minimum mass spectrometer dwell times for each m/z were based on the signal intensity and limiting signal for the sampling period. A maximum v_l may be calculated from dwell times, the number of m/z measured, and the detection limits required. These dwell times are specific to the ICP-MS system and experiments must be repeated for each system. Limiting signal experiments must be performed for each set of standards.

The number of data points for the signal to return to baseline levels was generally equivalent for v_l equal to 1, 2 and 3 times x_s per second. The number of data points increased for scan speeds of 4 and 5 times the spot diameter; however this increase was not significant, especially when compared to washout times for the standard ablation cell. The upper limits of increased speed are yet to be determined, and are likely to be limited by the scanning speed of the quadrupole. Washout of ablated material from the sample cell and transfer lines could also play a significant role in blurring of images and carry-over when using v_l in excess of 5 times x_s per second.

***Chapter 5: Applications of
increased speed elemental bio-
imaging***

Chapter 5: Applications of increased speed elemental bio-imaging

5.1 Chapter outline

Utilising the results discussed in Chapter 4, images were prepared using increased acquisition speeds according to the proposed equation (Equation 4-1).

Two applications were developed utilising increased ν_i . Both applications were related to the study of the neurodegenerative disorder Alzheimer's disease (AD) and examined a number of variables and their resulting effects on metal distribution in the brain. These applications were;

- Application 1: Imaging the metal distribution and redistribution in the brains of ZnT3 Knockout mice treated with a drug known as PBT-2; and
- Application 2: The effect on metal distribution was examined in the brains of mice that were fed varying levels of advanced glycation end-products (AGEs) in their diets and subjected to varying periods of hypoxia.

5.2 Background

5.2.1 Neurodegeneration

Substantial evidence has accumulated over recent years implicating the role of metal ions in the pathophysiology and pathogenesis of neurodegenerative disorders [89]. Neurodegeneration is a condition characterised by the loss of cells from the CNS. The condition occurs when interactions between redox-active metal ions and proteins lead to the damage of critical biological systems and initiate a cascade of events that lead to oxidative damage and cell death.

There is growing evidence of a fundamental relationship between iron, copper, zinc and manganese in the generation of oxygen and protein radicals that tend to cause the major neurological diseases [89]. Abnormalities of metal ion biochemistry arise by two mechanisms; protein aggregation mediated by metal ions and oxidative reactions catalysed by redox-active metals. These metals are able to generate radicals, reactive oxygen species (ROS) and reactive nitrogen species (RNS) by abnormally accepting or donating electrons.

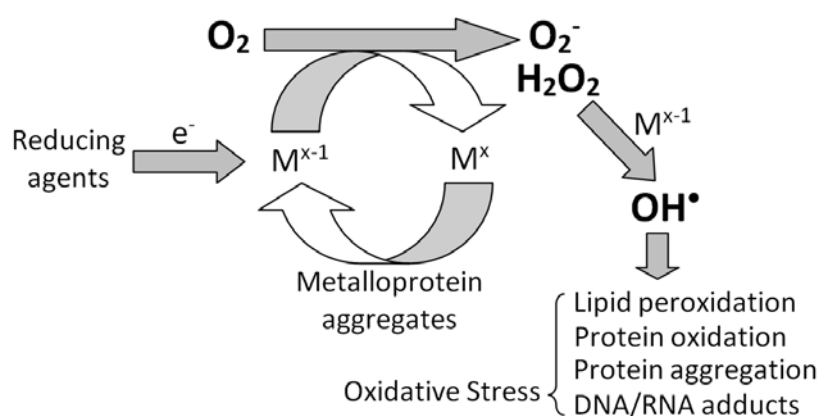
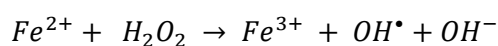


Figure 5-1: Reactive oxygen species generation by redox-active metals as the basis for neurodegenerative disorders that are related to oxidative damage [89]

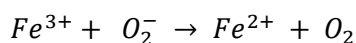
Transition metals such as iron and copper accept and donate single electrons and therefore greatly facilitate the reduction of O_2 . O_2 prefers to accept one electron at a time. The process of the reduction of O_2 is outlined in Figure 5-1. The super oxide radical, O_2^- , is the first ROS to be formed in this process by the automatic oxidation of metal complexes. Adding the second electron gives the peroxide ion, O_2^{2-} , which is not a free radical and at neutral pH converts to hydrogen peroxide, H_2O_2 . The most dangerous of the ROS is the hydroxyl ion, OH^\bullet , capable of causing enormous damage to biological molecules. This hydroxyl ion is produced by the one-electron reduction of H_2O_2 , also known as the Fenton reaction (Equation 5-1). Manganese (II) is also able to initiate a Fenton-type reaction. [89; 90]

Equation 5-1: Fenton Reaction

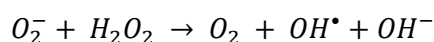


It has also been proposed that superoxide acts as a redox-active species and is able to reduce Fe^{3+} by what is known as the Haber-Weiss reaction (Equation 5-3), where Equation 5-1 and Equation 5-2 are combined. It can be noted that the iron ions act as a catalyst for the reaction and are only needed in very small amounts. [91-95]

Equation 5-2



Equation 5-3: Haber-Weiss Reaction



Normally, the body's defence systems will rapidly detoxify these reactive species however, under certain conditions, greater amounts of ROS and RNS are produced which overwhelm the cellular defence and this results in oxidative damage [89]. Another way the body prevents oxidative damage is chaperoning redox-active metals with metalloproteins so the abnormal transfer of electrons is prevented. Because the brain has physical barriers, such as the blood-

brain barrier (BBB), to prevent the passive fluctuation of the major metal ions, the origin of neurodegenerative disease is more often due to the homeostatic failure of endogenous metals rather than environmental or nutritional exposure. The involvement of metals and the proteins they interact with in neurological diseases is summarised in Table 5-1. [89]

Table 5-1: Organisational framework for the involvement of metals in neurological diseases. The disorders listed are confined to instances where there is a prominent or primary neurological phenotype, and does not address secondary syndromes. Adapted from [89]

Metal	Neurological Phenotype	Protein Interaction
1. Genetic disorders of metal metabolism		
Copper	Wilson's Disease	Cu7B ATPase
Copper	Menkes' Disease	Cu7A ATPase
Iron	Neurodegeneration with brain iron accumulation (NBIA)	Pantothenate kinase 2
Iron	Friedreich's ataxia	Frataxin
Iron, copper	Aceruloplasminemia	Ceruloplasmin
2. Toxicological exposure to metal		
Aluminium	Alzheimer's Disease (?)	?
Cadmium	Various	? Glutathione
Lead	Various	? Glutathione
Mercury	Various	? Glutathione
Manganese	Parkinsonism	Cis-aconitase
3. Protein aggregation disorders involving metals in pathogenesis		
Zinc, copper	Alzheimer's Disease	β-amyloid
Iron, copper	Parkinson's Disease	α-synuclein
Copper, zinc	Amyotrophic lateral sclerosis	Superoxide dismutase 1
Copper, zinc, manganese	Transmissible spongiform encephalopathy (including Creutzfeldt-Jakob disease)	PrP
Zinc	Drusen, Sorby's fundus dystrophy	Tissue inhibitor of matrix metalloproteinase-3 (TIMP3)

In an ageing global population, the occurrence of neurodegenerative disorders in the community is ever increasing. In Australia alone, there were more than 162 000 people diagnosed with dementia in 2002. It is estimated that this number will increase by 10 per cent each year, reaching up to 500 000 by 2040, with resulting financial costs in the region of A\$6.6 billion [96].

5.2.2 Alzheimer's disease

Alzheimer's disease (AD) is a progressive degenerative disease of the brain, ultimately resulting in dementia. Between 5 and 15% of people over 65 develop AD and up to half of those over 85 die of resulting complications [97]. In Australia, complications resulting from AD and dementia are currently the fourth largest cause of death and affect one quarter of people over 85 years. Around 100 000 Australians currently suffer from AD with more females on average suffering from the disease than males. [98; 99]

Early symptoms of AD include forgetfulness, confusion and changes in personality, mood or behaviour. These symptoms are difficult to diagnose as they develop gradually and could be due to other factors such as stress and depression. These symptoms become more pronounced and more frequent as the disease progresses. Later onset symptoms include inability to care for oneself, difficulties eating and sleeping, and loss of speech [97; 99].

5.2.2.1 AD pathogenesis

Alzheimer's disease is characterised pathologically by synaptic and neuronal degeneration, deposition of amyloid plaques, and development of neurofibrillary tangles in the brain [89]. Amyloid plaques are composed primarily of the β -amyloid (A β) peptide which accumulates in a region of the brain known as the neocortex. A β in the brain has been described as membrane associated, aggregated and soluble [89; 100].

The most popular hypothesis for the pathogenesis of AD in recent years has been the *Amyloid Cascade Hypothesis* which concludes that all pathology in the AD brain occurs downstream of the excessive accumulation of A β in the CNS [101]. The central role of A β in AD pathogenesis is not disputed, however an alternate theory recently proposed by *Bush and Tanzi* [101] known as the *Metal Hypothesis for Alzheimer's Disease* specifies that the effects of A β on an

AD brain are promoted by and possibly dependent on A β -metal interactions. This metal hypothesis will be the theory focused on for the purpose of this study.

Under normal conditions, most A β is membrane associated. The concentration of extracellular, soluble A β is relatively low. The normal interaction of A β with biometals in the brain is outlined in Figure 5-2. The expression of A β in the brain promotes the outflow of Fe and Cu from cortical cells and the influx of Zn. A low concentration of baseline extracellular Zn²⁺ is maintained by the transport of Zn²⁺ into neurons with the aid of ZnT3, a zinc transporter protein, via a mechanism which is still not completely understood. Another protein, α_2 -Macroglobulin (α_2 M), might also participate in the uptake of Zn²⁺ by binding to A β as indicated in Figure 5-2. [100]

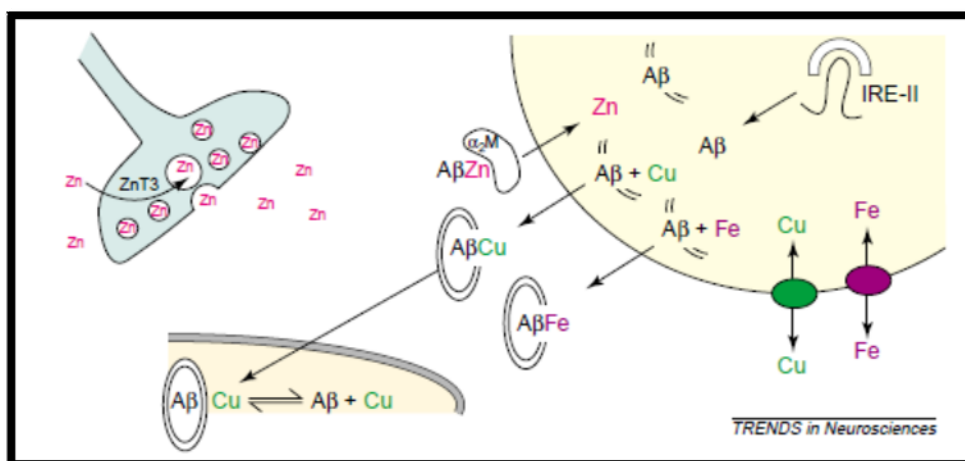


Figure 5-2: Model for the non-pathogenic metallobiology of β -amyloid (A β)

NB: With the exception of Zn²⁺ released as an exchangeable ionic form during synaptic transmission, the metal ions are not in free ionic forms but, for simplicity, the metal ions are represented without their transport or binding proteins. [100]

The accumulated evidence suggests that A β precipitation and toxicity is caused by abnormal interactions with zinc, copper and iron ions. In an AD brain, the soluble and aggregated A β increases markedly from the primarily membrane-associated A β in healthy individuals. This rise in soluble A β suggests that A β could be abnormally liberated from the membrane. Zn²⁺ seems to be the major neurochemical factor responsible for aggregating A β . Zinc, copper and

iron have been found at relatively high levels in A β deposits. At pH 7.4, Zn²⁺ is the only physiologically available metal ion to precipitate A β , however Cu²⁺, and to a lesser extent Fe³⁺, induce limited aggregation of A β with aggregation increasing in slightly acidic conditions. [100]

The interaction of Cu²⁺ and Fe³⁺ with A β catalyses H₂O₂ production through the reduction of the metal ions, using O₂ and other biological reducing agents as substrates. H₂O₂ is permeable across all tissue membranes and unless scavenged, has the ability to cause severe oxidative damage via the Fenton and Haber-Weiss reactions (page 113) which in turn generate lipid peroxidation adducts, protein carbonyl modifications and nucleic acid adducts in various cellular compartments. This oxidative damage typifies AD and occurs prior to A β deposition. [89; 100]

The pathogenesis of AD is generally age related. A mechanism proposed by A.I. Bush [100] for the pathogenesis of AD is represented in Figure 5-3. The proposed sequence of events is as follows:

1. The concentrations of Cu and Fe in the cortex increase with age and this facilitates the overproduction of amyloid precursor protein (APP) and A β in an attempt to suppress the metal ion levels in the cells. Hypermetallation of A β , facilitated by mild acidosis, occurs if the metal ion levels continue to rise.
2. Some of the hypermetallated A β catalytically produces H₂O₂ from O₂ and biological reducing agents.
3. H₂O₂ oxidises A β Cu which generates soluble and cross-linked forms of A β and these are released from the membrane. Oxidised A β makes it protease-resistant which

means that the hydrolytic degradation of A β into smaller amino acid polymers cannot take place.

4. Oxidised forms of A β are the major components of plaque deposits. High concentrations of Zn released in the vicinity of the synapses aids in the precipitation of soluble A β which is released. Plaques are ultimately A β with high concentrations of Zn, Cu and Fe.
5. Oxidised A β also initiates the activation of microglia which characteristically reacts to produce high concentrations of H₂O₂ as well as myeloperoxidase (MPO). This further facilitates cross-linking of A β and the build-up of H₂O₂ outside cortical cells.
6. The H₂O₂ then freely permeates across the lipid membrane of the cell and reacts with the elevated levels of Cu and Fe to produce the highly reactive OH^{*} leading to the aforementioned oxidative damage.

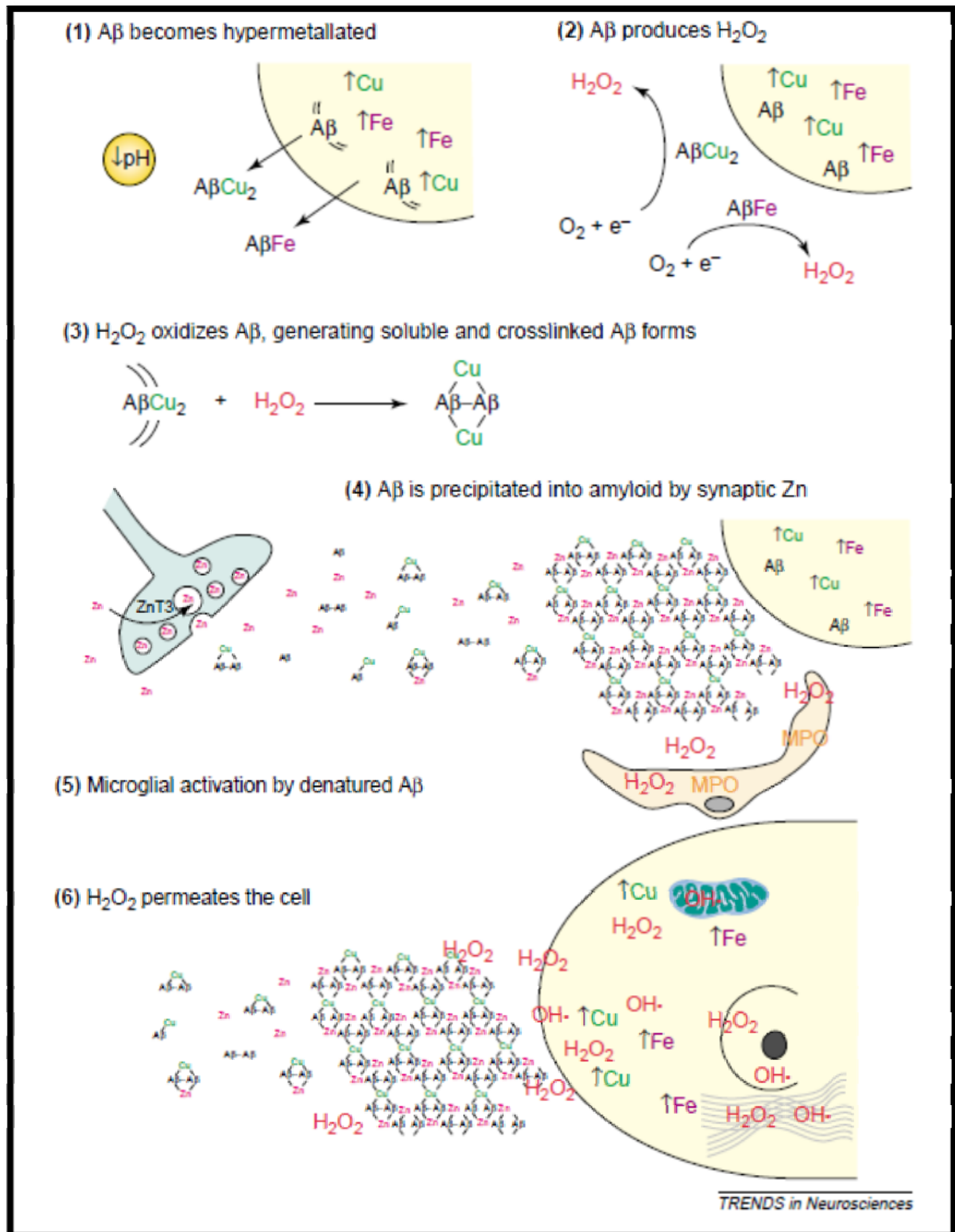


Figure 5-3: Model for the metallobiology of β -amyloid ($A\beta$) in Alzheimer's Disease. Proposed sequence of events leading to AD [100]

5.3 Application 1: The effect of PBT-2 on metal distribution in the brains of ZnT3 KO mice

5.3.1 Outline

Zinc transporter-3 (ZnT3) regulates Zn^{2+} transport in the brain and its dysfunction is hypothesised to be linked to impaired cognitive function at advanced ages. It is also known that ZnT3 mediates age-related Alzheimer's disease-like β -amyloid ($A\beta$) neuropathology in transgenic mice.

Currently, there are no definitive treatments or cures for AD with treatments focusing on targeting the symptomatic relief of the disease. Clioquinol (CQ) has been used with a degree of success in the past to treat AD based on the metal theory of AD. However, it has a number of downsides and large-scale production is hindered by the formation of di-iodo contaminants. PBT-2 is a second generation derivative of CQ and does not possess its negative characteristics.

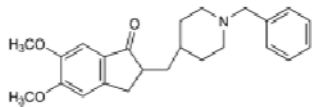
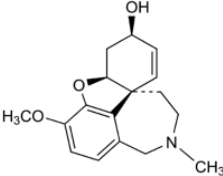
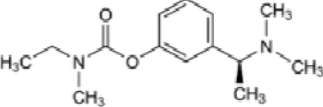
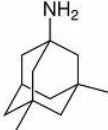
A comparison of the ^{66}Zn concentrations in wildtype and ZnT3 knockout (KO) mice was conducted. The results from Chapter 4 were used to prepare images for ^{66}Zn , ^{63}Cu and ^{56}Fe to observe the effect of PBT-2 on metal redistribution in the brains of ZnT3 KO mice. Average concentrations for regions of interest were extracted from the images and compared.

5.3.2 Treatment strategies for AD

At present there is no definitive treatment or cure for AD. Current AD drug treatments focus on inhibiting the degradation of acetylcholine in the synapses as well as the more recent glutamate receptor antagonists. These drug therapies however, target symptomatic relief of AD and do not halt or slow the progression of the disease [101; 102].

Symptomatic drug therapies are based on knowledge of AD presenting with a prominent loss of cholinergic, noradrenergic, dopaminergic, and GABAergic neuron transmission [102]. Drug therapies for AD have currently focused on modifying neurotransmitter systems to maximise remaining activity of affected neuronal circuits [102]. In current use are neurotransmitter-based treatments with cholinesterase inhibitors (ChEIs), particularly acetylcholinesterase (AChE) and butyrylcholinesterase (BuChE) inhibitors, and *N*-methyl-D-aspartate (NMDA) receptor antagonists. Current symptomatic drug therapies are outlined in Table 5-2.

Table 5-2: Current symptomatic drug therapies for Alzheimer's disease [103-105]

Drug Therapy	Chemical name	Structure	Actions	Use
Donepezil (Aricept®)	(RS)-1-benzyl-4-[5,6-dimethoxy-1-indanon)-2-yl] - methylpiperidine		Specific and reversible AChEI	Mild to severe AD
Galantamine (Reminyl®)	(4aS, 6R, 8aS)-4a,5,9,10,11,12-hexahydro-3-methoxy-11- methyl-6H-benzofuro[3a,3,2-ef][2]benzazepin-6-ol		Reversible AChEI and enhances the intrinsic action of ACh on nicotinic receptors	Mild to moderate AD
Rivastigmine (Exelon®)	(S)-N-ethyl-N-methyl-3-[1-(dimethylamino)ethyl] - phenyl carbamate		Brain selective pseudoirreversible inhibitor of AChE and BuChE	Mild to moderately severe AD
Memantine (Ebixa®)	1-amino-3,5-dimethyladamantane		NMDA antagonist	Moderately severe to severe AD

More recent drug therapy strategies have targeted prevention of the progression of AD. Pharmaceutical approaches are being researched and trialled to reduce abnormal A β interactions without causing systemic disturbance to essential elements used in the brain [101]. Therapeutics such as these are based on the metal theory of AD discussed earlier. Using this hypothesis, it would be noted that metal chelation could possibly be an effective way to remove excesses of metals in the brain. This is however a risk as chelation therapy on the brain could remove essential metals leading to adverse effects. Therefore, it has been found that there is a need for the development of more sophisticated molecules such as metal-protein attenuation compounds (MPACs) that serve as metal exchangers and ionophores. Logically, small molecule MPACs should target A β oligomerisation and A β -related generation of free radicals in order to prevent the aforementioned oxidative stress on the brain. MPACs should also be able to freely cross the BBB which excludes a number of common metal chelators because of their hydrophilic properties. [101]

Desferrioxamine is a detoxifying agent which is mainly used to treat acute iron poisoning and chronic iron overload [105] and has also been found to be a chelator of zinc, copper and aluminium. Crapper-McLachlan *et al.* found in 1991 that there was a significant reduction in the rate of decline for a 2-year period in AD patients who were treated intramuscularly with desferrioxamine twice a day [101; 106; 107]. Derivatives of a 14-membered saturated tetramine (JKL169 for example) have also been shown to be effective in reducing copper levels in the cortex of the brain while maintaining normal copper levels elsewhere [101].

Clioquinol (CQ or 5-Chloro-7-iodo-quinolin-8-ol), as seen in Figure 5-4, was used in 1950–1970s as an oral anti-parasitic agent for the treatment and prevention of intestinal amebiasis [108]. Oral CQ was taken off the market in the 1970s after reports of neurotoxicity in Japanese patients. It has however recently been studied as an oral treatment for AD. [101; 108]

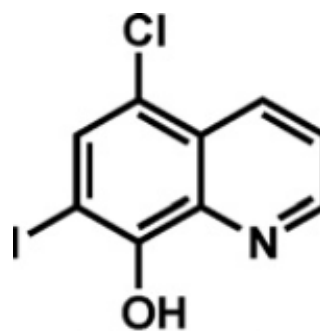


Figure 5-4: Chemical structure of Clioquinol (CQ)

In recent studies it has been found that treatment with oral CQ in Tg2576 mice (mice that over express A β) reduced cortical deposition of amyloid with an improvement or stability of general health compared to untreated mice. In moderately severe AD patients, oral administration of CQ over 36 weeks slowed cognitive decline and reduced plasma levels of A β 42 when compared to the placebo controls. [101]

CQ is able to cross the BBB and has a relatively low affinity (but high selectivity) for Cu²⁺ and Zn²⁺. This affinity however is sufficient to dissociate the metal ions from the low-affinity metal binding sites of A β . This removal of copper and zinc from A β therefore prevents oligomerisation and promotes the dissolution of non-covalently cross-linked species of A β . This increases the levels of biologically available copper and zinc in the brains of treated mice. Because of the low affinity of CQ for Cu²⁺ and Zn²⁺, it is unlikely that the metals accompany the drug into the urine at doses used so it is likely that the CQ treatment favours redistribution of the metals rather than excretion. [101; 109; 110]

A proposed mechanism of action for CQ and other similar MPACs is presented in Figure 5-5. The drug enters the brain and is first attracted to collections of extracellular metals before interacting with the metals and aiding their dissociation. These dissociated metal ions may be in a ternary complex with the drug itself or in a complex with dissociated A β . Neighbouring cells take up the complexes and the elements are separated. The breakdown

and clearance of A β is further facilitated by copper and zinc ions which activate matrix metalloproteases 2 and 3 and phosphorylation of GSK-3 β . Other predicted benefits of CQ are the dissolutions of A β aggregates and the inhibition of toxic A β redox activity.

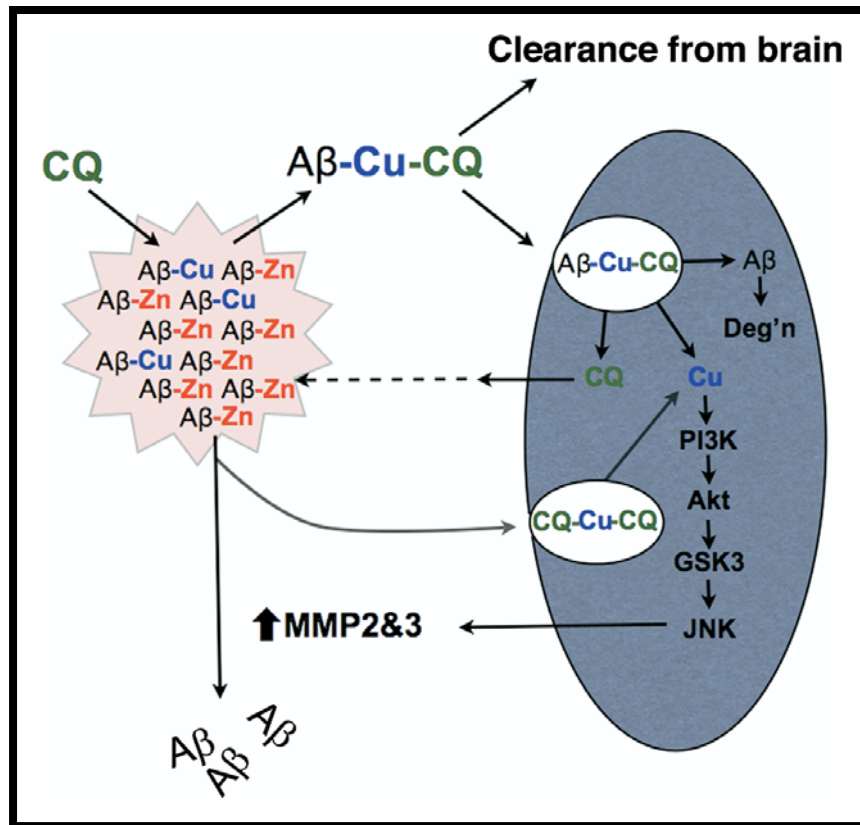


Figure 5-5: Proposed mechanism of action of clioquinol and similar metal-protein attenuation compounds (MPACs).

NB: the figure only shows an example of CQ and copper for simplicity, but this also relates to zinc and other MPACs, such as PBT-2. Deg'n = degeneration; GSK3 = glycogen synthase kinase 3; JNK = Jun N-terminal kinase [101]

The use of CQ for treatment of AD has obvious benefits however clinical trials had to be terminated because, during large scale drug manufacture, a di-iodo contaminant was being generated. A second generation derivative of CQ has recently been found to possess greater BBB penetration, significantly reduce the plaque burden and A β levels in transgenic AD mice, improve transgenic AD mice performance in the Morris Water Maze, and reduce A β -induced impairment of long-term potentiation (LTP) in hippocampal slices [101]. This second

generation derivative is currently only known to the public as PBT-2 (Prana Biotechnology, Ltd.) and may be one of the first manufactured, disease-modifying drugs for AD which is based on the metal theory of AD.

PBT-2, being an 8-hydroxy quinoline, has a similar structure to CQ but lacks the iodine. Therefore no di-iodo contaminant is formed during production. It was specifically designed to be easier to synthesise, have a higher solubility and have increased blood-brain barrier permeability [111].

5.3.3 ZnT3 knockout mice

The zinc transporter-3 (ZnT3) gene has been shown to be essential for loading Zn^{2+} into synaptic vesicles. ZnT3 is primarily localised to regions of the brain where mediation of higher cognitive functions take place, such as the hippocampus and neocortex. ZnT3 is likely to be the major synaptic vesicular Zn^{2+} transporter. Zn^{2+} is believed to play a key role in learning and memory via its function as a neuronal messenger and a modulator of synaptic transmission and plasticity. ZnT3 has been predicted to regulate cognition. It has recently been hypothesised that ZnT3 dysfunction, and the subsequent dyshomeostasis of synaptic zinc, may represent the key mechanism underlying the memory decline associated with normal and pathological aging. [112]

ZnT3 knockout (KO) mice exhibit a 20% reduction in total zinc levels and a specific absence of histochemically reactive Zn^{2+} in synaptic vesicles. Studies of ZnT3 KO mice 6-10 weeks old had no apparent spatial or memory deficits however it is believed that there are sufficient compensatory mechanisms to overcome the effect of the missing ZnT3 gene. It is hypothesised that ZnT3 animals may only express the cognitive phenotype with aging based on previous work that shows the involvement of ZnT3 in age-related AD-like amyloid neuropathology. [112]

5.3.4 Zinc deficits in ZnT3 KO animals

All animal experimentation was approved by the Howard Florey Animal Ethics Committee and conformed to the Code of Practice established by the National Health and Medical Research Council of Australia for the Care and Use of Animals for Scientific Purposes, Seventh Edition (2004).

Female ZnT3 KO and wildtype littermates were raised to 3, 6 and 24 months of age. In the four weeks prior to culling, animals underwent behavioural testing. Animals were then culled and tissues collected. One hemisphere of the brain was fixed with 4% paraformaldehyde for 4 hours and retained for histological endpoints. The other hemisphere was micro-dissected and frozen for LA-ICP-MS analysis. Brain hemispheres were cryosectioned at 30 μm .

Images of ^{66}Zn in the wild type and ZnT3 KO brain sections were prepared using the operational parameters in Table 5-3. These images were prepared prior to the development of the method for imaging with increased ν_i .

Table 5-3: LA-ICP-MS operational parameters prior to the development of imaging with increased v_l

Laser parameters	
x_s	40 μm
v_l	40 $\mu\text{m s}^{-1}$
Line spacing (centre to centre)	40 μm
Laser energy output	$\approx 0.9 \text{ J cm}^{-2}$ (40%)
Frequency	20 Hz
ICP-MS parameters	
t_{sc}	0.6152 s
Dwell times for masses imaged	
m/z 13	0.100 s
m/z 31	0.100 s
m/z 56	0.100 s
m/z 57	0.100 s
m/z 63	0.100 s
m/z 66	0.100 s

Figure 5-6 shows the level of deficit of ^{66}Zn in 6 month old ZnT3 KO mice compared to wildtype mice. A significant reduction in ^{66}Zn was seen, especially in the cortex and hippocampus of the ZnT3 KO mice.

Because these images were prepared without the use of Equation 4-1, the dimensions of the images in Figure 5-6 are not consistent with the dimensions of the original tissue section. This is seen more clearly when comparing these hemispheres to the whole brain sections in the figures in Section 5.3.5, *infra*.

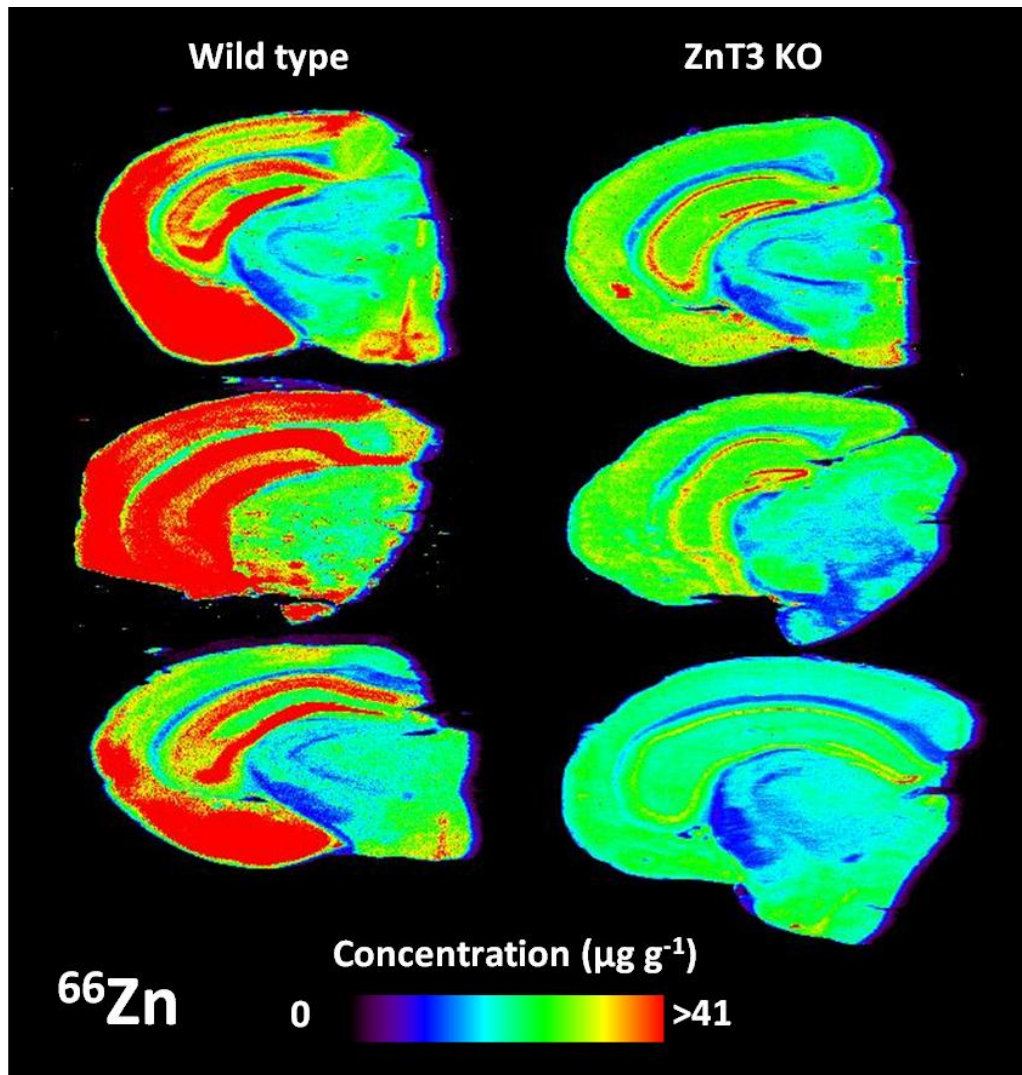


Figure 5-6: Comparison of ^{66}Zn distribution in the brains of wild type mice and ZnT3 KO mice ($x_s = 40 \mu\text{m}$, $v_1 = 40 \mu\text{m s}^{-1}$)

5.3.5 PBT-2 treated animals

ZnT3 KO mice and wildtype littermates were aged to 6 months, at which point they were culled. For six weeks prior to culling, animals were treated with a daily gavage of sham (SSV; control) or PBT-2 ($30 \mu\text{g g}^{-1}$, made up in SSV). Behaviour testing was carried out prior to culling. The brain was dissected and frozen before being cryosectioned at $30 \mu\text{m}$ for LA-ICP-MS analysis.

The LA-ICP-MS operational parameters using increased v_l are outlined in Table 5-4. Parameters were chosen in accordance with Equation 4-1 in order to maintain the relative dimensions of the original tissue section. Images of the mouse brain sections treated with SSV and PBT-2 were prepared for ^{66}Zn , ^{63}Cu and ^{56}Fe . The average concentrations for the cortex, hippocampus, pyramidal layer of the hippocampus and the amygdala were extracted from the images within the ENVI Imaging Suite software. The regions of interest are highlighted in Figure 5-7 and were individually selected for each brain section imaged.

Table 5-4: LA-ICP-MS operational parameters

Laser parameters	
x_s	$30 \mu\text{m}$
v_l	$120 \mu\text{m s}^{-1}$
Line spacing (centre to centre)	$30 \mu\text{m}$
Laser energy output	$\approx 0.35 \text{ J cm}^{-2}$ (25%)
Frequency	20 Hz
ICP-MS parameters	
t_{sc}	0.2502 s
Dwell times for masses imaged	
m/z 13	0.020 s
m/z 31	0.005 s
m/z 55	0.010 s
m/z 56	0.020 s
m/z 57	0.090 s
m/z 63	0.030 s
m/z 66	0.010 s
m/z 70	0.050 s

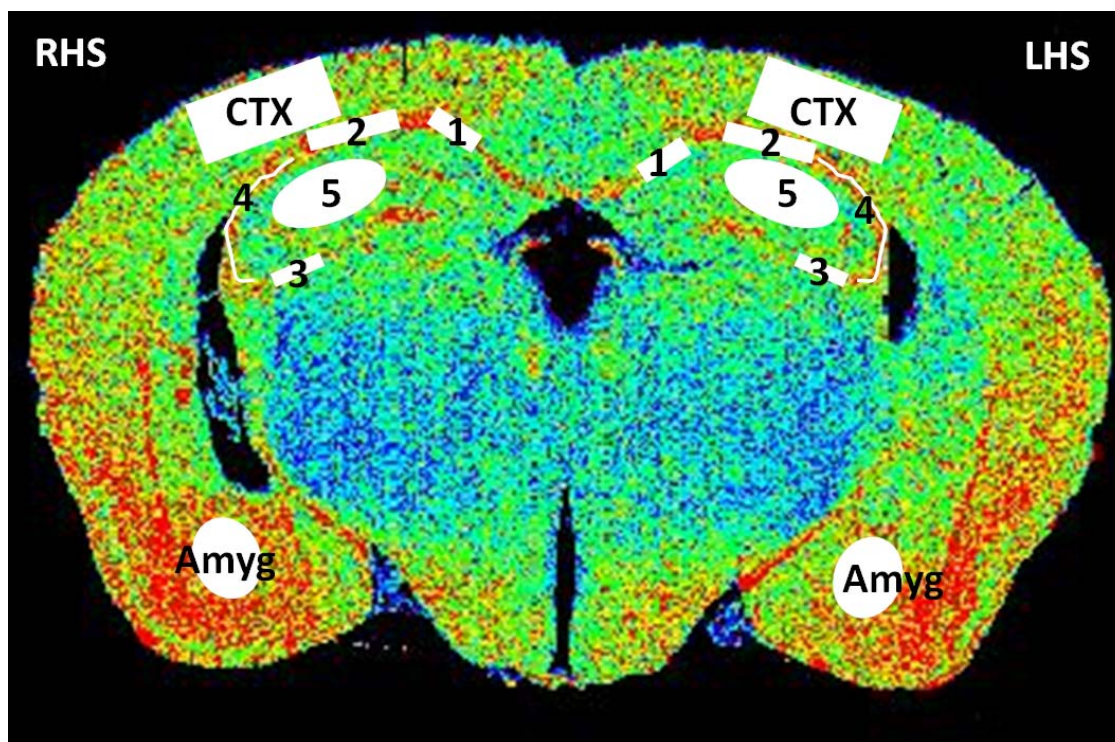


Figure 5-7: Regions of interest from where data was extracted; RHS = right hand side, LHS = left hand side, CTX = cortex, Amyg = amygdala, 5 = hippocampus (HIPP), 1-4 = pyramidal layer of the hippocampus (HIPP)

5.3.5.1 Zinc

Images for ^{66}Zn were successfully constructed using Equation 4-1 (Figure 5-8). The levels of ^{66}Zn appeared highest in the pyramidal layer of the hippocampus and amygdala. The average concentrations for the regions ranged from $11.1 \pm 1.5 \mu\text{g g}^{-1}$ in the hippocampus to $19.1 \pm 4.3 \mu\text{g g}^{-1}$ in the pyramidal layer. Although the concentrations of ^{66}Zn in the PBT-2 mice appear higher than SSV mice in Figure 5-9, statistical analyses of the regions of interest indicated that no significant differences in the distribution of ^{66}Zn were observed in the regions between sections from mice treated with PBT-2 or SSV. The P-values for the two-tailed t-tests assuming equal variances for each of the regions of interest are presented in Table 5-5. Region HIPP2 of the pyramidal layer on the LHS of the brain was the only region to show significant difference between PBT-2 and SSV mice ($P = 0.04$). The current data indicate that PBT-2 has no effect on the concentration of ^{66}Zn in the midbrain of ZnT3 KO mice.

Further analyses using higher resolving powers may result in differences between PBT-2 and SSV mice being observed at the cellular level.

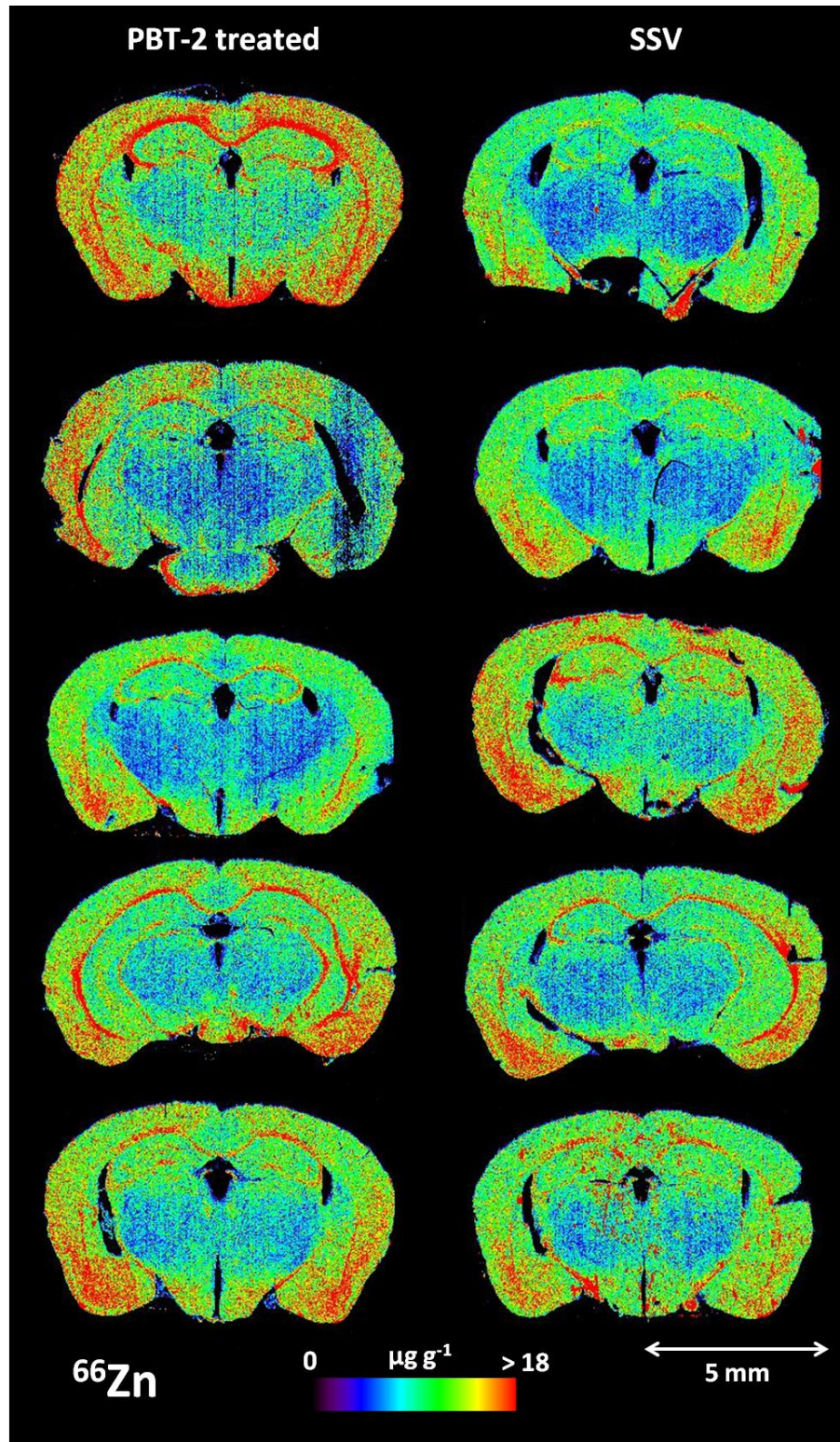


Figure 5-8: Images of ^{66}Zn for PBT-2 treated mouse brains compared to SSV mouse brains ($x_s = 30 \mu\text{m}$, $v_l = 120 \mu\text{m s}^{-1}$)

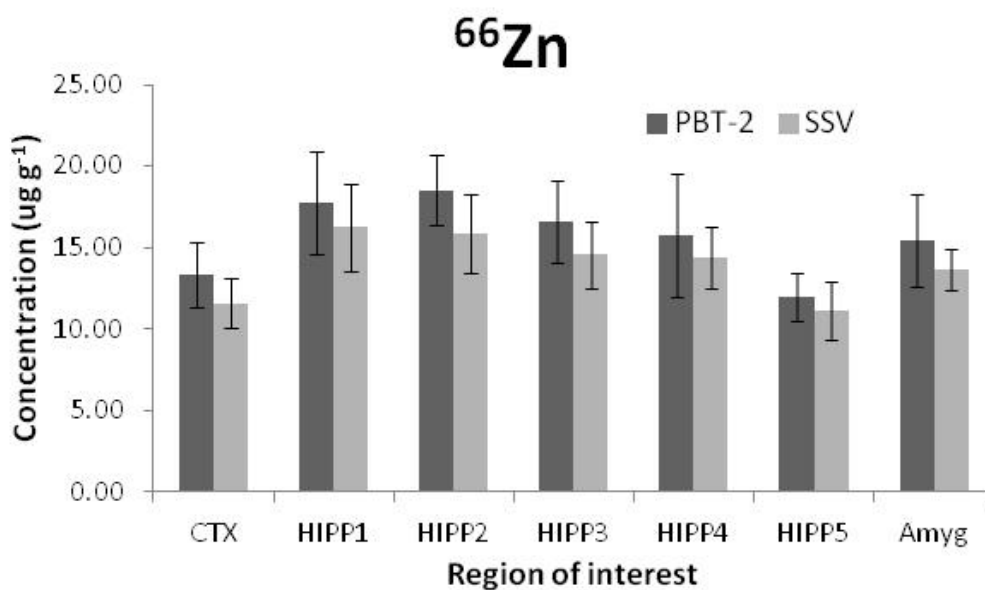


Figure 5-9: Concentrations of ⁶⁶Zn ± 95% confidence interval for the selected regions of interest in PBT-2 and SSV mouse brains

Table 5-5: P-values from two-tailed t-tests assuming equal variances for the concentration of ⁶⁶Zn in selected regions of interest between PBT-2 and SSV mice

⁶⁶Zn			
	LHS	RHS	Overall
CTX	0.17	0.26	0.08
HIPP1	0.44	0.68	0.41
HIPP2	0.04	0.40	0.06
HIPP3	0.47	0.14	0.09
HIPP4	0.17	0.99	0.45
HIPP5	0.99	0.28	0.52
Amyg	0.23	0.49	0.16

5.3.5.2 Other elements

No significant differences in the ^{63}Cu or ^{56}Fe concentrations in the regions of interest were observed between PBT-2 and SSV mice. The P-values for the two-tailed t-tests assuming equal variances for each of the regions of interest are presented in Table 5-6 and Table 5-7. The only difference between PBT-2 and SSV mice was seen in the amygdale for ^{56}Fe when the RHS and LHS data was combined. Images for ^{63}Cu and ^{56}Fe were also successfully prepared using Equation 4-1 and are presented in Figure 5-10 and Figure 5-11 respectively. These results indicate that PBT-2 has no effect on the concentration of ^{63}Cu and ^{56}Fe in the midbrain of ZnT3 KO mice.

Table 5-6: P-values from two-tailed t-tests assuming equal variances for the concentration of ^{63}Cu in selected regions of interest between PBT-2 and SSV mice

^{63}Cu			
	LHS	RHS	Overall
CTX	0.68	0.11	0.19
HIPP1	0.74	0.25	0.20
HIPP2	0.23	0.45	0.22
HIPP3	0.67	0.28	1.00
HIPP4	0.32	0.13	0.72
HIPP5	0.28	0.56	0.96
Amyg	0.60	0.28	0.21

Table 5-7: P-values from two-tailed t-tests assuming equal variances for the concentration of ^{56}Fe in selected regions of interest between PBT-2 and SSV mice

^{56}Fe			
	LHS	RHS	Overall
CTX	0.11	0.66	0.62
HIPP1	0.27	0.61	0.26
HIPP2	0.41	0.20	0.10
HIPP3	0.07	0.17	0.20
HIPP4	0.23	0.69	0.37
HIPP5	0.14	0.89	0.41
Amyg	0.08	0.18	0.03

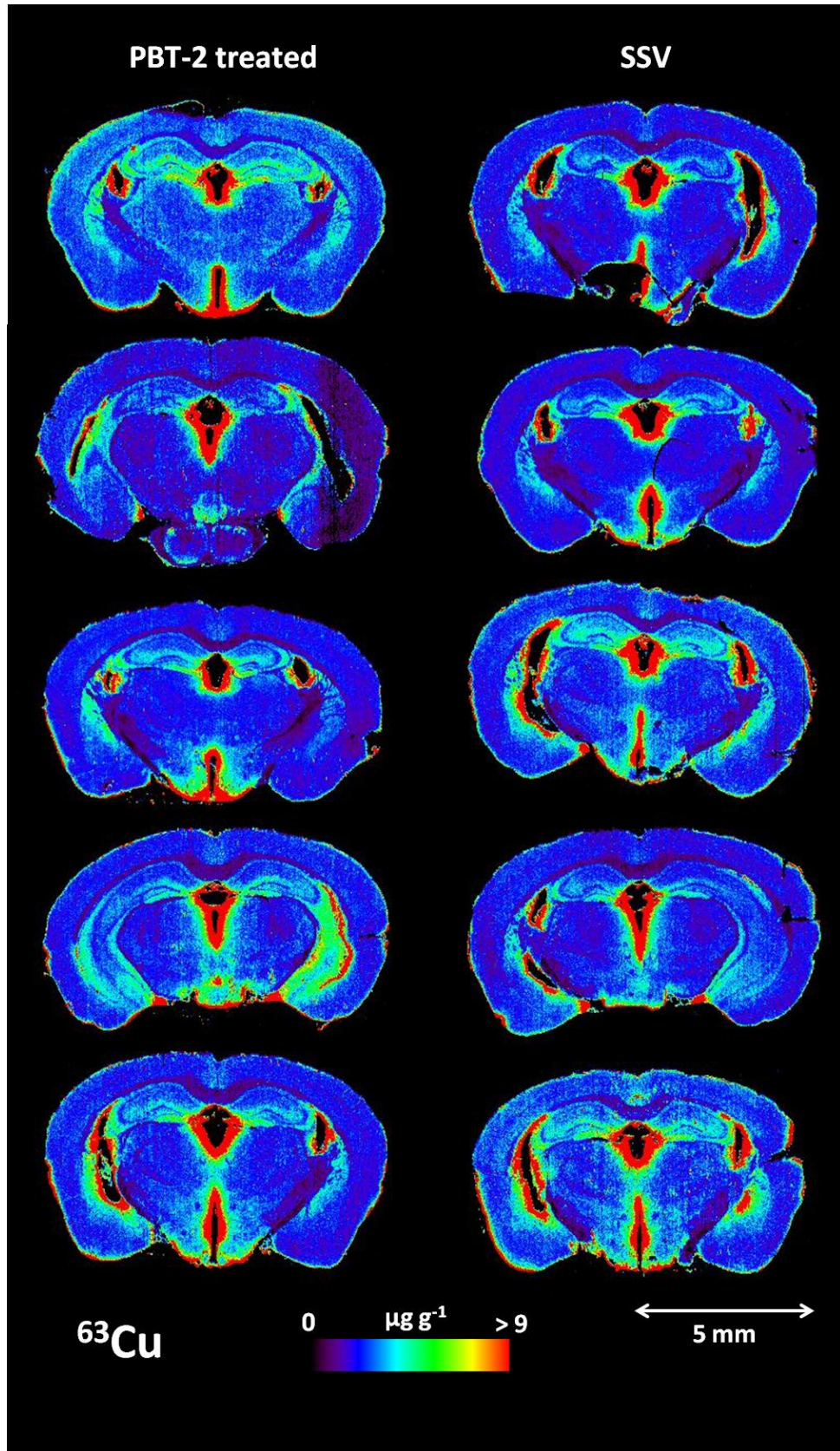


Figure 5-10: Images of ^{63}Cu for PBT-2 treated mouse brains compared to SSV mouse brains ($x_s = 30 \mu\text{m}$, $v_1 = 120 \mu\text{m s}^{-1}$)

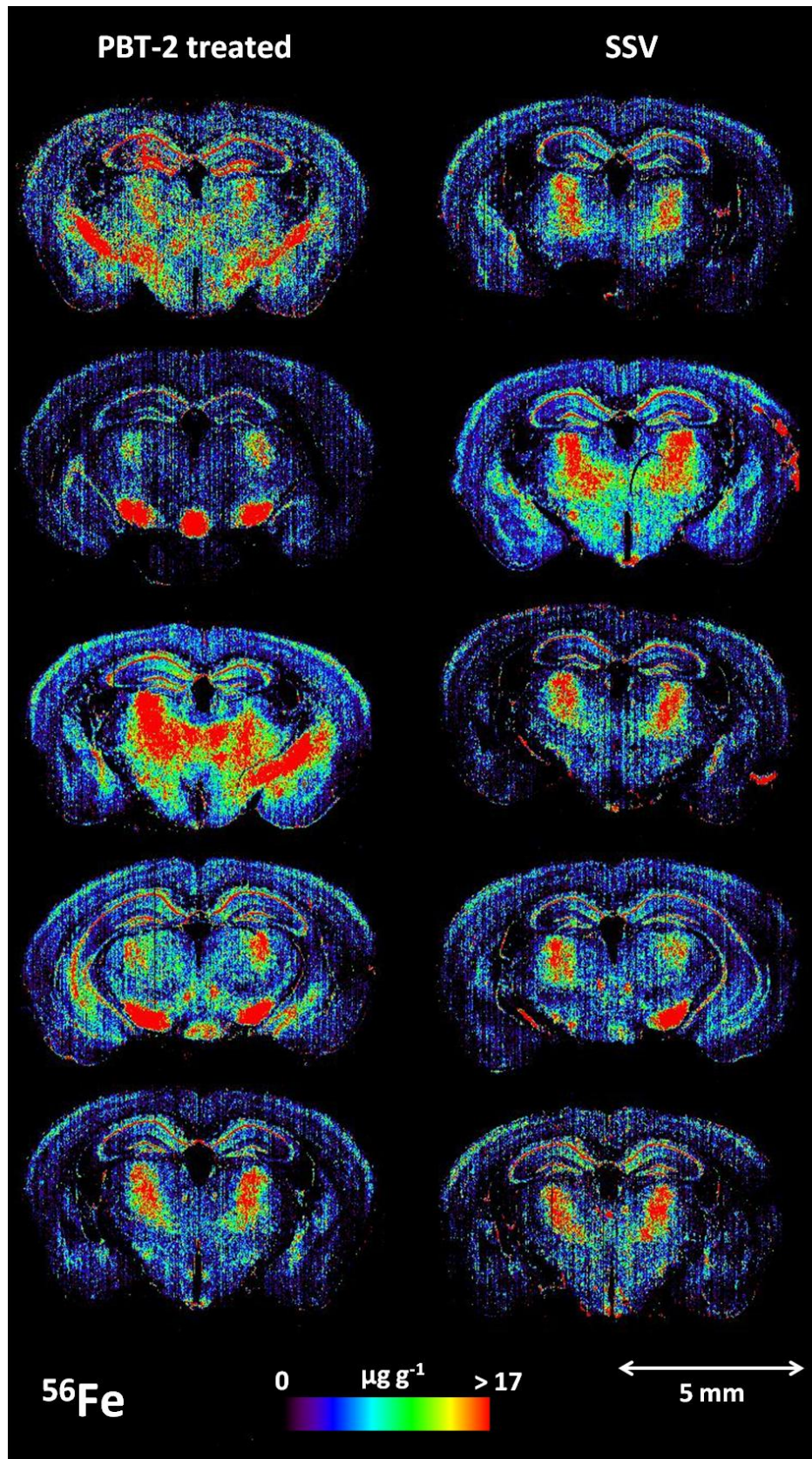


Figure 5-11: Images of ^{56}Fe for PBT-2 treated mouse brains compared to SSV mouse brains ($x_s = 30 \mu\text{m}$, $v_1 = 120 \mu\text{m s}^{-1}$)

5.4 Application 2: The effect of AGEs and sleep apnoea on the distribution of metals in the brain

5.4.1 Outline

The method proposed in Chapter 4 was used to observe element distribution in the brains of mice that were fed high and low advanced glycation end-product (AGE) diets, and between mice exposed to a long term of intermittent hypoxia (LTIH) and mice under sham intermittent hypoxic (SIH) conditions. AGEs are thought to play an important role in the pathogenesis of AD and can be obtained from the diet or they can form as a natural part of the aging process. During sleep apnoea, the body is deprived of adequate oxygen supply, a condition known as hypoxia, and has been implicated in the increased production and decreased degeneration of A β .

The most intriguing results were seen in the images for ^{59}Co . A 100-fold elevation in the concentrations of ^{59}Co was observed between LTIH, and SIH and control mice. Virtually all cobalt is present in mammalian tissue in the form of cobalamin (Vitamin B $_{12}$). Each cobalamin molecule contains a single cobalt ion at its active site. Therefore, the concentration distribution of ^{59}Co can be interpreted to be directly proportional to the cobalamin concentration distribution.

Applying the methods outlined in Chapter 4, images with equivalent tissue dimensions to the original tissue sections were prepared so there was no loss of resolution.

Article under review:

Lear, J., Veasey, S. C., Zhu, Y., Doble, P., Hare, D., Wang, S., et al. (2012). Long-term Intermittent Hypoxia Results in Cobalt Accumulation in the Brain: Implications for Vitamin B12 in Obstructive Sleep Apnea. *Sleep*, Under Review.

5.4.2 Advanced glycation end-products

Advanced glycation end-products (AGEs) are products of an irreversible reaction of carbohydrates and protein in the Maillard or browning reaction, a process outlined in Figure 5-12 and broken down in Figure 5-13 [113-115]. They are protein-bound oxidation products of sugars generated by the non-enzymatic reaction of a sugar ketone or aldehyde group with free amino groups of proteins or amino acids. The formation of AGEs is irreversible and protease resistant cross-linking of peptides and proteins [115-117]. AGEs have been implicated in the chronic complications of diabetes mellitus and renal complications, and have been reported to play an important role in the pathogenesis of Alzheimer's disease (AD) [118-121].

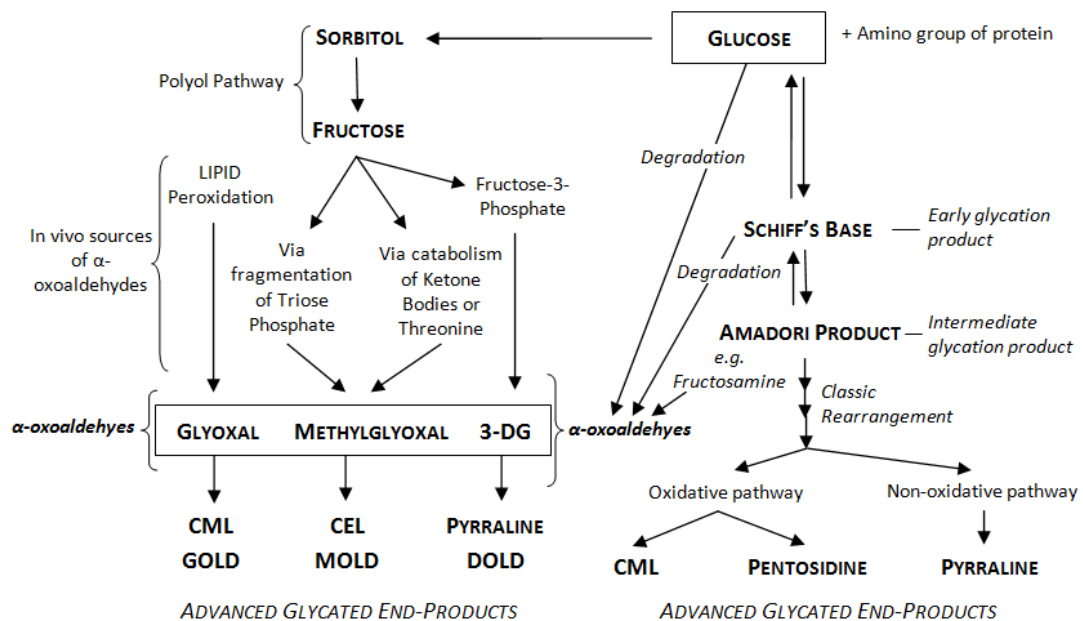


Figure 5-12: Glucose and AGE formation pathways incorporating the polyol pathway and AGE formation by the α -oxoaldehydes glyoxal, methyl glyoxal and 3-DG. [114]
 3-DG, 3-deoxyglucosone; MGO, methylglyoxal; CML, N- ϵ -(carboxymethyl)lysine; CEL, N- ϵ -(carboxyethyl)lysine; DOLD, deoxyglucosone-lysine dimer; MOLD, methyl glyoxal-lysine dimer; GOLD, glyoxal-lysine dimer

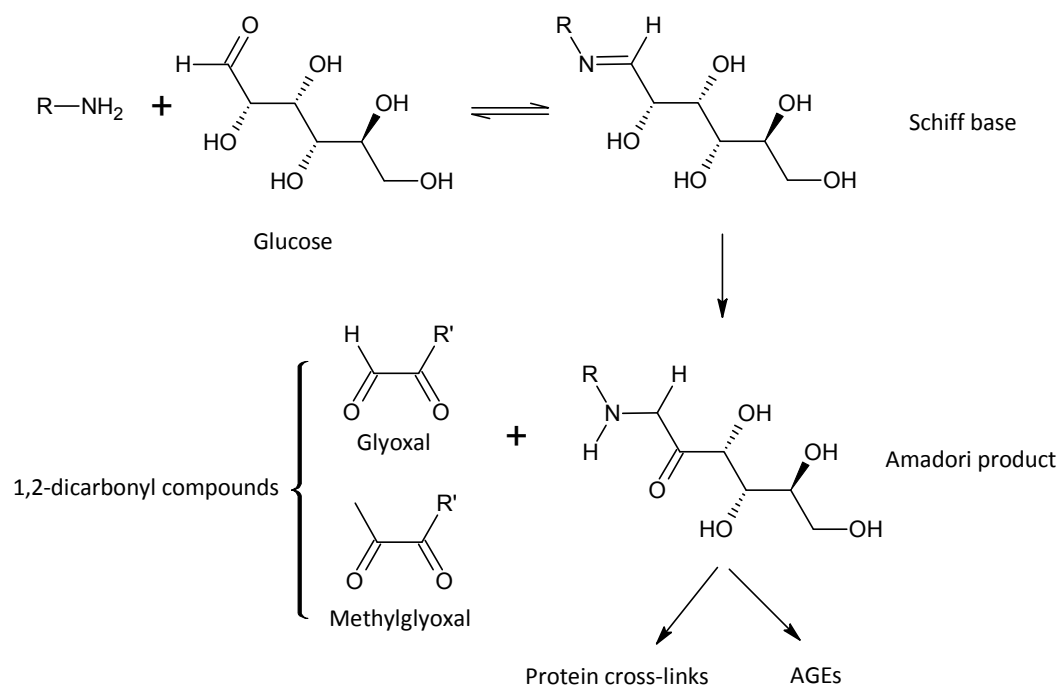


Figure 5-13: Formation of advanced glycation end-products (AGEs) starts by a reaction of the amino group of a protein and a reducing sugar (here: glucose) and completed by the reaction between 1,2-dicarbonyl compounds (here: glyoxal and methylglyoxal) and the Amadori product [115]

AGEs may be formed exogenously during the process of heating or endogenously through metabolism and the aging process.

Exogenous formation of AGEs occurs most commonly during the cooking process. AGEs in the diet are known to contribute to increased oxidant stress and inflammation, which are linked to diabetes and cardiovascular disease [120]. When proteins are cooked with sugars in the absence of water, AGEs are formed rapidly. This is characterised by the “browning” of food during frying, baking, broiling, roasting, grilling and sautéing, for example. A large number of foods are subjected to cooking and thermal processing for the purpose of safety and convenience, and also to enhance flavour, colour and appearance. AGE formation can be prevented by boiling, steaming and stewing meats and vegetables [119; 120]. Selected examples of the AGE content in foods are presented in Table 5-8. Recent studies have shown that diets rich in AGEs play an important role in human health and the pathogenesis of certain diseases. Elevated levels of circulating and tissue AGEs have been associated with

kidney disease and atherosclerosis in mice that have diets rich in AGEs. Conversely, restricting AGEs in the diet can prevent vascular and kidney dysfunction, diabetes type 1 and type 2, improves insulin sensitivity and accelerates wound healing [119-126].

Table 5-8: Advanced glycation end-product (AGE) content of selected foods prepared by standard cooking methods [119; 120]

Food item	AGE*
Fats	
Almonds, roasted	66.5 kU/g
Oil, olive	120 kU/mL
Butter	265 kU/g
Mayonnaise	94 kU/g
Proteins	
Chicken breast, fried X 15 min	61 kU/g
Beef, broiled X 15 min	60 kU/g
Beef, boiled X 1 h	22 kU/g
Tuna, roasted X 40 min	6 kU/g
Tuna, broiled X 10 min	51 kU/g
Cheese, American	87 kU/g
Cheese, Brie	56 kU/g
Egg, fried	27 kU/g
Egg yolk, boiled	12 kU/g
Tofu, raw	8 kU/g
Tofu, broiled	41 kU/g
Carbohydrates	
Bread, whole-wheat centre	0.54 kU/g
Pancake, homemade	10 kU/g
Milk, cow, whole	0.05 kU/mL
Milk, human, whole	0.05 kU/mL
Enfamil (infant formula)	4.86 kU/mL
Apple	0.13 kU/g
Banana	0.01 kU/g
Carrots	0.1 kU/g
Green beans	0.18 kU/g
*AGE denotes N-carboxymethyl-lysine (CML)-like immunoreactivity, assessed by enzyme-linked immunosorbent assay based on monoclonal antibody (4G9)	

Endogenous AGEs form as a natural part of metabolism and the aging process. AGE accumulation is accelerated in AD and levels have been found to be elevated. AGEs have been detected in AD's characteristic amyloid plaques and neurofibrillary tangles (NFTs). It is thought that many of the neuropathological and biochemical features of AD such as extensive

protein cross-linking, inflammation, oxidative stress and neuronal death may be explained by the presence of AGEs and they may influence the disease's progression [113; 115-118; 127-132].

It is proposed that AGEs contribute to the pathogenesis of AD by two major mechanisms;

- intracellular AGEs which cross-link cytoskeletal proteins and render them insoluble, and
- extracellular proteins accumulating on long-lived protein deposits like the senile plaques and thus chronically activate micro- and astroglial cells which constantly produce free radicals and neurotoxic cytokines which put more burden on neurons in close proximity. [115]

Figure 5-14 outlines the structures of methylglyoxal-derived AGEs found in AD. Methylglyoxal (MG) has been implicated in the increased AGE levels in age-related diseases including AD. The hypothesis that MG is one of the major sources of intracellular reactive carbonyl compounds is supported by the presence of specific MG-derived AGEs in intracellular protein deposits in neurofibrillary tangles and cerebrospinal fluid. [115; 133-135]

5.4.3 Sleep apnoea and AD

Sleep disordered breathing is common, especially in older people, and the clinical spectrum ranges from snoring to obstructive sleep apnoea (OSA) [136]. During OSA, the levels of oxygen circulating throughout the body and brain are reduced and the body is deprived of adequate oxygen supply, a condition known as hypoxia. Each apneic episode is associated with a partial desaturation of serum hemoglobin followed by re-oxygenation, and these repeated cycles of transient hypoxia cause oxidative stress. Since the brain is particularly vulnerable to hypoxia, moderate-severe levels of OSA are associated with brain injury, especially within white matter regions of the forebrain [137-139]. Evidence in recent years has revealed that hypoxia increases production and decreases degeneration of A β , and affects the clearance of A β from the brain. It is also speculated to be involved in hyperphosphorylation of tau, dysfunction of the blood-brain barrier (BBB), and degeneration of neurons. The dysfunction of the BBB may be caused by hypoxia inducing neuroinflammatory responses which further accelerate the accumulation of A β [140]. OSA has also been shown to lead to increased level of AGEs [141].

5.4.4 Imaging

Images were prepared in order to visualise any effects that intermittent hypoxia and varying AGE diets had on the distribution of elements in the mid-brains of mice.

Images were prepared using increased acquisition speeds as discussed in Chapter 4. LA-ICP-MS operation parameters are outlined in Table 5-9.

Table 5-9: LA-ICP-MS operational parameters

Laser parameters	
x_s	30 μm
v_l	127 $\mu\text{m s}^{-1}$
Line spacing (centre to centre)	30 μm
Laser energy output	$\approx 0.8 \text{ J cm}^{-2}$ (30%)
Frequency	20 Hz
ICP-MS parameters	
t_{sc}	0.2372 s
Dwell times for masses imaged	
m/z 13	0.010 s
m/z 31	0.010 s
m/z 55	0.010 s
m/z 56	0.015 s
m/z 57	0.090 s
m/z 59	0.020 s
m/z 63	0.020 s
m/z 66	0.010 s
m/z 85	0.010 s
m/z 208	0.020 s

Mice used in this experiment were subjected to varying periods of intermittent hypoxia and fed diets consisting of varying levels of AGEs. Mice were subjected to both long-term intermittent hypoxia (LTIH) and sham intermittent hypoxia (SIH) where a dummy treatment, with all variables being consistent except level of hypoxia, is rendered to the control group. Both groups were fed either a diet high in AGEs or low in AGEs resulting in four experimental groups being generated.

5.4.4.1 Effectiveness of the speed equation

An image acquired utilising the speed equation (Equation 4-1) was overlaid with a photograph of the same brain section taken with the aid of a microscope in order to compare the dimensions of the images. Figure 5-15 shows that the dimensions of the image acquired are the same as the dimensions of the original tissue section indicating the usefulness of Equation 4-1 in maintaining the dimensions of the original tissue section during data acquisition.

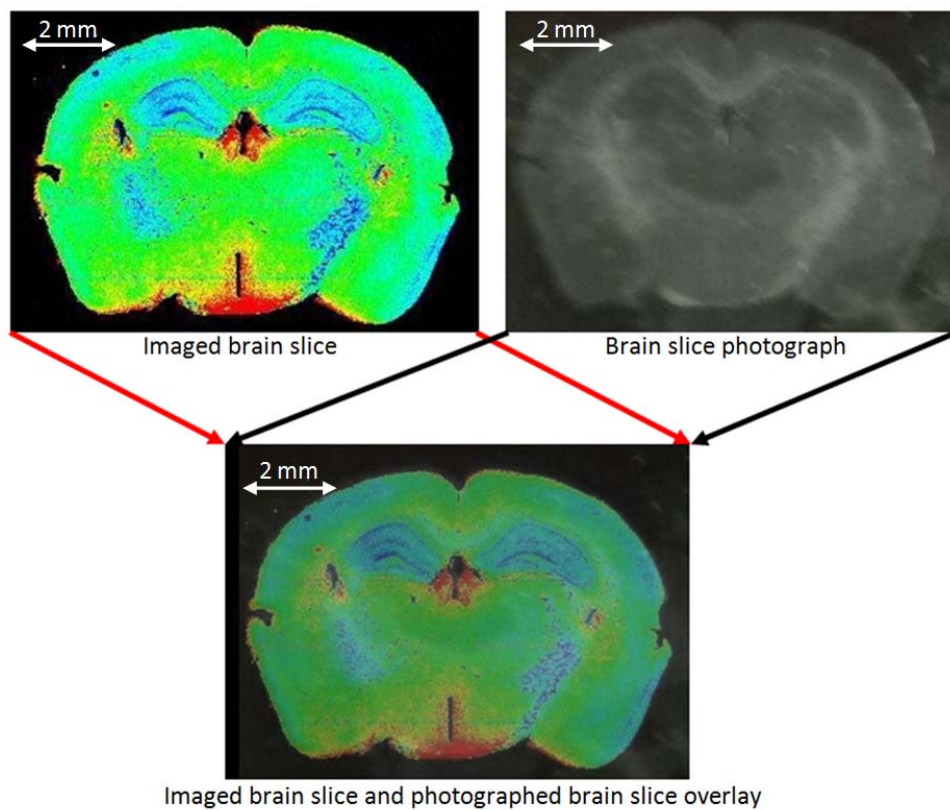


Figure 5-15: Effectiveness of $v_1 = x_s / t_{sc}$ in reproducing images with equivalent dimensions to the original tissue section

5.4.4.2 Cobalt

The most interesting results were seen for the concentrations of ^{59}Co between LTIH, and SIH and control groups. Table 5-10 presents the average concentration of ^{59}Co in the control, SIH and LTIH mouse brain sections. There was a 100-fold elevation in cobalt concentration in the LTIH mice which is highly significant ($P < 0.0001$). All brains were analysed randomly with some LTIH and SIH analysed on the same day and some on different days so instrument error can be discounted. There were no differences in ^{59}Co concentrations observed between the different AGE diets.

All LTIH mice showed detectable and quantifiable levels of ^{59}Co . All SIH and control mice showed insignificant levels of ^{59}Co with a minimal number of pixels indicating detection above background levels. Figure 5-16 presents the images for ^{59}Co in the LTIH mouse brains contrasted against the SIH and control mouse brains. Because ^{59}Co was at concentrations too low to image for the SIH and control brains, black and white images are presented which represent the positioning of the sections.

Table 5-10: Average concentrations of ^{59}Co in the mouse brain sections

	^{59}Co concentration ($\mu\text{g g}^{-1}$)
Control	0.017 \pm 0.003
SIH	0.062 \pm 0.007
LTIH	5.6 \pm 0.6

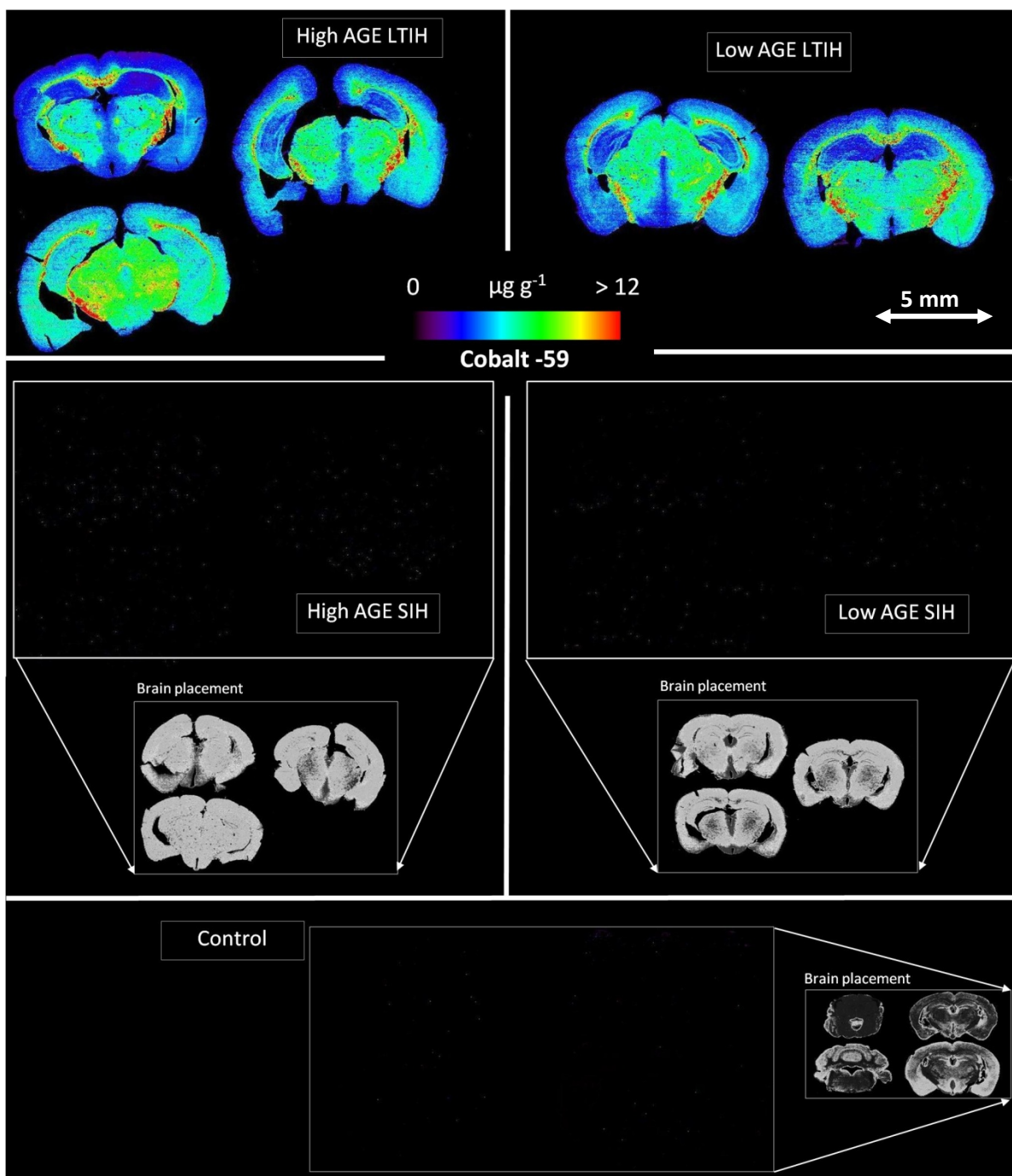


Figure 5-16: ^{59}Co distribution in the brains of LTIH and SIH mice fed low and high AGE diets, and control mice. Black and white images show where the brain sections should be had ^{59}Co been detected.

In the LTIH mice, ^{59}Co was concentrated in regions that contain a dominance of myelin: internal capsule, cerebral peduncles, medullary white matter of cortex, medial lemniscus and the corpus callosum. Brain regions that contain high densities of neurons (cortical grey matter, hippocampus and hypothalamus) contained relatively low concentrations of ^{59}Co .

Cobalt is an essential element in humans. It is necessary for the formation of vitamin B₁₂ complex, or hydroxycobalamin (Figure 5-17). Cobalamins account for virtually all of the cobalt that is present in mammalian tissues, and since each cobalamin molecule contains a single cobalt ion, the elemental distribution of cobalt in brain sections corresponds to the distribution and concentration of cobalamin.

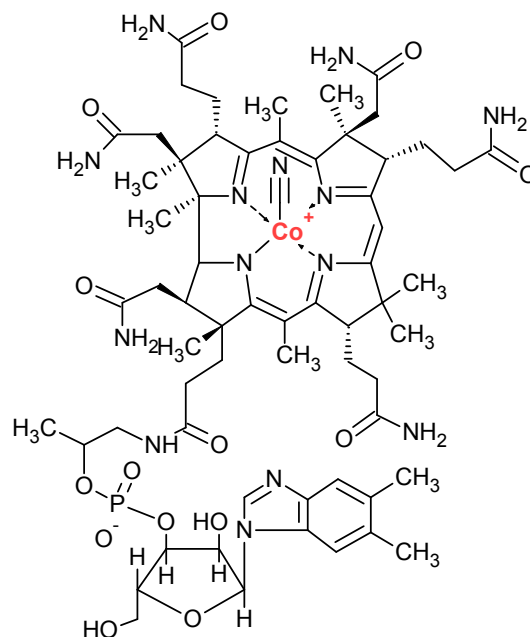


Figure 5-17: Cobalt in Vitamin B₁₂ (cobalamin)

The difference of two orders of magnitude observed in the brain concentration of ⁵⁹Co provides unequivocal evidence that LTIH causes a major disruption in the metabolism of cobalamin. In LTIH mice, ⁵⁹Co was concentrated in white matter regions, which is consistent with earlier reports that cobalamin levels are higher in homogenates of human white matter compared to grey matter [142; 143]. The higher levels in white matter may be associated with the essential role of cobalamin in stabilising myelin. The results are also consistent with the theory that LTIH stimulates a strong requirement for cobalamin which is needed to assist the repair of neurons and myelin that have been damaged by oxidative stress.

5.4.4.3 Other elements

Other elements were also successfully imaged however definitive results are not yet known as further analyses need to be performed. A larger sample set needs to be prepared so the experiments may be repeated however these were not able to be completed for the purpose of this thesis due to animal preparation time restraints. There were no differences in element concentrations observed between the different AGE diets.

The levels of ^{63}Cu were highest in the periventricular regions of the hypothalamus, thalamus and inferotemporal cortex. The lowest levels of ^{63}Cu were observed in the corpus callosum, deep white matter of parietal cortex and lateral thalamus. No differences in the overall distribution of ^{63}Cu were observed between sections from mice treated with LTIH or SIH (Figure 5-18). The mean concentration of elemental copper was $7.1 \pm 1.3 \mu\text{g g}^{-1}$ in LTIH and $7.0 \pm 0.6 \mu\text{g g}^{-1}$ in SIH.

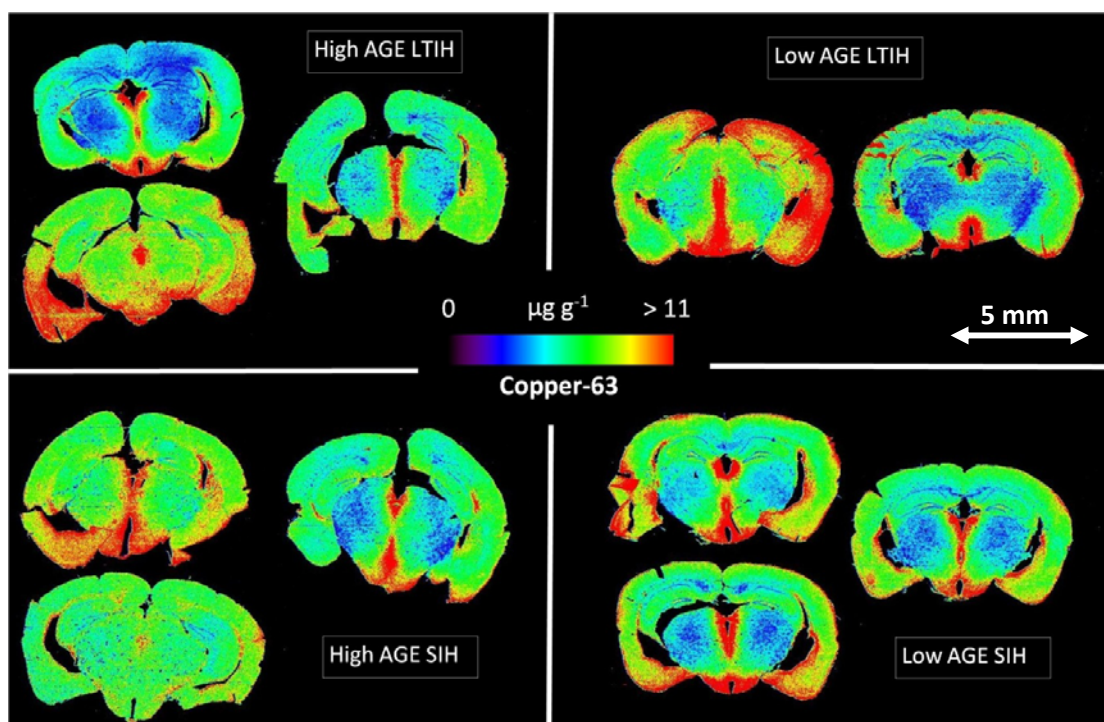


Figure 5-18: ^{63}Cu distribution in the brains of LTIH and SIH mice fed low and high AGE diets

No differences in the overall distribution of ^{66}Zn were observed between sections from mice treated with LTIH or SIH (Figure 5-19). The mean concentration of ^{66}Zn was $17.2 \pm 1.4 \mu\text{g g}^{-1}$ in LTIH and $17.3 \pm 1.3 \mu\text{g g}^{-1}$ in SIH. ^{66}Zn was concentrated in sectors CA2 and CA3 of the hippocampus, as well as in the amygdala and inferotemporal cortex. ^{66}Zn was uniformly distributed throughout the remaining tissue.

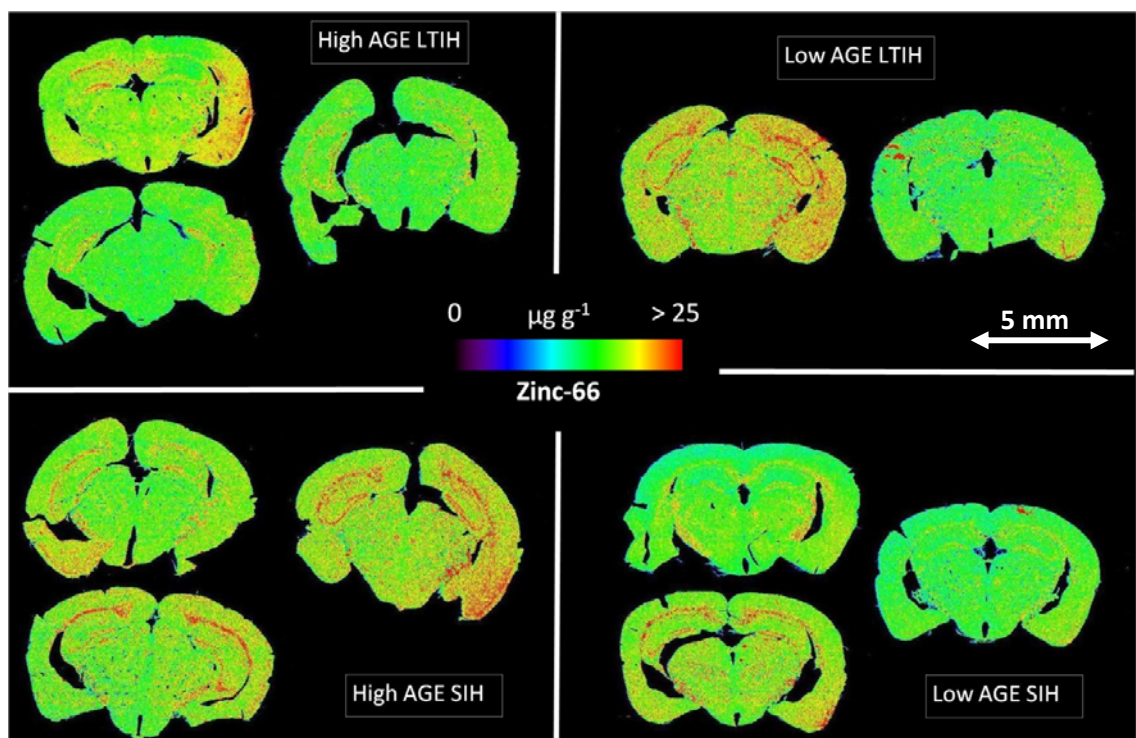


Figure 5-19: ^{66}Zn distribution in the brains of LTIH and SIH mice fed low and high AGE diets

The levels of ^{57}Fe tended to be highest in grey matter regions that contain a high density of neuronal cell bodies and lowest in white matter regions. ^{57}Fe was most strongly concentrated in the granule cell layer of the dentate gyrus, pyramidal cell layer of the hippocampus, the ventromedial hypothalamus and layers 1-4 of parietal cortex (Figure 5-20). No differences in the overall distribution of ^{57}Fe were observed between sections from mice treated with LTIH or sham-LTIH. The mean concentration of elemental iron was $8.9 \pm 0.7 \mu\text{g g}^{-1}$ in LTIH and $10.4 \pm 1.5 \mu\text{g g}^{-1}$ in SIH.

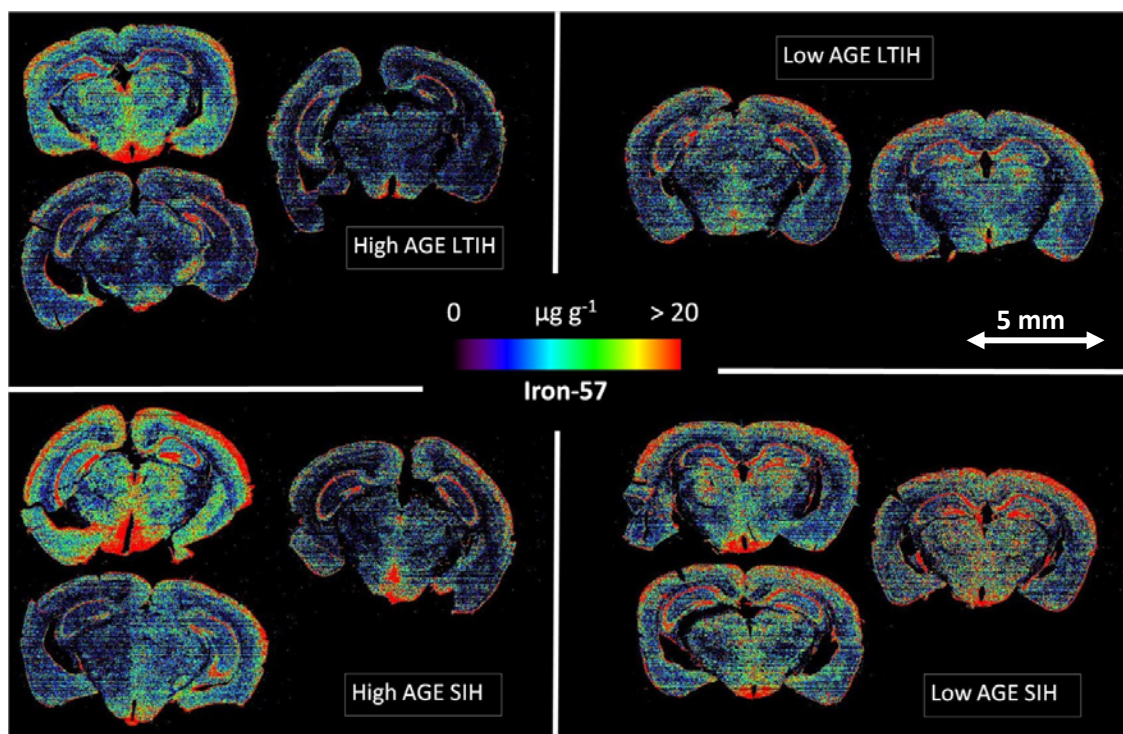


Figure 5-20: ^{57}Fe distribution in the brains of LTIH and SIH mice fed low and high AGE diets

5.5 Conclusions

EBI using increased v_1 was successful in imaging metal distributions in the thin sections of mouse brain. Utilising Equation 4-1, the relative dimensions of the original tissue were maintained in the images and the analysis time was effectively reduced. The shorter analysis time resulted in a higher sample throughput than studies previously undertaken in the LA-ICP-MS field.

Images prepared for Application 1 effectively showed the differences in ^{66}Zn distribution for wildtype and ZnT3 KO mice which supports the evidence for Zn^{2+} deficits in ZnT3 KO mice. Images were successfully prepared using Equation 4-1 for PBT-2 and SSV-treated ZnT3 KO mice. Comparison of the results of mice showed no significant difference in ^{66}Zn , ^{63}Cu or ^{56}Fe concentrations between the two groups of mice for the selected regions of interest. These results indicate that PBT-2 had no observable effect on the concentrations of these elements in the midbrains of ZnT3 KO mice.

Application 2 resulted in images with intriguing results for ^{59}Co concentrations. Those mice subjected to long term intermittent hypoxia showed a 100-fold elevation in the average concentration of ^{59}Co in the mid-brain sections. No detectable levels of ^{59}Co were present in mice subjected to sham intermittent hypoxic conditions. It is suggested that this increase reflects an unmet requirement for active cobalamin. Further investigations of these findings are required to confirm these results and investigate whether similar results occur in humans with OSA.

***Chapter 6: Using H₂ reactive gas
to improve sensitivity for EBI***

Chapter 6: Using H₂ reactive gas to improve sensitivity for EBI

6.1 Chapter outline

Reaction/collision gases are not typically used in LA-ICP-MS analysis, due mostly to the significant impact on the reduction in signal intensity. Only two studies to date have examined the usefulness of the reaction cell in image preparation, both using H₂ to remove ⁴⁰Ar⁺ interference on ⁴⁰Ca [144; 145].

A variety of biologically useful elements other than ⁴⁰Ca have polyatomic interferences stemming from argide- and oxide-based species. Reducing polyatomic interferences reduces background levels of analytes and therefore has the ability to reduce the limits of analysis. Subtraction of high backgrounds from prepared images currently reduces image quality and loss of data is observed. A decrease in background levels will prevent this occurring and improve image quality.

For an improvement to be observed for each analyte tested there must be;

- a decrease in analyte background levels
- a decrease in the limits of analysis
- increased signal to noise ratios; and
- increased image quality.

These experiments employed hydrogen gas in the removal of interfering species. The capability of using hydrogen in the reaction cell to improve EBI analysis was further examined.

Accompanying Publication:

Lear, J., Hare, D., Fryer, F., Adlard, P., Finkelstein, D., & Doble, P. (2012). High-resolution elemental bio-imaging of Ca, Mn, Fe, Co, Cu and Zn employing LA-ICP-MS and hydrogen reaction gas. *Analytical Chemistry*. DOI: 10.1021/ac301156f [146]

6.2 Restrictions to high resolution EBI

The majority of published LA-ICP-MS imaging applications have presented images with spatial resolution in the mid- μm range, produced by using x_s of 30 to 50 μm and above [62; 63; 67; 72; 144]. For many biological applications, greater emphasis is being placed upon higher resolution images for monitoring cellular metal change [147]. In work preceded by Seuma *et al.* [148], Geisen *et al.* [71] recently described an innovative immunohistochemical technique for labelling fibroblast cells with iodine, which were subsequently imaged using x_s of 4 μm . Iodine images depicted not only the external cellular structure, but also some nuclear features.

The major restriction for increasing resolution is sensitivity. Instrument response is often limited by high background signals for certain biologically relevant elements, with first row transition metals in particular. Reducing the x_s can result in instrument responses that do not exceed background signal intensities. As x_s is decreased, the amount of material ablated decreases according to Equation 6-1, where x_1 and x_2 are laser spot diameters (μm), h is the depth of laser penetration (μm) and V is the volume of material ablated (μm^3), assuming the crater is cylindrical. Figure 6-1 graphically represents the resulting power law for increasing x_s , and thus increasing ablated material in LA-ICP-MS experiments. For example, if x_1 is 6 μm and x_2 is 30 μm and the depth of penetration for both x_s is equal, $V_{30} = 25 V_6$.

$$\frac{\left(\frac{x_2}{2}\right)^2 V_{x_1}}{h_{x_1}} = \frac{\left(\frac{x_1}{2}\right)^2 V_{x_2}}{h_{x_2}}$$

Equation 6-1

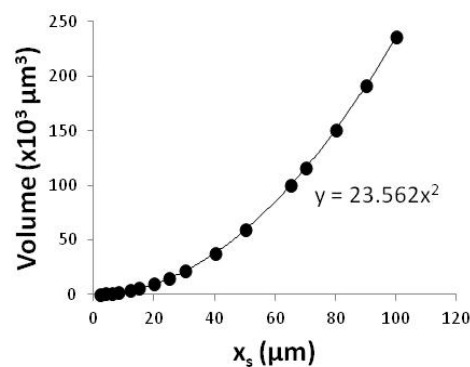


Figure 6-1: Effect of varying x_s on the volume of tissue ablated per laser pulse ($h = 30 \mu\text{m}$)

6.3 The reaction cell and hydrogen as a reactive gas

Chemical resolution is a well-documented technique that utilises the reaction cell (Figure 6-2) to initiate ion-molecule interactions to overcome spectral interferences produced during ICP-MS analysis [15; 145; 149-166]. This technique is useful provided a gas of sufficient reactivity and selectivity is used. Another consideration in ion-molecule reactions is the formation of reaction products which have the potential to introduce new interferences into the system which are not normally observed during standard operational conditions. This means that certain analytes may benefit from analysis using a reaction gas and some may need to be analysed without. [149; 155; 156; 162]

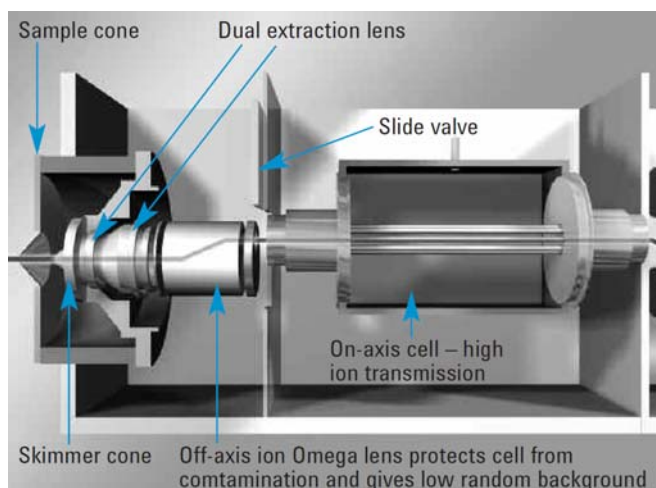


Figure 6-2: Schematic of Agilent ICP-MS showing the Octopole Reaction System (ORS) cell [88]

Reaction pathways include neutralisation, association, condensation and fragmentation reactions. It is possible through these pathways that new interferences are formed and these interferences include the formation of cluster ions, the appearance of fragment ions from the reactive gas, and association of fragment ions with neutral ions to form polymer compounds, which is particularly important when hydrocarbons or their derivatives are used as a reaction gas [156; 162]. Possible reaction pathways that can resolve the analyte from interferences in the reaction cell are presented in Table 6-1.

Table 6-1: Possible reaction pathways that can resolve the analyte from interferences in a reaction cell [162]

Interferent neutralisation	$I^+ + R$	$\rightarrow I + R^+$
Interferent association	$I^+ + R$	$\rightarrow IR^+$
Interferent condensation	$I^+ + R$	$\rightarrow IR1^+ + R2$
Interferent fragmentation	$I^+ + R$	$\rightarrow I1^+ + I2 + R$
		$\rightarrow I1 + I2 + R^+$
		$\rightarrow I1^+ + I2^+ + R (R1 + R2^+)$
Analyte association/condensation	$A^+ + R$	$\rightarrow AR^+$
	$A^+ + R$	$\rightarrow AR1^+ + R2$

NB: I indicates an interferent, R is the reactive component, A is the analyte, 1 and 2 are fragments

In the laser ablation system, a dry aerosol is produced. The level of interferences, especially from oxides, is reduced when compared to a wet aerosol produced in SN-ICP-MS analysis. Contribution to polyatomic interference levels from H₂O in the sample matrix is generally lower, combined with reduced plasma RF power and shorter sampling depth. Regardless, elevated backgrounds in LA-ICP-MS are caused by trace impurities in the carrier gas, namely CO₂, N₂, H₂O and O₂. Several analytes which are particularly important for EBI experiments have significant interferences from polyatomic ions in laser ablation experiments. These are listed in Table 6-2.

Table 6-2: Important analytes for EBI analysis and their interferences

Analyte	Interfering Species
²⁴ Mg ⁺	¹² C ₂ ⁺
²⁵ Mg ⁺	¹² C ₂ H ⁺
⁴⁰ Ca	⁴⁰ Ar ⁺
⁴⁴ Ca ⁺	¹² C ¹⁶ O ₂ ⁺ , ¹⁴ N ₂ ¹⁶ O ⁺
⁵⁵ Mn ⁺	⁴⁰ Ar ¹⁴ NH ⁺
⁵⁶ Fe ⁺	⁴⁰ Ar ¹⁶ O ⁺
⁵⁷ Fe ⁺	⁴⁰ Ar ¹⁶ OH ⁺
⁸⁰ Se ⁺	⁴⁰ Ar ₂ ⁺

When selecting a reactive gas, one important consideration is the interaction of the gas with the analyte and the resulting reaction thermochemistry. For hydrogen, interfering species undergo one of three reaction chemistries [167];

- Hydrogen atom transfer: $\text{Ar}^+ + \text{H}_2 \rightarrow \text{ArH}^+ + \text{H}$
- Proton transfer: $\text{ArH}^+ + \text{H}_2 \rightarrow \text{H}_3^+ + \text{Ar}$
- Charge transfer: $\text{Ar}^+ + \text{H}_2 \rightarrow \text{H}_2^+ + \text{Ar}$

The reaction thermochemistry of each step defines whether the reaction proceeds, as in an exothermic reaction (ideally the reaction between gas and polyatomic species), or the reaction is forbidden or hindered, as in an endothermic reaction (reaction between gas and analyte). For example, NH₃, CO, H₂ and N₂ react rapidly with ArO⁺ and slowly with Fe⁺. These

reagents therefore can be used to chemically resolve $^{40}\text{Ar}^{16}\text{O}^+$ from $^{56}\text{Fe}^+$. H₂ is effective for removing ArO⁺-derivative interferences as flow rates increase [159]. However, beyond a certain point, total signal intensity decreases.

Hattendorf and Günther [162] were the first to examine the characteristics of the reaction cell with dry aerosol conditions common to LA. Comparison of NH₃ and H₂ as reactive gases showed that while NH₃ had a distinctively higher reaction rate than H₂, side reactions with analyte ions were severe and lead to increased interferences. It was reported that H₂, having a smaller reactivity, reduced cluster formation and retained analyte sensitivity, even at high concentration. H₂ is therefore better suited to short measurement times, like the transient signals observed in laser ablation. J.S. Becker [168] also found that there was a significant reduction in the $^{40}\text{Ar}^{16}\text{O}^+$ interference on $^{56}\text{Fe}^+$ when using hydrogen as the reaction gas. This also improved the limits of detection. Arnold *et al* [159] conducted an in depth study of the use of hydrogen as a reactive gas in a hexapole collision cell to reduce the plasma derived interferences $^{40}\text{Ar}^{16}\text{O}^+$ and $^{40}\text{Ar}^{16}\text{OH}^+$ that are isobaric with $^{56}\text{Fe}^+$ and $^{57}\text{Fe}^+$ respectively. They found that different H₂ flow rates affected the formation of $^{40}\text{Ar}^{16}\text{O}^+$ and $^{40}\text{Ar}^{16}\text{OH}^+$ differently and increasing the H₂ flow rate caused a decrease in the background equivalent concentrations of both masses. Hydrogen was consequently chosen as the reactive gas for these experiments and Table 6-3 outlines the experimental operational parameters used here.

Table 6-3: LA-ICP-MS operational parameters

Laser parameters	
x_s	30 μm
v_l	30, 60 and 90 $\mu\text{m s}^{-1}$
Line spacing (centre to centre)	30 μm
Laser energy output	$\approx 0.60 \text{ J cm}^{-2}$ (25%)
Frequency	20 Hz
ICP-MS parameters	
Reaction cell H ₂ flow rate	0.0, 1.0, 1.5, 2.0 and 3.0 mL min^{-1}
Monitored masses	13, 24, 25, 31, 39, 43, 44, 52, 53, 55, 56, 57, 59, 60, 63, 66, 80, 82
t_{sc}	0.3332 s
Dwell times for masses analysed	
m/z 13	0.010 s
m/z 24	0.005 s
m/z 25	0.006 s
m/z 31	0.005 s
m/z 39	0.010 s
m/z 43	0.010 s
m/z 44	0.010 s
m/z 52	0.020 s
m/z 53	0.020 s
m/z 56	0.016 s
m/z 57	0.090 s
m/z 59	0.010 s
m/z 60	0.020 s
m/z 63	0.020 s
m/z 66	0.010 s
m/z 80	0.010 s
m/z 82	0.020 s

6.4 Background levels of biologically relevant analytes

Data for a 10 second period prior to ablation of the tissue was collected to obtain a background signal for each m/z from the gas blank. The background signal for measured analytes is presented in Figure 6-3.

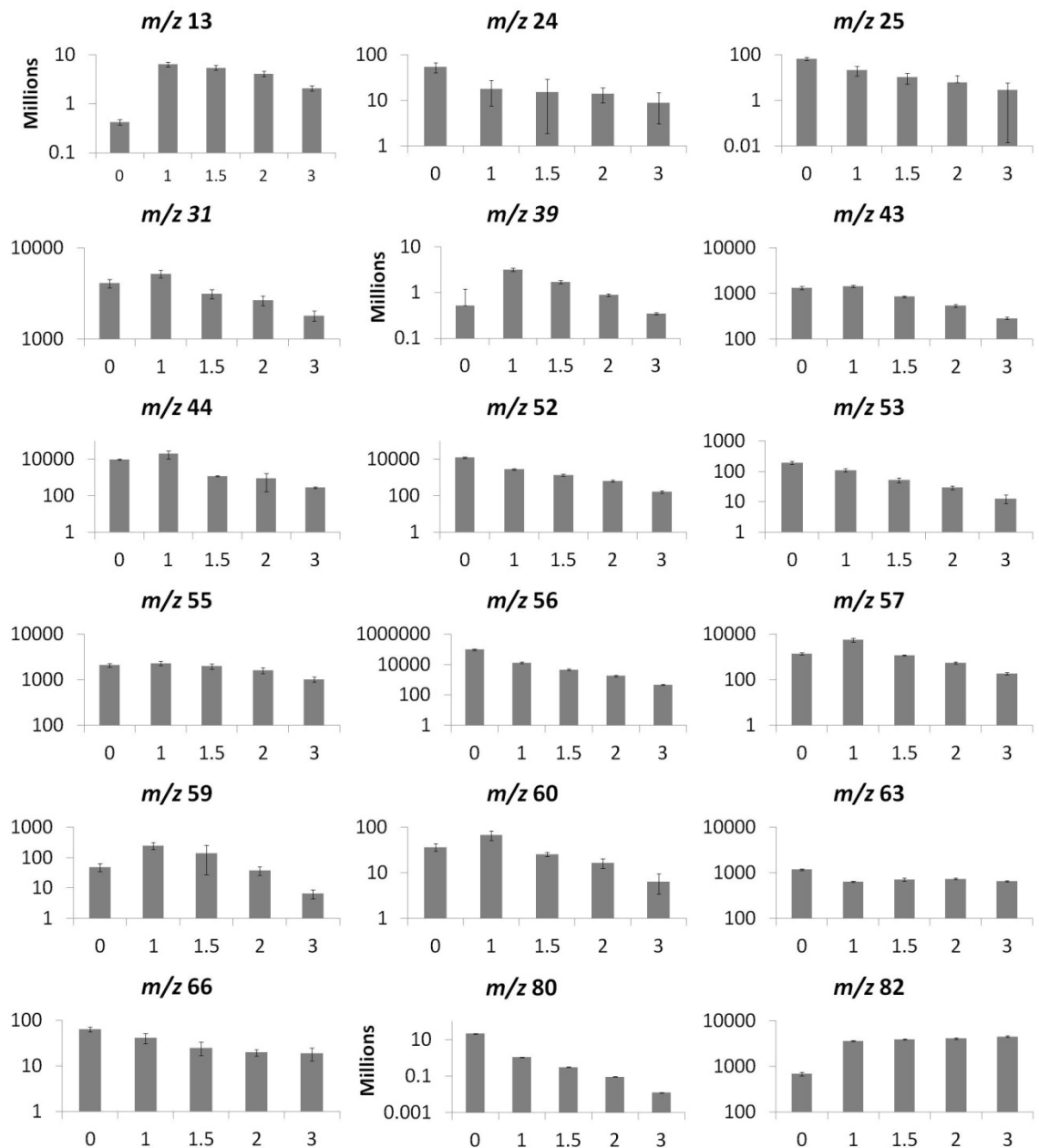
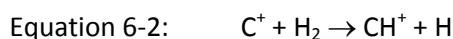


Figure 6-3: Comparison of background signals; Log₁₀ (counts per second) versus H₂ flow rate (mL min⁻¹)

There was an overall reduction in the background signal as the H₂ flow rate increased from 0.0 to 3.0 mL min⁻¹ for 16 out of the 18 masses analysed. Increasing H₂ flow rates elevates cell pressure, increasing the number of ion-molecule collisions. This transfers more energy from translation into internal energy, leading to an enhanced probability of dissociation and removal of the polyatomic interferences [158].

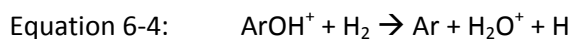
Increased background signals for *m/z* 13 and *m/z* 82 indicate an interfering isobaric product is produced in the reaction cell. The increase in the background signal for *m/z* 82 across all H₂ flow rates is most likely from continuous formation of ⁴⁰Ar₂H₂⁺ in the reaction cell [41]. The increase in *m/z* 13 is a consequence of the formation of ¹²CH⁺ from the reaction (Equation 6-2) [158].



Even though this reaction is endothermic, the reaction still proceeds. Unlike reactions in condensed phases, the rarified environment of the gas phase means that long-range attractive interactions between charged particles and molecules often overcome barriers associated with reactions in other environments such as the liquid matrices of SN-ICP-MS [158]. The efficiency of ¹²CH⁺ formation is increased by the relatively high abundance of ¹²C⁺ generated from CO₂ impurities in the plasma gas. At higher H₂ flow rates, the kinetic energy of the ion beam is reduced as it passes through the reaction cell, thus the efficiency of the fragmentation of ¹²CH⁺ improves and there is a gradual decrease in the background levels of *m/z* 13.

The initial increase in the background levels for *m/z* 57 at low H₂ flow rates were consistent with the observations of Arnold *et al* [159] when using hydrogen as a reactive gas in a

hexapole collision cell. Equation 6-3 sees the conversion of ArO⁺ to ArOH⁺ followed by its fragmentation shown in Equation 6-4.



ArOH⁺ is formed from the high abundance ArO⁺ in the plasma gas. Equation 6-3 has a low kinetic barrier to reaction and proceeds rapidly. Conversely, fragmentation of ArOH⁺ has a higher kinetic barrier to reaction, which explains the persistence of ArOH⁺ and the increase in *m/z* 57 at low H₂ flow rates. In much the same way as *m/z* 13, higher H₂ flow rates improve the fragmentation reaction efficiency. This produces an overall decrease in background signal intensity of *m/z* 57, and most other analytes, when the H₂ flow rate is equal to 3.0 mL min⁻¹.

The increase in background signal at a H₂ flow rate of 1.0 mL min⁻¹ for *m/z* 39 is likely caused by the formation of ³⁸ArH⁺ and its subsequent increased collisional fragmentation efficiency as the H₂ flow rate increases. Similar results were also observed for *m/z* 59 (⁴⁰Ar¹⁸OH⁺).

An initial increase in the background signal at low H₂ flow rates is also observed for ⁶⁰Ni. This is likely to be caused by a polyatomic interference of ⁴³Ca¹⁶O¹H⁺. This interference is not spectral and does not arise in the plasma gas but is rather caused by contamination either in the ablation cell or the tubing, highlighting the need to regularly maintain the instrument's cleanliness.

The use of the reaction cell shows little effect on ⁶⁶Zn and ⁶³Cu. These elements do not have significant spectral Ar-based interferences so the background is expected to remain fairly

constant. The slight decrease in the background is due to collisions with a small number of these atoms in the reaction cell.

A reduction in the background signal for each analyte reduced the need for normalisation of the data. The most influential factor on signal drift is the background signal of the analyte, especially for that of m/z 56. Because of the 14-fold increase in ¹³C signal intensity when using H₂ reaction gas, normalisation by ¹³C is impractical due to poor signal-to-noise ratios [9]. Normalisation with ¹³C also becomes less useful as the division of each data point by the ¹³C signal moves towards being a division of each data point with a constant. There is no difference between normalised and raw data at this stage.

6.5 Calibration using increasing volumes of hydrogen

Prepared matrix-matched tissue standards were used to construct calibration curves to determine the limits of analysis and sensitivity of analytes at varying H₂ flow rates. Calibration curves were prepared for x_s at 30 μm and v_l at 30, 60 and 90 $\mu\text{m s}^{-1}$ using H₂ flow rates of 0.0, 1.0, 1.5, 2.0 and 3.0 mL min^{-1} with the reaction mode off (H₂ gas valve closed) for 0.0 mL min^{-1} H₂.

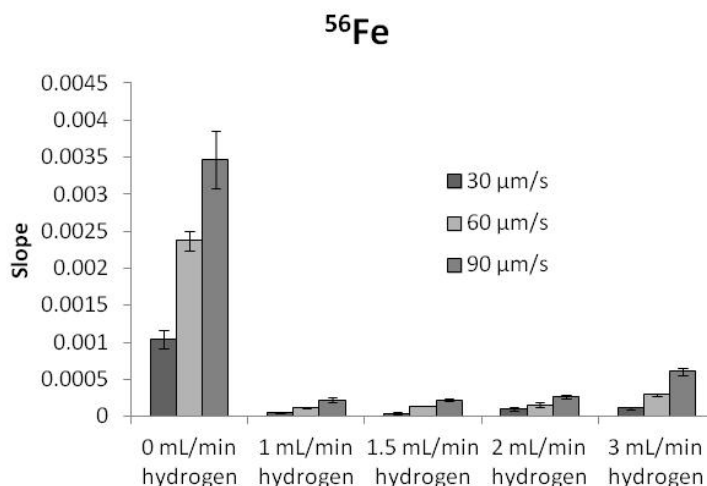


Figure 6-4: Comparison of the slope of calibration curves constructed for ⁵⁶Fe with increasing v_l and increasing H₂ flow rates in the reaction cell. ($x_s = 30 \mu\text{m}$)

As previously discussed in Chapter 4:, when t_{sc} remains constant, there is an increase in the slope of the calibration curve for increasing v_l as presented for ⁵⁶Fe in Figure 6-4. This was expected as the amount of material ablated per unit time increased as v_l increased, thus increasing the material being analysed by the ICP-MS, and increasing the sensitivity. Similar patterns were observed for all analytes. Because the slope increased as the limits of analysis decreased, only results for $v_l = 3 x_s s^{-1} = 90 \mu\text{m s}^{-1}$ are discussed below.

6.5.1 Limits of analysis

As expected there is an overall improvement in the limits of analysis for each analyte as H₂ flow rate increases (Figure 6-5). The decreased LODs and LOQs are most prevalent for analytes suffering high background signals under normal ‘no gas’ conditions, including ⁵⁶Fe and ⁴⁴Ca. A more than tenfold reduction in the LOD and LOQ was observed for both ⁵⁶Fe and ⁴⁴Ca. Improved limits of analysis effectively mean the influence of the background signal on the analytes has been reduced. A moderate H₂ flow rate (3 mL min⁻¹) shifted ⁵⁶Fe and ⁴⁴Ca LODs and LOQs from above or within the calibration range to equal to or below the lowest

concentration tissue standard (Figure 6-6). Limits of analysis were greater at low H₂ flow rates for ⁵⁷Fe and ⁵⁹Co due to ArOH⁺ formation outlined previously.

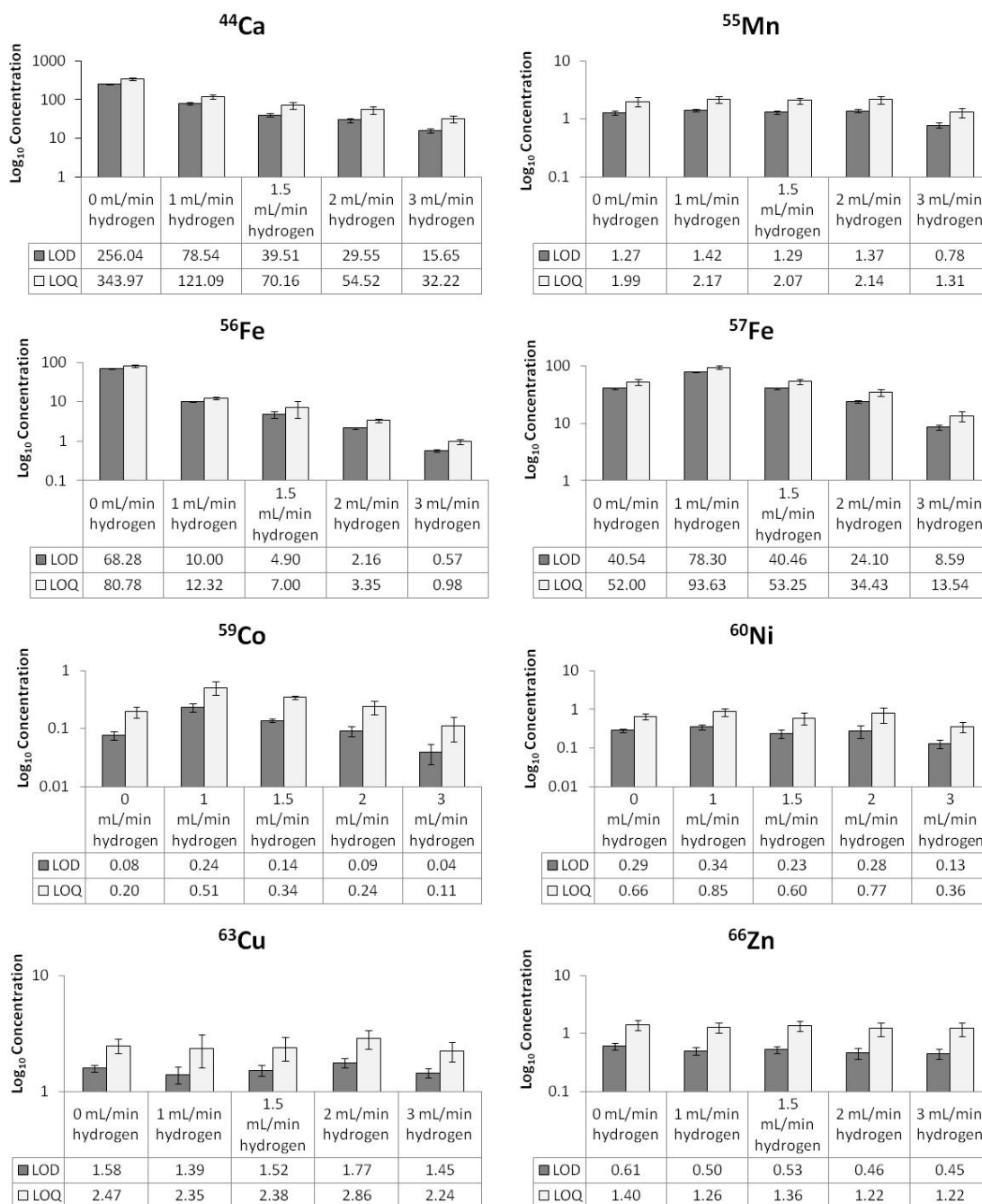


Figure 6-5: Limits of analysis ($\mu\text{g g}^{-1}$) for calibrated analytes with increasing H₂ flow rates in the reaction cell ($x_s = 30 \mu\text{m}$, $v_1 = 90 \mu\text{m s}^{-1}$)

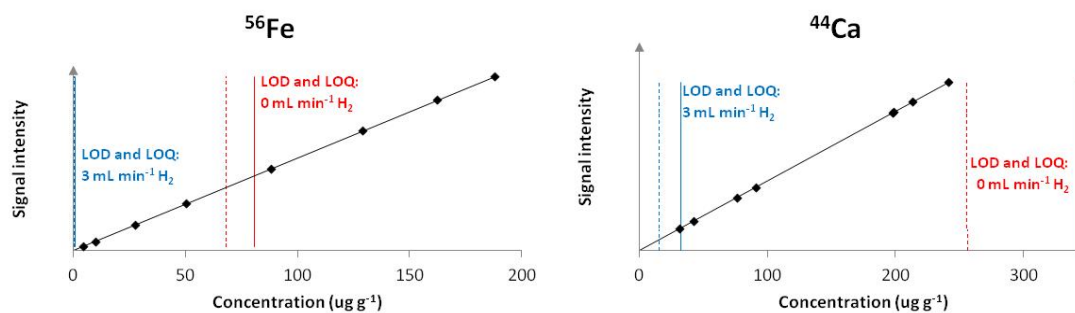


Figure 6-6: Comparison of the LODs (dashed lines) and LOQs (solid lines) for ⁵⁶Fe and ⁴⁴Ca for H₂ flow rates of 0 (red) and 3 mL min⁻¹ (blue) against the concentrations of the calibration standards

The influence of the background signal on the limits of analysis is also noticeable for ⁵⁷Fe and ⁵⁹Co. The initial increase in the limits of analysis at 1.0 mL min⁻¹ is directly related to the same increases seen in the background signals at these masses for the reasons described *supra* in Section 6.4.

6.5.2 Sensitivity

Another consequence of decreasing background signals is an increase in signal (per µg g⁻¹) to noise ratios (SNR) (Figure 6-7). Higher SNRs are beneficial as the influence on the signal from background noise is reduced. The initial decrease in the SNR for ⁵⁷Fe and ⁵⁹Co is again directly related to the increase in background signal from ArOH⁺ derivatives. A general upward trend in the SNR was observed for all analytes as the H₂ flow rate was increased to 3.0 mL min⁻¹.

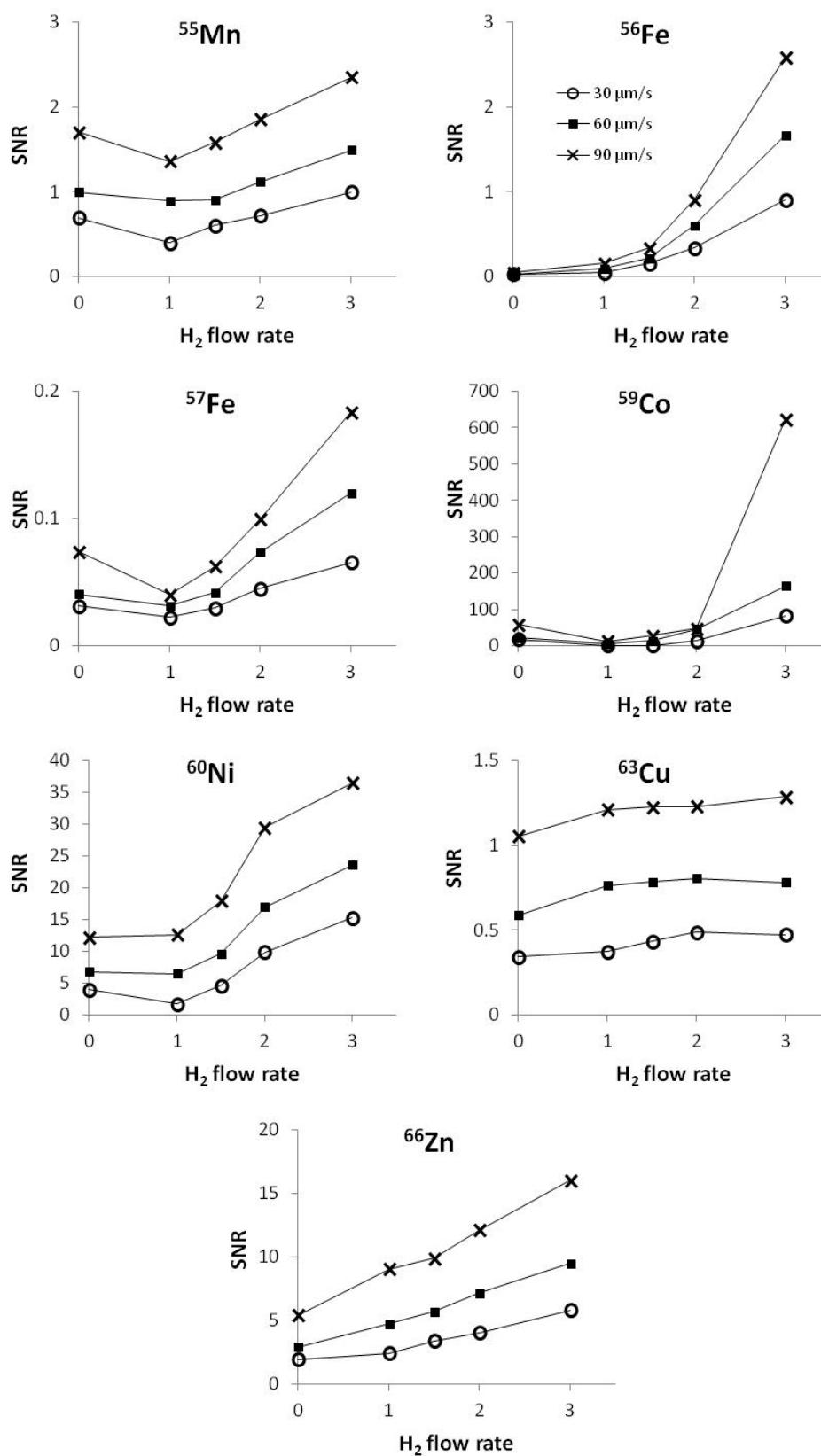


Figure 6-7: Signal (per $\mu\text{g g}^{-1}$) to noise ratios (SNR) for the calibrated analytes with increasing H_2 flow rates and increasing ν . ($x_s = 30 \mu\text{m}$, $\nu = 30$ [○], 60 [■] and 90 $\mu\text{m s}^{-1}$ [×]).

6.6 Imaging using increasing volumes of hydrogen

Representative mouse brain sections at similar stereotaxic coordinates from the same brain were imaged to test the applicability of the use of the reaction cell on imaging experiments. Brain sections were sourced from adult wild-type mice prepared by the Mental Health Research Institute (MHRI), Victoria, Australia. All methods conformed to the Australian National Health and Medical Research Council published code of practice for animal research and was approved by the University of Melbourne Animal Ethics Committee. One hemisphere of each brain was sectioned at 30 μm and mounted on microscope slides.

Five brain sections were ablated using x_s at 30 μm and v_l at 90 $\mu\text{m s}^{-1}$. A $t_{sc} = 0.3332$ s was chosen in order to maintain the relative dimensions of the sample. Each brain section was analysed using separate H₂ flow rates in the reaction cell, namely 0.0, 1.0, 1.5, 2.0 and 3.0 mL min⁻¹. Quantification was performed using matrix-matched tissue standards. A new calibration curve was constructed for every change in H₂ flow rate allowing comparison of images on the same scale.

The improvement in image quality with increasing H₂ flow rate is depicted in Figure 6-8. Concentrations and regional distributions for ⁵⁶Fe and ⁵⁷Fe are essentially identical at 3.0 mL min⁻¹ H₂, indicating that contribution from polyatomic interferences has been removed. ⁵⁷Fe can be comparatively problematic to image. This is due to its relatively low isotopic abundance when compared to ⁵⁶Fe (2.1 % versus 91.8 % natural abundance). Imaging ⁵⁷Fe showed benefit from reduced background signal in the same manner as ⁵⁵Mn. From H₂ flow rates of 0.0 mL min⁻¹ to 1.5 mL min⁻¹ the signal was inflated by additional ⁴⁰Ar¹⁶OH⁺ and there was no discernable contrast in the image. Background subtraction removed almost all analytical data, demonstrated by elevated LOD and LOQ. At 3.0 mL min⁻¹, the influence of

background signal intensity is mitigated and vastly improved contrast (comparable to ⁵⁶Fe) is observed.

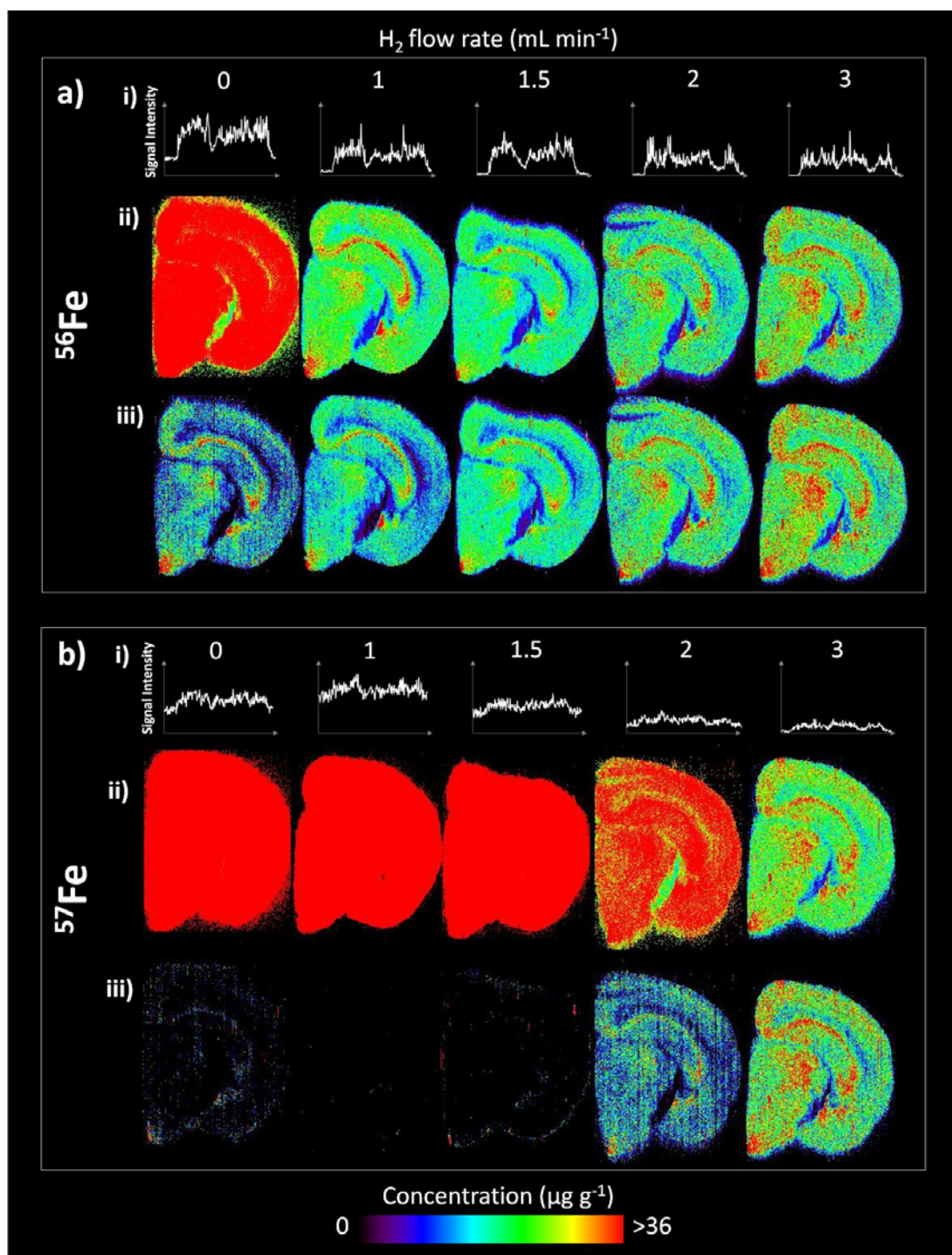


Figure 6-8: Comparison of iron imaged with increasing H₂ flow rates

a) ⁵⁶Fe b) ⁵⁷Fe; i) graphs showing the representative enhanced signal intensities when a high background is observed, resulting in inflated concentrations ii) images representing iron prior to background removal iii) images showing the effect of background subtraction on the image.
($x_s = 30 \mu\text{m}$, $v_1 = 90 \mu\text{m s}^{-1}$)

The benefit of using H₂ in the reaction cell is also demonstrated by the improved image quality of ⁵⁵Mn (Figure 6-9). The concentration range of ⁵⁵Mn is relatively low (approximately 0 - 2 $\mu\text{g g}^{-1}$), thus background signal intensity has a substantial effect on the image quality. The reduction in the background signal improved the image contrast and allowed visualisation of the concentration range.

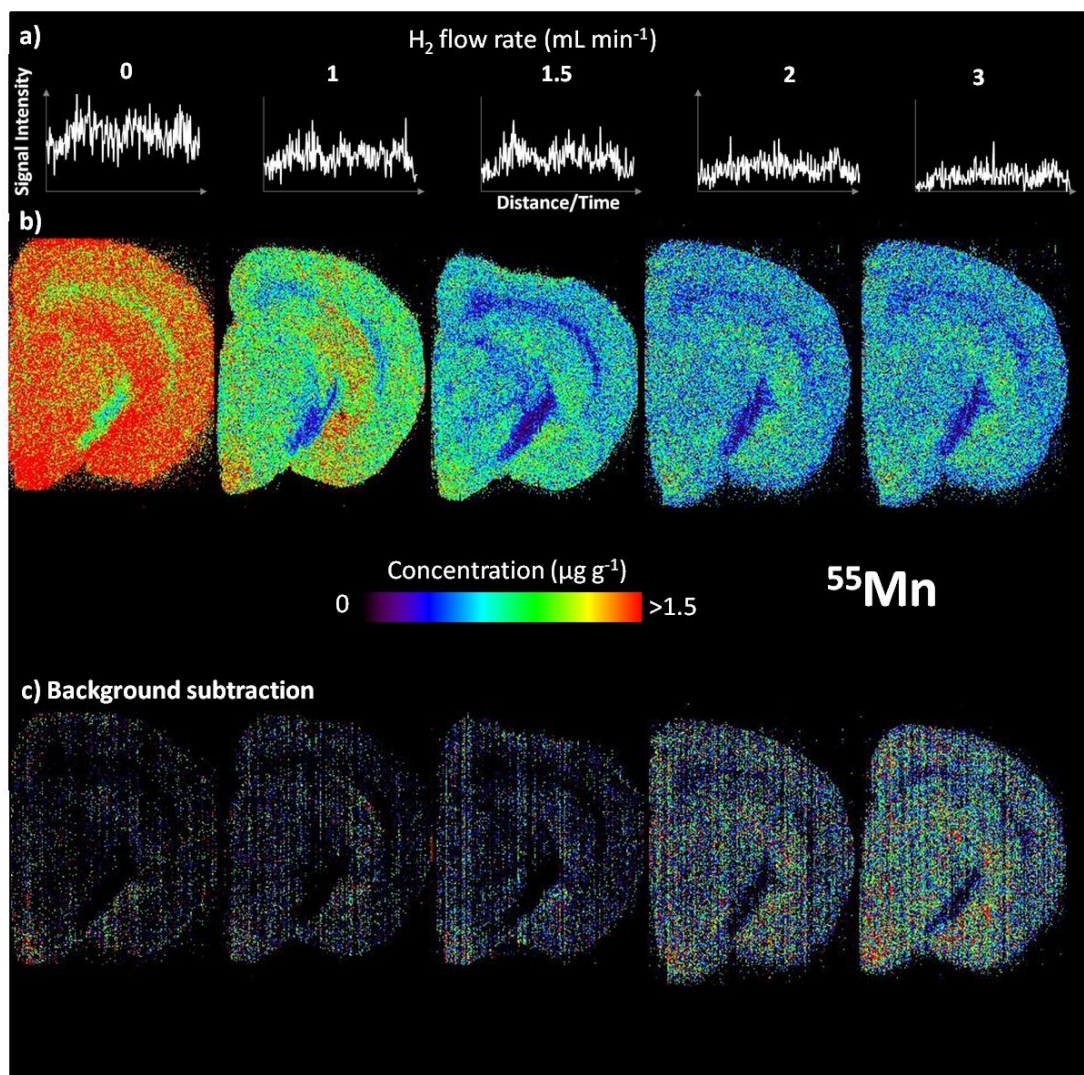


Figure 6-9: Comparison of ⁵⁵Mn imaged with increasing H₂ flow rates

a) graphs showing the representative enhanced signal intensities when a high background signal is observed, resulting in inflated concentrations b) images representing ⁵⁵Mn prior to background removal c) images showing the effect of background subtraction on the resulting image. ($x_s = 30 \mu\text{m}$, $v_1 = 90 \mu\text{m s}^{-1}$)

Unexpectedly, the images for ⁶³Cu showed a decrease in background signal as the H₂ flow rate increased. The likely cause of the higher background levels is a contamination in the instrument. There is an hypothesised spectral Ar-based interference of ³⁶Ar¹²C¹⁴NH⁺ [169] however a signal for *m/z* 67, representing the polyatomic containing the major isotope of Ar (⁴⁰Ar¹²C¹⁴NH⁺), was not observed in the background signal. ⁴⁰Ar²³Na⁺ is another polyatomic interference for *m/z* 63 however it is also unlikely to be the cause of the problem as analysis of the Na-rich NIST glass does not have a proportional effect on increasing the signal of *m/z* 63. Energy and physical processes also govern the interference removal for the majority of this interference [170]. The *m/z* 63 background signal is effectively halved which does not support findings that the overall signal suppression without removal of interferences is around 10 % when using the reaction mode because of ion scattering [171]. The likely cause of the higher background levels is a contamination in the instrument during acquisition. H₂ would be able to remove an unknown interference either by reaction or collisional fragmentation if the conditions were favourable [155]. Further investigation into the cause of the *m/z* 63 signal suppression is required.

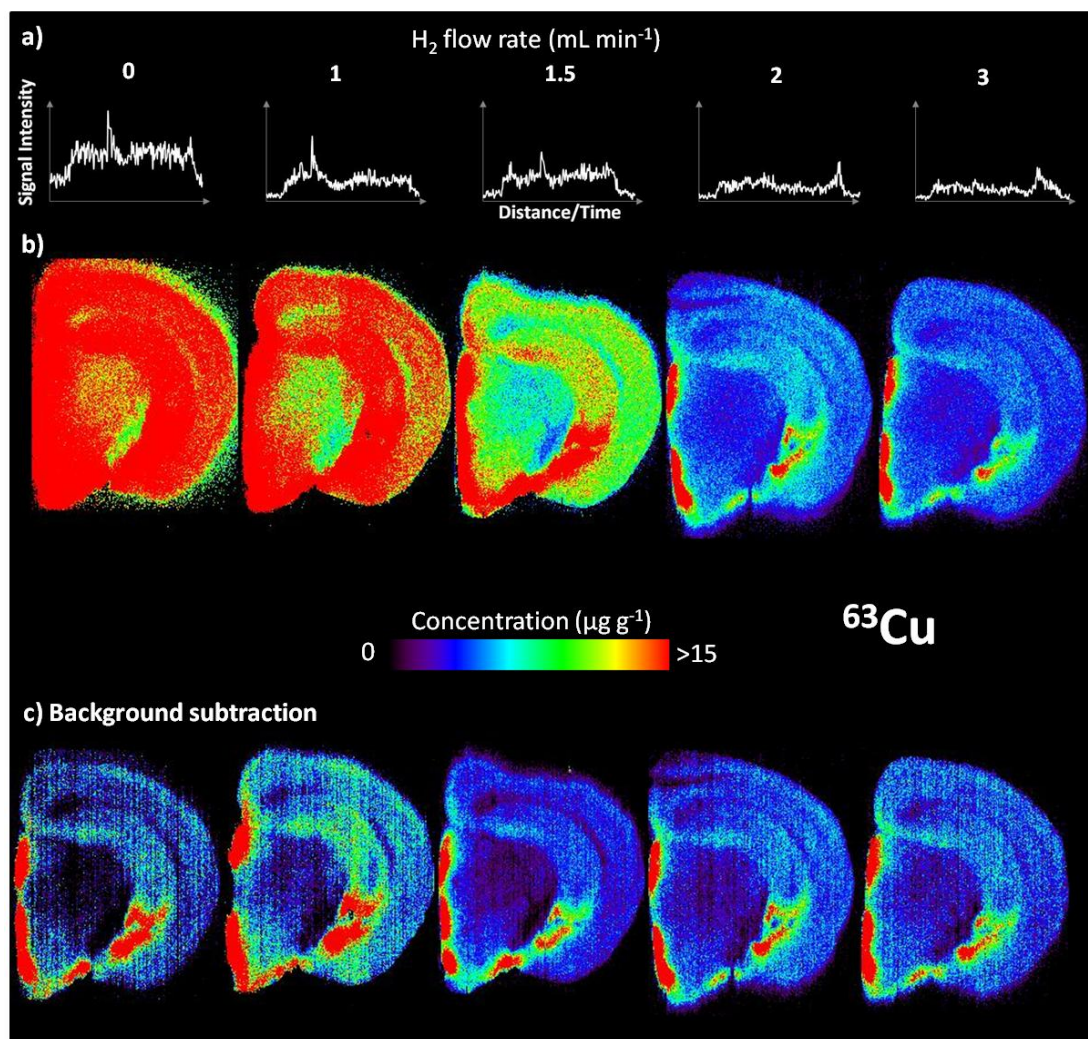


Figure 6-10: Comparison of ^{63}Cu imaged with increasing H_2 flow rates

a) graphs showing the representative enhanced signal intensities when a high background signal is observed, resulting in inflated concentrations b) images representing ^{63}Cu prior to background removal c) images showing the effect of background subtraction on the resulting image. ($x_s = 30 \mu\text{m}$, $v_1 = 90 \mu\text{m s}^{-1}$)

⁶⁶Zn does not possess any spectral interferences. Significant Ar-, O- or N-based polyatomic species are not predicted at this mass, thus increasing H₂ flow rates did not significantly alter already low background signal intensities. Even though a decrease in signal intensity was observed with reaction mode engaged, the image quality for ⁶⁶Zn was not adversely affected (Figure 6-11).

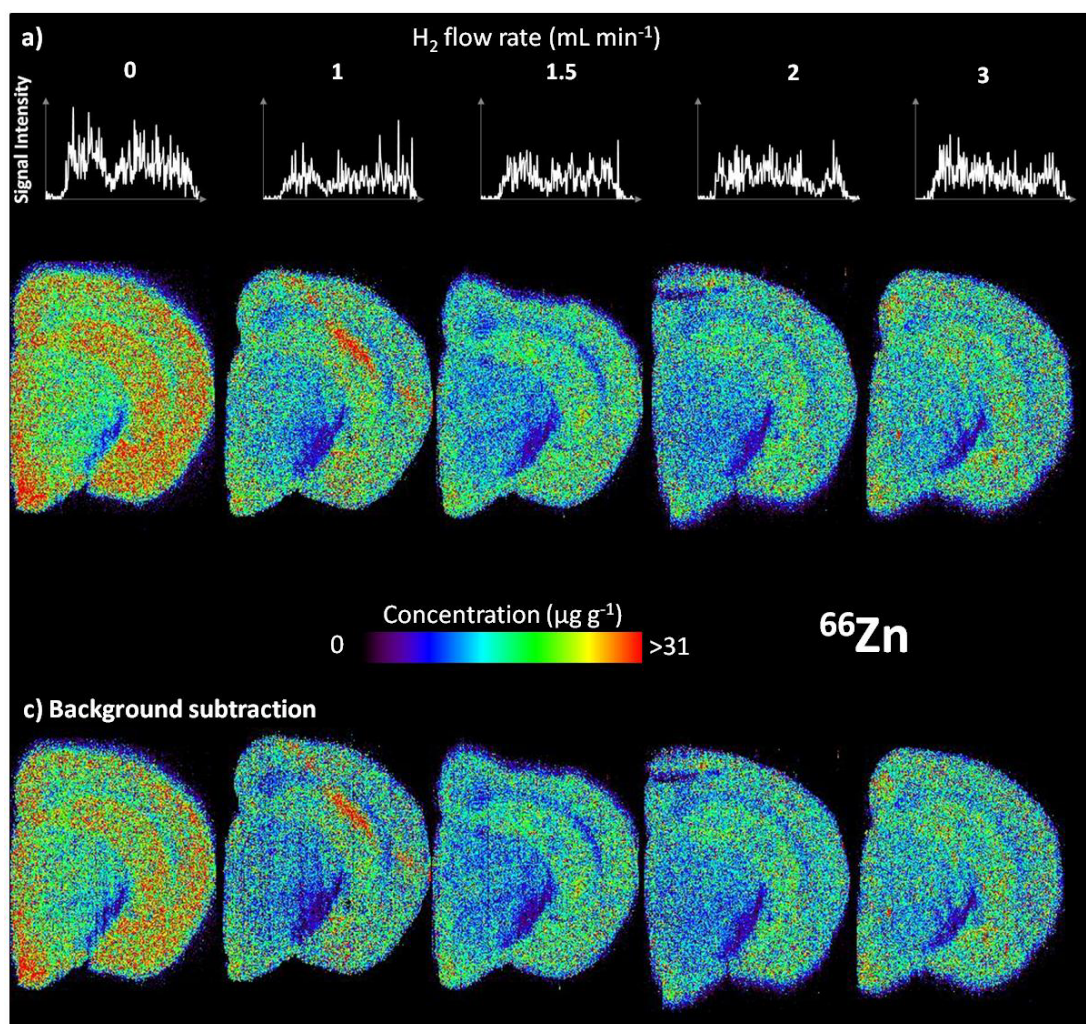


Figure 6-11: Comparison of ⁶⁶Zn imaged with increasing H₂ flow rates

a) graphs showing the representative enhanced signal intensities when a higher background signal is observed, resulting in inflated concentrations b) images representing ⁶⁶Zn prior to background removal c) images showing the effect of background subtraction on the resulting image. ($x_s = 30 \mu\text{m}$, $v_1 = 90 \mu\text{m s}^{-1}$)

6.7 Conclusions

Hydrogen reaction gas is a useful means for reducing the inherent polyatomic interferences in LA-ICP-MS for biologically relevant elements. Using a moderate H₂ flow rate of 3.0 mL min⁻¹, a significant decrease in analyte background levels, decrease in the limits of analysis, increase in signal to noise ratios, and increase in image quality was observed for several measured masses. No detrimental effects were observed for the analytes imaged, indicating all imaged masses can be analysed simultaneously under the same analytical conditions.

The formation of new interfering species was observed for some masses of interest. New interferences were also observed for ⁵⁷Fe, ⁵⁹Co and ⁶⁰Ni at lower H₂ flow rates, though these interferences are reduced overall with the use of 3.0 mL min⁻¹ H₂. Elevated backgrounds were observed for ¹³C and ⁸²Se.

An improvement in resultant image quality was also observed for a H₂ flow rate of 3.0 mL min⁻¹. A reduction in the background signal has resulted in the influence of background subtraction being negligible for all imaged elements. The improvement was most notable for ⁵⁶Fe and ⁵⁷Fe where the H₂ flow rate of 3.0 mL min⁻¹ produced images of almost identical concentration and contrast not previously observed. The interference removal observed in the images for *m/z* 63 requires further investigation. The use of H₂ did not alter the already low background signal intensities for ⁶⁶Zn and minimal differences in the images for ⁶⁶Zn are observed. This indicates that no imaged masses are adversely affected by the use of the reaction cell with a H₂ flow rate of 3.0 mL min⁻¹.

***Chapter 7: High resolution
imaging employing H₂ reactive
gas***

Chapter 7: High resolution imaging employing H₂ reactive gas

7.1 Chapter outline

The concentration of iron in the substantia nigra (SN) is an important factor for Parkinson's disease research. There is a need to increase the resolution of images prepared using LA-ICP-MS in order to observe fine detail in the mouse brains. High resolutions also ensure EBI remains at the forefront of trace element imaging technology.

Difficulties in the analysis of ⁵⁶Fe and ⁵⁷Fe without the use of the reaction cell mean that analytically valid data is difficult to obtain as high background levels mean detection limits and limits of quantification are often above the experimental concentration range, as discussed in Chapter 6. The improvement in the background signals for these analytes means the detection limits are lower, and a signal above background levels is observed. This also implies that the determination of iron in samples at higher resolutions is possible.

Combining the use of the reaction cell with increased image acquisition speeds resulted in a high quality image of the area of the brain including the SN with a resolution of 6 μm x 6 μm for ⁵⁶Fe.

Accompanying Publication:

Lear, J., Hare, D., Fryer, F., Adlard, P., Finkelstein, D., & Doble, P. (2012). High-resolution elemental bio-imaging of Ca, Mn, Fe, Co, Cu and Zn employing LA-ICP-MS and hydrogen reaction gas. *Analytical Chemistry*. DOI: 10.1021/ac301156f [146]

7.2 Parkinson's disease and the substantia nigra

Parkinson's disease (PD) is a chronic progressive neurodegenerative disorder of insidious onset. Physical symptoms of the disease include bradykinesia, rest tremor, rigidity and postural disturbances, and late-onset motor symptoms such as speech and swallowing difficulties [172-180].

Parkinson's disease occurs globally with a crude incidence rate of 4.5 to 19 per 100 000 population per year, however prevalence has also been reported at more than 300 per 100 000 population per year. The variation in the estimate is likely due to differences in methodology and case ascertainment along with differences in the age distribution of the sample population as age is a key factor in the development of PD [172; 181].

The pathophysiology of PD involves the progressive loss of dopamine containing neurons within the pars compacta of the substantia nigra (SN). This leads to the nerve supply of the nigrostriatal tract being cut off and a significant reduction of the neurotransmitter dopamine in the striatum region of the brain. Genetic factors in combination with environmental factors are thought to be responsible for the cellular changes which lead to neuronal degeneration. Mitochondrial dysfunction, oxidative stress and failure of protein degradation mechanisms at the cellular level are thought to be involved in the diseases pathogenesis. The pathological indication of PD is the presence of Lewy bodies in surviving dopaminergic neurons. [172-180]

Neuronal death in PD may be triggered by oxidative stress caused by excess iron available for the Fenton reaction (see Chapter 5, Equation 5-1). Recent evidence suggests that there is a significant increase in the total iron concentration in the Parkinsonian SN when compared to control SN [1; 10; 172-180]. Because of these findings, quantitative imaging of the SN is a

benefit to further research into the mechanism and treatment of PD. A previous study by Hare *et al.* imaged the SN with x_s equal to $12\ \mu\text{m}$ [10]. With the use of the reaction cell, these experiments aimed to increase resolution and image the SN (Figure 7-1) with x_s equal to $6\ \mu\text{m}$.

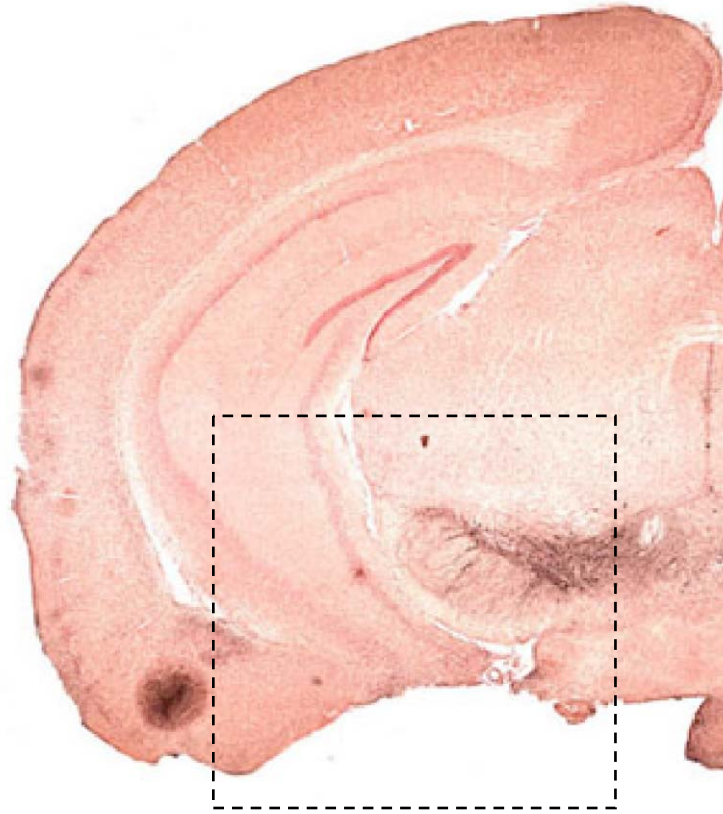


Figure 7-1: Immunohistochemical stain of the right side of a section of mouse brain [1]. The area outlined corresponds to the area containing the SN. The area in the square represents an example of the area analysed in this experiment.

7.3 Imaging iron at high resolution

The lower half of two consecutive sections of brain containing the iron-rich substantia nigra (compacta and reticulata) [7] were imaged. One section was analysed at H₂ flow rate of 0.0 mL min⁻¹ with reaction mode off and the other was analysed at H₂ flow rate of 3.0 mL min⁻¹. A new calibration curve was constructed for each H₂ flow rate.

The volume of H₂ gas used was the optimal level of H₂ required to significantly improved the detection limits, SNR, background signal and image quality, as determined in Chapter 6. The preparation of the images also applied those techniques outlined in Chapter 4 whereby equivalent image dimensions to the original brain section were maintained and the image acquisition speed was increased as per Equation 4-1. The operational parameters for this experiment are outlined in Table 7-1.

Table 7-1: LA-ICP-MS operational parameters

Laser parameters	
x_s	6 μm
v_l	16 $\mu\text{m s}^{-1}$
Line spacing (centre to centre)	6 μm
Laser energy output	$\approx 1.0 \text{ J cm}^{-2}$ (35%)
Frequency	20 Hz
ICP-MS parameters	
Reaction cell H ₂ volume	0 mL min ⁻¹ and 3.0 mL min ⁻¹
Monitored masses	13, 31, 56, 57, 63, 66, 197
t_{sc}	0.3772 s
Dwell times for masses imaged	
m/z 13	0.010 s
m/z 31	0.010 s
m/z 56	0.080 s
m/z 57	0.100 s
m/z 63	0.060 s
m/z 66	0.050 s
m/z 197	0.050 s

7.3.1 Images

The effectiveness of H₂ for producing high-resolution images is depicted in Figure 7-2 to Figure 7-4, showing a comparison of the images produced using the reaction cell operating at 3.0 mL min⁻¹ H₂ and operating under standard conditions without the reaction cell.

In Figure 7-2, the graphical depictions of the signal intensities show a significant drop in signal as H₂ removes the spectral interference of ⁴⁰Ar¹⁶O⁺. The SNR has improved for the 3.0 mL min⁻¹ H₂ image and definitive changes in signal intensity related to changes in ⁵⁶Fe concentration are observed. The iron rich area of the substantia nigra is still visible in the 0.0 mL min⁻¹ H₂ image but there is poor definition with surrounding regions. Acquisition of a high resolution image for ⁵⁶Fe using a H₂ flow rate of 3.0 mL min⁻¹ is possible and shows significant contrast and detail not present in the image constructed without the use of the reaction cell. This has allowed the visualisation of iron distribution approaching the low- μ m dimensions single cells of the mouse brain.

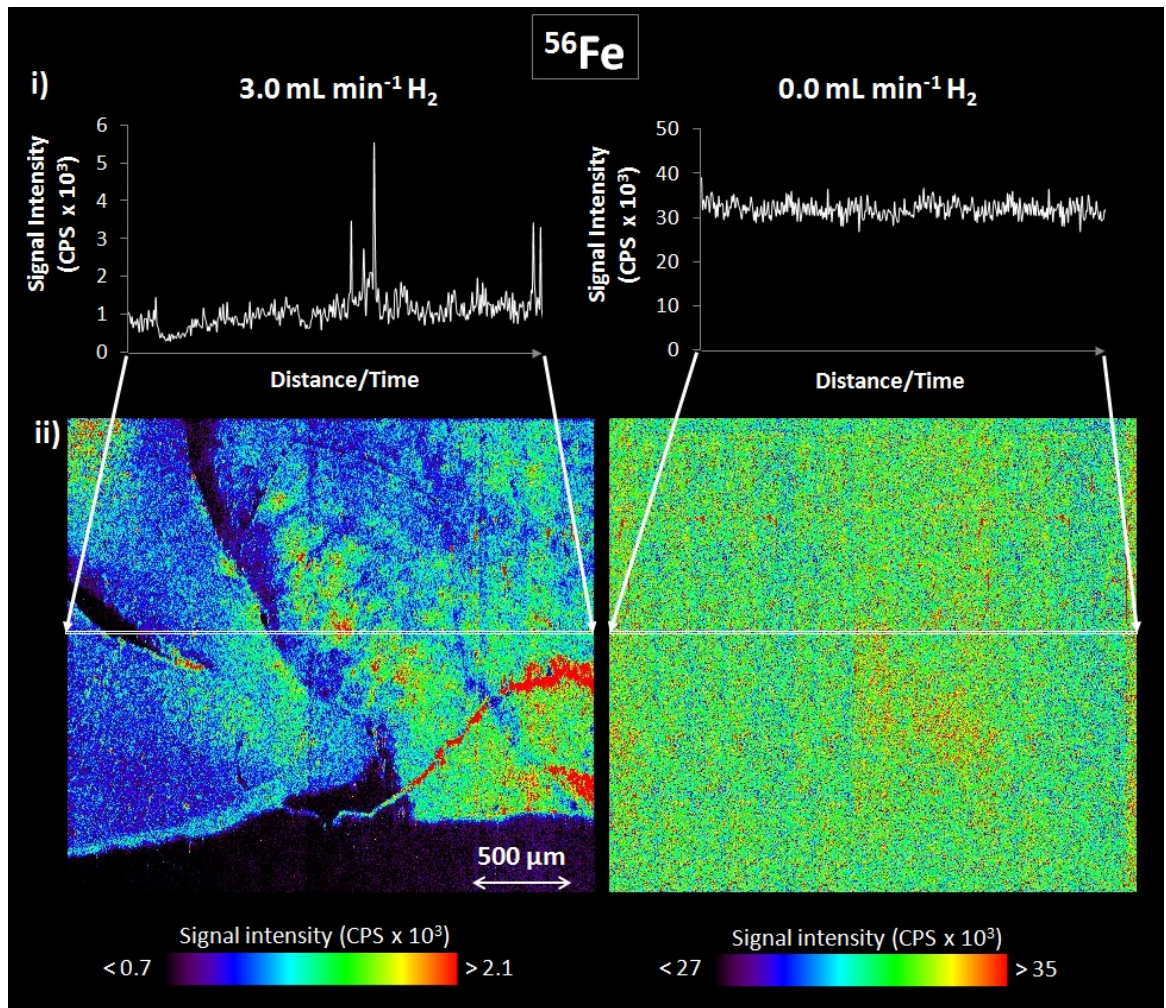


Figure 7-2: ⁵⁶Fe image of the lower left quarter of a mouse brain containing the substantia nigra
 i) signals ($\mu\text{g g}^{-1}$) for the highlighted row of pixels; ii) images for H₂ flow rates of 3.0 (left) and 0.0 (right) mL min⁻¹ ($x_s = 6 \mu\text{m}$; $v_l = 16 \mu\text{m s}^{-1}$)

Figure 7-3 shows the comparison between H₂ flow rates for ⁶³Cu. While images were achieved for both H₂ flow rates, there is an improvement in the contrast for the image prepared with a H₂ flow rate of 3.0 mL min⁻¹. The left hand side of the 3.0 mL min⁻¹ H₂ image shows much more detail in the ⁶³Cu distribution than the 0.0 mL min⁻¹ H₂ image. The change in signal intensity between the gas flow rates supports the results for ⁶³Cu from Chapter 6: 6.

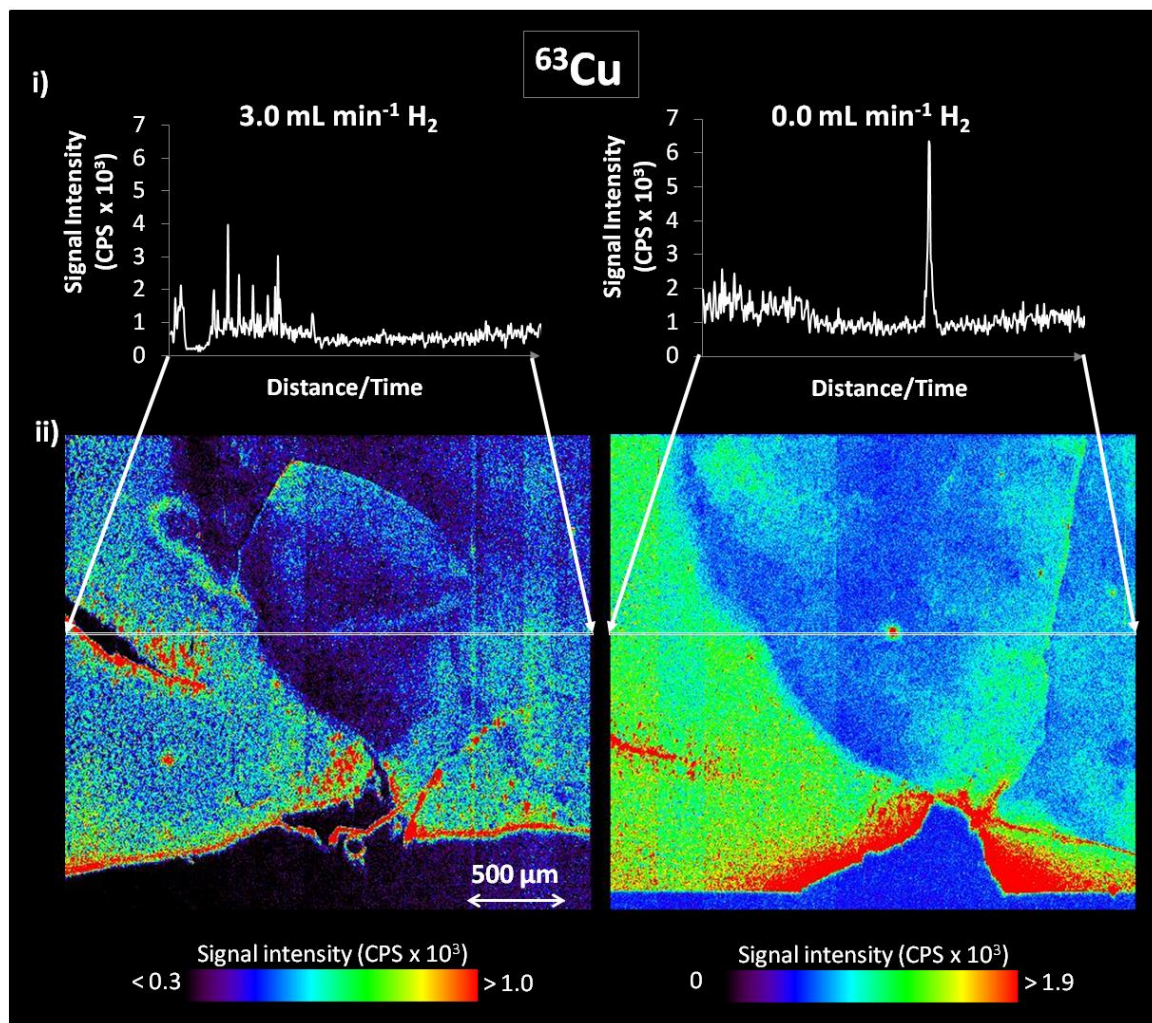


Figure 7-3: ⁶³Cu image of the lower left quarter of a mouse brain containing the substantia nigra

i) signals ($\mu\text{g g}^{-1}$) for the highlighted row of pixels; ii) images for H₂ flow rates of 3.0 (left) and 0.0 (right) mL min⁻¹ ($x_s = 6 \mu\text{m}$; $v_l = 16 \mu\text{m s}^{-1}$)

The images for ⁶⁶Zn at both H₂ flow rates are similar. As with ⁶³Cu, there has been a reduction in the signal intensity however contrast has not been altered upon addition of 3.0 mL min⁻¹ H₂. The reduction in sensitivity by using a small x_s has resulted in noisy images.

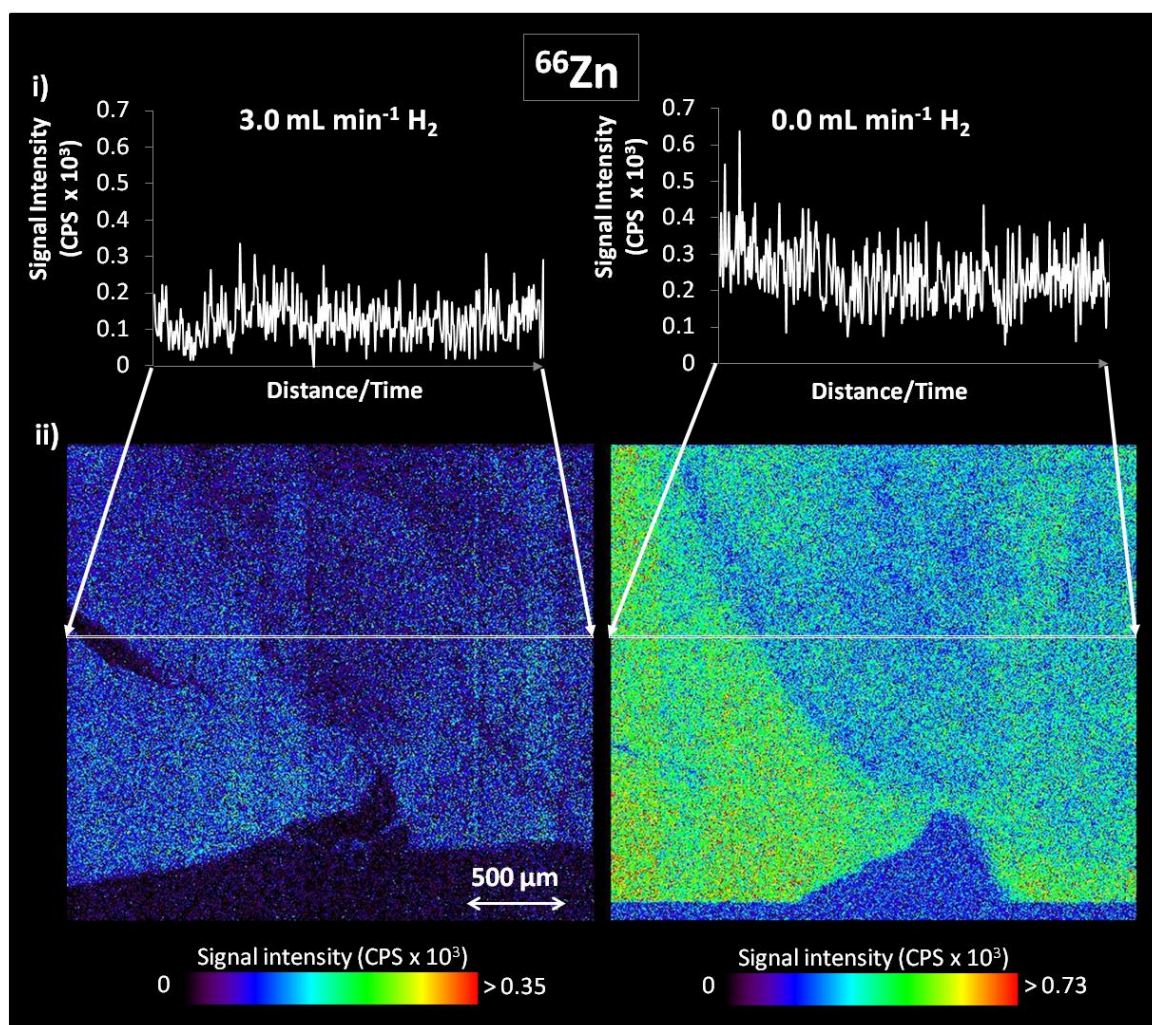


Figure 7-4: ⁶⁶Zn image of the lower left quarter of a mouse brain containing the substantia nigra
 i) signals ($\mu\text{g g}^{-1}$) for the highlighted row of pixels; ii) images for H₂ flow rates of 3.0 (left) and 0.0 (right) mL min⁻¹ ($x_s = 6 \mu\text{m}$; $v_l = 16 \mu\text{m s}^{-1}$)

7.3.2 Calibration

The statistics for the calibration of ⁵⁶Fe, ⁶³Cu and ⁶⁶Zn are outlined in Table 7-2. The linearity and detection limits are comparable to those results obtained for 30 μm resolution outlined in Chapter 6. The detection limits are higher than those for x_s equal to 30 μm using 3 mL min⁻¹ H₂ in the reaction cell. This is expected as the analytical signal is lower and there is a reduction in relative sensitivity. Compared to the calibration statistics for an H₂ flow rate of 0.0 mL min⁻¹ for x_s equal to 6 μm (Table 7-3), there is a notable improvement in the quality of the quantification data, especially for ⁵⁶Fe.

Table 7-2: Calibration statistics for isotopes with the use of reaction cell at 3.0 mL min⁻¹ H₂, $x_s = 6 \mu\text{m}$; $v_l = 16 \mu\text{m s}^{-1}$

	Isotope		
	⁵⁶ Fe	⁶³ Cu	⁶⁶ Zn
Slope ± 95% confidence interval	23.58 ± 1.57	25.79 ± 1.47	4.85 ± 0.65
Intercept ±95% confidence interval (CPS)	584.2 ± 165.8	254.8 ± 39.7	114.6 ± 31.4
Correlation coefficient - r^2	0.9956	0.9978	0.9881
Detection limit ± 95% confidence interval (μg g ⁻¹)	1.29 ± 2.82	1.32 ± 1.74	10.28 ± 10.78
Average background signal ± 95% confidence interval (CPS)	533 ± 66.5	234 ± 44.7	100.4 ± 52.2
BEC (μg g ⁻¹)	-2.17	-0.81	-2.93

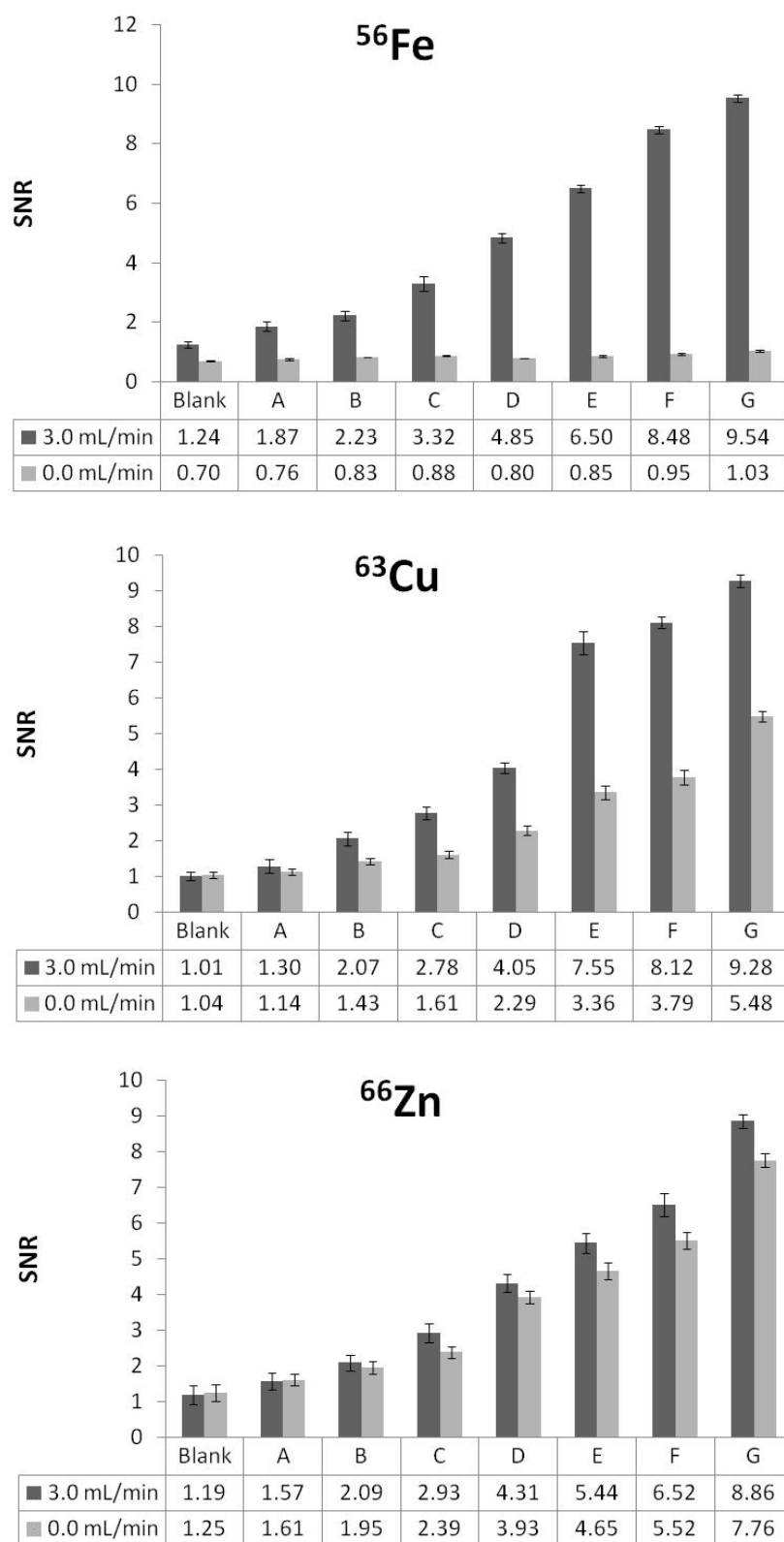
NB: BEC is the influence of the background signal intensity on the measured signal. A negative BEC is a result of the intercept being greater than the background signal.

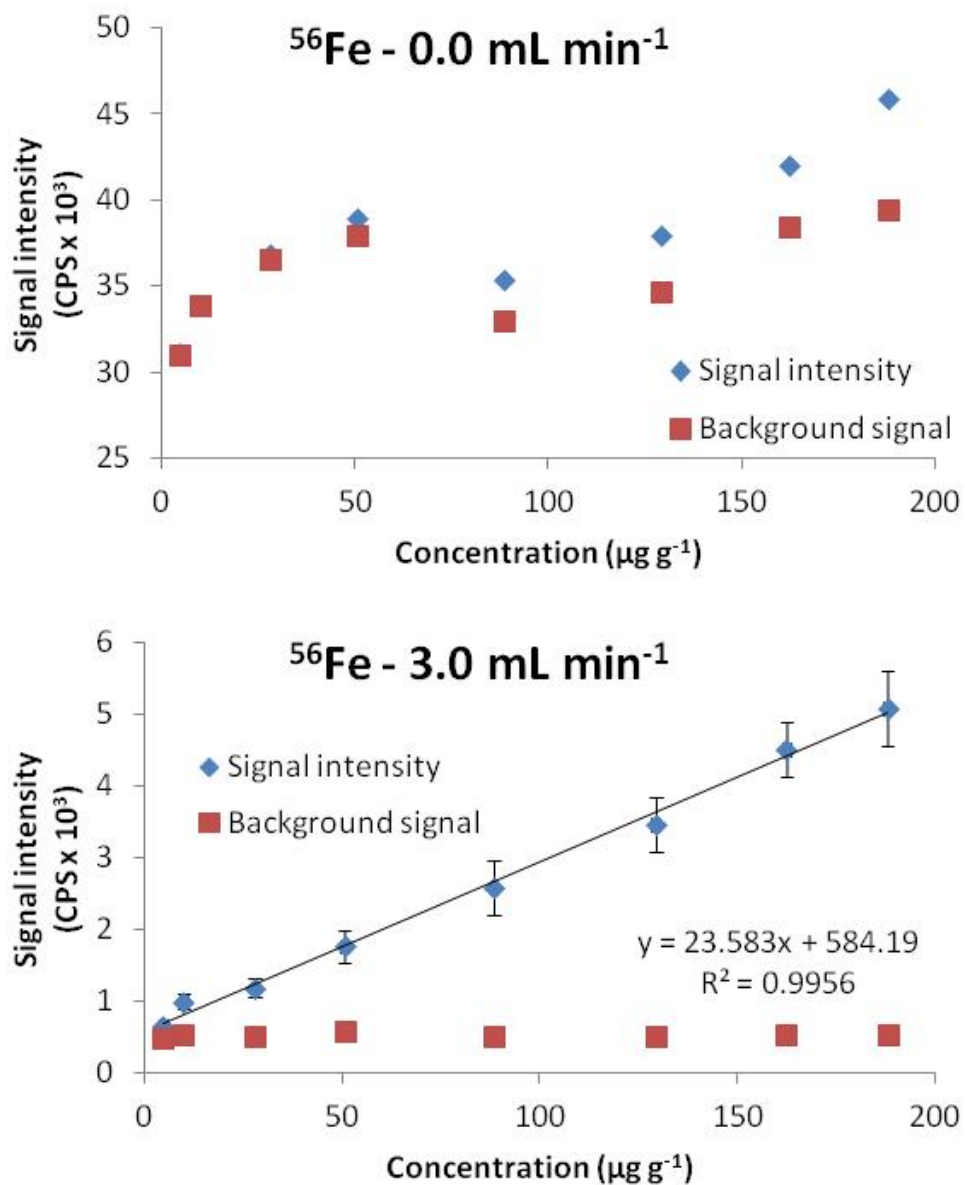
Table 7-3: Calibration statistics for isotopes with the use of reaction cell at 0.0 mL min⁻¹ H₂, x_s = 6 μm; v_l = 16 μm s⁻¹

	Isotope		
	⁵⁶ Fe	⁶³ Cu	⁶⁶ Zn
Slope ± 95% confidence interval	56.96 ± 32.38	23.45 ± 3.07	5.42 ± 0.91
Intercept ± 95% confidence interval (CPS)	33066 ± 3429	651.4 ± 83.3	162.4 ± 44.0
Correlation coefficient - r ²	0.7554	0.9886	0.9815
Detection limit ± 95% confidence interval (μg g ⁻¹)	248 ± 39.9	2.13 ± 3.720	8.82 ± 10.9
Average background signal ± 95% confidence interval (CPS)	44389 ± 2268	594 ± 87.2	137.8 ± 59.1
BEC (μg g ⁻¹)	199	-2.43	-4.55

NB: BEC is the influence of the background signal intensity on the measured signal. A negative BEC is a result of the intercept being greater than the background signal.

A calibration for ⁵⁶Fe was unachievable without the use of the reaction cell. Observing Figure 7-5, the SNR without the use of the reaction cell is between 0.7 and 1.03, indicating the signal is below or only partially above the gas blank signal. This resulted in difficulty calibrating ⁵⁶Fe in these circumstances because of substantial interference from the background signal and a lack of sensitivity. The analytical signal for ⁵⁶Fe seen in Figure 7-6 is reliant on the gas blank signal and only a slight deviation from the background signal is observed for the high concentration standards. This is somewhat insignificant in this application as the working concentration range in this image is between 0 and 100 μg g⁻¹. Operating the reaction cell with the addition of 3.0 mL min⁻¹ H₂ has resulted in a reduction of noise enabling the formation of a clear and analytically valid calibration, enabling the subsequent quantification of the data. An improvement in the SNR is observed for ⁶³Cu and ⁶⁶Zn for the calibrations conducted at 3.0 mL min⁻¹ H₂ however calibration curves were able to be prepared for both H₂ flow rates.

Figure 7-5: Signal to noise ratios for imaged isotopes using 3.0 and 0.0 mL min⁻¹ H₂ in the reaction cell

Figure 7-6: Comparison of the calibration data for ⁵⁶Fe with 3.0 and 0.0 mL min⁻¹ H₂

7.4 Conclusion

An image of the substantia nigra in a section of mouse brain was successfully produced at a resolution of 6 μm x 6 μm using the reaction cell with hydrogen as the reaction gas running at 3.0 mL min⁻¹. The improvement in sensitivity allowed for images showing the isotope distribution for ⁵⁶Fe, ⁶³Cu and ⁶⁶Zn to be prepared. An improvement in contrast for the ⁵⁶Fe and ⁶³Cu images means greater detail in the distribution of these isotopes is observed. The results support those results obtained in Chapter 6 and none of the masses imaged are adversely affected by the use of the reaction cell with 3.0 mL min⁻¹ H₂.

***Chapter 8: Conclusions and
recommendations***

Chapter 8: Conclusions and recommendations

This project effectively examined the instrumental considerations of EBI and was able to successfully;

- develop an improved method of matrix-matched tissue preparation which increased homogeneity and the number of analytes per standard.
- provide a simple equation to increase image acquisition speed and reduce experimental analysis time. Decreasing the scan cycle of the quadrupole and increasing the laser scan speed was a viable means for reducing the acquisition times for EBI.
- improve sensitivity by reducing O- and N-based polyatomic interferences using H₂ as a reactive gas whilst maintaining the analytical integrity of analytes not subject to spectral interferences. Using a moderate H₂ flow rate of 3.0 mL min⁻¹, a significant decrease in analyte background levels, decrease in the limits of analysis, increase in signal to noise ratios, and increase in image quality was observed for several measured masses.

As a consequence of these considerations, several neurological applications were examined. Improved matrix-matched tissue standards and increased image acquisition speeds were used to prepare images of;

- ZnT3 KO mouse brains treated with PBT-2. These results indicated that PBT-2 has no significant effect on the relative concentration distribution of elements in the midbrain of ZnT3 KO mice.
- mouse models for intermittent hypoxia and diets of varying levels of AGEs. Results for ^{59}Co were of most interest. A 100-fold increase in the ^{59}Co concentration in the brains of mice subjected to intermittent hypoxia was observed. Other elements remained unaffected and an AGE diet had no effect on the element concentrations.

Improved matrix-matched tissue standards, increased image acquisition speeds and H_2 as a reactive gas were used to prepare a high resolution image of the substantia nigra. Utilising the improvement in the sensitivity, it was possible to image ^{56}Fe with a resolution of $6\ \mu\text{m} \times 6\ \mu\text{m}$ and a laser scan speed of $16\ \mu\text{m}\ \text{s}^{-1}$.

This project has advanced the use of LA-ICP-MS for imaging thin sections of tissue. The ability of this technology to approach the analysis of element distribution in single mouse brain cells enables the potential advancement of our understanding of neurodegenerative disorders. It also exhibits the current and future prospects of a cost-effective and relatively fast analytical practice that appeals to a wide range of research areas.

With technology constantly improving, EBI will undoubtedly become more sensitive, faster and develop ever better quantification strategies. Instrument design plays a central role in the improvement of EBI – large ablation cells capable of rapid washout will improve sensitivity further and enable larger and a greater number of samples to be analysed; a mass spectrometer with a rapid scan cycle will allow increased laser scan speeds and even higher throughput without compromising image quality; altering carrier gas composition may enable

more efficient sample ablation; and improvements to the removal of interferences will further increase sensitivity and reduce detection limits.

A number of recommendations have emanated from this project. These recommendations include the following;

- With regards to the increased image acquisition speeds, the upper limits of increased speed are yet to be determined, and likely to be limited by the scan speed of the quadrupole. Washout of ablated material from the sample cell and transfer lines also plays a significant role in blurring of images and carry-over. It is recommended that these limitations are investigated in order to know to what extent the instrumentation can be utilised and whether the instrument's current capabilities exceed or fail to meet the current and future potential of EBI.
- With improvements to sensitivity, the extent to which the image resolution can be increased needs further examination. By determining the upper limits of increased acquisition speed, higher resolution images than those prepared in this project become increasingly viable as analysis times are reduced. With experimentation, current technologies have a potential to reach higher resolutions than 6 µm x 6 µm and with the implementation of increasingly faster and more efficient laser technologies, resolutions in the nanometre range may soon be possible enabling detailed images of single cells.
- The results for ⁵⁹Co in the intermittent hypoxia mice are intriguing and further investigation could have a number of implications for the understanding of sleep related disorders. Investigations are needed to confirm whether homeostasis is re-

established during the course of the day, and whether similar changes occur in humans with OSA.

Appendix

Appendix

Appendix Table 1: Visual Basic for Applications 6.0 programming language Microsoft Excel 2003 macro

```
Sub ISselect()
'
' ISselect Macro
' Macro recorded 11/02/2008 by Administrator
'
' Keyboard Shortcut: Ctrl+u

Dim LineCount As Integer
Dim NumPoints As Integer
Dim NumBooks As Integer
Dim BookNum As Integer
Dim NumLines As Integer
Dim NumIsotopes As Integer
Dim SampleNumber As String * 4
Dim InternalStandard As Integer
Dim i As Integer
Dim j As Integer

SampleNumber = InputBox("Enter the sample number as **-*:")
NumLines = InputBox("Enter the number of lines (files):")
NumIsotopes = InputBox("Enter the number of isotopes:")
NumPoints = InputBox("Enter the number of points in each line:")
InternalStandard = InputBox("Enter the column of the internal standard:")
NumBooks = Int(NumPoints / 256) + 1

For BookNum = 1 To NumBooks

Workbooks.Add

Next

For LineCount = 1 To 9

    Workbooks.Open Filename:= _
        "C:\Documents and Settings\*****\Desktop\Sample " & SampleNumber & "\00" & LineCount &
        ".D\00" & LineCount & ".csv"

    Rows("1:3").Select
    Selection.Delete Shift:=xlUp

    Columns("A:A").Select
    Selection.Delete Shift:=xlToLeft

    For j = 1 To (InternalStandard - 1)
    For i = 1 To NumPoints
```

Cells(i, (j + NumIsotopes)).Select

Cells(i, (j + NumIsotopes)).Value = (Cells(i, j).Value) / Cells(i, InternalStandard).Value

Next

Next

For j = (InternalStandard + 1) To NumIsotopes

For i = 1 To NumPoints

Cells(i, (j + NumIsotopes)).Select

Cells(i, (j + NumIsotopes)).Value = (Cells(i, j).Value) / Cells(i, InternalStandard).Value

Next

Next

References

References

- 1 Hare, D. (2009). *Elemental bio-imaging: In situ analysis of trace elements in tissue by laser ablation – inductively coupled plasma – mass spectrometry*. University of Technology, Sydney, Sydney.
- 2 Hare, D., Tolmachev, S., James, A., Bishop, D., Austin, C., Fryer, F., et al. (2010). Elemental Bio-imaging of Thorium, Uranium, and Plutonium in Tissues from Occupationally Exposed Former Nuclear Workers. *Analytical Chemistry*, 82(8), 3176-3182.
- 3 Hare, D., Burger, F., Austin, C., Fryer, F., Grimm, R., Reedy, B., et al. (2009). Elemental bio-imaging of melanoma in lymph node biopsies. *The Analyst*, 134, 450-453.
- 4 McRae, R., Bagchi, P., Sumalekshmy, S., & Fahrni, C. J. (2009). In situ imaging of metals in cells and tissues. *Chemical Reviews*, 109(10), 4780-4827.
- 5 Becker, J. S., Zoriy, M., Becker, J. S., Pickhardt, C., Damoc, E., Juhacz, G., et al. (2005). Determination of phosphorus-, copper-, and zinc-containing human brain proteins by LA-ICPMS and MALDI-FTICR-MS. *Analytical chemistry*, 77(18), 5851-5860.
- 6 Jackson, B., Harper, S., Smith, L., & Flinn, J. (2006). Elemental mapping and quantitative analysis of Cu, Zn, and Fe in rat brain sections by laser ablation ICP-MS. *Analytical and Bioanalytical Chemistry*, 384(4), 951-957.
- 7 Hare, D. J., George, J. L., Grimm, R., Wilkins, S., Adlard, P. A., Cherny, R. A., et al. (2010). Three-dimensional elemental bio-imaging of Fe, Zn, Cu, Mn and P in a 6-hydroxydopamine lesioned mouse brain. *Metallomics*, 2(11), 745-753.
- 8 Lear, J., Hare, D., Adlard, P., Finkelstein, D., & Doble, P. (2012). Improving acquisition times of elemental bio-imaging for quadrupole-based LA-ICP-MS. *Journal of Analytical Atomic Spectrometry*, 27(1), 159-164.
- 9 Austin, C., Fryer, F., Lear, J., Bishop, D., Hare, D., Rawling, T., et al. (2011). Factors affecting internal standard selection for quantitative elemental bio-imaging of soft tissues by LA-ICP-MS. *Journal of analytical atomic spectrometry*, 26(7), 1494-1501.
- 10 Hare, D., Reedy, B., Grimm, R., Wilkins, S., Volitakis, I., George, J., et al. (2009). Quantitative elemental bio-imaging of Mn, Fe, Cu and Zn in 6-hydroxydopamine Parkinsonism mouse models. *Metallomics*, 1, 53.
- 11 Matusch, A., Depboylu, C., Palm, C., Wu, B., Höglinger, G. U., Schäfer, M. K. H., et al. (2010). Cerebral Bioimaging of Cu, Fe, Zn, and Mn in the MPTP Mouse Model of Parkinson's Disease Using Laser Ablation Inductively Coupled Plasma Mass Spectrometry (LA-ICP-MS). *Journal of the American Society for Mass Spectrometry*, 21(1), 161-171.

- 12 Arora, M., Hare, D., Austin, C., & Doble, P. (2011). Spatial distribution of manganese in enamel and coronal dentine of human primary teeth. *Science and the Total Environment*, 409(7), 1315-1319.
- 13 Nelms, S. M. (2005). *ICP Mass Spectrometry Handbook*. Oxford: Blackwell Publishing Ltd. CRC Press.
- 14 Thomas, R. (2004). *Practical Guide to ICP-MS*. New York: Marcel Dekker, Inc.
- 15 ICP-MS: Inductively Coupled Plasma Mass Spectrometry - A Primer [Electronic. (2005). Version],
- 16 Hoffmann, E. (2007). *Mass Spectrometry: Principles and Applications*: John Wiley & Sons Ltd.
- 17 Wanner, K. T., & Höfner, G. (Eds.). (2007). *Mass Spectrometry in Medicinal Chemistry* (1st ed.). Weinheim: Wiley-VCH Verlag GmbH & Co. KGaA.
- 18 Henderson, W., & McIndoe, S. (2005). *Mass Spectrometry of Inorganic and Organometallic Compounds*: John Wiley & Sons Ltd.
- 19 Boyd, R. K., Basic, C., & Bethem, R. A. (2008). *Trace Quantitative Analysis by Mass Spectrometry*: John Wiley & Sons Ltd.
- 20 Heeren, R. M. A., Smith, D. F., Stauber, J., Kükreer-Kaletas, B., & MacAleese, L. Imaging mass spectrometry: Hype or Hope? *Journal of the American Society for Mass Spectrometry*, *In Press, Accepted Manuscript*.
- 21 Pacholski, M. L., & Winograd, N. (1999). Imaging with Mass Spectrometry. *Chemical Reviews*, 99, 2977-3005.
- 22 Quadrupole Mass Spectrometer, University of Adelaide, Adelaide (2009). Retrieved 21/9, 2009, from <http://www.chemistry.adelaide.edu.au/external/soc-rel/content/images/quad-sch.png>
- 23 What is ICP-MS and laser ablation?, Institute of Geochemistry, Mineralogy and Mineral Resources: Charles University, Prague (2007). Retrieved 14/9, 2009, from www.natur.cuni.cz/ugmnz/icplab/pic/laschema.jpg
- 24 Durrant, S. F. (1999). Laser ablation inductively coupled plasma mass spectrometry: achievements, problems, prospects. *Journal of Analytical Atomic Spectrometry*, 14(9), 1385-1403.
- 25 Eggins, S. M., Kinsley, L. P. J., & Shelley, J. M. G. (1998). Deposition and element fractionation processes during atmospheric pressure laser sampling for analysis by ICP-MS. *Applied Surface Science*, 127-129, 278-286.
- 26 Margetic, V., Bolshow, M., Stockhaus, A., Niemax, K., & Hergenroeder, R. (2001). Depth profiling of multi-layer samples using femtosecond laser ablation. *Journal of Analytical Atomic Spectrometry*, 16, 616-621.

- 27 Poitrasson, F., Mao, X. L., Mao, S. S., Freydier, R., & Russo, R. E. (2003). Comparison of ultraviolet femtosecond and nanosecond laser ablation inductively coupled mass spectrometry analysis in glass, monazite, and zircon. *Analytical Chemistry*, *75*(6184-6190).
- 28 Russo, R. E., Mao, X., Gonzalez, J. J., & Mao, S. S. (2002). Femtosecond laser ablation ICP-MS. *Journal of Analytical Atomic Spectrometry*, *17*(9), 1072-1075.
- 29 Gonzalez, J. J., Fernandez, A., Oropeza, D., Mao, X., & Russo, R. E. (2008). Femtosecond laser ablation: Experimental study of the repetition rate influence on inductively coupled plasma mass spectrometry performance. *Spectrochimica Acta, Part B: Atomic Spectroscopy*, *63B*(2), 277-286.
- 30 Russo, R. E., Mao, X., Liu, H., Gonzalez, J., & Mao, S. S. (2002). Laser ablation in analytical chemistry--a review. *Talanta*, *57*(3), 425-451.
- 31 Horn, I., & Günther, D. (2003). The influence of ablation carrier gasses Ar, He and Ne on the particle size distribution and transport efficiencies of laser ablation-induced aerosols: implications for LA-ICP-MS. *Applied Surface Science*, *207*(1-4), 144-157.
- 32 Sample Chambers, Kenelec Scientific, (2012). Retrieved 20 March, 2012, from <http://www.kenelec.com.au/products/id/976/cid/267/parent/0/t/products/title/Sample%20Chambers>
- 33 Günther, D., & Heinrich, C. A. (1999). Enhanced sensitivity in laser ablation-ICP mass spectrometry using helium-argon mixtures as aerosol carrier. *J. Anal. At. Spectrom.*, *14*, 1363-1368.
- 34 Gunther, D., & Heinrich, C. A. (1999). Enhanced sensitivity in laser ablation-ICP mass spectrometry using helium-argon mixtures as aerosol carrier. *Journal of Analytical Atomic Spectrometry*, *14*(9), 1363-1368.
- 35 Horn, I., & Gunther, D. (2003). The influence of ablation carrier gasses Ar, He and Ne on the particle size distribution and transport efficiencies of laser ablation-induced aerosols: implications for LA-ICP-MS. *Applied Surface Science*, *207*(1-4), 144-157.
- 36 Hare, D., Reedy, B., Grimm, R., Wilkins, S., Volitakis, I., George, J., et al. (2008). Quantitative elemental bio-imaging of Mn, Fe, Cu and Zn in 6-hydroxydopamine Parkinsonism mouse models. *Metallomics*, *1*, 53.
- 37 Guillong, M., Kuhn, H.-R., & Günther, D. (2003). Application of a particle separation device to reduce inductively coupled plasma-enhanced elemental fractionation in laser ablation-inductively coupled plasma-mass spectrometry. *Spectrochimica Acta Part B: Atomic Spectroscopy*, *58*(2), 211-220.
- 38 Horn, I., Guillong, M., & Günther, D. (2001). Wavelength dependant ablation rates for metals and silicate glasses using homogenized laser beam profiles -- implications for LA-ICP-MS. *Applied Surface Science*, *182*(1-2), 91-102.
- 39 Russo, R. E., Mao, X., & Borisov, O. V. (1998). Laser ablation sampling. *TrAC Trends in Analytical Chemistry*, *17*(8-9), 461-469.

- 40 Mason, P. R. D., & Jeroen Kraan, W. (2002). Attenuation of spectral interferences during laser ablation inductively coupled plasma mass spectrometry (LA-ICP-MS) using an rf only collisions and reaction cell. *Journal of Analytical Atomic Spectrometry*, *17*, 858-867.
- 41 May, T. W., & Wiedmeyer, R. H. (1998). A table of polyatomic interferences in ICP-MS. *Atomic Spectroscopy*, *19*(5), 150-155.
- 42 GÜNTHER, D., FRISCHKNECHT, R., HEINRICH, C. A., & H.-J., K. (1997). Capabilities of an argon fluoride 193 nm excimer laser for laser ablation inductively coupled plasma mass spectrometry microanalysis of geological materials. *Journal of analytical atomic spectrometry*, *12*(9), 939-944.
- 43 Pacholski, M. L., & Winograd, N. (1999). Imaging with Mass Spectrometry. *Chemical Reviews*, *99*(10), 2977-3005.
- 44 Tarohda, T., Ishida, Y., Kawai, K., Yamamoto, M., & Amano, R. (2005). Regional distributions of manganese, iron, copper, and zinc in the brains of 6-hydroxydopamine-induced parkinsonian rats. *Analytical and Bioanalytical Chemistry*, *383*(2), 224-234.
- 45 Tarohda, T., Yamamoto, M., & Amamo, R. (2004). Regional distribution of manganese, iron, copper, and zinc in the rat brain during development. *Analytical and Bioanalytical Chemistry*, *380*(2), 240-246.
- 46 Jiang, P., & Guo, Z. (2004). Fluorescent detection of zinc in biological systems: recent development on the design of chemosensors and biosensors. *Coordination Chemistry Reviews*, *248*(1-2), 205-229.
- 47 Morawski, M., Meinecke, C., Reinert, T., Dörffel, A. C., Riederer, P., Arendt, T., et al. (2005). Determination of trace elements in the human substantia nigra. *Nuclear Instruments and Methods in Physics Research Section B: Beam Interactions with Materials and Atoms*, *231*(1-4), 224-228.
- 48 Vrensen, G., & De Groot, D. (1974). Osmium-zinc iodide staining and the quantitative study of central synapses. *Brain Research*, *74*(1), 131-142.
- 49 Castaing, R., & Slodzian, G. (1962). Microanalyse par emission ionique secondaire. *Journal of Microscopy*, *1*, 31-38.
- 50 Baruchel, J., Bleuët, P., Bravin, A., Coan, P., Lima, E., Madsen, A., et al. Advances in synchrotron hard X-ray based imaging. *Comptes Rendus Physique*, *9*(5-6), 624-641.
- 51 Chandra, S. (2008). Challenges of biological sample preparation for SIMS imaging of elements and molecules at subcellular resolution. *Applied Surface Science*, *255*(4), 1273-1284.
- 52 Chaurand, P., Sanders, M. E., Jensen, R. A., & Caprioli, R. M. (2004). Proteomics in Diagnostic Pathology: Profiling and Imaging Proteins Directly in Tissue Sections. *America Journal of Pathology*, *165*(4), 1057-1068.

- 53 Cornett, D. S., Reyzer, M. L., Chaurand, P., & Caprioli, R. M. (2007). MALDI imaging mass spectrometry: molecular snapshots of biochemical systems. *Nature Methods*, 4(10), 828-833.
- 54 Devès, G., Isaure, M. P., Lay, P. L., Bourguignon, J., & Ortega, R. (2005). Fully quantitative imaging of chemical elements in *Arabidopsis thaliana* tissues using STIM, PIXE and RBS. *Nuclear Instruments and Methods in Physics Research Section B: Beam Interactions with Materials and Atoms*, 231(1-4), 117-122.
- 55 Lobinski, R., Moulin, C., & Ortega, R. (2006). Imaging and speciation of trace elements in biological environment. *Biochimie*, 88(11), 1591-1604.
- 56 Lobinski, R., Schaumloeffel, D., & Szpunar, J. (2006). Mass Spectrometry in Bioinorganic Analytical Chemistry. *Mass Spectrometry Reviews*, 25, 255-289.
- 57 Miller, L. M., & Dumas, P. (2006). Chemical imaging of biological tissue with synchrotron infrared light. *Biochimica et Biophysica Acta (BBA) - Biomembranes*, 1758(7), 846-857.
- 58 Miller, L. M., Wang, Q., Telivala, T. P., Smith, R. J., Lanzirotti, A., & Miklossy, J. (2006). Synchrotron-based infrared and X-ray imaging shows focalized accumulation of Cu and Zn co-localized with [beta]-amyloid deposits in Alzheimer's disease. *Journal of Structural Biology*, 155(1), 30-37.
- 59 Nakata, Y., Yamada, H., Honda, Y., Ninomiya, S., Seki, T., Aoki, T., et al. (2009). Imaging mass spectrometry with nuclear microprobes for biological applications. *Nuclear Instruments and Methods in Physics Research Section B: Beam Interactions with Materials and Atoms*, 267(12-13), 2144-2148.
- 60 Stoeckli, M., Chaurand, P., Hallahan, D. E., & Caprioli, R. M. (2001). Imaging mass spectrometry: a new technology for the analysis of protein expression in mammalian tissues. *Nature Medicine*, 7(4), 493-496.
- 61 Becker, J. S., Dietrich, R. C., Matusch, A., Pozebon, D., & Dressler, V. L. (2008). Quantitative images of metals in plant tissues measured by laser ablation inductively coupled plasma mass spectrometry. *Spectrochimica Acta Part B: Atomic Spectroscopy*, 63(11), 1248-1252.
- 62 Becker, J. S., Zoriy, M. V., Pickhardt, C., Palomero-Gallagher, N., & Zilles, K. (2005). Imaging of Copper, Zinc, and Other Elements in Thin Section of Human Brain Samples (Hippocampus) by Laser Ablation Inductively Coupled Plasma Mass Spectrometry. *Analytical Chemistry*, 77(10), 3208-3216.
- 63 Zoriy, M. V., & Becker, J. S. (2007). Imaging of elements in thin cross sections of human brain samples by LA-ICP-MS: A study on reproducibility. *International Journal of Mass Spectrometry*, 264(2-3), 175-180.
- 64 Durrant, S. F., & Ward, N. I. (1994). Laser ablation-inductively coupled plasma mass spectrometry (LA-ICP-MS) for the multielemental analysis of biological materials: a feasibility study. *Food Chemistry*, 49, 317-323.

- 65 Wang, S., Brown, R., & Gray, D. J. (1994). Application of Laser Ablation-ICPMS to the Spatially Resolved Micro-analysis of Biological Tissue," *Applied Spectroscopy*, *48*, 1321-1325.
- 66 Becker, J. S., Becker, J. S., Zoriy, M. V., Dobrowolska, J., & Matusch, A. (2007). Imaging mass spectrometry in biological tissues by laser ablation inductively coupled plasma mass spectrometry. *European Journal of Mass Spectrometry*, *13*, 1-6.
- 67 Dobrowolska, J., Dehnhardt, M., Matusch, A., Zoriy, M., Palomero-Gallagher, N., Koscielniak, P., et al. (2008). Quantitative imaging of zinc, copper and lead in three distinct regions of the human brain by laser ablation inductively coupled plasma mass spectrometry. *Talanta*, *74*(4), 717-723.
- 68 Wu, B., Zoriy, M., Chen, Y., & Becker, J. S. (2009). Imaging of nutrient elements in the leaves of *Elsholtzia splendens* by laser ablation inductively coupled plasma mass spectrometry (LA-ICP-MS). *Talanta*, *78*(1), 132-137.
- 69 Zoriy, M., Matusch, A., Spruss, T., & Becker, J. S. (2007). Laser ablation inductively coupled plasma mass spectrometry for imaging of copper, zinc, and platinum in thin sections of a kidney from a mouse treated with cis-platin. *International Journal of Mass Spectrometry*, *260*(2-3), 102-106.
- 70 Zoriy, M. V., Dehnhardt, M., Reifenberger, G., Zilles, K., & Becker, J. S. (2006). Imaging of Cu, Zn, Pb and U in human brain tumor resections by laser ablation inductively coupled plasma mass spectrometry. *International Journal of Mass Spectrometry*, *257*(1-3), 27-33.
- 71 Geisen, C., Waentig, L., Mairinger, T., Drescher, D., Kneipp, J., Roos, P. H., et al. (2011). Iodine as an elemental marker for imaging of single cells and tissue sections by laser ablation inductively coupled plasma mass spectrometry. *Journal of Analytical Atomic Spectrometry*, *26*(11), 2160.
- 72 Becker, J. S., Matusch, A., Depboylu, C., Dobrowolska, J., & Zoriy, M. V. (2007). Quantitative Imaging of Selenium, Copper, and Zinc in Thin Sections of Biological Tissues (Slugs-Genus *Arion*) Measured by Laser Ablation Inductively Coupled Plasma Mass Spectrometry. *Analytical Chemistry*, *79*(16), 6074-6080.
- 73 Zoriy, M. V., Dehnhardt, M., Matusch, A., & Becker, J. S. (2008). Comparative imaging of P, S, Fe, Cu, Zn and C in thin sections of rat brain tumor as well as control tissues by laser ablation inductively coupled plasma mass spectrometry. *Spectrochimica Acta Part B: Atomic Spectroscopy*, *63*(3), 375-382.
- 74 Bleiner, D., Hametner, K., & Günther, D. (2000). Optimization of a laser ablation-inductively coupled plasma "time of flight" mass spectrometry system for short transient signal acquisition. *Fresenius' Journal of Analytical Chemistry*, *368*(1), 37-44.
- 75 Russo, R. E., Klunder, G. L., Grant, P., & Andresen, B. D. (1999). Laser ablation ion-storage time-of-flight mass spectrometry. *Applied Physics A: Materials Science & Processing*, *69*(7), S895-S897.

- 76 Hare, D., Austin, C., & Doble, P. (2012). Quantification strategies for elemental imaging of biological samples using laser ablation-inductively coupled plasma-mass spectrometry. *Analyst*, *137*, 1527-1537.
- 77 Austin, C., Hare, D., Rawling, T., McDonagh, A., & Doble, P. (2010). Quantification method for elemental bio-imaging by LA-ICP-MS using metal spiked PMMA films. *Journal of Analytical Atomic Spectrometry*, *25*, 722-725.
- 78 Bellis, D. J., & Santamaria-Fernandez, R. (2010). Ink jet patterns as model samples for the development of LA-ICP-SFMS methodology for mapping of elemental distribution with reference to biological samples. *Journal of Analytical Atomic Spectrometry*, *25*, 957.
- 79 Margetic, V., Pakulev, A., Stockhaus, A., Bolshov, M., Niemax, K., & Hergenröder, R. (2000). A comparison of nanosecond and femtosecond laser-induced plasma spectroscopy of brass samples. *Spectrochimica Acta Part B: Atomic Spectroscopy*, *55*(11), 1771-1785.
- 80 Garcia, C. C., Waelle, M., Lindner, H., Koch, J., Niemax, K., & Guenther, D. (2008). Femtosecond laser ablation inductively couple mass spectrometry: transport efficiencies of aerosols released under argon atmosphere and the importance of the focus position. *Spectrochimica Acta Part B: Atomic Spectroscopy*, *63B*(2), 271-276.
- 81 Gonzalez, J., Dundas, S. H., Liu, C. Y., Mao, X., & Russo, R. E. (2006). UV-femtosecond and nanosecond laser ablation-ICP-MS: internal and external repeatability. *Journal of analytical atomic spectrometry*, *21*(8), 778-784.
- 82 Hergenröder, R., Samek, O., & Hommes, V. (2006). Femtosecond laser ablation elemental mass spectrometry. *Mass Spectrometry Reviews*, *25*(4), 551-572.
- 83 Russo, R. E., Mao, X., Liu, C. Y., & Gonzalez, J. (2004). Laser assisted plasma spectrochemistry: Laser ablation. *Journal of analytical atomic spectrometry*, *19*(9), 1084-1089.
- 84 Pearce, N. J. G., WPerkins, W. T., Westgate, J. A., Gorton, M. P., Jackson, S. E., Neal, C. R., et al. (1997). A compilation of new and published major and trace element data for NIST SRM 610 and NIST SRM 612 glass reference materials. *Geostandards Newsletter*, *21*(1), 115-144.
- 85 EPA Method 3050B - Acid digestion of sediments, sludges and soils. Revision 2, (1996).
- 86 Gozal, D., Daniel, J. M., & Dohanich, G. P. (2001). Behavioral and anatomical correlates of chronic episodic hypoxia during sleep in the rat. *Journal of Neuroscience*, *21*, 2442 - 2450.
- 87 Veasey, S. C., Davis, C., Zahn, G., Hsu, Y. J., Fenik, P., Pratico, D., et al. (2004). Intermittent hypoxia in mice: protracted hypersomnolence and basal forebrain redox alterations. *Sleep*, *27*, 194-201.

- 88 *ICP-MS: Inductively Coupled Plasma Mass Spectrometry - A Primer*. (2005). Agilent Technologies.
- 89 Sigel, A., Sigel, H., & Sigel, R. K. O. (Eds.). (2006). *Metal Ions in Life Sciences: Neurodegenerative Disorders and Metal Ions* (Vol. 1): John Wiley & Sons, Ltd.
- 90 Takeda, A. (2003). Manganese action in brain function. *Brain Research Reviews*, 41(1), 79-87.
- 91 Crichton, R. R., & Ward, R. J. (2006). *Metal-based Neurodegeneration: From Molecular Mechanisms to Therapeutic Strategies*: John Wiley & Sons, Ltd.
- 92 Haber, F., & Weiss, J. (1932). Über die Katalyse des Hydroperoxydes. *Naturwissenschaften*, 20(51), 948-950.
- 93 Haber, F., & Weiss, J. (1934). The catalytic decomposition of hydrogen peroxide by iron salts. *Proceedings of the Royal Society A*, 147, 332-351.
- 94 Radák, Z. (2000). *Free radicals in exercise and aging*: Human Kinetics.
- 95 Fenton, H. J. H. (1894). Oxidation of tartaric acid in the presence of iron. *Chemical Society Journal*, 65, 899-909.
- 96 CSIRO, (2008). Neurodegenerative diseases and mental disorders Retrieved 16/6, 2009, from <http://www.csiro.au/science/Neurodegenerative-Diseases.html>
- 97 Marieb, E. N. (2004). *Human Anatomy & Physiology* (6th ed.). San Francisco: Benjamin Cummings.
- 98 ABS, Canberra (2009). 3303.0 - Causes of Death, Australia 2007 Retrieved 16/6, 2009, from <http://www.abs.gov.au/ausstats/abs@.nsf/Products/9982A795F3C13BE2CA25757C001EF4D9?opendocument>
- 99 MHRI, (2004). Alzheimer's Disease Retrieved 16/6, 2009, from <http://www.mhri.edu.au/alzhiemers.htm>
- 100 Bush, A. I. (2003). The Metallobiology of Alzheimer's Disease. *Trends in Neurosciences*, 26(4), 207-214.
- 101 Bush, A. I., & Tanzi, R. E. (2008). Therapeutics for Alzheimer's Disease Based on the Metal Hypothesis. *Neurotherapeutics*, 5(3), 421-432.
- 102 Silvestrelli, G., Lanari, A., Parnetti, L., Tomassoni, D., & Amenta, F. (2006). Treatment of Alzheimer's disease: From pharmacology to a better understanding of disease pathophysiology. *Mechanisms of Ageing and Development*, 127(2), 148-157.
- 103 Cummings, J. L., Mackell, J., & Kaufer, D. (2008). Behavioral effects of current Alzheimer's disease treatments: A descriptive review. *Alzheimer's and Dementia*, 4(1), 49-60.

- 104 Moffat, A. C., Osselton, M. D., & Widdop, B. (Eds.). (2004). *Clarke's analysis of drugs and poisons : in pharmaceuticals, body fluids and postmortem material*. London: Pharmaceutical Press.
- 105 Dudev, T., & Lim, C. (2003). Principles governing Mg, Ca, and Zn binding and selectivity in proteins. *Chemical Reviews*, *103*, 773-787.
- 106 Crapper Mclachlan, D. R., Dalton, A. J., Kruck, T. P. A., & al., E. (1991). Intramuscular desferrioxamine in patients with Alzheimer's disease. *Lancet*, *337*, 1304-1308.
- 107 Peder Flaten, T., Garruto, R., Davies, P., Weiner, M., Ray Holleman, D., Richard Goldstone, J., et al. (1991). Desferrioxamine for Alzheimer's disease. *The Lancet*, *338*(8762), 324-326.
- 108 Mao, X., & Schimmer, A. D. (2008). The toxicology of Clioquinol. *Toxicology Letters*, *182*(1-3), 1-6.
- 109 Bush, A. I. (2002). Metal complexing agents as therapies for Alzheimer's disease. *Neurobiology of Aging*, *23*, 1031-1038.
- 110 Bush, A. I. (2002). Response: '...and C is for Clioquinol' - the A[beta]Cs of Alzheimer's disease. *Trends in Neurosciences*, *25*(3), 123-124.
- 111 Barnham, K., Gautier, E., Kok, G., & Krippner, G. (2003). *8-hydroxy quinoline derivatives*, [Prana Biotechnology Limited, World] Patent No. AU033/00914.
- 112 Adlard, P. A., Parncutt, J. M., Finkelstein, D. I., & Bush, A. I. (2010). Cognitive loss in zinc transporter-3 knock-out mice: a phenocopy for the synaptic and memory deficits of Alzheimer's disease? *The Journal of Neuroscience*, *30*(5), 1631-1636.
- 113 Ko, S.-Y., Lin, Y.-P., Lin, Y.-S., & Chang, S.-S. (2010). Advanced glycation end products enhance amyloid precursor protein expression by inducing reactive oxygen species. *Free Radical Biology and Medicine*, *49*(3), 474-480.
- 114 Singh, R., Barden, A., Mori, T., & Beilin, L. (2001). Advanced glycation end-products: a review. *Diabetologia*, *44*, 129-146.
- 115 Krautwald, M., & Muench, G. (2010). Advanced glycation end products as biomarkers and gerontotoxins - A basis to explore methylglyoxal-lowering agents for Alzheimer's disease? *Experimental Gerontology*, *45*(10), 744-751.
- 116 Thome, J., Muench, G., Mueller, R., Schinzel, R., Kornhuber, J., Blum-Degen, D., et al. (1996). Advanced glycation endproducts - associated parameters in the peripheral blood of patients with Alzheimer's disease. *Life Sciences*, *59*(8), 679-685.
- 117 Wong, A., Lueth, H.-J., Deuther-Conrad, W., Dukic-Stefanovic, S., Gasic-Milenkovic, J., Arendt, T., et al. (2001). Advanced glycation endproducts co-localize with inducible nitric oxide synthase in Alzheimer's disease. *Brain Research*, *920*(1-2), 32-40.
- 118 Gella, A., Valente, T., Unzeta, M., Fernandez-Busquets, X., & Durany, N. (2008). P3-012: Immunochemical analysis of advanced glycation endproducts and amyloid in

- Alzheimer's disease and diabetic post-mortem brain tissue. *Alzheimer's and Dementia*, 4(4, Supplement), T520.
- 119 Goldberg, T., Cai, W., Peppas, M., Dardaine, V., Baliga, B. S., Uribarri, J., et al. (2004). Advanced glycoxidation end products in commonly consumed foods. *Journal of the American Dietetic Association*, 104(8), 1287-1291.
- 120 Uribarri, J., Cai, W., Sandu, O., Peppas, M., Goldberg, T., & Vlassara, H. (2005). Diet-Derived Advanced Glycation End Products Are Major Contributors to the Body's AGE Pool and Induce Inflammation in Healthy Subjects. *Annals of the New York Academy of Sciences*, 1043(1), 461-466. 10.1196/annals.1333.052
- 121 Goldin, A., Beckman, J. A., Schmidt, A. M., & Creager, M. A. (2006). Advanced glycation end products: sparking the development of diabetic vascular injury. *Circulation*.
- 122 Cai, W., He, J. C., Zhu, L., Chen, X., Zheng, F., Striker, G. E., et al. (2008). Oral glycotoxins determine the effects of calorie restriction on oxidant stress, age-related diseases, and lifespan. *American Journal of Pathology*, 173, 327-336.
- 123 He, C. J., Sabol, J., Mitsuhashi, T., & Vlassara, H. (1999). Dietary glycotoxins: Inhibition of reactive products by aminoguanidine facilitates renal clearance and reduces tissue sequestration. *Diabetes*, 48, 1308-1315.
- 124 Koschinsky, T., He, C. J., Mitsuhashi, T., Bucala, R., Liu, C., Buenting, C., et al. (1997). Orally absorbed reactive advanced glycation end products (glycotoxins): An environmental risk factor in diabetic neuropathy. *Proceedings of the National Academy of Sciences*, 94, 6474-6479.
- 125 Zheng, F., He, C. J., Cai, W., Hattori, M., Steffes, M., & Vlassara, H. (2002). Prevention of diabetic nephropathy in mice by a diet low in glycoxidation products. *Diabetes/Metabolism Research Reviews*, 18, 224-237.
- 126 Hofmann, S. M., Dong, H. J., Li, Z., Cai, W., Altomonte, J., Thung, S. N., et al. (2002). Improved insulin sensitivity is associated with restricted intake of dietary glycoxidation products in the db/db mouse. *Diabetes*, 51, 2082-2089.
- 127 Li, X.-H., Lv, B.-L., Xie, J.-Z., Liu, J., Zhou, X.-W., & Wang, J.-Z. (2011). AGEs induce Alzheimer-like tau pathology and memory deficit via RAGE-mediated GSK-3 activation. *Neurobiology of Aging*(0).
- 128 Muench, G., Cunningham, A. M., Riederer, P., & Braak, E. (1998). Advanced glycation endproducts are associated with Hirano bodies in Alzheimer's disease. *Brain Research*, 796, 307-310.
- 129 Muench, G., Thome, J., Foley, P., Schinzel, R., & Riederer, P. (1996). Advanced glycation endproducts in ageing and Alzheimer's disease. *Brain Research Reviews*, 23, 134-143.

- 130 Cruz-Sanchez, F. F., Girones, X., Ortega, A., Alameda, F., & Lafuente, J. V. (2010). Oxidative stress in Alzheimer's disease hippocampus: A topographical study. *Journal of the Neurological Sciences*, 299(1-2), 163-167.
- 131 Seneff, S., Wainwright, G., & Mascitelli, L. (2011). Nutrition and Alzheimer's disease: The detrimental role of a high carbohydrate diet. *European Journal of Internal Medicine*, 22(2), 134-140.
- 132 Takuma, K., Fukuzaki, E., Funatsu, Y., Stern, D. M., Yamada, K., & Yan, S. D. (2008). P4-227: Role of receptor for advanced glycation endproducts in neuronal amyloid β -peptide membrane transport. *Alzheimer's and Dementia*, 4(4, Supplement), T738.
- 133 Ahmed, N., Ahmed, U., Thornalley, P. J., Hager, K., Fleischer, G., & Muench, G. (2005). Protein glycation, oxidation and nitration adduct residues and free adducts of cerebrospinal fluid in Alzheimer's disease and link to cognitive impairment. *Journal of Neurochemistry*, 92, 255-263.
- 134 Hipkiss, A. R. (2006). Does chronic glycosylation accelerate aging? Could this explain how dietary restriction works? *Annals of the New York Academy of Sciences*, 1067, 361-368.
- 135 Jono, T., Kimura, T., Takamatsu, J., Nagai, R., Miyazaki, K., Yuzuriha, T., et al. (2002). Accumulation of imidazolone, pentosidine and N(epsilon)-(carboxymethyl)lysine in hippocampal CA4 pyramidal neurons of aged human brain. *Pathology International*, 52, 563-571.
- 136 Kalaria, R. N., Spoor, L., Laude, E. A., Emery, C. J., Thwaites-Bee, D., Fairlie, J., et al. (2004). Hypoxia of sleep apnoea: cardiopulmonary and cerebral changes after intermittent hypoxia in rats. *Respiratory Physiology & Neurobiology*, 140(1), 53-62.
- 137 Alchanatis, M., Deligiorgis, N., Zias, N., Amfilochiou, A., Gotsis, E., Karakatsani, A., et al. (2004). Frontal brain lobe impairment in obstructive sleep apnoea: a proton MR spectroscopy study. *European Respiratory Journal*, 24, 980-986.
- 138 Macey, P. M., Kumar, R., Woo, M. A., Valladares, E. M., Yan-Go, F. L., & Harper, R. M. (2008). Brain structural changes in obstructive sleep apnea. *Sleep*, 31, 967-977.
- 139 Zhang, X. Q., Lu, B. X., & Li, T. P. (2009). Correlation between white matter lesion and memory impairment in patients with obstructive sleep apnea syndrome. *Nan Fang Yi Ke Da Xue Xue Bao*, 29, 825-829.
- 140 Zhang, X., & Le, W. (2010). Pathological role of hypoxia in Alzheimer's disease. *Experimental Neurology*, 223, 299-303.
- 141 Lam, J. C. M., Tan, K. C. B., Lai, A. Y. K., Lam, D. C. L., & Ip, M. S. M. (2011). Increased serum levels of advanced glycation end-products is associated with severity of sleep disordered breathing but not insulin sensitivity in non-diabetic men with obstructive sleep apnoea. *Sleep Medicine*(0).

- 142 Inada, M., Toyoshima, M., & Kameyama, M. (1982). Brain content of cobalamin and its binders in elderly subjects. *Journal of nutritional science and vitaminology*, 28(4), 351-357.
- 143 Tanaka, N. (1992). Vitamin B12(cobalamin) contents of serum and organs in various diseases and its clinical significance. *Journal of nutritional science and vitaminology, Spec No*, 104-109.
- 144 Austin, C., Hare, D., Rozelle, A. R., Robinson, W. H., Grimm, R., & Doble, P. (2009). Elemental bio-imaging of calcium phosphate crystal despoits in knee samples from arthritic patients. *Metallomics*, 1, 142-147.
- 145 Becker, J. S., Sela, H., Dobrowolska, J., Zoriy, M., & Becker, J. S. (2008). Recent applications on isotope ratio measurements by ICP-MS and LA-ICP-MS on biological samples and single particles. *International Journal of Mass Spectrometry*, 270(1-2), 1-7.
- 146 Lear, J., Hare, D., Fryer, F., Adlard, P., Finkelstein, D., & Doble, P. (2012). High-resolution elemental bio-imaging of Ca, Mn, Fe, Co, Cu and Zn employing LA-ICP-MS and hydrogen reaction gas. *Analytical Chemistry*. 10.1021/ac301156f
- 147 Ortega, R., Deves, G., & Carmona, A. (2009). Bio-metals imaging and speciation in cells using proton and synchrotron radiation x-ray microspectroscopy. *Journal of the Royal Society Interface*, 6(S649-S658).
- 148 Seuma, J., Bunch, J., Cox, A., McLeod, C., Bell, J., & Murray, C. (2008). Combination of immunohistochemistry and laser ablation ICP mass spectrometry for imaging of cancer biomarkers. *Proteomics*, 8, 3775-3784.
- 149 Bandura, D. R., Baranov, V. I., & Tanner, S. D. (2001). Reaction chemistry and collisional processes in multipole devices for resolving isobaric interferences in ICP-MS. *Fresenius' Journal of Analytical Chemistry*, 370(5), 454-470.
- 150 Bandura, D. R., Baranov, V. I., & Tanner, S. D. (2002). Inductively coupled plasma mass spectrometer with axial field in a quadrupole reaction cell. *Journal of the American Society for Mass Spectrometry*, 13(10), 1176-1185.
- 151 Bandura, D. R., Baranov, V. I., & Tanner, S. D. (2002). Detection of ultratrace phosphorus and sulfur by quadrupole ICPMS with dynamic reaction cell. *Analytical Chemistry*, 74(7), 1497-1502.
- 152 Douglas, D. J., & Tanner, S. D. (1998). Fundamental considerations in ICPMS. In A. Montasser (Ed.), *Inductively Coupled Plasma Mass Spectrometry*: Wiley-VCH.
- 153 Koyanagi, G. K., Baranov, V. I., Tanner, S. D., & Bohme, D. K. (2000). An inductively coupled plasma/selected-ion flow tube mass spectrometric study of the chemical resolution of isobaric interferences. *Journal of Analytical Atomic Spectrometry*, 15, 1207-1210.
- 154 Koyanagi, G. K., Lavrov, V. V., Baranov, V. I., Bandura, D., Tanner, S. D., McLaren, J. W., et al. (2000). A novel inductively coupled plasma/selected-ion flow tube mass

- spectrometer for the study of reactions of atomic and atomic oxide ions. *International Journal of Mass Spectrometry*, 194, L1-L5.
- 155 Tanner, S. D. (2002). Reaction cells and collision cells for ICP-MS: a tutorial review. *Spectrochimica Acta Part B*, 57, 1361-1452.
- 156 Tanner, S. D., & Baranov, V. I. (1999). A dynamic reaction cell for inductively coupled plasma mass spectrometry (ICP-DRC-MS). II. Reduction of interferences produced within the cell. *Journal of the American Society for Mass Spectrometry*, 10(11), 1083-1094.
- 157 Tanner, S. D., & Baranov, V. I. (1999). Theory, design, and operation of a dynamic reaction cell for ICP-MS. *Atomic Spectroscopy*, 20(2), 45-52.
- 158 Armentrout, P. B. (2004). Fundamentals of ion-molecule chemistry. *Journal of analytical atomic spectrometry*, 19, 571-580.
- 159 Arnold, T., Harvey, J. N., & Weiss, D. J. (2008). An experimental and theoretical investigation into the use of H₂ for the simultaneous removal of ArO⁺ and ArOH⁺ isobaric interferences during Fe isotope ratio analysis with collision cell based Multi-Collector Inductively Coupled Plasma Mass Spectrometry. *Spectrochimica Acta Part B: Atomic Spectroscopy*, 63(6), 666-672.
- 160 Chéry, C. C., Günther, D., Cornelis, R., Vanhaecke, F., & Moens, L. (2003). Detection of metals in proteins by means of polyacrylamide gel electrophoresis and laser ablation-inductively coupled plasma-mass spectrometry: Application to selenium. *Electrophoresis*, 24(19-20), 3305-3313.
- 161 D'Illio, S., Violante, N., Majorani, C., & Petrucci, F. (2011). Dynamic reaction cell ICP-MS for determination of total As, Cr, Se and V in complex matrices: Still a challenge? A review. *Analytica Chimica Acta*, 698(1-2), 6-13.
- 162 Hattendorf, B., & Gunther, D. (2000). Characteristics and capabilities of an ICP-MS with a dynamic reaction cell for dry aerosols and laser ablation. *Journal of Analytical Atomic Spectrometry*, 15(9), 1125-1131.
- 163 Jackson, G. P., King, F. L., & Duckworth, D. C. (2003). Efficient polyatomic interference reduction in plasma-source mass spectrometry via collision induced dissociation. *Journal of Analytical Atomic Spectrometry*, 18(9), 1026-1032.
- 164 Mason, P. R. D., & Jeroen Kraan, W. (2003). Attenuation of spectral interferences during laser ablation inductively coupled plasma mass spectrometry (LA-ICP-MS) using an rf only collisions and reaction cell. *Journal of Analytical Atomic Spectrometry*, 17, 858-867.
- 165 Resano, M., Marzo, P., Perez-Arantegui, J., Aramendia, M., Cloquet, C., & Vanhaecke, F. (2008). Laser ablation-inductively coupled plasma-dynamic reaction cell-mass spectrometry for the determination of lead isotope ratios in ancient glazed ceramics for discriminating purposes. *Journal of Analytical Atomic Spectrometry*, 23(9), 1182-1191.

- 166 Vanhaecke, F., Balcaen, L., De Wannemacker, G., & Moens, L. (2002). Capabilities of inductively coupled plasma mass spectrometry for the measurement of Fe isotope ratios. *Journal of Analytical Atomic Spectrometry*, 17(8), 933-943.
- 167 Feldmann, I., Jakubowski, N., Thomas, C., & Stuewer, D. (1999). Application of a hexapole collision and reaction cell in ICP-MS. Part 2. Analytical figures of merit and first applications. *Fresenius' Journal of Analytical Chemistry*, 365(5), 422-428.
- 168 Becker, J. S. (2002). Applications of inductively coupled plasma mass spectrometry and laser ablation inductively coupled plasma mass spectrometry in materials science. *Spectrochimica Acta Part B: Atomic Spectroscopy*, 57B(12), 1805-1820.
- 169 Reed, N. M., Cairns, R. O., Hutton, R. C., & Takaku, Y. (1994). Characterization of polyatomic ion interferences in inductively coupled plasma mass spectrometry using a high resolution mass spectrometer. *Journal of Analytical Atomic Spectrometry*, 9, 881.
- 170 Woods, G. (2005). *Direct elemental analysis of gaoline by Agilent 7500ce ORS ICP-MS*: Agilent Technologies
- 171 McCurdy, E., & Potter, D. (2001). Multielement analysis of unknown sample matrices with a reaction cell system. *ICP-MS Journal*(10), 2-3.
- 172 *Neurological Disorders: Public Health Challenges*. (2006). Geneva: World Health Organization
- 173 Wolozin, B., & Golts, N. (2002). Iron and Parkinson's disease. *Neuroscientist*, 8(1), 22-32.
- 174 Berg, D. (2007). Disturbance of iron metabolism as a contributing factor to SN hyperechogenicity in Parkinson's disease: implications for idiopathic and monogenetic forms. *Neurochemical Research*, 32(10), 1646-1654.
- 175 Berg, D., Gerlach, M., Youdim, M. B. H., Double, K. L., Zecca, L., Riederer, P., et al. (2001). Brain iron pathways and their relevance to Parkinson's disease. *Journal of Neurochemistry*, 79(2), 225-236.
- 176 Braak, H., Tredici, K. D., Rüb, U., de Vos, R. A. I., Jansen Steur, E. N. H., & Braak, E. (2003). Staging of brain pathology related to sporadic Parkinson's disease. *Neurobiology of Aging*, 24(2), 197-211.
- 177 He, Y., Thong, P. S. P., Lee, T., Leong, S. K., Shi, C. Y., Wong, P. T. H., et al. (1996). Increased iron in the substantia nigra of 6-OHDA induced parkinsonian rats: a nuclear microscopy study. *Brain Research*, 735(1), 149-153.
- 178 Kaur, D., & Andersen, J. K. (2002). Ironing out Parkinson's disease: Is therapeutic treatment with iron chelators a real possibility? *Aging Cell*, 1(1), 17-21.
- 179 Wypijewska, A., Galazka-Friedman, J., Bauminger, E. R., Wszolek, Z. K., Schweitzer, K. J., Dickson, D. W., et al. (2010). Iron and reactive oxygen species activity in parkinsonian substantia nigra. *Parkinsonism and Related Disorders*, 16, 329-333.

- 180 Snyder, A. M., & Connor, J. R. (2009). Iron, the substantia nigra and related neurological disorders. *Biochemica et Biophysica Acta*, 1790, 606-614.
- 181 Barlow, B. K., Cory-Slechta, D. A., Richfield, E. K., & Thiruchelvam, M. (2007). The gestational environment and Parkinson's disease: Evidence for neurodevelopmental origins of a neurodegenerative disorder. *Reproductive Toxicology*, 23(3), 457-470.